



EUROPEAN COMMISSION
DIRECTORATE-GENERAL
Joint Research Centre

**Neutron ($n, x\gamma$) cross-section measurements
for ^{52}Cr , ^{209}Bi and $^{206,207,208}\text{Pb}$ from threshold
up to 20 MeV**

Liviu-Cristian Mihaiescu

Institute for Reference Materials and Measurements

2006

EUR 22343 EN

The mission of IRMM is to promote a common and reliable European measurement system in support of EU policies.

European Commission
Directorate-General Joint Research Centre
Institute for Reference Materials and Measurements

Contact information

Arjan Plompen
Address: Retieseweg 111, B-2440 Geel, Belgium
E-mail: Arjan.Plompen@ec.europa.eu
Tel.: +32-14-571 381
Fax: +32-14-571 376

<http://www.irmm.jrc.be>
<http://www.jrc.cec.eu.int>

Legal Notice

Neither the European Commission nor any person acting on behalf of the Commission is responsible for the use which might be made of this publication.

A great deal of additional information on the European Union is available on the Internet.
It can be accessed through the Europa server
<http://europa.eu>

EUR 22343 EN
ISBN 92-79-02885-5
ISSN 1018-5593
Luxembourg: Office for Official Publications of the European Communities

© European Communities, 2006

Reproduction is authorised provided the source is acknowledged

Printed in Belgium

University of Bucharest
Faculty of Physics

**Neutron ($n, xn\gamma$) cross-section measurements
for ^{52}Cr , ^{209}Bi and $^{206,207,208}\text{Pb}$ from threshold
up to 20 MeV**

by

Liviu-Cristian Mihailescu

Thesis submitted for the degree of Doctor of Science

Promotor:
Prof. Dr. D. Bucurescu

Academic year 2005 - 2006

**Neutron ($n, xn\gamma$) cross-section measurements
for ^{52}Cr , ^{209}Bi and $^{206,207,208}\text{Pb}$ from threshold
up to 20 MeV**

by

Liviu-Cristian Mihăilescu

**This thesis is based on the research performed under the daily
supervision of Dr. A. J. M. Plompen**

**This investigation is part of the research program of the Joint Research
Centre of the European Comission and has been carried out at the
Institute for Reference Materials and Measurements (IRMM) in Geel,
Belgium**

Contents

List of Figures	x
List of Tables	1
1 Introduction	3
1.1 The aim of this work	3
1.2 Neutron inelastic scattering, $(n,2n)$ and $(n,3n)$ cross-sections	4
1.3 Motivation of the measurements	5
1.3.1 Waste transmutation in ADS	6
1.3.2 Benchmark for the nuclear codes	7
1.4 Theoretical predictions of the inelastic, $(n,2n)$ and $(n,3n)$ reaction cross-sections and nuclear codes	8
1.5 Structure of this work	10
2 Measurements of the $(n,xn\gamma)$ cross-sections with large volume HPGe detectors	13
2.1 The current standard measurement techniques	13
2.1.1 The (n,n') -technique	14
2.1.2 The $(n,xn\gamma)$ -technique	14
2.2 Characteristics of the time-of-flight measurements	18
2.3 Cross-sections measurement by γ -ray spectroscopy with HPGe detectors	19
2.3.1 Properties of HPGe detectors	19
2.3.2 Gamma ray angular distribution	26
2.3.3 Angle integration - Gauss quadrature	29
2.4 Neutron beam properties at GELINA	32
3 Experimental setup for the $(n,xn\gamma)$ cross-section measurements at GELINA	37
3.1 Experimental setup	38
3.1.1 HPGe detectors	38
3.1.2 Fission chamber	38
3.1.3 Samples	40
3.2 Data acquisition system with conventional electronics	41
3.2.1 The electronics	41
3.2.2 The pulse amplitude channel	43

3.2.3	The time-of-flight channel	45
3.2.4	Gamma flash rejection	47
3.2.5	HPGe absolute peak efficiency measurement	48
3.3	Data analysis	49
3.3.1	Differential gamma production cross-section calculation	50
3.3.2	Sorting the HPGe data	50
3.3.3	HPGe efficiency corrections	51
3.3.4	Neutron fluence	54
3.3.5	Grouping the time-of-flight bins	54
3.3.6	Multiple scattering and neutron flux attenuation	55
3.3.7	Measurement uncertainties	56
3.4	Conclusions	57
4	Data acquisition system with a fast digitizer	59
4.1	The goal of a new acquisition system	60
4.2	Working principle of a fast digitizer	60
4.3	Digital algorithms for signal analysis	62
4.3.1	Auxiliary algorithms	62
4.3.2	Timing algorithms	66
4.3.3	Pulse amplitude algorithm - trapezoid filter	69
4.4	Results of the tested algorithms	72
4.4.1	Start-stop experimental setup for testing different algorithms .	72
4.4.2	Results of the timing algorithms	73
4.4.3	Results of the amplitude algorithm	77
4.4.4	Maximum counting rate	80
4.5	Electronic scheme for the t.o.f. measurement with the digitizer	81
4.6	Results of the $(n, xn\gamma)$ cross-section measurement with the digitizer .	82
4.6.1	Absolute efficiency calibration of the fast digitizer	82
4.6.2	Amplitude and t.o.f. spectra	85
4.6.3	Differential gamma production cross-section	85
4.7	Conclusions	87
5	Results and discussion	89
5.1	^{52}Cr neutron inelastic scattering and $(n, 2n)$ cross-sections	89
5.1.1	Introduction	89
5.1.2	Gamma production cross-sections	90
5.1.3	Total inelastic and level cross-sections	99
5.1.4	Conclusions	103
5.2	^{209}Bi neutron inelastic scattering and $(n, 2n)$ cross-sections	105
5.2.1	Introduction	105
5.2.2	Gamma production cross-sections	105
5.2.3	Total inelastic and level cross-section	123
5.2.4	Conclusions	129
5.3	^{206}Pb neutron inelastic scattering and $(n, 2n)$ cross-sections	130
5.3.1	Introduction	130

5.3.2	Gamma production cross-sections	130
5.3.3	Total inelastic and level cross-sections	142
5.3.4	Conclusions	147
5.4	^{207}Pb neutron inelastic scattering and (n,2n) cross-sections	149
5.4.1	Introduction	149
5.4.2	Gamma production cross-sections	152
5.4.3	Total inelastic and level cross-sections	162
5.4.4	Conclusions	165
5.5	^{208}Pb neutron inelastic scattering, (n,2n) and (n,3n) cross-sections	168
5.5.1	Introduction	168
5.5.2	Gamma production cross-sections	170
5.5.3	Total inelastic and level cross-sections	183
5.5.4	Conclusions	188
6	Conclusions	191
Bibliography		194
Acknowledgements		208
Summary		209
Rezumat		214

List of Figures

1.1	Schematic representation of the neutron inelastic and (n,2n) reactions.	4
2.1	Simplified level scheme of ^{52}Cr	15
2.2	Schematic representation of the band structure in a semiconductor	21
2.3	Schematic representation of an HPGe detector	22
2.4	Shapes for a coaxial semiconductor detector	23
2.5	Schematic representation of a preamplifier	24
2.6	Calculated and experimental signals at the preamplifier output of a large volume HPGe detector	26
2.7	Schematic representation of the inelastic scattering	27
2.8	Typical angular distribution shapes	29
2.9	Even order Legendre polynomials.	31
2.10	Neutron fluence measured at 200 m flight path length.	32
2.11	Beam collimation for the Flight Path 3	33
2.12	Amplitude and t.o.f. spectra of the scattered gamma-flash on the sample	35
3.1	Detectors setup at the 200 m flight path station.	39
3.2	The electronic scheme of the conventional acquisition system.	42
3.3	Amplitude spectrum of an HPGe detector for $^{52}\text{Cr}(\text{n},\text{n}'\gamma)^{52}\text{Cr}$ reaction	44
3.4	Amplitude spectrum for the (n,2n) and (n,3n) reactions on ^{208}Pb sample	44
3.5	The time resolution spectra of the large volume HPGe detectors with conventional electronics.	45
3.6	The dependence of the time resolution spectra on the CFD threshold	46
3.7	Comparison of the efficiency measurement between the two operation modes of the MMPM: free mode and coincidence mode.	49
3.8	Comparison between the measured and the MCNP calculated values of the <i>detector efficiency</i> .	52
3.9	The ratio between the measured <i>acquisition system efficiency</i> and the MCNP calculation.	52
3.10	Example of the HPGe detector absolute peak efficiencies for ^{208}Pb sample	53
3.11	The fission chamber amplitude spectrum.	55
3.12	The neutron flux attenuation and multiple scattering coefficient.	56

4.1	The HPGe preamplifier output recorded with the fast digitizer	61
4.2	Analog shaping circuits	64
4.3	Representation of the LET and ELET timing methods.	67
4.4	Representation of the CFD timing methods.	68
4.5	Pulse shaping procedures: cusp-like, triangular and trapezoidal shaping	70
4.6	The output signal of the trapezoid algorithm.	71
4.7	Start-stop experimental setup for testing different signal processing algorithms.	72
4.8	Results of LET algorithm	74
4.9	Results of the ELET algorithm	75
4.10	The dependence of the resolution of the CFD algorithm on TFA parameters differentiation and integration time.	75
4.11	The dependence of the CFD algorithm resolution on the fraction f and delay.	76
4.12	The comparison of the time resolution with the digitizer and conventional electronics	76
4.13	Results of the trapezoid algorithm	78
4.14	Comparison of the ^{60}Co amplitude spectra with the digitizer and with the conventional electronics.	78
4.15	Rate tests for the Acqiris DC440 digitizer.	80
4.16	The t.o.f. setup based on the fast digitizer Acqiris DC440.	81
4.17	Efficiency measurement with the fast digitizer	83
4.18	The ratio between the measured <i>detector efficiencies</i> with the digitizer and the simulated efficiencies with the MCNP	83
4.19	Detection efficiency comparison between the digitizer and the conventional acquisition system.	84
4.20	Integral amplitude and t.o.f. spectra for the ^{208}Pb measurement with the digitizer	85
4.21	Differential gamma production cross-sections obtained with the fast digitizer for ^{208}Pb	86
4.22	High resolution differential gamma production cross-sections obtained with the fast digitizer for ^{206}Pb	86
5.1	Differential gamma production cross-section for the 1434.07 keV transition from ^{52}Cr at 110° and 150°	90
5.2	Resonance structures in the differential gamma production cross-section of the 1434.07 keV transition of ^{52}Cr	91
5.3	Smooth curve for the integral gamma production cross-section for the 1434.07 keV transition in ^{52}Cr	91
5.4	Full energy resolution for the integral gamma production cross-section for the 1434.07 keV transition in ^{52}Cr	92
5.5	Differential gamma production cross-section for the 935.54 keV transition in ^{52}Cr at 110° and 150°	93
5.6	Integral gamma production cross-section for the 935.54 keV transition in ^{52}Cr	94

5.7	Differential gamma production cross-section for the 1530.67 keV transition in ^{52}Cr at 110° and 150°.	94
5.8	Integral gamma production cross-section for the 1530.67 keV and 1333.65 keV transitions in ^{52}Cr	95
5.9	Integral gamma production cross-section for transition that decay from higher excited levels of ^{52}Cr	96
5.10	The peaks from $^{52}\text{Cr}(\text{n},2\text{n})^{51}\text{Cr}$ HPGe yield integrated over neutron energies between 12 MeV and 20 MeV	98
5.11	$^{52}\text{Cr}(\text{n},2\text{n})^{51}\text{Cr}$ gamma production cross-section	98
5.12	Total uncertainty for the gamma production cross-section of the 749 keV transition from the $^{52}\text{Cr}(\text{n},2\text{n})^{51}\text{Cr}$ reaction.	99
5.13	Total inelastic cross-section of ^{52}Cr	100
5.14	Cross-section of the 1434.09 keV level and its corresponding total uncertainty.	101
5.15	Cross-section of the 2369.63 keV and 2646.9 keV levels.	101
5.16	Cross-section of the higher energy levels.	102
5.17	The γ -ray spectrum of an HPGe detector with the ^{209}Bi sample.	106
5.18	Simplified level scheme of ^{209}Bi	107
5.19	Differential gamma production cross-section for the 896.28 keV transition in ^{209}Bi	108
5.20	Integral gamma production cross-section for the 896.28 keV transition in ^{209}Bi	109
5.21	High resolution integral gamma production cross-section for the 896 keV transition in ^{209}Bi	109
5.22	Differential gamma production cross-section for the 1608.53 keV transition in ^{209}Bi	110
5.23	Integral gamma production cross-section for the 1608.53 keV transition in ^{209}Bi	111
5.24	Differential gamma production cross-section for the 1608.53 keV transition in ^{209}Bi	112
5.25	Integral gamma production cross-section for the 1546.51 keV and 2492.9 keV transition in ^{209}Bi	112
5.26	Integral gamma production cross-section for the transitions from higher lying levels in ^{209}Bi -1-	113
5.27	Integral gamma production cross-section for the transitions from higher lying levels in ^{209}Bi -2-	114
5.28	Integral gamma production cross-section for the transitions from higher lying levels in ^{209}Bi -3-	115
5.29	Integral gamma production cross-section for the transitions from higher lying levels in ^{209}Bi -4-	116
5.30	Integral gamma production cross-section for the transitions from higher lying levels in ^{209}Bi -5-	117
5.31	Simplified level scheme of ^{208}Bi	120
5.32	The (n,2n) γ -ray spectrum of an HPGe detector with the ^{209}Bi sample.	121

5.33 Integral gamma production cross-section for the transitions from the $^{209}\text{Bi}(n,2n)^{208}\text{Bi}$ reaction.	122
5.34 Total inelastic gamma production cross-section of ^{209}Bi	123
5.35 High resolution data for the total inelastic gamma production cross-section of ^{209}Bi	124
5.36 Cross-section of 896.29 keV excited level in ^{209}Bi	125
5.37 Cross-section of levels with higher excited energy in ^{209}Bi -1-	127
5.38 Cross-section of levels with higher excited energy in ^{209}Bi -1-	128
5.39 Simplified level scheme of ^{206}Pb	131
5.40 The γ -ray spectrum of a HPGe detector with the ^{206}Pb sample.	132
5.41 Differential gamma production cross-section for the 803.06 keV transition in ^{206}Pb	133
5.42 Full resolution gamma production cross-section for the 803.06 keV transition in ^{206}Pb	133
5.43 Integral gamma production cross-section for the 803.06 keV transition in ^{206}Pb	134
5.44 Differential gamma production cross-section for the 537.47 keV transition in ^{206}Pb	135
5.45 Integral gamma production cross-section for the 537.47 keV transition in ^{206}Pb	136
5.46 Integral gamma production cross-section for the transitions from higher lying levels in ^{206}Pb -1-	137
5.47 Integral gamma production cross-section for the transitions from higher lying levels in ^{206}Pb -2-	138
5.48 Integral gamma production cross-section for the transitions from higher lying levels in ^{206}Pb -3-	139
5.49 γ -ray spectrum with the ^{206}Pb sample integrated over neutron energies above 8.1 MeV.	141
5.50 Integral production cross-section for the γ -rays from the $^{206}\text{Pb}(n,2n)^{205}\text{Pb}$ reaction.	142
5.51 Total neutron inelastic cross-section for ^{206}Pb - smooth data.	142
5.52 Total neutron inelastic cross-section for ^{206}Pb - full resolution.	143
5.53 The cross-section of the 803.06 keV level in ^{206}Pb	144
5.54 The cross-section of the excited levels above 1.3 MeV in ^{206}Pb -1-.	145
5.55 The cross-section of the excited levels above 1.3 MeV in ^{206}Pb -2-.	146
5.56 Simplified evaluated level scheme of ^{207}Pb	150
5.57 803 keV γ -ray yield from the ^{207}Pb sample	151
5.58 The γ -ray spectrum of an HPGe detector with the ^{207}Pb sample.	153
5.59 Differential gamma production cross-section for the 569.7 keV transition in ^{207}Pb	153
5.60 Full resolution gamma production cross-section for the 569.7 keV transition in ^{207}Pb	154
5.61 Integral gamma production cross-section for the 569.7 keV transition in ^{207}Pb	154

5.62 Differential gamma production cross-section for the 897.78 keV transition in ^{207}Pb .	155
5.63 Integral gamma production cross-section for the 897.78 keV transition in ^{207}Pb .	156
5.64 Integral gamma production cross-section for the transitions from higher lying levels in ^{207}Pb -1-	157
5.65 Integral gamma production cross-section for the transitions from higher lying levels in ^{207}Pb -2-	158
5.66 γ -rays spectrum for the ^{207}Pb measurement integrated over neutron energies above 8.1 MeV.	160
5.67 Integral production cross-section of the γ -rays from the $^{207}\text{Pb}(\text{n},2\text{n})^{206}\text{Pb}$ reaction.	161
5.68 Total neutron inelastic cross-section for ^{207}Pb - smooth data.	163
5.69 Total neutron inelastic cross-section for ^{207}Pb - full resolution.	163
5.70 The cross-section of the 569.7 keV level in ^{207}Pb .	164
5.71 The cross-section of the excited levels above 570 keV in ^{207}Pb -1-.	166
5.72 Simplified evaluated level scheme of ^{208}Pb	169
5.73 Background spectrum with the ^{208}Pb sample in position and no beam.	170
5.74 The prompt γ -ray spectrum of an HPGe detector with the ^{208}Pb sample.	171
5.75 Differential gamma production cross-section for the 2614.5 keV transition in ^{208}Pb .	172
5.76 Full resolution gamma production cross-section for the 2614.5 keV transition in ^{208}Pb .	173
5.77 Integral gamma production cross-section for the 2614.5 keV transition in ^{208}Pb .	173
5.78 Differential gamma production cross-section for the 583.19 keV transition in ^{208}Pb .	175
5.79 Integral gamma production cross-section for the 583.19 keV and 860.56 keV transitions in ^{208}Pb .	175
5.80 Integral gamma production cross-section for the transitions from higher lying levels in ^{208}Pb -1-	177
5.81 Integral gamma production cross-section for the transitions from higher lying levels in ^{208}Pb -2-	178
5.82 Integral gamma production cross-section for the transitions from higher lying levels in ^{208}Pb -3-	179
5.83 Integral gamma production cross-section for the transitions from higher lying levels in ^{208}Pb -4-	180
5.84 γ -ray spectrum with the ^{208}Pb sample integrated over neutron energies above 7.4 MeV.	181
5.85 Integral cross-section of the γ -rays from the ($\text{n},2\text{n}$) and ($\text{n},3\text{n}$) reactions on ^{208}Pb .	182
5.86 Total neutron inelastic cross-section for ^{208}Pb .	184
5.87 The cross-section of the 2614.5 keV level in ^{208}Pb .	185
5.88 The cross-section of the excited levels above 2614 keV in ^{208}Pb -1-.	186
5.89 The cross-section of the excited levels above 2614 keV in ^{208}Pb -2-.	187

List of Tables

2.1	The roots and weights for integration of gamma-ray angular distributions with the Gauss quadrature.	31
3.1	HPGe detectors used during the 5 runs with different samples	39
3.2	Samples dimensions and isotopic composition	40
4.1	RMS _{noise} values with and without the detector coupled to the digitizer input.	63
4.2	HPGe detector amplitudes for different full scale range of the digitizer. .	79
5.1	Branching ratios for levels in ²⁰⁹ Bi nucleus.	119
5.2	Branching ratios for levels in ²⁰⁶ Pb nucleus.	140
5.3	Corrections for the isotopic composition of ²⁰⁷ Pb sample	149
5.4	Branching ratios for levels in ²⁰⁷ Pb nucleus.	159
5.5	Corrections for the isotopic composition of ²⁰⁸ Pb sample results . . .	168
5.6	Branching ratios for levels in ²⁰⁸ Pb nucleus.	180
6.1	The number of observed γ -ray in every studied reaction.	192

Chapter 1

Introduction

1.1 The aim of this work

The need for energy in the future motivates a major part of the research that is done in nuclear physics. Detailed calculations are needed for the design of the future generation of nuclear reactors (e.g. Accelerator Driven Systems (ADS)) in order to increase the safety of such devices and to reduce the construction costs. Reliable nuclear data are needed to increase the confidence in the reactor calculations. Such nuclear data can be produced either directly from the experiments or indirectly with nuclear codes. The latter one has the advantage to predict the nuclear data at energies and for nuclei that are not easily accessed by the experiments. But, in order to achieve a reliable prediction power, the nuclear codes need to be validated by experimental results. Moreover, the present nuclear codes are able to predict only average cross-sections, while the experiments show fine resonance structures in the cross-sections of different reactions.

The goal of the present work can be divided in two parts. Firstly, one aimed to measure very precisely the cross-sections of the neutron inelastic scattering on five different isotopes: ^{52}Cr , ^{209}Bi and $^{206,207,208}\text{Pb}$. In addition to the neutron inelastic scattering, the $(n,2n)$ cross-sections were measured for all five nuclei and the $(n,3n)$ cross-section was measured for ^{208}Pb . The energy range of interest for this set of experiments was from the inelastic threshold up to 20 MeV. The precision of the present experiments consists of unprecedented resolution in the energy of the incident neutron and in a total uncertainty of about 5 % for the main quantities that were measured. Such precision of the data is needed for the applications. To obtain this precision of the data, long data acquisition runs were expected.

Secondly, in order to increase the efficiency of the data acquisition, it was proposed to investigate the possibility to use a fast digitizer for the data acquisition in the $(n,xn\gamma)$ cross-sections measurements. This investigation went in parallel with the $(n,xn\gamma)$ cross-sections measurements with the conventional electronics. Following the feasibility tests, a new data acquisition system based on a fast digitizer was created and it can be used at GELINA for further measurements.

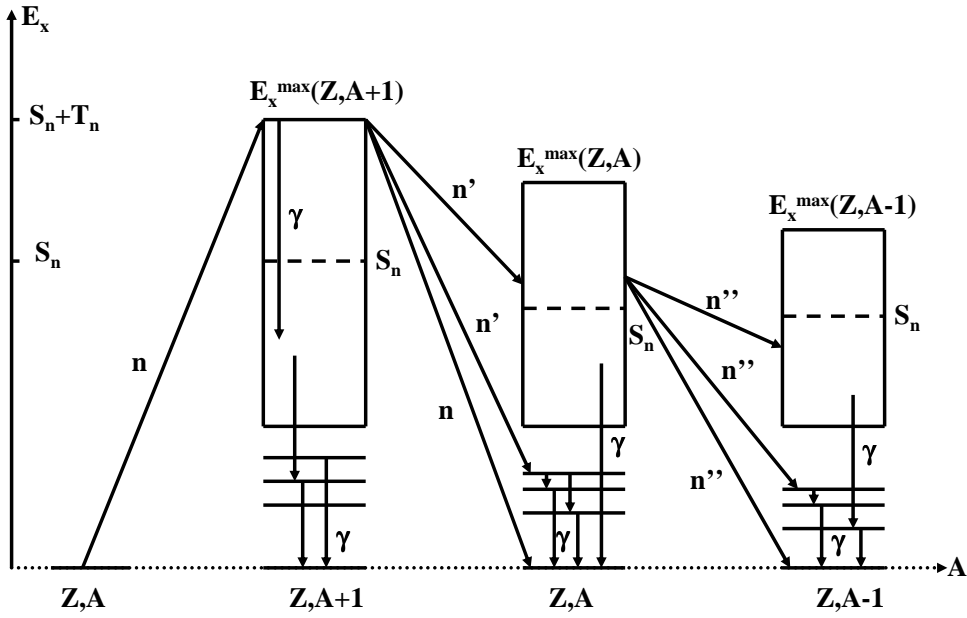


Figure 1.1: Schematic representation of the neutron inelastic and $(n,2n)$ reactions. The elastic scattering and the neutron capture are always in competition with the $(n,xn\gamma)$ reactions with $x=1,2,3\dots$

1.2 Neutron inelastic scattering, $(n,2n)$ and $(n,3n)$ cross-sections

At incident neutron energies below 20 MeV, different reaction channels are opened and their importance in the total neutron cross-section changes with the energy. A schematic representation is shown in Fig. 1.1 for the most important reaction channels opened at energies below 20 MeV. An important reference on the energy scale is the energy of the inelastic threshold. For the nuclei that were studied in this work, the inelastic threshold varies from several hundreds of keV up to few MeV.

For most non-fissile nuclei, below the inelastic threshold the elastic scattering and the neutron capture reactions are the only observable reaction channels. The reactions with emission of charged particles have in general a higher threshold or if they are energetically possible, their cross-section is very small.

In Fig. 1.1, after the interaction of the incident neutron with the kinetic energy T_n with the target nucleus (Z,A) , the system $(Z,A+1)$ has a maximum excitation energy equal to $S_n + T_n$, where S_n is the binding neutron energy in the $(Z,A+1)$ nucleus. If T_n is lower than the energy of the first excited level in (Z,A) nucleus, the $(Z,A+1)$ system can decay only by a cascade of γ -rays to its ground state, process named neutron capture, or the neutron n is emitted and the (Z,A) nucleus is left in the ground state. The latter process is the elastic scattering.

At energies higher than the inelastic threshold, the inelastic scattering becomes possible. The $(Z,A+1)$ system emits a neutron n' and the residual nucleus is left in an excited state. From this excited state, the residual nucleus (Z,A) decays to the

ground state either directly through a single γ -ray, or through a cascade of γ -rays.

If the incident neutron energy exceeds the threshold of the ($n,2n$) reaction, the emission of the n' neutron could be followed by the emission of a second neutron n'' and the nucleus ($Z,A-1$) is produced. Differently to the inelastic scattering, the residual nucleus ($Z,A-1$) can be left directly in the ground state after the emission of the two neutrons in the ($n,2n$) reaction. With the increase of the incident neutron energy, more neutrons can be emitted.

In the other reaction channels that are open at energies below 20 MeV charged particles are emitted. In most of the cases, because of the Coulomb barrier, these reactions with emission of charged particle have small cross-section compared with the reactions described above.

The cross-sections of the reactions studied in this work (neutron inelastic, ($n,2n$) and ($n,3n$)) can be measured in two different ways: either the outgoing neutrons or the γ -rays are detected. The latter were detected in the experiments described in this work and the method will be named ($n,xn\gamma$)-technique. The main quantities that are measured in such experiment are defined in the following.

The basic measured quantity in these experiments is the production cross-section of the γ -rays emitted by the residual nucleus. This is the probability that an incident neutron interacts with a target nucleus and a given γ -ray is emitted. These can be easily generalized to the other ($n,xn\gamma$) reactions with $x=2,3,\dots$. The total inelastic cross-section represents the probability that an incident neutron interacts inelastically with a target nucleus without any condition on the energy of the emitted γ -ray. In the inelastic scattering, the level cross-section is the probability that the residual nucleus is left in a given excited state directly after the emission of the neutron.

1.3 Motivation of the measurements

Despite the large number of experiments performed in the past, there is still a lot to be improved for the neutron cross-section data at energies below 20 MeV and especially for the cross-sections of the ($n,xn\gamma$) reactions with $x=1,2,3$.

The existing experimental cross-sections data for ($n,xn\gamma$) ($x=1,2,3$) reaction on ^{52}Cr , ^{209}Bi , ^{206}Pb , ^{207}Pb and ^{208}Pb are in majority of the cases point data and in many cases they contradict with each other. Moreover, the total uncertainty of the existing data did not meet the requirements of the applications. From previous measurements (ex. Ref. [99]) resonance structures were observed in the neutron inelastic scattering cross-sections at energies just above the inelastic threshold. Such resonance structures can have an impact to the precise reactor calculations. To improve the cross-sections data for the ^{52}Cr , ^{209}Bi , ^{206}Pb , ^{207}Pb and ^{208}Pb isotopes, a new set of measurements were needed that should cover the full energy range of interest, from the inelastic threshold up to 20 MeV with a very good neutron energy resolution.

The ($n,xn\gamma$) reactions represent an important energy loss mechanism. Compared with the elastic scattering, at least an energy equal to the excitation energy of the

first excited level is lost in only one inelastic scattering. Much more energy is lost in the $(n,2n)$ and $(n,3n)$ reactions. Moreover, in the $(n,xn\gamma)$ reactions with $x \geq 2$ more neutrons are produced. Usually for materials like Cr, Bi and Pb, the inelastic process represents about 30% of the total neutron cross-section. With the increase of the energy of the incident neutron the $(n,xn\gamma)$ reactions with $x \geq 2$ enter in competition with the inelastic scattering and at the maximum they have comparable cross-sections. Because of this, precise cross-sections for the $(n,xn\gamma)$ reactions are needed for calculations of neutron propagations in applications. The new generation of nuclear reactors and in particular the Accelerator Driven Systems used for waste transmutation are the immediate application where precise neutron data are needed. Other application where such data may be used are the spallation targets of different research facilities, the dosimetry calculations for the space crafts, the fusion reactors, production of isotopes for medicine or even in the prediction of the single upsets events in the electronic devices. From these applications, only the Accelerator Driven Systems will be described in the following. The use of precise nuclear data for benchmarking of the nuclear codes will be detailed as well.

1.3.1 Waste transmutation in ADS

The disposal of radioactive wastes resulting from industrial nuclear energy production has still to find a fully satisfactory solution, especially in terms of environmental and social acceptability. One solution is to reduce the volume and the radio-toxicity of the waste before the final storage in deep geological repositories.

The volume and the radio-toxicity of the waste can be reduced both in critical reactors and sub-critical accelerator driven system (ADS). Critical reactors, however, loaded with fuel containing large amounts of minor actinides pose safety problems caused by unfavorable reactivity coefficients and small delayed neutron fraction.

The main characteristics of ADS are the sub-criticality and the fact that it allows to reach maximum transmutation rates while operating in a safe manner. The ADS is a combination of a sub-critical core and an external neutron source which may be a linear accelerator or a cyclotron. The external neutrons are produced in a spallation reaction of the accelerated particles on a target with a high atomic number. Many of the present designs for the ADS consider protons to be accelerated at energies of the order of about 1 GeV. For a lead target one proton of an energy of 1 GeV produces about 30 highly energetic neutrons.

Two are the main conditions that the accelerator that drives the ADS has to fulfill: beam powers in the MWatt range and an energetic efficiency of about 50 %, which means that the beam power represents about half of the consumed power. For the spallation target, the Pb-Bi eutectic is one of the most studied solutions. Such target has the advantage of high Z number, implicitly producing a large number of neutrons and has a low melting point of about $125^{\circ}C$. At these temperatures, vast experience exists already from the sodium cooled reactors. The Pb-Bi eutectic mixture can be used also for the cooling system, through natural convection.

The recent study of Aliberti [43] stressed the impact of the nuclear data uncertainties on the reactor parameters uncertainties in the particular case of the ADS.

With the actual reaction cross-sections databases the estimated uncertainties for the ADS parameters (e.g. k_{eff}) are fairly significant and higher than the corresponding values obtained for standard critical cores. Cross-sections measurement for both fuel components (e.g. minor actinide) and structure materials are needed especially below 20 MeV.

In terms of nuclear reactions, the required data for the design calculation of the ADS refers to the elastic scattering, neutron capture, $(n,xn\gamma)$ and (n,f) . The precision of $(n,xn\gamma)$ cross sections influences the calculations for the neutron propagation in the reactor and the calculations for the shielding design and radioprotection.

In the reactor calculations certain limits on the uncertainty of different parameters are defined as an objective. Such target uncertainties for important reactor quantities (ex. k_{eff}) have been converted to target uncertainties for, amongst others, inelastic scattering cross sections by sensitivity analyses [43–46], resulting in requirements that vary between 5 and 20% according to isotope abundance and inelastic threshold. To achieve this type of accuracy, additional efforts are required.

1.3.2 Benchmark for the nuclear codes

Various nuclear codes were developed to describe the physics behind the interaction of different incident particles with the atomic nucleus. The nuclear codes can be seen first as a nuclear physics tool and secondly as tool for producing nuclear data.

As a tool for nuclear physics, different models were implemented in the nuclear codes for the reaction mechanisms and for the structure of the nucleus. The cross-sections obtained with such codes are first compared with the experimental results. From the comparison of the two types of results, calculated and experimental, one can improve the values for the parameters of the models implemented in the code. Reversely, if the nuclear code reaches a certain precision the calculation can be used to give an indication on the reliability of new experiments.

The nuclear codes can be used for the prediction of the reaction cross-section where the experimental data are missing. Such predictions can be made either for the nuclei that are difficult to be studied experimentally or for energies and processes that are not easy to achieve. The nuclear codes may produce reaction cross-sections on the entire energy range of interest for the applications, from thermal neutrons up to hundreds of MeV. An advantage of the nuclear codes is that the cross-section of all the reaction channels may be obtained in one calculation.

Reliability of the nuclear model calculations is limited by the considerable freedom in the choice of the parameters as for example the parameters of the optical model, the level densities and pre-equilibrium reactions [47–50]. Furthermore, low energy cross sections exhibit fluctuations as a consequence of the underlying nuclear resonances, whose energy spacing and widths are inherently stochastic. Nuclear models only handle such fluctuations on average, whereas transport calculations benefit from knowing the actual structure [51,52]. Clearly, new measurement efforts are inevitable in order to make substantial progress.

1.4 Theoretical predictions of the inelastic, ($n,2n$) and ($n,3n$) reaction cross-sections and nuclear codes

The reaction mechanisms used in the description of the interaction between the incident neutron (or any other incident particle in general) and the atomic nucleus may be classified in three categories according to the interaction time. The first type is the direct reaction in which the interaction time between the neutron and the nucleus is very short and one or two collisions take place inside the nucleus. The other extreme is the compound mechanism in which the incident neutron spends sufficient time inside the nucleus to allow the statistical equilibrium to be established. Many interactions take place between the incident neutron and the nucleons inside the nucleus. The third reaction mechanism is the pre-equilibrium, which is an intermediate step between the direct and the compound nucleus mechanisms. In the pre-equilibrium reactions, several interactions take place between the neutron and the nucleus, but the statistical equilibrium is not yet reached.

In absence of fission and of any reaction with emission of charged particles, below the inelastic threshold, the only other opened reaction channels are the elastic scattering and the neutron capture. The neutron capture reaction is completely described in the frame of the compound nucleus mechanism. The elastic scattering has a major direct component (shape elastic scattering) and a small component described by the compound nucleus mechanism (compound elastic scattering). In the reaction models, the cross-section of the shape elastic scattering is deduced from the optical model. The reaction cross-section, which is the difference between the total and the shape elastic cross-section, is shared between the neutron capture and the compound elastic scattering.

The inelastic scattering reaction channels open above the inelastic threshold. At energies below the continuum, at about 4 MeV, the inelastic scattering has a compound nucleus component and a direct component. The compound interaction rises rapidly just above the threshold and then decreases with the increase of the incident energy. The cross-section from direct interaction increases slowly with the increase of the energy.

At energies where the continuum starts, the pre-equilibrium interaction has to be considered in the calculations for a better description of the experimental cross-sections. Even if the direct and the pre-equilibrium interactions have a higher contribution to the total cross-section with the increase of the neutron energy, the compound mechanism is still the dominant one below 20 MeV.

These reaction mechanisms were implemented in different nuclear codes in order to reproduce as well as possible the experimental data. In this work, the results of the present measurements are compared with existing experimental data, with theoretical cross-sections and with evaluated data. The theoretical cross-sections were obtained with the Talys code [6] with the default input parameters of the version 0.57. The results of these calculations were provided by the authors of the code. The purpose of this comparison was only to illustrate how well the calculations

of the present days can describe the experimental data. No investigation was done in this work for the impact of different code parameters on the calculated cross-sections. Such investigations for the large amount of experimental cross-section data that are presented in this work could be very complex and time consuming.

Talys [6] is a state-of-art code that includes some of the most recent evaluations of the parameters for the nuclear models. It can be used for projectiles as neutron, proton, deuteron, triton, ^3He , alpha and γ -ray and for target nuclei with the mass number between 12 and 339. The energy of the incident particle can be between 1 keV and 250 MeV. The code is continuously updated and improved by its authors [6].

A short description of the nuclear reaction models that are used to described the $(n, xn\gamma)$ reactions will be given in the following.

Optical model

One of the first ingredients used in the cross-sections calculation is the optical model potential. The optical model describes the complex interaction between the projectile and the target in a more simple way, by means of a phenomenological potential. This model divides the reaction flux into a shape elastic interaction and a part describing all the non-elastic reaction channels.

The basic observables predicted by the optical model are the elastic cross-sections and the reaction cross-sections. Other observable predicted by the optical model are the angular distribution of the elastically scattered projectile and the transmission coefficients and the distorted wave functions that are used for the further steps of the cross-section calculations.

The optical model potential has two components, a real one and an imaginary one. Every of these two components have a term that describes the volume interaction, the surface interaction and the spin-orbit interaction. To describe these interactions the optical model uses parameters as the well depths, the nuclear radius and the diffuseness. An additional term that accounts for the Coulomb interaction is needed for the description of the interaction of the charged projectile with a nucleus. All these parameters of the optical model potential depend on the incident energy, on the projectile type and on the target. Global and local sets of such parameters exist along the whole nuclear chart. In the Talys code, the local set of optical model parameters is used when such set is available [6].

Direct reactions

The direct reactions are described by models like the Distorted Wave Born Approximation (DWBA) for the near-spherical nuclei and coupled channels for the deformed nuclei. For the coupled channels formalism, the ground state and several inelastic states are included in the coupling scheme. Various collective models (symmetric rotational model, harmonic rotational model, vibration-rotational model, asymmetric rotational model) are used to describe the structure of the deformed nuclei.

Compound reactions

In the compound nucleus model, the projectile and the target form a compound system that reaches the statistical equilibrium. The compound nucleus has maximum excitation energy and a range of values for the spin and parity. From this state of statistical equilibrium the compound nucleus decays. The compound nucleus reaction cross-section is proportional with the transmission factors through the nuclear surface. A width fluctuation correction factor is considered for the correlation that exists between the incident and the outgoing waves. Above few MeV, where many reaction channels are opened, the width fluctuation correction factor can be neglected.

Pre-equilibrium

The pre-equilibrium reactions are described by means of the exciton model. In this model, the nuclear state is characterized by the total energy and the total number of particles and holes above and respectively below the Fermi surface. The particle-hole pairs are called excitons. In the exciton model, the way of sharing the excitation energy between different particle-hole configurations have an equal probability. The number of excitons changes in time as a result of two-body intranuclear collisions. Once an exciton is formed, it is subject to a particle emission. Further interactions can change the number of excitons either by creation of another particle-hole pair or by annihilation of the particle-hole pair. In the pre-equilibrium reactions, the emitted particles have some memory of the incident energy and direction, which is not the case for the compound nucleus model. In the Talys code the two-component exciton model is used in which the protons and the neutrons are considered as distinct particles. A more simple case is the one-component exciton model that assumes no difference between the protons and the neutrons [6].

Level densities

In the statistical models for predicting cross-sections, nuclear level densities are used at excitation energies where discrete level information is not available or incomplete. The default level density model in Talys is the Gilbert and Cameron model. In this model, the excitation energy range is divided in a low energy part from zero to a matching energy and high energy part from the matching energy to infinity. For the low excitation energy, the number of discrete levels increases exponentially according to the constant temperature law. For higher energies, the level density is described by the Fermi gas model with the Ignatyuk correction for the shell effects.

1.5 Structure of this work

The introduction chapter of this thesis describes the measured quantities and shortly motivates the work done for this project. In this chapter a short description is given for the reaction mechanisms and for the models used in the theoretical calculation that served as a comparison for the experimental results from this work.

The second chapter presents the techniques currently used for the measurements of the $(n, xn\gamma)$ cross-sections ($x=1,2,3$). More details were given for the $(n, xn\gamma)$ -technique that was used in the present set of experiments. The general characteristics of γ -ray spectroscopy and of the time-of-flight measurements with germanium detectors are given in the same chapter.

Chapter 3 describes the experimental setup used for the cross-section measurements. Prior to this project the setup was used for the measurements of ^{58}Ni inelastic cross-sections. For the measurements presented in this work, the setup was continuously changed and upgraded in order to gain detection efficiency. The data acquisition with conventional electronics and the details regarding the data analysis are given here.

In parallel with the cross-section measurements it was investigated the possibility to replace the data acquisition system with the conventional electronics with an innovative data acquisition based on a fast digitizer. The feasibility tests for the use of a fast digitizer for time-of-flight measurements at GELINA with large volume HPGe detectors were presented in Chapter 4. This chapter contains also the comparison of the acquisition system based on the conventional electronics and the acquisition system with the fast digitizer.

Chapter 5 contains the results for the cross-section measurements of the five nuclei that were investigated here: ^{52}Cr , ^{209}Bi , ^{206}Pb , ^{207}Pb and ^{208}Pb . This chapter is structured in 5 relatively independent sections, one for each nucleus. Conclusions were given for every section.

Chapter 6 presents the final conclusions of this thesis.

Chapter 2

Measurements of the $(n,xn\gamma)$ cross-sections with large volume HPGe detectors

2.1 The current standard measurement techniques

The measurement of the neutron inelastic cross-sections below 20 MeV neutron energy may be done using two different techniques: the (n,n') technique and the $(n,n'\gamma)$ -technique. The last will be named in the following $(n,xn\gamma)$ because the technique may be easily extended to the measurement of (n,xn) cross-sections with $x=2,3,\dots$ [152].

The first technique is based on the detection of the outgoing neutrons with a neutron sensitive detector. The incident neutron beam is usually mono-energetic and the primary measured quantities are the level cross-sections.

The second technique, $(n,xn\gamma)$, is based on the detection of the emitted γ -rays by the residual nucleus from the (n,xn) reaction. The $(n,xn\gamma)$ -technique can also be used with a white neutron source and the primary measured quantities are the gamma production cross-sections. For inelastic scattering ($x=1$), based on the level scheme of the studied nucleus, the level cross-sections and the total inelastic cross-sections can be constructed.

The two techniques provide some complementary information. First of all, the angular distribution of the emitted neutrons and to some degree the secondary neutron energy distribution can only be determined with the (n,n') -technique. The comparison of the level cross-section obtained in the two techniques may give information about the γ -ray feeding from higher excitation energies to that particular level. In the set of experiments presented in this work the $(n,xn\gamma)$ -technique was used. A general description of the two techniques will be given in the following, with more emphasis on the $(n,xn\gamma)$ -technique.

2.1.1 The (n,n') -technique

The (n,n') -technique is used with a quasi-monoenergetic incident neutron beam. The inelastic scattered neutrons are detected with neutron sensitive detectors (e.g. plastic scintillators, liquid scintillators, Li glass detectors) placed at given angles with respect to the direction of the incident beam. The scattered neutron energy is determined by the time-of-flight method. The double differential (angle and energy) cross-section of individual levels are measured. When the energy resolution of the spectrometer is larger than the energy spacing between excited levels the method provides only the cross-section of a group of levels. The total inelastic cross-section can be constructed as a sum of the level cross-sections up to the energy of the highest observed excited level.

The (n,n') -technique has the advantage that it allows the measurement of the level cross-section for isomer excited levels and for the 0^+ excited levels. It has also some disadvantages. To obtain the excitation functions, the measurement has to be repeated for different incident neutron energies when a quasi-monoenergetic beam is used. Two problems are common to this technique. The first one is that detailed information is needed for the angular distribution of the outgoing neutrons to perform the angle integration. Secondly at low energies the response function of the detector is difficult to be determined. Some neutron detectors have a poor sensitivity below energies of about 800 keV and extrapolations below this threshold are needed for the integral yield. The determination of the response function of the detector needs special attention. Usually this is done with calibration sources. The background from the scattered neutrons around the setup has to be treated with special care because this may reduce the detection sensitivity.

Some examples for the use of the (n,n') -technique are given in Refs. [40, 41].

2.1.2 The $(n,xn\gamma)$ -technique

In the $(n,xn\gamma)$ -technique the prompt γ -rays emitted by the residual nucleus are detected. The first experiments that applied this technique used scintillators, mainly NaI detectors, for the gamma-ray detection. These detectors have a poor energy resolution and the identification of the gamma rays in complex spectra was difficult. The development of the semiconductor detectors, first Ge(Li) and then HPGe (High Purity Germanium) detectors, improved significantly the performances of such experiments. With HPGe detectors γ -ray peaks separated by about 2 keV may be resolved, allowing a very good identification of the transitions of the residual nucleus. With such detectors γ -rays and implicitly decaying levels from relatively high excitation energy (up to 4-5 MeV) can be identified. Moreover, in addition to the neutron inelastic cross-section measurement ($x=1$), the technique can be used easily for the (n,xn) cross-section measurement with $x \geq 2$. It has to be mentioned that the technique can be used for capture measurements ($x=0$) as well, but for lower neutron energies. By γ -ray identification it is possible to identify the (n,xn) reaction channels ($x \geq 1$) for incident energies above threshold.

The $(n,xn\gamma)$ -technique may be used both with quasi-monoenergetic beams [56,

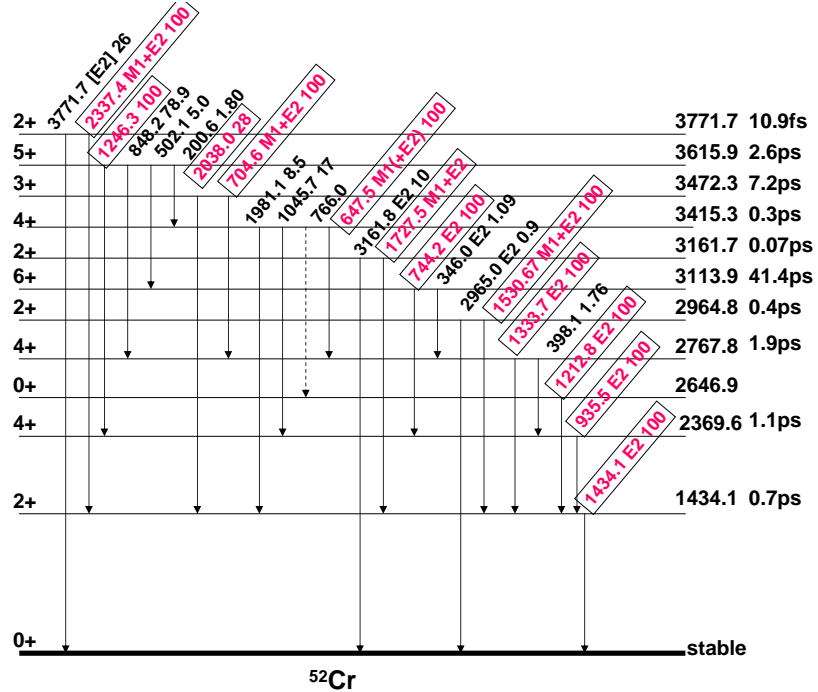


Figure 2.1: Simplified level scheme of ^{52}Cr . Observed transitions are highlighted.

147] and with white neutron beams [58, 59, 99, 152]. In this work the white neutron beam from GELINA was used. The advantage of a white neutron beam over a quasi-monoenergetic one is that the excitation functions are measured simultaneously for all neutron energies, in only one experiment. In the ideal case, the excitation function may appear continuous.

The γ -ray detector is placed at a given angle with respect to the incident neutron beam direction. Differential gamma production cross-sections are obtained as primary quantities. For the γ -ray angular integration, knowledge of the γ -ray angular distribution from additional experiments is necessary if the measurement is done only at one angle. For the particular case of two detection angles a special γ -ray angular integration procedure was used in the present work (see Sec. 2.3.3 for details). Following the angular integration the $(n, xn\gamma)$ technique gives the gamma-ray production cross sections $\sigma_{n'\gamma}(L_i \rightarrow L_j)$ of observed transitions (L_i is the i^{th} excited level and $i=0$ is the ground state — g.s.).

For inelastic scattering, besides the gamma-ray production cross sections, important quantities are the total inelastic cross section $\sigma_{n'}$ and the level cross sections σ_{n',L_i} . The latter are the cross sections for leaving the target nucleus in the excited state L_i , immediately following scattering but before gamma-decay. The total inelastic cross-section may be written as a sum of all level cross-sections:

$$\sigma_{n'}(E) = \sum_{i=1}^{E_x(L_i) \leq E_{in}} \sigma_{n',L_i}(E), \quad (2.1)$$

where E is the energy of the incident neutron in the center of mass. Always in

in the experiment there is a maximum excitation energy up to which excited levels are observed. Because of this, above this maximum energy Eq. 2.1 becomes only a lower limit for the total inelastic cross-section. As an example, for ^{52}Cr (see Fig. 2.1) the maximum observed excited level was 3.77 MeV. Since for each excited level one γ -ray is observed, the sum in Eq. 2.1 could be performed over all excited levels up to 3.77 MeV. Above 3.77 MeV energy of the incident neutrons, the total inelastic cross-section calculated with Eq. 2.1 is a lower limit for the total inelastic cross-section as mentioned above.

Gamma-ray production cross sections are linked to the cross section that leads to a particular excited level, including the contribution of higher excited levels that populate the level following de-excitation. Let's call this the level population cross section (or level production cross section) σ_{n',L_i}^p . This level population cross-section may be written as:

$$\sigma_{n',L_i}^p = \frac{\sigma_{n'\gamma}(L_i \rightarrow L_{k_i})}{p_\gamma(L_i \rightarrow L_{k_i})} \quad (2.2)$$

where k_i is the level populated by the γ -ray that was observed following the decay of the initial level L_i . $p_\gamma(L_i \rightarrow L_{k_i})$ is the gamma-ray emission probability for the transition from level L_i to L_{k_i} . The level population cross section may be determined as soon as one of the emitted gamma-rays is measured and its emission probability is known (e.g. from the Nuclear Data Sheets [53, 131]).

The total inelastic scattering cross section is the sum of the cross-sections carried by all transitions that decay directly to the ground state. If the direct transition to the ground state is weak and cannot be observed, any other strong transition from that particular level may be used in the construction of total inelastic scattering cross section, taking into account the appropriate branching ratio. With these considerations the total inelastic scattering cross section may be written as:

$$\begin{aligned} \sigma_{n'}(E) &= \sum_{i=1}^{E_x(L_i) \leq E} p(L_i \rightarrow g.s.) \sigma_{n',L_i}^p(E) \\ &= \sum_{i=1}^{E_x(L_i) \leq E} \sigma_{n',\gamma}(E, L_i \rightarrow L_{k_i}) \frac{p(L_i \rightarrow g.s.)}{p_\gamma(L_i \rightarrow L_{k_i})} \end{aligned} \quad (2.3)$$

where $p(L_i \rightarrow L_j)$ is the transition probability from level L_i to level L_j . The last expression is the practical one for the application of this technique. Obviously, the nature of this expression is such that the transition of the first level to the ground state serves as the basis. The direct transitions of higher lying levels to the ground state become effective when the incident energy exceeds the excitation energy of a level.

As an example, for ^{52}Cr the total inelastic cross-section was constructed using the gamma-production cross-section of only the following transitions (see Fig. 2.1): 1434 keV, 1530 keV, 1727 keV and 2337 keV. The last three transitions were used instead of 2965 keV, 3161 keV and respectively 3771 keV transitions that decay directly to the ground state but have a low intensity. Above about 3.77 MeV neutron

energy, the so constructed inelastic cross-section is only a lower limit to its exact value.

Finally, by similar reasoning a level cross section is given by

$$\sigma_{n',L_i}(E) = \sigma_{n',L_i}^p(E) - \sum_{j>i}^{E_x(L_j) \leq E} p(L_j \rightarrow L_i) \sigma_{n',j}^p(E) \quad (2.4)$$

where, as before, each $\sigma_{n',j}^p$ is determined from a measurement of the most suitable gamma-ray depopulating the level L_j . The above expression is only sensitive to incomplete knowledge of the level scheme. An alternative expression

$$\sigma_{n',L_i}(E) = \sigma_{n',L_i}^p(E) - \sum_{j>i}^{E_x(L_j) \leq E} \sigma_\gamma(E, L_j \rightarrow L_{k_i}) \frac{p(L_j \rightarrow L_i)}{p_\gamma(L_j \rightarrow L_{k_i})} \quad (2.5)$$

requires the gamma-production cross sections for all transitions feeding the level L_i and is therefore more sensitive to unobserved transitions, whether weak, obscured by background or entirely converted.

For example, using Eq. 2.4, the level cross-section of the second excited level of ^{52}Cr , 2369 keV (Fig. 2.1), was constructed using the gamma production cross-section of the 935 keV transition as the basis and from this was subtracted the weighted sum of the gamma production cross-section of the following transitions: 1333 keV, 744 keV, 647 keV, 1246 keV.

In summary, for an optimal application of the $(n, nx\gamma)$ -technique, one must identify and measure at least one gamma-ray per excited level. These gamma-rays appear among possibly many weaker gamma-rays, so that gamma-ray energy resolution must be as high as possible. Of course background should be minimal and peak efficiency should be as high as possible.

The method can only be applied fully for the sequence of levels starting from the first excited level up to the highest excited level for which decay information is complete and for which it is sure that no levels were omitted with lower excitation energy. The nature of the expression 2.3 is such that incomplete information or missed transitions that decay directly from higher levels to the ground state result in a lower bound to the total inelastic cross section.

This method of constructing the total inelastic cross-section should work better for the even-even nuclei where almost all excited levels decay to the ground state through the first excited level. In the inelastic scattering process the residual nucleus is formed with relatively high angular momenta and in consequence the direct transitions from the highly excited states to the 0^+ ground state are strongly inhibited [152]. All these highly excited states decay preferentially through a cascade of transitions. For these nuclei the Eq. 2.3 is a very good approximation for the exact value of total inelastic cross-section. From the nuclei that were studied in this work this remark will apply to ^{52}Cr , ^{206}Pb and ^{208}Pb . In contrast, the same conditions for Eq. 2.4 and Eq. 2.5 lead to upper bounds for the level inelastic cross section above the highest observed excited level. For the level cross-sections this method is very

18 Measurements of the $(n,xn\gamma)$ cross-sections with large volume HPGe detectors

sensible to any missing transition. The resulting upper bounds for the level inelastic cross-section may differ significantly from the exact values.

Unlike the (n,n') technique, the $(n,xn\gamma)$ -technique does not allow the measurement of the level cross-section of the isomeric states. One example is the ^{207}Pb nucleus. The 3rd excited level, 1633.368 keV, is an isomer with a life time of 0.806 ns. Limitations appear as well in the case of the 0⁺ excited levels that decay through an E0 to the ground state of an even-even nucleus. This is the case for example in ^{206}Pb where the second excited level, 1165 keV, decays directly to the ground state through an E0 transition that is fully converted and in addition the branching ratio to the first excited level is smaller than 0.3. Such level cross-section cannot be measured with the $(n,xn\gamma)$ -technique.

For the (n,xn) cross-section with $x \geq 2$ the total cross-sections cannot be constructed as in the case of inelastic scattering because the branching of the (n,xn) reaction directly to ground state of the residual nucleus cannot be measured with this technique. Unlike in the case of inelastic scattering, after the (n,xn) reactions with $x \geq 2$ the residual nucleus may be left in the ground state and no γ -ray is emitted. The branching to the ground state makes a large contribution to the total (n,xn) cross-section for $x \geq 2$.

When using the $(n,xn\gamma)$ -technique for a wide range of nuclei three observations have to be considered:

- for the transitions between closely spaced levels, internal conversion strongly decreases the γ -ray emission,
- for high Z materials γ -ray absorption in the sample is important and can lead to a very small detection efficiency for low energy transitions,
- when the fission channel is open, an increased γ background results above the fission threshold.

These three conditions occur for actinides. From all these considerations it results that the $(n,xn\gamma)$ -technique can be applied with success for all the nuclei proposed for this project (^{52}Cr , ^{209}Bi , ^{206}Pb , ^{207}Pb and ^{208}Pb) with the possibility of obtaining a complete set of the various cross-sections.

2.2 Characteristics of the time-of-flight measurements

The time-of-flight technique is the most suitable method for neutron energy determination. It is based on the precise measurement of the time interval between the moment when the neutrons are produced (commonly named t_0) and the moment when they interact with the detector. This time interval is called time-of-flight. The distance (L) that the neutrons travel during the time-of-flight (t) is called flight-path

length. The relativistic expression for the kinetic energy (E) of the neutron is:

$$E = m_0 c^2 \left[\frac{1}{\sqrt{1 - \left(\frac{L}{ct}\right)^2}} - 1 \right], \text{ where} \quad (2.6)$$

m_0 is the neutron rest mass and c is the speed of light. In the classical approximation the neutron energy is:

$$E[\text{keV}] = \left(72.3 \frac{L[\text{m}]}{t[\text{ns}]} \right)^2. \quad (2.7)$$

By derivation of Eq. 2.7 the energy resolution for time-of-flight measurements is obtained:

$$\frac{\Delta E}{E} = 2\sqrt{\left(\frac{\Delta t}{t}\right)^2 + \left(\frac{\Delta L}{L}\right)^2} = 2\sqrt{E \left(\frac{\Delta t}{72.3L}\right)^2 + \left(\frac{\Delta L}{L}\right)^2}. \quad (2.8)$$

The neutron energy resolution in a time-of-flight method is affected by the following uncertainty sources:

- the time resolution of the acquisition system (detector and time coder),
- the duration of the neutron burst,
- the dimensions of the neutron source,
- the sample dimensions,
- the neutron multiple scattering in the neutron source and in the sample.

The first two sources influence the time resolution ($\frac{\Delta t}{t}$) and the last two the uncertainty of the flight path-length($\frac{\Delta L}{L}$). It results that for a good neutron energy resolution the measurement should be done at a longer flight-path length and with detectors of a good time resolution. For the neutron source, special efforts were done to reduce the neutron burst length in order to least affect the time resolution [65].

The time-of-flight measurements are done with pulsed neutron beams and the pulse repetition rate is chosen such that the slow neutrons from one burst do not overlap with the fast neutrons from the next burst.

2.3 Cross-sections measurement by γ -ray spectroscopy with HPGe detectors

2.3.1 Properties of HPGe detectors

When applying the (n,xn γ)-technique below 20 MeV neutron energy, the following three proprieties of the γ -ray detectors need to be as good as possible:

- the energy resolution. Complex γ -ray spectra need to be resolved.

20 Measurements of the $(n,xn\gamma)$ cross-sections with large volume HPGe detectors

- the time resolution. The time-of-flight method is used for the neutron energy determination.
- the detection efficiency. High detection efficiency reduces the acquisition time. Besides the advantages for beam time allocation, shorter acquisition periods avoid large fluctuations in the setup settings.

The most used detectors in γ -ray spectroscopy are the scintillators (NaI, BaF₂, BGO) and the semiconductor diodes (Ge(Li), Si(Li), HPGe). From these detectors the best energy resolution is obtained for the germanium detectors. On the other hand, the time resolution and the detection efficiency are better for the scintillators. A compromise between the three characteristics of the γ -ray detector can be found in HPGe (High Purity Germanium) detectors with a large volume. Such detectors can have an energy resolution of about 2 keV at 1.33 MeV and detection efficiencies comparable with a cylindrical NaI crystal of 3 inch diameter and 3 inch height (100% relative efficiency at 1.33 MeV). The only inconvenience of large volume HPGe detectors is the relatively poor time resolution (several ns) that deteriorates with the increase of the volume.

With all this in mind it was decided to use large volume HPGe detectors with the $(n,xn\gamma)$ -technique at GELINA neutron beam facility. In the following the basic proprieties of large volume HPGe detectors will be explained.

Conduction mechanism in semiconductors

In general for a semiconductor detector the energy resolution is determined by the crystal structure. The periodic lattice of crystalline materials forms allowed energy bands for the electrons. These bands are separated by energy gaps or forbidden bands. A schematic representation of the band structure of the crystals is given in Fig. 2.2. Any electron from the crystal may occupy states in the allowed bands. The lower band is the valence band and corresponds to the bound electrons. The upper band corresponds to the free electrons and is called conduction band. For pure semiconductors (called intrinsic) and for insulators, in absence of any thermal motion (temperature of 0 K), the valence band is fully occupied and there is no electron in the conduction band. At this temperature both the intrinsic semiconductors and the insulators have no electrical conductivity. The size of the forbidden band determines whether the material is classified as semiconductor or insulator (much larger forbidden bands for the insulators). In semiconductors, at temperatures different from 0 K, due to the thermal motion some electrons pass from the valence band in the conduction band. For every such electron, a hole remains in the valence band and under the influence of an electric field this will start moving in the opposite direction compared with the electron. Thus electrons and holes will contribute to the charge collection.

In an ideal semiconductor detector the free charge carriers are produced only from the interaction of the radiation with the crystal. Ge detectors are cooled at low temperature to reduce the number of electron-hole pairs due to the thermal motion. Moreover it is preferably that one particle that interacts with the crystal

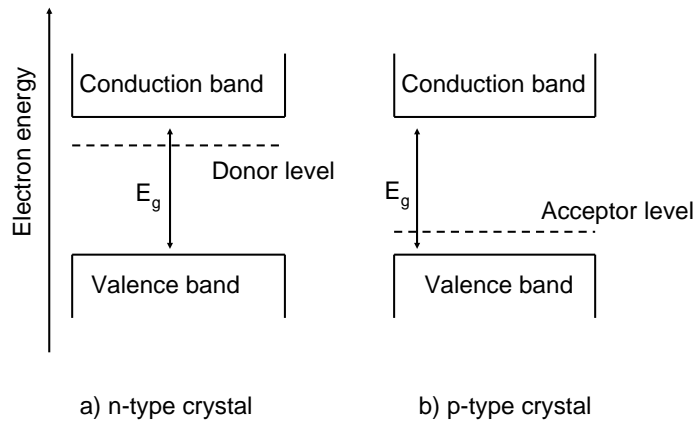


Figure 2.2: Schematic representation of the band structure in a semiconductor. Typical values of the forbidden band are 0.665 eV for germanium and 1.115 eV for silicon at 300 K [86]

produces as many charges as possible. In this respect the semiconductors are much better than the insulators. A low energy gap between the bands will result in a small necessary energy for the formation of an electron-hole pair (2.96 eV for Ge and 3.76 eV for Si) and consequently in a larger number of charge carriers for the same gamma energy deposited in the crystal. Because of this conduction mechanism the semiconductors and especially the Ge detectors have a very good energy resolution.

Types of the HPGe detectors

In practice it is virtually impossible to obtain pure semiconductors and the crystal still has very small concentrations of impurities. An impurity level of about 10^{10} atoms/cm³ was achieved for Ge and that represents one of the best purity levels obtained for a commercial material. Detectors with such purity level are called high purity germanium (HPGe) detectors. The electrical properties of the real crystal are dominated by the small level of impurities. Depending by the type of the impurities, donor or acceptors, the real semiconductors are *n*-type or *p*-type. The high purity *n*-type (*p*-type) semiconductors are usually called ν -type (π -type). The extra electrons of the donor impurities in the *n*-type crystals are not very tightly bound and they create donor levels close to the conduction band (Fig. 2.2). These electrons from the donor levels need very small energies to pass in the conduction band. Similarly the extra holes of the acceptor impurities create acceptor levels close to the valence band.

Semiconductor materials that have an unusually high concentration of impu-

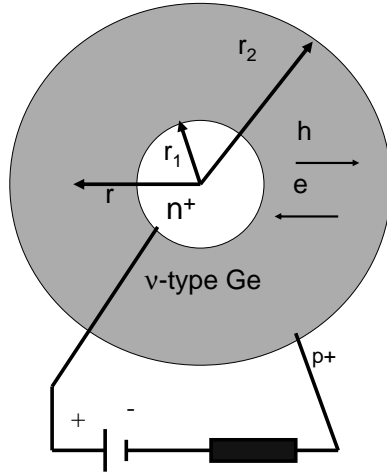


Figure 2.3: Schematic representation of a coaxial HPGe detector. The semiconductor junction is formed between the p^+ contact and the ν -type material. The n^+ contact is a blocking contact that do not allow that the charge carriers initially removed by the application of the electric field are not replaced at this contact.

rity are often given a special notation. Thus n^+ and p^+ designate n - and p -type layers which have a very high impurity concentration and consequently very high conductivity.

In general the semiconductor detectors use the properties of the junctions between the n - and p -type materials. Around the semiconductor junction a net diffusion of the electrons from the n -type to the p -type material takes place. The accumulated space charge creates an electric field that diminishes the tendency of further diffusion. The region over which the charge imbalance exists is called depletion region. If the acceptor concentration in the p -type material is higher than the donor concentration in the n -type material, the holes diffusing in the p -type region travel a longer distance before all have recombined with electrons. The depletion region extends then farther in the n -type side.

Within the depletion region the electric field causes any created electron to be swept toward the n -type material and any hole toward the p -type material.

Thin layers of n^+ (p^+) materials are often used for the electrical contacts with the semiconductor because they reduce the leakage current in the detector to a very low value. The n^+ contact (Fig.2.3) do not allow that the charge carriers initially removed by the application of the electric field are not replaced at the opposite electrode.

In the case of a ν -type HPGe detector (Fig.2.3) the semiconductor junction is between the p^+ contact and the ν -type material. When a reverse bias is applied as in Fig. 2.3, the depletion region extends progressively from the p^+ contact in the ν -type material with the increase of the applied voltage.

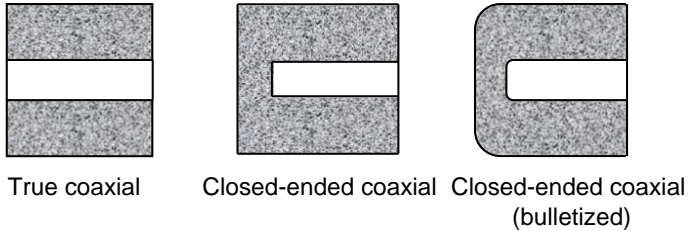


Figure 2.4: Most common shapes for a coaxial detector. The detectors used in the experiments described in this paper have bulletized crystals and large volume.

For a constant reverse bias, the depletion voltage of a high purity semiconductor increases linearly with the decrease of the impurities density ρ [86]. High purity level implies high bias voltage and the latter has practical limitations (safety requirements) to about 5 kV. In consequence, large volume semiconductor detectors require a high purity level.

Two main shapes are common for the germanium detectors: planar and coaxial. The typical shape of a planar semiconductor detector is a thin disk, with relatively small active volume. Planar detectors are suitable for X-ray and low energy gamma ray detection. The detection of the more energetic gamma rays requires coaxial detectors (Fig. 2.4). This is because a larger active volume can be achieved in a coaxial geometry. In the further discussion, for the calculations a ν -type true-coaxial HPGe detector will be considered. This is a simple case for which the electric field and the charge collection process can be calculated analytically and can be considered as a starting point for a comparison with more detailed cylindrical shapes (close ended bulletized detector, Fig. 2.4).

The preamplifier

The preamplifier is the first element in the pulse processing chain of the detector. It is an interface between the detector and the electronics that follow. Three types of preamplifiers can be distinguished: voltage-sensitive, current sensitive and charge-sensitive. The voltage-sensitive preamplifier provides an output pulse whose amplitude is proportional to the amplitude of the voltage pulse supplied to its input. The amplitude of the output pulse of the current-sensitive preamplifier is proportional to the input current.

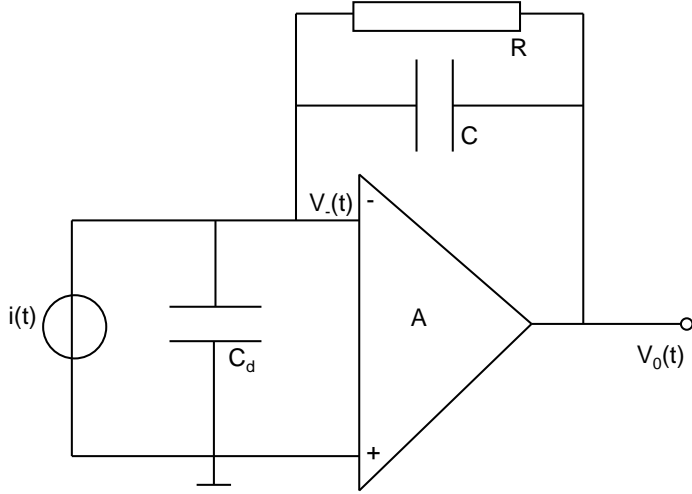


Figure 2.5: Schematic representation of a charge-sensitive preamplifier. The current due to the ionization generated by the photon in the Ge crystal is $i(t)$. C_d is the detectors capacitance. The charge is integrated over the feedback capacitance C , which is discharged through the feedback resistor R . $V_o(t)$ is the output voltage.

For the use with semiconductor detectors a charge-sensitive detector is more suitable. The schematic representation of such preamplifier is given in Fig. 2.5.

The charge-sensitive preamplifier has four main functions:

- integrates the deposited charge over the capacitance C . The output voltage is proportional with the total integrated charge in the pulse provided to the input, as long the duration of the pulse is short compared with time constant RC . The decay time of the pulse is made quite large (50 or 100 μs) to allow the full charge collection before the pulse decay becomes significant.
- preserves the linearity of the input pulse. Ideally, the rise time of the pulse produced from the preamplifier is determined only by the charge collection time in the detector and is independent of the capacitance of the detector or preamplifier input. The minimal distortion of the pulse is an important characteristic for the use with fast digitizer.
- has a low noise despite the high detector capacitance. The noise is made smaller by increasing the resistance value, R , but longer time constant leads to a very long tail on the output pulses. The noise is strongly dependent on the capacitance from the preamplifier input. The input capacitance arises from both the detector capacitance and from the connecting cables between the detector and the preamplifier. The preamplifier is therefore kept close to the detector to minimize the cable length. Because it has also small output impedance, the preamplifier allows a connection through long cables with the following pulse processing module, without introducing additional noise.

- provides a fast response with minimal distortions of the signal,
- provides a convenient means for supplying bias voltage to the detector.

Output signal characteristics for a coaxial HPGe detectors

The starting point for the calculation of the electric field \mathcal{E} is the Poisson equation:

$$\nabla \cdot \mathcal{E} = -\frac{\rho}{\epsilon} \quad (2.9)$$

where ρ is the charge density and ϵ is the dielectric constant. For a coaxial geometry as given in Fig. 2.3 the electric field at the radius r from the centre is [86]:

$$\mathcal{E} = \frac{\rho}{2\epsilon}r - \frac{V + (\rho/4\epsilon)(r_2^2 - r_1^2)}{rln(r_2/r_1)}. \quad (2.10)$$

r_1 and r_2 are the inner and the outer radii of the cylinder (Fig. 2.3). V is the applied voltage. The electric current that results from the deposition of a charge q in the crystal in one point at the radius r is:

$$i(t) = \frac{q}{V}[\mathcal{E}(r_e)v_eH(t_e - t) + \mathcal{E}(r_h)v_hH(t_h - t)], \quad (2.11)$$

where v_e and v_h are the electron and the hole drift velocities. t is the time interval from the moment of the charge deposition. $H(t)$ is the step function:

$$H(t) = \begin{cases} 0 & ; t < 0 \\ 1 & ; t \geq 0 \end{cases}$$

The holes will drift inward with $r_h = r - v_h t$ until $t_h = (r - r_1)/v_h$ and the electrons will drift outward with $r_e = r + v_e t$ until $t_e = (r_2 - r)/v_e$. The output voltage (V_o) from a charge-sensitive preamplifier (Fig. 2.5) with a decay constant $\tau = RC$ that is coupled to an HPGe true-coaxial detector is:

$$V_o(t) = V_o(0)e^{-t/\tau} - \frac{1}{C}e^{-t/\tau} \int_0^{t_m} i(t')e^{t'/\tau} dt', \quad (2.12)$$

where t_m is the maximum charge collection time. The output voltage as a function of the time t was calculated for a true coaxial detector with the inner radius $r_1=0.45$ cm and outer radius $r_2=4.35$ cm (Fig. 2.6). The rapid changes in the slope reflect the moment that one of the two charge carriers is fully collected. Large variations in the shape of the output pulse are observed. For qualitative comparison preamplifier output signals from a close-ended bulletized coaxial detector with the same radii were measured. In Fig. 2.6 the calculated and the experimental shapes of the output signal are compared. The true coaxial shape is an approximation for such a real detector. Large deviations from the calculated shape of the electric field are expected at the crystal extremities, especially in the end-cap and at the crystal corners. The approximation that the charge deposition takes place in one point is not valid in the real case. This simple calculation does not take into account the trapping

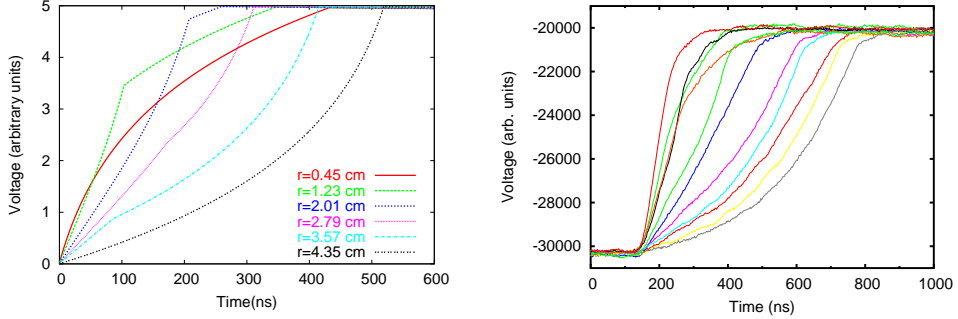


Figure 2.6: Signal at the preamplifier output of a 100% efficiency detector . Left: calculation with in a simple approximation of Eq. 2.12 for different radii at which the charge was deposited. It was supposed that the charge is deposited in only one point. Right: Experimental signals recorded with a fast digitizer (see also Chapter 4)

effects and the effect of the noise. Because of this even more complicated shapes and larger differences in the rise time are expected in the real detector. However, many of the experimental features are present in this simplified model. In the calculation (Fig. 2.6), the maximum rise time for this detector is about 500 ns while experimentally one observes a maximum rise time of about 700 ns. Many of the calculated shapes in the left side of the Fig. 2.6 can be seen also experimentally in the right panel of the same figure.

The variations in the pulse shape and in the rise time are the cause for a poor time resolution in a large volume HPGe detector. For the detectors used in the experiments described in this work the time resolution obtained with a conventional Constant Fraction Discriminator was between 4 ns and 6 ns depending by the detector volume. Detectors with relative efficiency between 48% and 105% were used.

In contrast to the time resolution, the energy resolution is not significantly affected by the pulse shape. Instead, the differences in the pulse rise time are the cause for the so called ballistic deficit effect that can deteriorate the energy resolution. Because the decay time of the preamplifier cannot be made infinitely long, simultaneously with the charge collection process amplitude decay takes place. The ballistic deficit is more important when large variations in the collection time (pulse rise time) appear and that is the case of the large volume HPGe detectors. When the rise time is almost constant the amplitude decrease due to the finite decay constant is the same for all pulses and the energy resolution does not deteriorate. The energy resolution depends mainly on the noise characteristics of the detector. The used detectors had an energy resolution between 1.9 keV and 2.4 keV at the second line of ^{60}Co (1.33 MeV).

2.3.2 Gamma ray angular distribution

The primary cross-sections obtained with the $(n, xn\gamma)$ technique are the differential cross-sections at the measurement angles. The angle integrated cross-sections are more useful quantities. The angular integration has to be done starting from

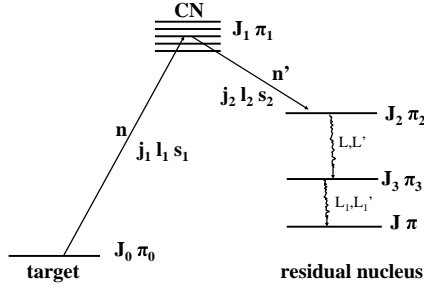


Figure 2.7: Spin and angular momenta representation of the neutron inelastic scattering reaction. Two γ -rays are emitted in cascade by the residual nucleus. J and π represent the spin and the parity of different energy levels in the target nucleus, compound nucleus (CN) and in the residual nucleus.

measured differential cross-sections at fixed angles and in consequence information about the γ -ray angular distribution is necessary.

The general expression for the gamma-ray differential cross-section in situations with cylindrical symmetry for transitions between states of well defined spin and parity are given as a finite sum of the even order Legendre polynomials [70, 71]:

$$\frac{d\sigma}{d\Omega_\gamma}(\theta_\gamma) = \sum_k a_{2k} P_{2k}(\cos \theta_\gamma) \quad (2.13)$$

with $k=0,1,2,\dots$ and θ_γ is the γ -ray emission angle relatively to the direction of the incident beam. The $(n, xn\gamma)$ reaction has cylindrical symmetry, with the incident beam direction as the symmetry axis. The dependence by the ϕ angle is isotropic. The maximum k value is given by the total momentum coupling conditions (see below). An immediate property that results from Eq. 2.13 is the symmetry around 90° . The symmetry of γ -ray angular distribution around 90° does not depend by the reaction mechanism (compound nucleus, direct or pre-equilibrium) in contrast with the outgoing neutron angular distribution that is symmetric only for a compound nucleus mechanism (in the center of mass).

With the $(n, nxn\gamma)$ technique the γ -ray angular distribution can be determined measuring at different angles θ_γ . Contrary, the $(n, xn\gamma)$ technique does not provide any information about the angular distribution of the outgoing neutrons.

The weighting coefficients a_{2k} can be decomposed in a product of angular momentum-dependent and energy-dependent terms. The latter are just the transmission coefficients, contained in the penetrability term τ in the next equations. For the particular case of the $(n, n'\gamma)$ reactions when only one γ -ray is emitted (see the schematic representation in Fig. 2.7). The differential gamma-ray cross-section can be written according to Ref. [42] as:

$$\frac{d\sigma}{d\Omega_\gamma} = \frac{\bar{\lambda}^2}{8} \sum N' C' W' M(\delta) \tau P_{2k}(\cos \theta_\gamma) \quad (2.14)$$

where

$$N' \equiv (-)^{J_0+J_3-j_2+\frac{1}{2}} \frac{(2J_1+1)^2(2j_1+1)(2J_2+1)}{2J_0+1},$$

$$\begin{aligned}
C' &\equiv \langle (2k)0|j_1 j_1 \frac{1}{2} - \frac{1}{2} \rangle, \\
W' &\equiv W(J_1 J_1 j_1 j_1; (2k)J_0) W(J_1 J_1 J_2 J_2; (2k)j_2), \\
M(\delta) &\equiv (1 + \delta^2) 6 - 1 [M(LL) + 2\delta M(LL') + \delta^2 M(LL')], \text{ with} \\
M(LL') &\equiv \sqrt{(2L+1)(2L'+1)} \langle (2k)0|LL'1-1\rangle W(J_2 J_2 LL'; (2k)J_3). \\
\tau &\equiv T_{l1}(E_1) T_{l2}(E_2) / \sum_{ljE} T_l(E).
\end{aligned}$$

δ is the mixing ratio and τ is the Hauser-Feshbach penetrability factor that contains the energy dependence. C' is the Clebsch Gordon coefficient and P_{2k} is the Legendre polynomial of order $2k$. The Racah coefficients W from Eq. 2.15 vanish unless k is restricted to the values

$$0 \leq k \leq j_1, J_1, J_2, L' \quad (2.15)$$

When the idealized differential cross-section presented in Eq. 2.14 is compared with the experimental results few additional observations has to be made.

In a calculation a cut off in the angular momenta l is done. In Ref. [42] it was found that an angular momentum $l_{max} = 4$ is enough to describe the γ -ray angular distributions few MeV above the inelastic threshold. Higher angular momenta do not change significantly the shape and the amplitude of the angular distributions.

When a cascade of unobserved transitions feeds the measured transition, an additional attenuation coefficient has to be considered. The effect of the cascade is usually to diminish the anisotropy of the distribution.

At this point it is necessary to make the distinction between the differential cross-section $\frac{d\sigma}{d\Omega}(\theta)$ and the angular distribution $W(\theta)$ that is normalized to the a_0 coefficient:

$$W(\theta) = \sum_{k=0}^{[J_i], L} c_{2k} P_{2k}(\cos \theta_\gamma), \quad (2.16)$$

with $c_0 = 1$. Based on Eq. 2.13 and Eq. 2.14 it is possible to make some general predictions regarding the behavior of the $(n, n'\gamma)$ angular distributions for some particular transitions. The most simple case is when the initial level of the γ -decay has the spin and the parity 0^+ . For such cases the angular distribution is limited to the $k=0$ and is isotropic.

At neutron energies sufficiently close to the threshold other particular cases can be considered for the even-even nuclei. Near the threshold only the s-wave outgoing neutrons contribute to the (n, n') cross-sections. In this approximation the angular distributions were tabulated in Ref. [42]. Three cases are presented below and the corresponding plots are given in Fig. 2.8. These angular distributions give the strongest angular anisotropy.

- $J_2^\pi = 2^+, L^\pi = E2, J_3^\pi = 0^+$. For $l_2 = 0$ it results that the possible values for J_1 are $\frac{3}{2}^+$ or $\frac{5}{2}^+$ and $l_1 = 2$ (Fig. 2.7). Near the threshold the following angular distribution results:

$$W(\theta_\gamma) = 1 + 0.5428 P_2(\cos \theta_\gamma) - 0.3428 P_4(\cos \theta_\gamma). \quad (2.17)$$

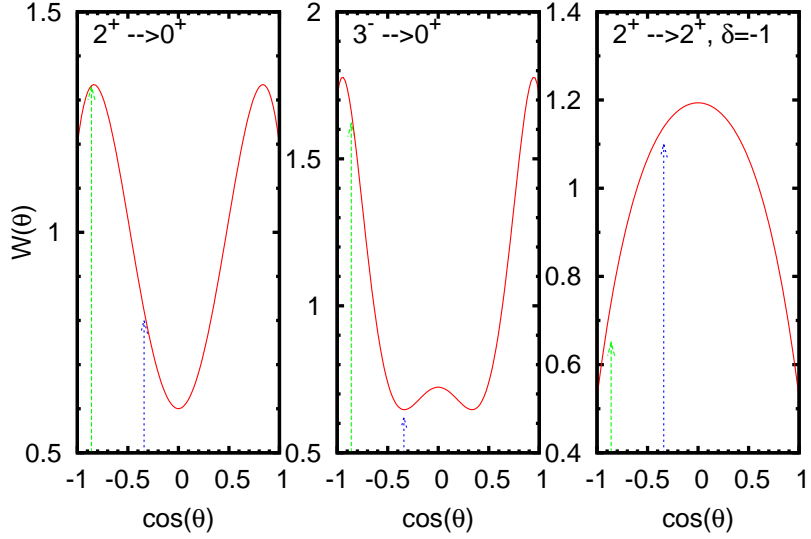


Figure 2.8: Typical angular distribution shapes for two pure transitions (E2 and E3) and one mixed transition M1+E2 with an arbitrary $\delta = -1$. The arrows show the angles (150° and 110°) used in the present experiment (see Sec. 2.3.3 for details).

- $J_2^\pi = 3^-$, $L^\pi = E3$, $J_3^\pi = 0^+$. If $l_2 = 0$ the possible sequences are $l_1 = 3$, $J_1 = \frac{5}{2}^-$ or $\frac{7}{2}^-$. The resulting angular distribution is:

$$W(\theta_\gamma) = 1 + 0.8776P_2(\cos \theta_\gamma) + 0.1614P_4(\cos \theta_\gamma) - 0.3247P_6(\cos \theta_\gamma). \quad (2.18)$$

This is one case when the 6th order Legendre polynomial has a contribution to the angular distribution.

- $J_2^\pi = 2^+$, $L^\pi = M1, E2$, $J_3^\pi = 2^+$ is a more complex case because of the multipole mixing. The angular distribution depends by the mixing ratio δ as well:

$$W(\theta_\gamma) = 1 + \frac{0.38 + 1.112\delta - 0.1163\delta^2}{1 + \delta^2} P_2(\cos \theta_\gamma) - \frac{0.0979}{1 + \delta^2} P_4(\cos \theta_\gamma). \quad (2.19)$$

With the increase of the incident neutron energy, the anisotropy diminishes because of the more values for the momenta l that have to be considered. Above the first excited level, the feeding has to be considered from other γ transitions (Fig. 2.7).

2.3.3 Angle integration - Gauss quadrature

Our primary interest concerns the angle-integrated gamma-ray production cross sections. In the present work these have to be determined as well as possible with a minimum number of detection angles. From Eq. 2.13 and Eq. 2.16 the differential gamma production cross-section is:

$$\frac{d\sigma}{d\Omega_\gamma}(\theta_\gamma) = \frac{\sigma}{4\pi} \sum_{k=0}^{[J_i],L} c_{2k} P_{2k}(\cos \theta_\gamma) \quad (2.20)$$

with $c_0 = 1$. Here J_i is the spin of the initial (decaying) state and $[J_i]$ is the largest integer smaller than or equal to J_i . L is the transition multipole. The Eq. 2.20 can be integrated by a Gaussian quadrature specialized to even degree polynomials [72]. Thus, in general, for a given number n of detectors we need the best angles ($x_i = \cos \theta_i$) and weights w_i such that the right hand sum (below) gives the exact result for the left hand integral for the highest degree of even polynomial possible.

$$\sigma = 2\pi \int_{-1}^1 \frac{d\sigma}{d\Omega}(x) dx = 2\pi \sum_{i=1}^n w_i \frac{d\sigma}{d\Omega}(x_i). \quad (2.21)$$

Demonstration for a particular case of 2 detection angles

For any polynomial $f(x)$, its integral in a given interval $[a,b]$ can be written as a weighted sum of functional values in a given set of N abscissas:

$$\int_a^b W(x)f(x)dx = \sum_{i=1}^n w_i f(x_i), \quad (2.22)$$

where the weighting function $W(x) > 0$. The approximation from Eq. 2.22 is very precise if the function $f(x)$ is sufficiently smooth in the integration interval $[a,b]$. For the particular case of the gamma ray angular distribution, where the Legendre polynomial are orthogonal and for the two detection angles ($n = 2$) the following relation is valid for *any* c_{2k} coefficient with $k = 0, 1, 2$ and 3 :

$$\begin{aligned} \sigma = 2\pi \int_{-1}^1 \frac{d\sigma}{d\Omega_\gamma}(\theta_\gamma) d(\cos \theta_\gamma) &= \frac{\sigma}{2} \int_{-1}^1 \sum_{k=0}^3 c_{2k} P_{2k}(x) dx = \\ &= \frac{\sigma}{2} \sum_{j=1}^2 w_j \left(\sum_{k=0}^3 c_{2k} P_{2k}(x_j) \right). \end{aligned} \quad (2.23)$$

Using the propriety of the Legendre polynomials that

$$\int_0^1 P_m(x) dx = \delta_{0,m}, \quad (2.24)$$

from the last equality in the Eq. 2.23 it results a non-linear equation system with four equations:

$$\begin{cases} w_1 + w_2 = 2 \\ w_1 P_2(x_1) + w_2 P_2(x_2) = 0 \\ w_1 P_4(x_1) + w_2 P_4(x_2) = 0 \\ w_1 P_6(x_1) + w_2 P_6(x_2) = 0, \end{cases}$$

where the Legendre polynomials are:

$$\begin{aligned} P_0(x) &= 1, \\ P_2(x) &= \frac{1}{2}(3x^2 - 1), \\ P_4(x) &= \frac{1}{8}(35x^4 - 30x^2 + 3), \\ P_6(x) &= \frac{1}{16}(231x^6 - 315x^4 + 105x^2 - 5). \end{aligned}$$

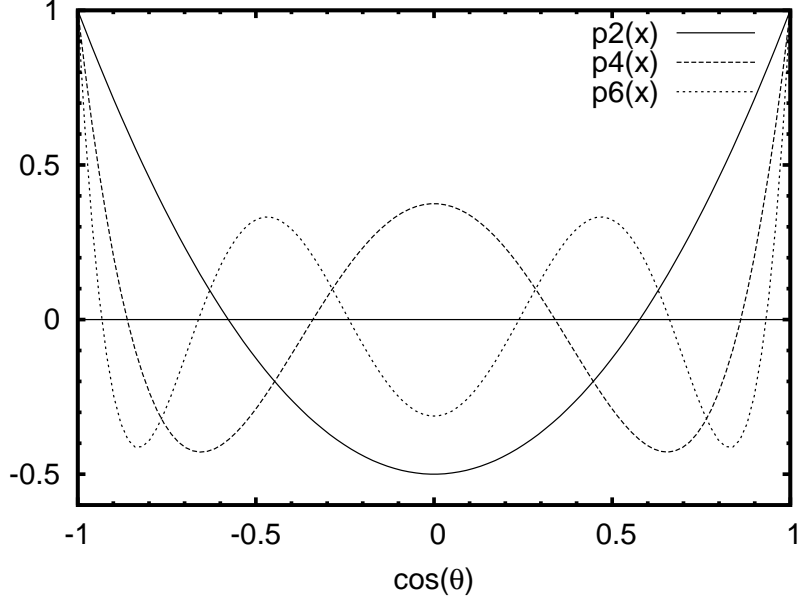


Figure 2.9: Even order Legendre polynomials. The roots of the 4th order polynomial (150° and 110° and their complements) are a good choice for the gamma ray detection in a neutron inelastic cross-sections measurement.

Table 2.1: The roots and weights for integration of gamma-ray angular distributions with 1, 2 and 3 detectors

nr	zero	weight	angle	nr	zero	weight	angle
one detector				three detectors			
1	0.57735	2	54.74, 125.26	1	0.05694	0.93583	76.19, 103.81
two detectors				2	0.43720	0.72152	48.61, 131.39
1	0.86114	0.69571	30.56, 149.44	3	0.86950	0.34265	21.18, 158.82
2	0.33998	1.30429	70.12, 109.88				

Solving the equation system 2.3.3 the nodes and the corresponding weights are the one given in Table 2.1 for two detectors. The nodes are the roots of the 4th order Legendre polynomials (see Fig. 2.9).

General demonstration

The Eq. 2.21 is achieved when we take the x_i to be the n positive roots of the Legendre polynomial P_{2n} and the w_i as

$$w_i = \frac{1}{\sum_{m=0}^{n-1} \frac{4m+1}{2} P_{2m}^2(x_i)}. \quad (2.25)$$

Eq. 2.25 is symmetric with respect to $x = 0$ ($\theta = 90^\circ$). This approach is exact for polynomials with degree up to $4n - 2$. In the present experiments were used the backward angles that correspond to the case of two detectors (Tab. 2.1). These angles are the roots of P_4 , so that the right hand sum of Eq. 2.21 is insensitive to P_4 .

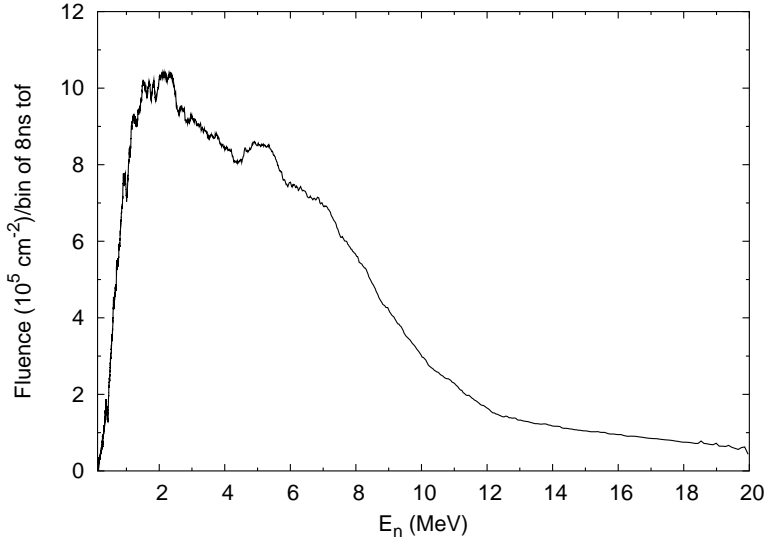


Figure 2.10: Neutron fluence measured during the ^{52}Cr experiment with the ^{235}U fission chamber.

Furthermore one verifies that $w_1 P_2(x_1) = -w_2 P_2(x_2)$ and $w_1 P_6(x_1) = -w_2 P_6(x_2)$ so that the sum is insensitive to P_2 and P_6 as well. On the contrary, $w_1 P_0(x_1) + w_2 P_0(x_2) = w_1 + w_2 = 2$, as required.

Most authors, aware of the need to account for the angular distribution, have used an angle of 125 degrees, the one detector case of table 2.1. It may be noted that for the most common transitions $L \leq 2$ and only for E3 there is a non-zero contribution from the 6th order Legendre polynomial. Our two point approach is exact for all transitions from the first excited level to the ground state in even-even nuclei and in general takes much better care of more complex distributions.

Finally, the two angles may of course also be used to extract information about the angular distribution. For instance, with $f = (4\pi/\sigma)d\sigma/d\Omega$ we can extract $c_2 \approx 1.065(f(x_1) - f(x_2))$. The presented integration method is rather insensitive to the finite opening angle of the detectors as long the angular distribution is a relatively smooth function. Moreover the angular distribution coefficients may be strongly affected by the detectors size.

2.4 Neutron beam properties at GELINA

GELINA is a multi-user neutron source that allows simultaneously measurements at 12 different flight-path stations with lengths between 10 m and 400 m. The present measurements were done at the 200 m stations of flight-path 3. For this flight-path the neutron beam direction is perpendicular to the direction of the incident electron beam.

The pulsed white neutron source GELINA produces neutrons in bursts of less than 1 ns full width at half maximum with a repetition rate of up to 800 per second. The neutron producing target is a rotating uranium disk that is bombarded by an

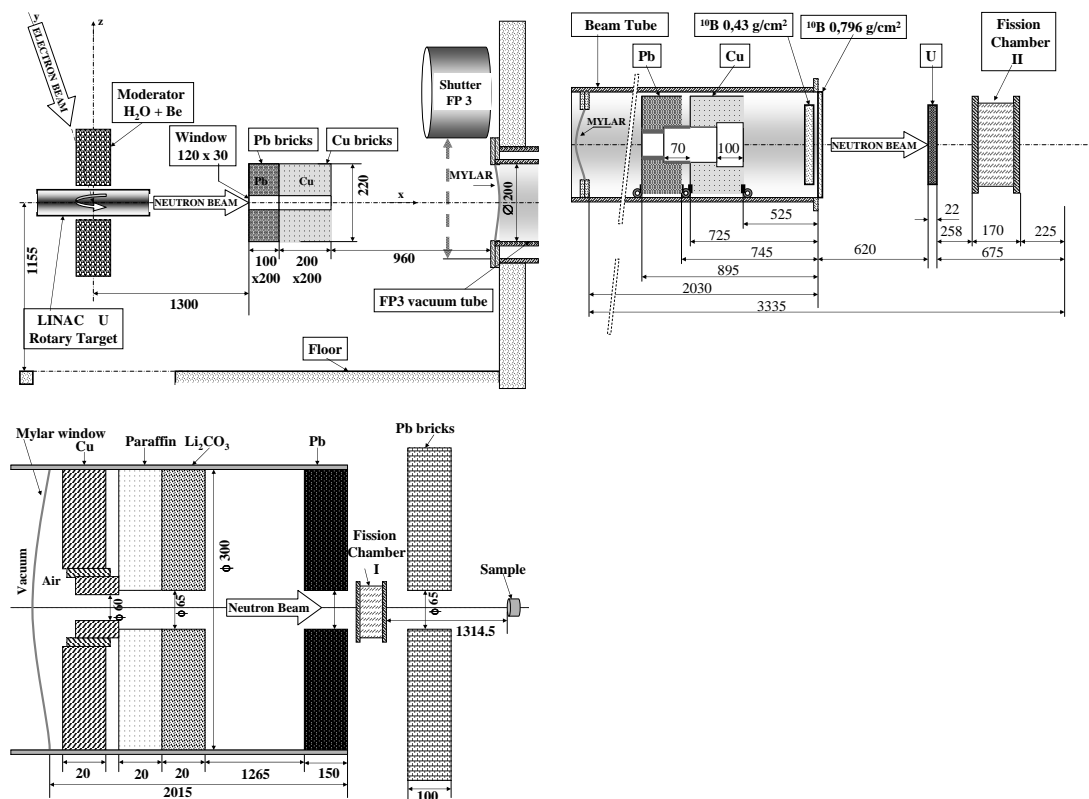


Figure 2.11: Beam definition. Neutron producing target and primary collimator (upper left panel), uranium and ^{10}B filters (upper right panel) and the beam defining collimators (bottom). These arrangements correspond to the target vault and the 100 and 200 m measurement stations of flight path 3 of GELINA.

electron beam with a mean energy of 105 MeV and an average current of 70 μA [64–66]. Neutrons result from (γ, xn) and (γ, F) reactions following bremsstrahlung. The neutrons that are produced have evaporation spectrum. The spectrum measured at 200 m station with a ^{235}U fission chamber is shown in Fig. 2.10. More details about this flux measurement are given in Chapter 3. The neutron spectrum approximately rises like $E^{1/2}$, peaks around 2 MeV and falls off roughly exponentially. Despite the intensity drop, the spectrum may be used up to 18 – 20 MeV.

The start signal for the measurement (t_0) is a pick-up signal collected at the last section of the LINAC that gives the moment when the electrons are leaving the accelerator and hit the uranium target. Another signal called pre-trigger (P_t) precedes the t_0 signal with about 10 μs and is used mainly to reset the digital acquisition systems before t_0 .

For the measurements described here, three main sources of background must be considered. The first is given by the slow neutrons arising from the target, the second by the beam defining collimator at the 200 m station and the third by the gamma-flash.

Slow neutrons from the target arise because the GELINA facility has two water moderators above and below the uranium target (Fig. 2.11) that enhance the flux for energies from 1 meV to about 100 keV. Thus, the GELINA allows the simultaneous use of moderated and unmoderated neutrons for different measurements. The slow neutrons from a previous Linac burst may overlap with the fast neutrons of the present burst. This interferes with the measurement. First, a background results for the HPGe detectors from interaction with the sample via capture reactions. Second, the fission chamber (Chapter 3) will see spurious events induced by the slow neutrons from the previous burst. The presence of slow neutrons is minimized in two ways. First, a 30 mm high by 120 mm wide Pb/Cu collimator is used in the target vault to block neutrons emerging from the moderators and pass only the neutrons emerging from the Linac target (the uranium target is 40 mm high). Second, two ^{10}B filters are placed at the 100 m station with a combined thickness of 1.23 g/cm². These filters absorb the slow neutrons that may overlap with the fast neutrons from another burst. The neutrons with an energy smaller than 130 eV overlap with the fast neutrons. The neutrons with an energy of approximately 130 eV have a transmission probability of about 1.9% through this filter, whereas the transmission is more than 80% for neutrons with energies above 1 MeV.

The last collimator that defines the beam at the 200 m station is made of copper and has an opening of 6 cm diameter. It is the main source of background in the form of scattered and moderated neutrons and secondary inelastic and capture gamma-rays. To minimize its impact on the measurement it is placed at 2.9 m upstream from the sample. Immediately behind it there is a paraffin moderator and a paraffin with lithium carbonate absorber that serve to eliminate forward scattered neutrons. A total of 25 cm of lead serves to minimize gamma-rays produced in this collimator arrangement. This lead is placed about 1 m downstream from the collimator to minimize the opening angle for gamma-rays from the collimator.

Although the uranium target is designed to stop the electrons and bremsstrahlung photons, an intense prompt gamma-flash leaks from the target. To achieve workable

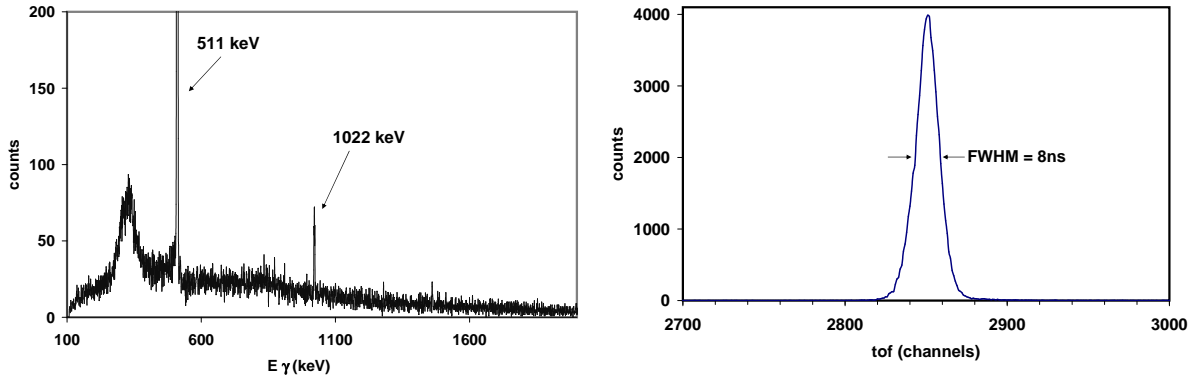


Figure 2.12: Left: A zoom on the y axis of the gamma flash amplitude spectrum measured with a 104.3% efficiency HPGe detector at the 200 m flight path length station. The spectrum is integrated over the time-of-flight values corresponding to the gamma flash arrival at the 200 m station. The 511 keV peak area represents about 30% of the full spectrum area. Right: The time-of-flight spectrum of the gamma flash integrated over all amplitudes. The FWHM of the t.o.f. gamma-flash peak was 8 ns.

conditions, a natural uranium disk of 36.8 g/cm^2 placed at the 100 m station serves to reduce the gamma-flash. For example, the transmission for 500 keV gammas is $T=1.1 \cdot 10^{-3}$ whereas for neutrons between 1 and 20 MeV the transmission varies between 0.47 and 0.58.

Nevertheless, the HPGe detectors of the present setup (details are given in Chapter. 3) see a gamma-flash induced event in 10% - 20% of the total number of the Linac bursts. The majority of the gamma-flash photons seen by the HPGe detectors are scattered on the sample and then detected. The fraction of the observed gamma-flash depends on the HPGe detector and on the sample. It increases at the forward angles, with the increase of the sample thickness and of the detector efficiency. The intensity of the scattered gamma-flash increases also with the increase of the atomic number Z of the sample. The gamma flash amplitude spectrum observed in the HPGe detector is mainly formed by a 511 keV peak superimposed on a wide bump spectrum (see Fig. 2.12).

GELINA flight paths are evacuated. The vacuum is interrupted in the Linac vault and at the 100 and 200 m stations for a total length of 10 m. Four Mylar windows of 0.1 mm thickness each guarantee the vacuum. The neutron beam is dumped 200 m downstream from the sample.

Chapter 3

Experimental setup for the (n,xn γ) cross-section measurements at GELINA

A new experimental setup was developed for the measurement of the (n,xn γ) cross-sections with x=1,2 and 3 at GELINA. The setup uses the (n,xn γ)-technique described in Sec.2.1.2 and large volume HPGe detectors. The neutron flux is monitored with a multi-layer ^{235}U fission chamber that recorded simultaneously with the HPGe detectors. Conventional electronics was used for both the HPGe detectors and the fission chamber. Enriched samples were used to simplify as much as possible the γ -ray spectra and to enable (n,2n) measurements. Relatively thick samples are necessary with the present detection efficiency (thicknesses between 2.2 g/cm² and 5.9 g/cm² were used) to have a small statistical uncertainty. In the setup development one aimed to accomplish the following requirements:

- – (n,xn γ) cross-sections measurement continuously for the *full energy range* from the threshold up to 18-20 MeV *in only one run* using the pulsed white neutron beam from GELINA.
- – *an unprecedented neutron energy resolution*. This could be achieved using a 200 m flight-path length and an 8 ns time-of-flight resolution. From these it results a neutron energy resolution of 1.1 keV at 1 MeV (36 keV at 10 MeV). Such resolution was obtained for the strong γ -rays and for the total inelastic cross-section.
- – *a total uncertainty of about 5%* for the gamma production cross-section of the main transitions was obtained below about 10 MeV neutron energy. Above this energy the total uncertainty was kept below 15-20%. The main source of uncertainty was the statistics of the measurement.
- – *very good energy resolution for the γ -ray detectors* to allow the γ -ray separation in complex spectra. The best choice for this problem is the HPGe detectors.

- – *good detection efficiency.* Large volume HPGe detectors were used. During the measurement of different nuclei new detectors were added to improve the detection efficiency.
- – *cross-sections normalization to a well known standard cross-section.* The measurement were normalized to the ^{235}U neutron induced fission cross-section.
- – *good beam collimation.* Special attention was given to the construction of the beam collimators (see Sec.2.4) to have a well defined beam.
- – *negligible acquisition dead time.* Avoiding the acquisition dead time simplifies the data analysis and reduces the total uncertainty.

Continuous improvements, especially to the detection efficiency and the electronic scheme, were brought to the setup during the measurement of different nuclei. In chronological order, the setup was used with success for the measurement of the following nuclei: ^{58}Ni (not part of this thesis), ^{52}Cr , ^{209}Bi , ^{207}Pb , ^{208}Pb and ^{206}Pb .

In the next two sections a detailed description of how the goals of the experimental setup were achieved will be presented. The third section will be focused on the data analysis procedure, while the last section is dedicated to the conclusions.

3.1 Experimental setup

3.1.1 HPGe detectors

The γ -rays produced in the $(n,xn\gamma)$ reactions on the sample were detected with large-volume coaxial HPGe detectors. The samples are placed at 198.551 m from the GELINA target center. The HPGe detectors were placed as close as possible to the sample, but out of the neutron beam of 6.1 cm diameter. The angles between the crystal axis and the incident beam were 150 degrees and 110 degrees. These angles were carefully checked with laser beams. The choice of these particular angles is explained by the γ -ray angular integration procedure that was used (Gauss-quadrature at two angles – Sec.2.3.3). The reason to place the germanium detectors at backward angles was to reduce the intensity of the detected gamma flash scattered on the sample (see Sec.2.4 and Sec.3.2.4). The arrangement of the HPGe detectors and of the fission chamber is given in Fig.3.1 for the ^{208}Pb run. An identical setup was used for ^{206}Pb . Table.3.1 gives the HPGe detectors characteristics used in the experimental setup from the ^{52}Cr run until the run with ^{206}Pb . All detectors have a coaxial bulletized crystal (Fig.2.4).

3.1.2 Fission chamber

The neutron flux was measured with a multilayer ^{235}U fission chamber. The fission chamber is placed about 1.3 m upstream from the sample at 197.214 m from the GELINA target center (Fig.3.1). The chamber consists of 8 deposits of 70.00 mm

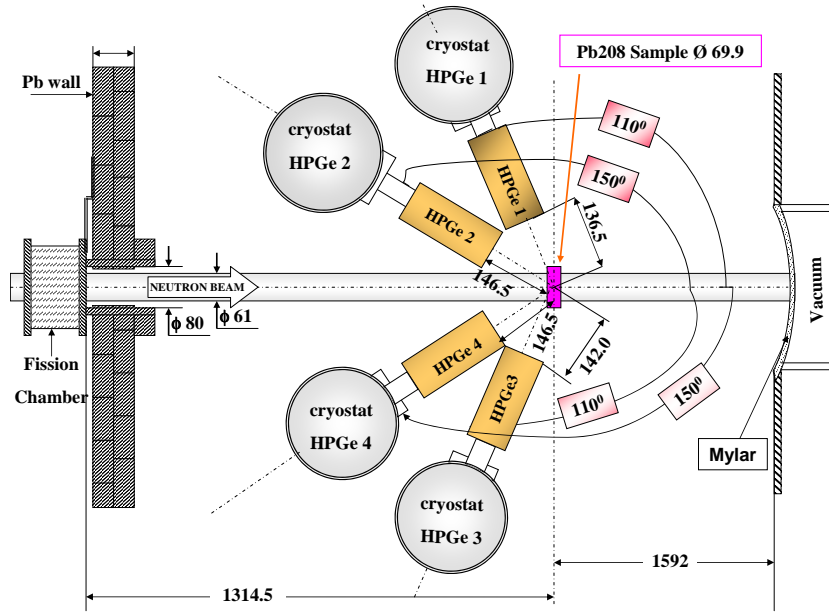


Figure 3.1: Configuration of the detectors in GELINA flight path number 3 at the 200 m measurement station. The germanium detectors are placed at 150° and at 110° with respect to the beam axis. The fission chamber for the fluence normalization was placed behind the lead shielding to reduce the γ -ray background around the HPGe detectors.

Table 3.1: The HPGe detectors used during the 5 runs with different samples. The relative efficiency, ϵ , is given at 1.33 MeV energy. The distance is measured from the sample position to the detector window. Only for the detectors with beryllium window an additional copper absorber of 0.4 mm thickness was glued on the front end.

nuclide	angle	name	serial no.	$\epsilon(\%)$	distance (mm)	window
^{52}Cr	110	HPGe 2	b092018	48.6	119	Al
	150	HPGe 1	b093061	75.9	154	Al
^{209}Bi	110	HPGe 2	b092018	48.6	114	Al
	150	HPGe 1	b093061	75.9	151	Al
^{207}Pb	110	HPGe 1	b093061	75.9	139	Al
	150	HPGe 2	b04036	104.3	146	Al
	125	HPGe 3	44-N31866A	105	125	Be
^{208}Pb and ^{206}Pb	110	HPGe 1	b093061	75.9	136.5	Al
	110	HPGe 3	44-N31866A	105	142.0	Be
	150	HPGe 2	b04036	104.3	146.5	Al
	150	HPGe 4	44-N31867A	98	146.5	Be

Table 3.2: Samples dimensions and isotopic composition. All samples had disk shape with the diameter Φ and the thickness t . The mass given for ^{52}Cr is the total mass of the oxide. The chromium powder was pressed with 5 tones in an Al can with the front wall of 0.6 mm and the lateral wall of 1.2 mm.

nuclide	type	Φ (mm)	t (mm)	mass (g)	composition
^{52}Cr	Cr_2O_3 powder	68.6	23.0	146.166	^{52}Cr 99.85%
^{206}Pb	metallic	50.0	2.02	43.2781	^{206}Pb 99.82%
^{207}Pb	metallic	50.9	3.9	89.992	^{207}Pb 92.40(10)%, ^{208}Pb 5.48(5)%, ^{206}Pb 2.16(5)%, ^{204}Pb \leq 0.02%
^{208}Pb	metallic	69.9	5.04	217.45	^{208}Pb 88.110(63)%, ^{206}Pb 10.988(64)%, ^{207}Pb 0.8943(84)%, ^{204}Pb 0.00758(45)%
^{209}Bi	metallic	80.0	6.0	296.7	^{209}Bi 99.5%

diameter on Al foils of 20 μm thickness that are supported by rings of 84 mm diameter. The outer electrodes have deposits on one side while the three inner electrodes have deposits on both sides. Electrode separation is 6 mm. The deposits were prepared by vacuum evaporation of ^{235}U with the isotopic composition 99.826(8)% ^{235}U , 0.062(8)% ^{234}U , 0.036(5)% ^{236}U and 0.073(9)% ^{237}U . The very small quantities of other U isotopes (^{234}U , ^{236}U and ^{237}U) have a negligible contribution to the fission chamber yield because their neutron induced fission cross-section is comparable with the one of ^{235}U . Homogeneity to better than 5% was guaranteed by placing the disks during evaporation at sufficient distance off the evaporation axis and rotating them around the evaporation source and around the axis of the disk. The area was defined precisely by a mask and the total quantity deposited was determined accurately with alpha-counting. The total thickness obtained in this way was 3.066(6) mg/cm² of U. Entrance and exit windows of the fission chamber are 0.2 mm thick Al foils. The chamber is operated at 500 V with a continuous flow of P10 mixture at atmospheric pressure. The fission chamber was positioned carefully so that the active deposit is centered with respect to the neutron beam and the position was not changed during the different runs presented in this work.

3.1.3 Samples

The limitations in the detection efficiency can be partially compensated by larger samples in the beam. Moreover there are four restrictions for the sample dimensions:

- The quantity of highly enriched materials is limited.
- The neutron beam diameter is only 6.1 cm and much larger sample diameters are useless. Anyway a sample diameter a bit larger than the beam diameter is preferred because in such conditions any beam profile can be neglected. In

this case, both fission chamber active diameter and sample diameter are larger than the beam diameter.

- A compromise has to be found between the sample thickness and the γ -ray attenuation in the sample. The neutron attenuation and multiple scattering have to be considered as well. All these effects increase with the sample volume.
- The number of the scattered gamma-flash photons on the sample increases with the atomic number Z and with the thickness of the material in the sample.

The samples dimensions and compositions are given in Table 3.2. The sample was perpendicular on the beam direction, except for the ^{209}Bi run when the sample was rotated with 20° to assure an equal view at the sample for both detectors.

The high purity samples (as ^{52}Cr , ^{209}Bi , ^{206}Pb) allow a better separation of the $(n, xn\gamma)$ reaction channels. In contrast, in a sample as ^{207}Pb with only 92.4% purity, above the $(n, 2n)$ threshold of the ^{208}Pb impurity ($\simeq 10$ MeV), the gamma peaks from the ^{207}Pb nucleus are produced in two reactions: one is the inelastic scattering on ^{207}Pb and another is the $(n, 2n)$ on ^{208}Pb impurity. Moreover, above 10 MeV, the yields of these two reactions become comparable, even if ^{208}Pb is only an impurity. This is because, above 10 MeV, the inelastic cross-section decreases significantly while the $(n, 2n)$ cross-section reaches the maximum. The channel mixing in the samples with low level of enrichment, leads to the necessity of two measurements with samples of different isotopic composition.

3.2 Data acquisition system with conventional electronics

The data acquisition was done with conventional NIM electronic modules. For the most complex version of the setup (^{208}Pb and ^{206}Pb), that included 4 HPGe detectors and one fission chamber three almost independent acquisitions systems were created. Two identical systems were used for the HPGe detectors and one system for the fission chamber. All three systems were running in parallel.

3.2.1 The electronics

The data-acquisition is based on a multiplexer (MMPM) [67] that is driven by LabVIEW¹ software from a Windows-NT PC via a PCI-bus IO card. Both the MMPM and the software were developed at IRMM. The MMPM controls the peak sensing ADC's, for the pulse amplitude determination and the fast time digitizer (FTD [68]). In the present setup one MMPM can accommodate a maximum of 2 ADCs and one FTD. Each of the HPGe acquisition systems had 2 ADCs and one FTD. The fission chamber acquisition system had one ADC and one FTD.

Commercial ADCs were used while the FTD is an in-house developed multi-hit time-to-digital converter with a resolution of 0.5 ns. It is used to record the arrival

¹LabVIEW is a trade mark of National Instruments

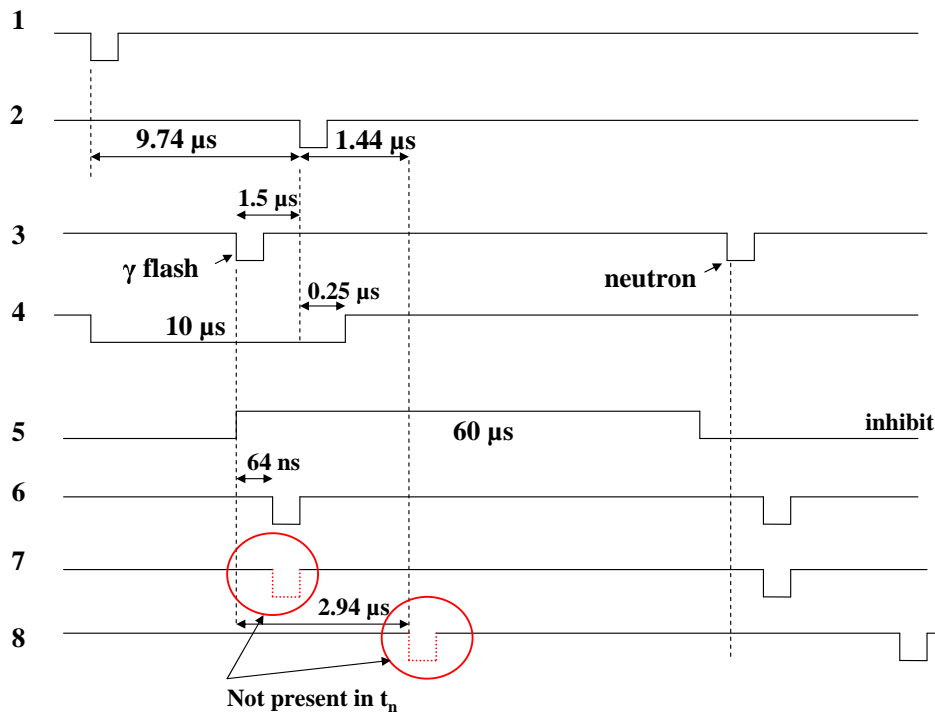
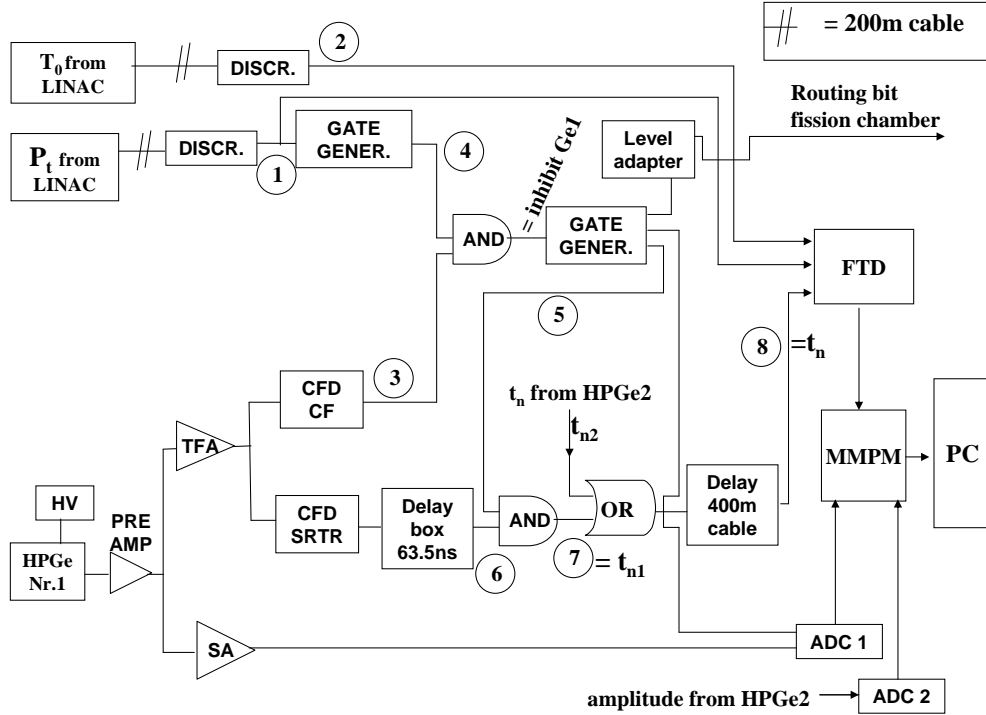


Figure 3.2: *Above:* Electronics scheme. The two detectors from one acquisition system were handled in the same way (only the electronics for one detector is shown here). One inhibit signal was created for every HPGe detector. The inhibit signal was split and used to block the ADC and the FTD and to set a flag (the routing bit) in the fission chamber acquisition system. The inhibit signal completely rejects the events in the time range of interest (even a bit longer) for that burst. The OR of the t_n signals from two detectors was sent through the long cable delay. *Below:* The widths and the delays for the signals in the scheme from above. After the coincidence between the SRTR signal (6) with the inhibit signal (5) the gamma-flash is rejected from the t_n signal (see also Sec.3.2.4).

time of a pulse for each detector. The start of the FTD is given by the pick-up signal t_0 (Sec.2.4) that indicates the arrival of the electron burst at the neutron producing target. Subsequently, each signal coming from the detectors at a time t_n generates a 24 bit time stamp. In addition, the FTD has four inputs for flag signals. If the flag signal and the t_n are coincident a routing bit is set. The time stamp and the routing bits are stored in 4 bytes for every event. The time range of interest for the present setup is about 25 μs after the arrival of the gamma-flash. This time interval corresponds to neutron energies down to about 300 keV, below the neutron inelastic threshold for the studied nuclei. The time measurement is ended by a reset signal, P_t , that is synchronous with the next accelerator burst but arrives about 10 μs in advance of the next t_0 (Fig.3.2).

The MMPPM is operated in coincidence mode to register the time-of-flight simultaneously with the pulse amplitude. A coincidence gate of 6 to 8 μs and a maximum response time (time-out) for the ADCs of 6.4 μs were set. The coincidence window was chosen in relation with the shaping time of the amplitude signals. The HPGe (respectively fission chamber) amplitude and the time are written in a list mode file (always 8 bytes per event). As is seen in Fig. 3.2, the times of both detectors are or-ed before they arrive at the t_n input. True event rates are low enough (< 10/s) to identify the detector that fired by the presence of the amplitude data.

As may be seen from Fig. 3.2, the preparation of the signals that are offered to the ADCs and the FTD is done with conventional electronics. Both HPGe detectors from one system are treated in the same way.

3.2.2 The pulse amplitude channel

The preamplifier amplitude signal is given to a spectroscopy amplifier with 4 μs or 6 μs shaping time, depending on the detector (Fig.3.2). This amplitude signal is given to the ADC. In figure 3.3, the pulse amplitude spectrum is shown. The gamma-rays associated with inelastic scattering are identified. The “triangular” shapes characteristic of inelastic scattering of fast neutrons on the Ge isotopes of the detector [86] are visible as well. At 1.33 MeV the present arrangement achieves 2.4 keV FWHM pulse height resolution and in spite of the neutrons scattered in to the detector no degradation of the performance was observed during the measurement campaign presented in this work.

The γ -ray peaks from the $(n,xn\gamma)$ reactions with $x=2$ and 3 are visible if the integration over the neutron energy is done from the corresponding threshold up to 20 MeV. An example of the amplitude spectrum where the $(n,2n)$ and $(n,3n)$ peaks are visible is given in Fig.3.4 for the ^{208}Pb sample. The 803 keV peak is the result of the $^{208}\text{Pb}(n,3n)^{206}\text{Pb}$ reaction. The other marked peaks results from $^{208}\text{Pb}(n,2n)^{207}\text{Pb}$ reaction. All these peaks have some spurious counts from the open $(n,xn\gamma)$ channels on other Pb isotopes except ^{208}Pb , because of the isotopic composition of the sample. The peaks not labeled are from the inelastic scattering on the sample or from the natural background.

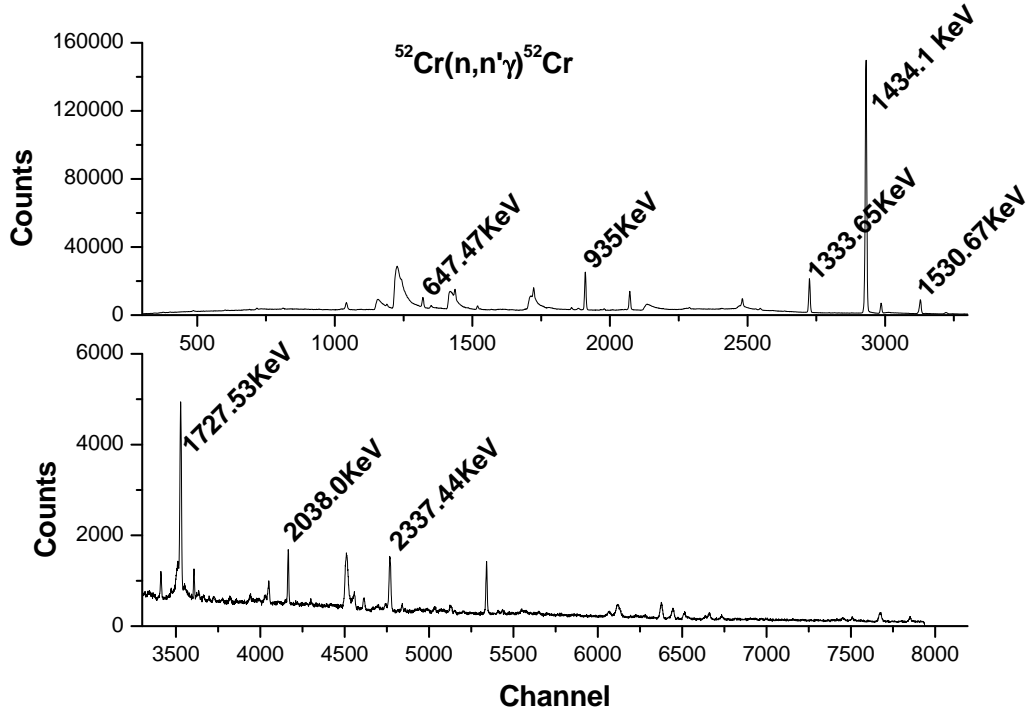


Figure 3.3: Amplitude spectrum obtained for the $^{52}\text{Cr}(n, n'\gamma)^{52}\text{Cr}$ reaction. The spectrum was integrated over the neutron energies from the inelastic threshold up to 20 MeV. Using the enriched $^{52}\text{Cr}_2\text{O}_3$ sample (Table. 3.2) the amplitude spectrum was very much simplified.

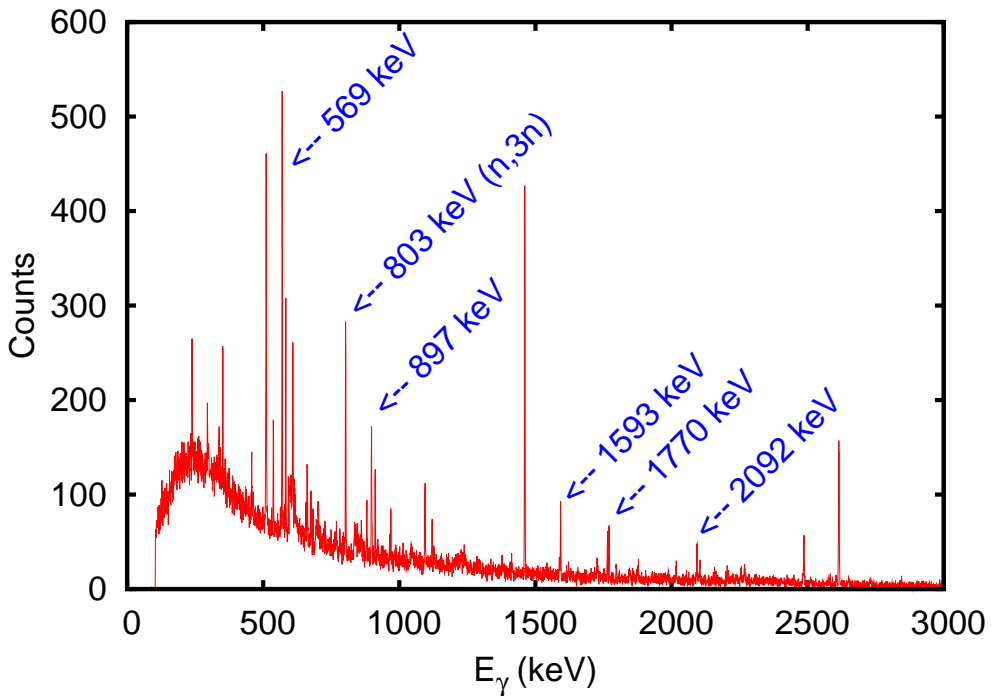


Figure 3.4: Amplitude spectrum obtained for the ^{208}Pb sample (Table. 3.2) with integration over the neutron energy from 8 MeV up to 20 MeV.

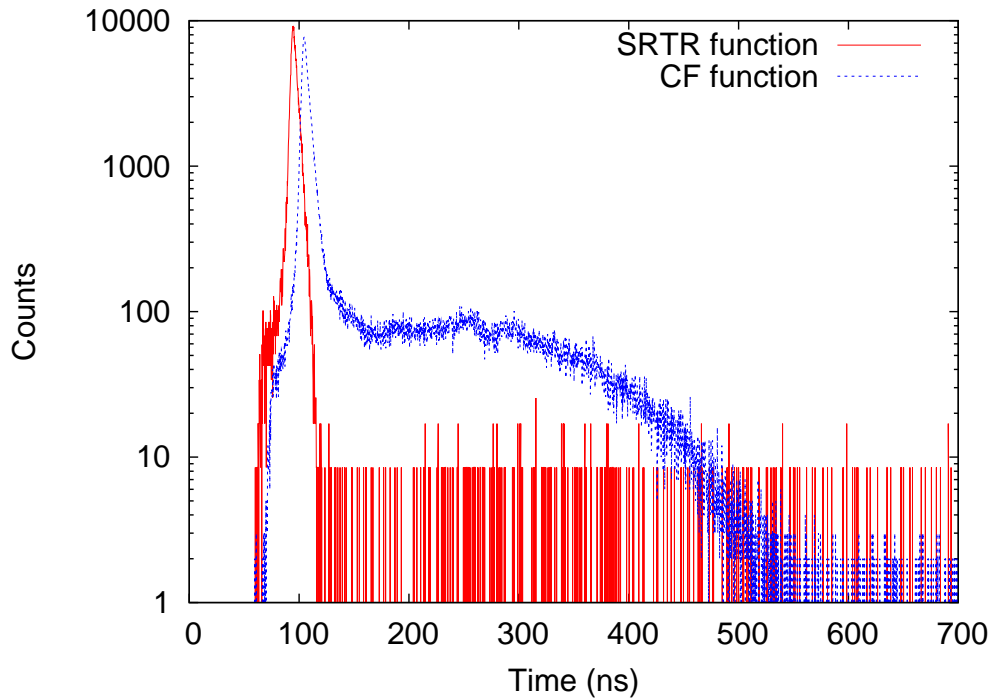


Figure 3.5: Comparison of start-stop spectra for a HPGe detector with 75.9% relative efficiency for which the stop is defined by constant fraction discriminator that is operated with slow rise time rejection applied (SRTR) or without the application of this rejection (CF). For this detector was found a FWHM of 4 ns. A threshold of the CFD module between 100 keV and 150 keV was used for all detector. In general the time resolution was between 4 ns and 6 ns depending on the detector.

3.2.3 The time-of-flight channel

In order to obtain high resolution time-of-flight measurements the time signal was handled as follows. The time signal from the HPGe pre-amplifier is given to a timing-filter amplifier with 10 ns integration and 200 ns differentiation (Fig.3.2). The output is split and one is given to a Constant Fraction Discriminator (CFD) with a Slow Rise Time Rejection (SRTR) function and the other to the CFD with Constant Fraction (CF) function. The CFD with CF function is used only to create the inhibit signal (Sec.3.2.4). In both CFD's the delay is set to 15 ns, corresponding to the so-called Amplitude and Rise-time Compensation (ARC) mode of operation [86]. In Fig. 3.5, the time response of this arrangement is demonstrated.

A coincidence spectrum obtained in a start-stop experiment with a ^{60}Co source is shown in Fig. 3.5. The start signal was given by a fast plastic scintillator (Pilot U) with a time resolution that is 200 ps full width at half maximum and the stop is given by an HPGe detector. For the Constant Fraction function (CF) the start-stop spectrum has a large tail on the right side of the coincidence peak that extends up to about 400 ns. This tail represents 40 - 60% of the total number of counts in the spectrum, depending on the detector and on the applied threshold to the CFD module. The same experiment with a ^{22}Na ($E_{\gamma}=511 \text{ keV}$) source showed that the

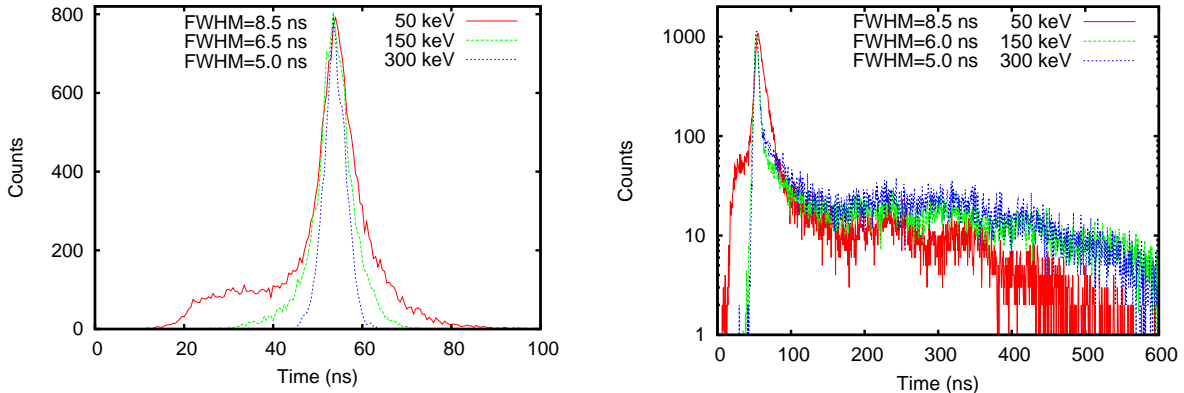


Figure 3.6: The dependence of the time resolution spectra of a 104.3% relative efficiency detector on the CFD threshold with the two functions: *Left*: SRTR and *Right*: CF. The CFD threshold was increased from 50 keV to 300 keV. The time resolution of the spectra (FWHM) was kept almost the same for a given threshold when changed from the SRTR to the CF function.

fraction of counts in the tail increases. On the contrary, the tail is almost completely eliminated when the SRTR option is used, leaving a single peak with the same full width at half maximum.

The dependence on the CFD threshold of the time resolution spectra with the SRTR and with the CF functions is given in Fig. 3.6. Increasing the CFD threshold from 50 keV to 300 keV, the FWHM of the time spectra decreases from 8.5 ns to 5 ns for a detector of 104.3% relative efficiency. For a very low CFD threshold (50 keV) a small tail appears on the left side of the spectra in both cases, SRTR and CF. This effect appears only for a very low threshold, close to the noise amplitude. This suggests again that the signals that give a poor time resolution are the signals with low amplitude. Moreover, the tails in the time spectra are larger for the detectors with larger volume of the crystal since the length of the tail corresponds to the charge collection time. This confirms the expectation that the differences in the shapes of the preamplifier output signals become larger with the increase of the detector volume.

As may be deduced from the tests with the sources, this excellent time-of-flight response using the SRTR option results in a strongly energy dependent efficiency that drops much more rapidly than usual below 500 keV (Fig.3.10). In the present cases studied the main transitions are above 500 keV, so this loss of efficiency can be accepted.

The origin of this behavior lies in the requirement that inside a constant fraction discriminator are a zero crossing detector and a leading edge detector. The first signal from either one of the two, arms the CFD. The last signal determines the time. For low amplitude events or for slow rise times the leading edge detector may trigger after the zero crossing detector so that the circuit produces a pulse with the time defined by the leading edge detector. The latter has a time spread that is strongly pulse amplitude dependent and may range up to the maximum

rise time (650 ns). This results in the behavior shown in Fig. 3.5. For the present measurements, all data were taken with the SRTR option selected and with a CFD threshold between 100 keV and 150 keV.

3.2.4 Gamma flash rejection

The gamma flash (Sec.2.4) causes an event by gammas which are scattered on the sample and then detected by HPGe detector. As already indicated, this happens for a substantial fraction of the total number of Linac bursts (10-20% in every detector), depending on the atomic number Z and on the thickness of the sample. The detection of the gamma-flash can introduce a dead time in the acquisition system in the case of a pile-up with a neutron induced event. In the present setup the detectors themselves are not saturated and can resolve the pile-ups. The FTD is working in the multihit mode and can separate the pile-ups with the gamma-flash.

The MMPM has a coincidence window of 8 μs and a maximum allowed conversion time for the ADCs (time-out) of 6.4 μs (see Sec.3.2.1). These give in total 14.4 μs dead time due only to the MMPM because in the coincidence mode, once an event is detected, the acquisition is blocked until all the connected ADCs finish the conversion. Another source of dead time appears in the spectroscopic amplifiers that are not able to resolve pulses that come closer than 4-6 μs (the shaping time) to each other. The dead time due to the spectroscopic amplifier is smaller than the dead time of the MMPM and is already included in the latest, having the same cause, the pile-up. The MMPM dead time is negligible for low counting rates.

In the present setup the time range of interest for the measurement is only about 25 μs after the t_0 . *The average neutron induced counting rate* is very small, about 6 counts/s per detector, in the time range of interest. This means that for every detector there is less than one neutron induced event in one burst, which means an average of $7.5 \cdot 10^{-3}$ neutrons in every burst. Due to the fact the prompt events are detected within the first 25 μs after the t_0 , the instantaneous counting rate after t_0 has to be also considered. This is about 0.4 neutrons/burst considering that the events are uniformly distributed within the first 25 μs after the t_0 . At these counting rates the probability to have two neutron induced events in one burst is very small.

The only problem to be solved is the pile-up of the neutron induced event with the gamma-flash events. The dead time in the MMPM becomes effective only when one gamma-flash and at least one neutron induced event are detected simultaneously in one burst. Then the MMPM is busy for 14.4 μs recording the gamma flash and any neutron induced event that comes in this time interval is lost. The time-of-flight of 14.4 μs , at 200 m flight path length, corresponds to about 1 MeV neutron energy. This means that any neutron with the energy larger than 1 MeV may be affected by the pile-up with a gamma flash induced event.

To avoid such a pile-up problem, which implies the difficulty to quantify a variable dead time, one decided to eliminate all bursts for which a gamma-flash induced event was detected. For this purpose an inhibit signal was created. Different improvements were brought to the construction of the inhibit signal during the measurement campaign. Here is presented the last version of the scheme (Fig.3.2).

If within a time interval around the arrival time of the gamma-flash at the 200 m flight path station there is a time signal from the HPGe detector an inhibit window is created. The HPGe detector time signal is generated by a CFD with the CF option and with a very low threshold setting.

The individual inhibit signals blocked the corresponding ADCs (Fig.3.2) for the full time interval of interest in that burst (at least 25 μ s). The t_n signal is blocked for the same time interval making a coincidence with the inhibit using a logic coincidence unit. The same inhibit signals were given to the fission chamber FTD and recorded as flags (routing bits). In this configuration, in the data analysis, different fission chamber yields were obtained for every HPGe detector. This was possible at the level of the data analysis looking for the simultaneous presence of the time stamp and of a routing bit corresponding to a given detector. Using the individual inhibit signals the inhibit rate was only 10%-20% from the total number of bursts.

The inhibit signal avoids completely the problem of the dead time in the acquisition system for the present counting rate of neutron induced events with the expense of losses in the detection efficiency.

3.2.5 HPGe absolute peak efficiency measurement

The HPGe absolute peak efficiency measurement was done with point-like calibration sources carefully placed in the sample position. Simultaneously, in one efficiency measurement two types of information were retrieved: one was the *detector efficiency* contained in the pulse amplitude spectra without any time coincidence and the second was the *acquisition system efficiency* contained in the pulse amplitude spectra obtained in coincidence with the time with SRTR. Both are *absolute peak efficiencies*.

For the efficiency measurement the t_0 and P_t signals were given by a pulse generator with the same 800 Hz repetition rate (Sec.2.4) as for the measurement with the sample. The gamma flash inhibit signal was disconnected during the efficiency measurement. The time spectrum with the calibration source shows a flat distribution and was used for the precise determination of the effective acquisition time. In this way the time interval between the P_t and the t_0 was precisely measured. During this time interval the acquisition system is not active and one has to account for it when calculating the effective acquisition time with the calibration source.

During the full measurement campaign, at least one efficiency measurement was done for detectors configuration used in every experiment. In some cases the measurement was repeated a few times for the same configuration to check the stability of the setup over long periods.

The point-like calibration sources used in the experiment and their activity at the measurement date were: ^{152}Eu (29 KBq), ^{60}Co (6.6 KBq), ^{57}Co (2.3 KBq), ^{137}Cs (31 KBq), ^{65}Zn (1.2 KBq) and ^{54}Mn (2.6 KBq). The efficiency measurement was extended above 1.4 MeV using two samples of Co and Al that were activated in the GELINA target vault producing ^{56}Co and ^{24}Na . With these sources the counting rates did not exceed 0.5 counts in every burst of 1.25 ms (800 Hz repetition rate). Therefore almost the same counting rate was used for both efficiency measurement

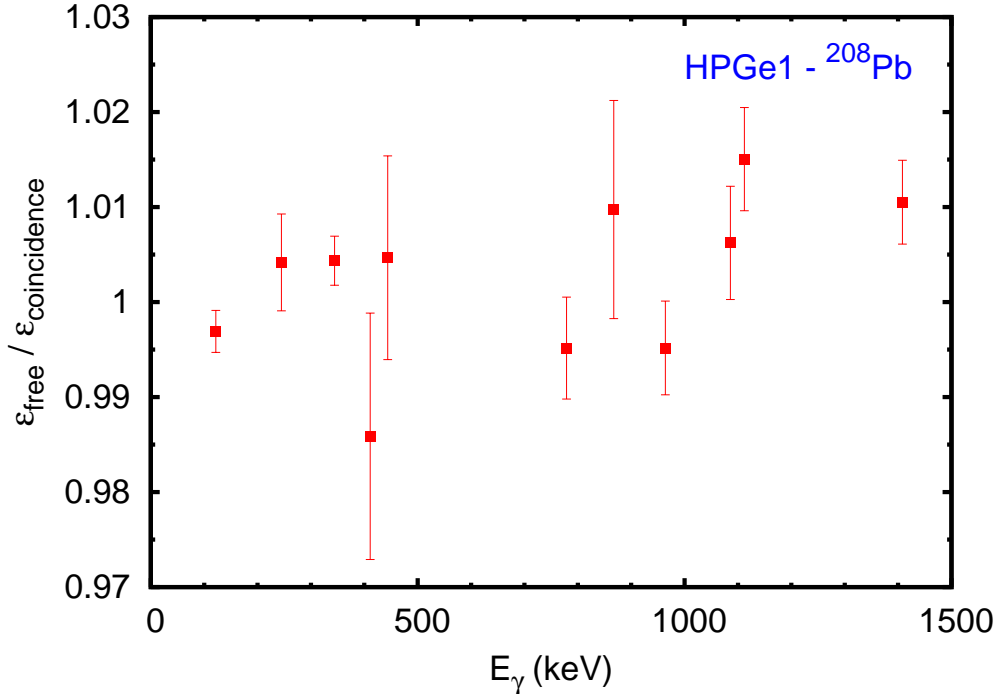


Figure 3.7: Comparison of the *detector efficiency* measurement with two different settings of the MMPM (Sec.3.2.1) : free mode and coincidence mode. There is no significant difference between the two operation modes for the *detector efficiency*.

and experiment with the neutron beam and the sample.

Fig.3.7 shows the ratio between the *detector efficiency* measured in two different operation modes of the MMPM: free and coincidence mode. The free mode operation does not use any coincidence window or time-out (Sec.3.2.1) that may introduce additional dead time. The fact that within the errors the efficiency ratio in the two cases equals one confirms the absence of the dead time in the coincidence mode operation of the setup during the efficiency measurement.

3.3 Data analysis

From the sorting of the list-mode file data recorded by the acquisition systems the net peak area of the γ -ray transition of interest is obtained as a function of neutron energy. The differential gamma production cross-sections at the two measurement angles 110° and 150° are obtained after the appropriate normalization of the net peak area. The goal of the data analysis is to obtain the integral gamma production cross-section as a function of neutron energy. For the particular case of the inelastic scattering ($x=1$), the total inelastic and the level cross-section can be constructed as well. The main steps followed in the data analysis and the applied corrections are described in the following.

3.3.1 Differential gamma production cross-section calculation

Let us consider a generalized version of the experimental setup described in this chapter. The differential gamma production cross-section is symmetric with respect to the azimuth angle ϕ ($\phi \in [0 : 2\pi]$). At the same angle θ_i ($\theta \in [0 : \pi]$) but different ϕ a number N_{θ_i} of detectors can be accommodated. In such a case the differential gamma production cross-section at the angle θ_i is given by the following relation:

$$\frac{d\sigma}{d\Omega}(\theta_i, E_k) = \frac{1}{4\pi} \frac{t_U}{t_s} \frac{A_s}{A_U} \frac{D_{beam}^2}{D_{sample}^2} \epsilon_{FC} \frac{\sigma_U(E_k)}{c_{ms}(E_k)} \frac{\sum_{j=0}^{j=N_{\theta_i}} \frac{Y_j(E_k)}{\epsilon_j Y_{FCj}(E_k)} \frac{1}{\delta(Y_j(E_k))}}{\sum_{j=0}^{j=N_{\theta_i}} \frac{1}{\delta(Y_j(E_k))}}, \quad (3.1)$$

For the last version of the setup (Table. 3.1) described in the present chapter, two detection angles were used, $\theta_1=110^\circ$ and $\theta_2=150^\circ$ and $N_{\theta_1} = N_{\theta_2} = 2$. k labels the time-of-flight bin. Thus, the above expression is applied to each k time-of-flight bin with its corresponding neutron energy E_k .

$Y_j(E_k)$ is the net peak yield for the gamma-ray of interest for HPGe detector j at time bin k and $\delta(Y_j(E_k))$ is its relative uncertainty. Due to the way of applying the inhibit signal to the fission chamber, the fission chamber yield $Y_{FCj}(E_k)$, is detector dependent. ϵ_j is the absolute peak efficiency of HPGe detector j for the γ -ray of interest. ϵ_{FC} is the fission chamber efficiency. t_U and t_s are the mass areal densities of ^{235}U for the fission chamber and for the sample. A_U and A_s are the respective atomic mass numbers. $\sigma_U(E_k)$ is the $^{235}\text{U}(n,\text{F})$ standard cross section for the energy bin k obtained from [69]. $c_{ms}(E_k)$ is a correction factor for the neutron beam attenuation and multiple scattering. Finally, D_{beam} is the beam diameter and D_{sample} is the effective diameter of the sample that intersects the beam. For the samples with a diameter greater than the beam diameter the convention is used that

$$\frac{D_{beam}}{D_{sample}} = 1. \quad (3.2)$$

Writing the differential gamma production cross-section as in Eq.3.1 allowed a better treatment of the quadratic propagation of the uncertainty. As resulted from Sec. 2.3.3, the integral gamma production cross-section can be calculated with the following relation:

$$\sigma(E_k) = 2\pi[w_1 \frac{d\sigma}{d\Omega}(110, E_k) + w_2 \frac{d\sigma}{d\Omega}(150, E_k)], \quad (3.3)$$

where the weights are w_1 and w_2 are given in Table 2.1.

Based on the level scheme of the nucleus, from the integral gamma-production cross-sections, the total inelastic and the level inelastic cross-sections are constructed as described in Sec.2.1.2.

3.3.2 Sorting the HPGe data

The data were recorded in list mode for 500 to 1000 hours per isotope in runs of a few days that were each subdivided in cycles of 2 hours. The cycles during which the

accelerator did not work continuously were identified and excluded from the sorting process. The list mode data were sorted by newly developed C++ codes that were tailored to the experiment. For each run the data was sorted in two-dimensional matrices (2500 time channels - 8192 amplitude channels). The time bins of 0.5 ns from the binary file were grouped in bins of 8 ns to obtain reasonable statistics per bin and to have a bin width larger than the time resolution of the HPGe detectors. The time axis of the matrices was chosen to include neutrons from the inelastic threshold up to 20 MeV. To compensate for the variations in the offset of the γ -ray energy calibration, these matrices were shifted such that the main transition is always in the same channel before they were summed together in one matrix for each detector.

Regions of interest for gamma-rays of sufficient intensity were determined from the amplitude projection (e.g. Fig. 3.3) of the matrix. Similarly, from such a figure the regions of interest for the background determination were fixed as well. For most cases a linear fit of the background was sufficient, but for some gamma-rays a quadratic fit was required. Peak areas and background subtraction were extracted for each time-channel of 8 ns. The validity of this approach was verified by checking the neutron-energy dependence of the amplitude projections in coarse energy bins.

The offset calibration of the time histograms was done relative to the position of the peak of the gamma-flash. The gamma flash position in the spectrum was checked periodically and no significant shifts were observed. In order to observe the gamma flash the inhibit signal was removed for a short time at the beginning and at the end of each run.

3.3.3 HPGe efficiency corrections

As seen from Sec.3.2.5, the HPGe efficiency measurement was done with point-like calibration sources while the samples used in the measurements had a finite size (Sec.3.1.3). This suggests that a correction for the extended volume source has to be done. Moreover, the γ -ray attenuation in the sample has to be considered. These two corrections were done simultaneously by means of MCNP calculations [73]. The MCNP-4C version of the code was used. The calculation was done in two steps:

- The experimental setup was carefully described in the MCNP input. Detailed descriptions of the HPGe detectors (dimensions of the crystals, of the contacts and of the crystal holders) were used. The monoenergetic point-like γ -ray source was placed in the position of the sample center. Different input files were created to cover the energy range of interest, from 250 keV up to 5 MeV, changing only the γ -ray energy. The results of these MCNP calculations were compared with the experimental *detector efficiency* (Sec.3.2.5). Small adjustments were done for the HPGe detectors geometry especially adding thin dead layers on the crystal and the calculation was repeated until a good agreement with the measurement was obtained. In Fig.3.8 two examples of the comparison between the point-like source MCNP calculation and the measurement are shown. The calculations matched the measurement within 5% to 15%,

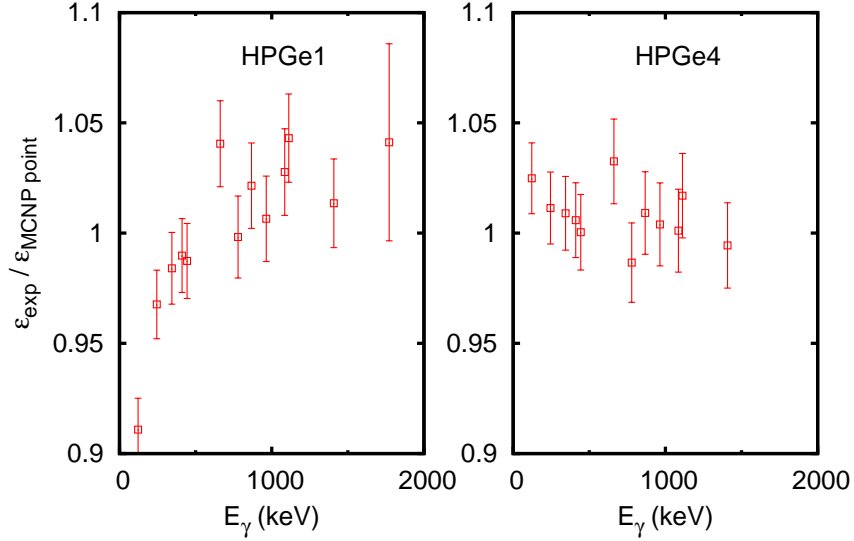


Figure 3.8: Comparison between the measured *detector efficiency* and the calculated values with MCNP using the point-like source and the "best" detector geometry. The agreement between the experiment and the calculation is between 5% and 15% depending by the detector.

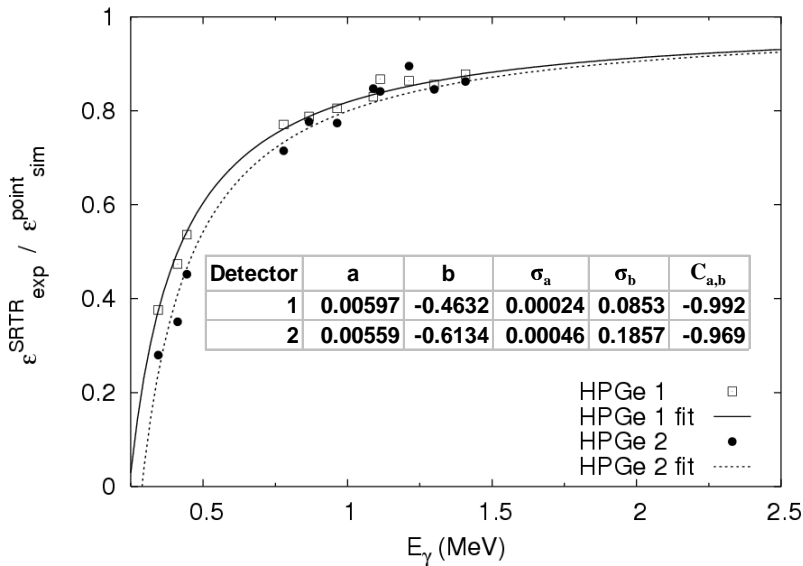


Figure 3.9: The ratio between the measured efficiency with SRTR function (*acquisition system efficiency*) and the simulated *detector efficiency* with a point source geometry was fitted in general with the function from Eq.3.5. For ^{52}Cr was used $1 - \frac{1}{ax+b}$. The inset shows the fit parameters, uncertainties and correlation coefficients for ^{52}Cr (see text for details).

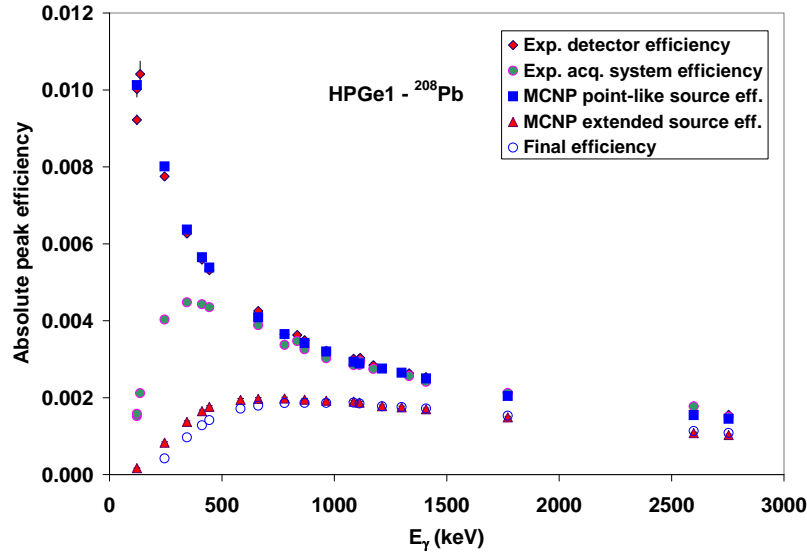


Figure 3.10: The absolute peak efficiencies for ^{208}Pb sample for HPGe1. The *detector efficiency* was measured with no time coincidence. The *acquisition system efficiency* was measured using the coincidence amplitude-time with SRTR (see Sec.3.2.5 for details). Both simulated efficiencies with MCNP are *detector efficiency*. The *final efficiency* was calculated with Eq.3.4.

depending by the detector. The same comparison may be seen from Fig.3.10, but because of the efficiency scale the differences are not so clear.

- Once the "best" HPGe detectors geometry description was found, the point-like γ -ray source was changed in the input file with a source that has the same geometry as the sample and the calculations were repeated. The results contain the effect of the extended volume and of the γ -ray attenuation in the sample.

Fig.3.10 shows the measured and the calculated efficiencies for the ^{208}Pb sample for HPGe1 detector. The calculated efficiency with the extended volume sample decreases significantly at low energies. The attenuation effect is sample dependent and is larger for the samples of heavy nuclei and large volumes. This was clearly seen when the calculations were done with different samples (from ^{52}Cr to ^{208}Pb).

The final efficiency was calculated with the relation:

$$\epsilon = \epsilon_{MCNP\,extended} \frac{\epsilon_{acquisition\,system}}{\epsilon_{MCNP\,point}}. \quad (3.4)$$

One chose to write the final efficiency as in Eq.3.4 to separate the ratio $\frac{\epsilon_{acquisition\,system}}{\epsilon_{MCNP\,point}}$. Empirically it was found that this ratio converges to a constant for high γ -ray energies. This ratio was fitted with a function of the type:

$$p_4 - \frac{1}{p_1 x^2 + p_2 x + p_3}, \quad (3.5)$$

where p_i ($i=1,2,3,4$) are the parameters of the fit. In this way the global trend of the ratio $\frac{\epsilon_{acquisitionsystem}}{\epsilon_{MCNP\ point}}$ was described better and the errors of the individual points were reduced. Such a fit served for the efficiency interpolation below the highest energy used in the measurement (1.4 MeV) and for the extrapolation above this energy.

Eq.3.4 includes simultaneously the following three effects:

- the finite size and the γ -ray attenuation of the sample,
- the decrease in the efficiency due to the application of the SRTR function on the CFD's,
- the difference between the MCNP point-like source calculation and the measured detector efficiencies (Fig.3.8).

3.3.4 Neutron fluence

The fission chamber data were treated similarly with cycles in one-to-one correspondence with the gamma-ray measurements and stored in a matrix of time versus amplitude. The time axis of this matrix was rebinned to account for the difference in flight path length (1.3 m) between the sample and the fission chamber.

The amplitude spectrum for the full time-range of interest is shown in Fig.3.11. The peak at low amplitude is due to the α decay of ^{235}U and the rest of the spectrum is due to neutron induced fission. The region between channels 850 and 8192 contains neutron induced events only. This pulse amplitude region was used to determine $Y_{FC}(E_k)$ for each time channel k of 8 ns (see also Fig.2.10). In this way the number of neutron induced events was underestimated. This is taken care of by the fission chamber efficiency in Eq. 3.1. which was determined by the following expression (see also Fig. 3.11).

$$\epsilon_{FC} = \frac{\text{spectrum area from channel 850 to 8192}}{\text{area extrapolated triangle} + \text{spectrum area from channel 850 to 8192}}$$

It was found that $\epsilon_{FC} = 0.984 \pm 1.6\%$. To reduce statistical fluctuations, the FC yield Y_{FC} was smoothed with a moving average window of 31 channels of 8 ns.

3.3.5 Grouping the time-of-flight bins

The 8 ns time-of-flight resolution is usually appropriate for the strong γ -ray transitions at low neutron energies. Above 10 MeV, even for the main transition of the studied nuclide the statistics in 8 ns bins may become poor. In consequence, for some γ -ray transitions a grouping of several t.o.f. bins in one is necessary. The grouping of the t.o.f. bins (neutron energy bins) must be done differently on different energy regions. For correct uncertainty propagation the t.o.f. bins are grouped at the level of the detector yield. In Eq.3.1 the time-of-flight bins, k , must be grouped for all detectors, HPGe and fission chamber, in the same way.

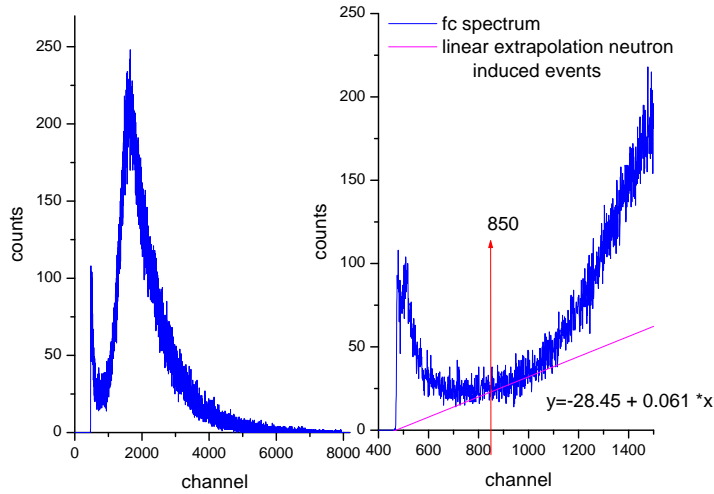


Figure 3.11: Left: fission chamber amplitude histogram sliced from the 2D matrix, with the time-of-flight from channel 1 up to 1500, which means neutrons from below inelastic threshold up to about 20 MeV. Right: expanded spectrum and the extrapolation of the neutron induced events.

The grouping of n time-of-flight consecutive bins in one is done according to the equation:

$$Y'_j(E_{k'}) = \sum_{k=j}^{k=j+n} Y(E_k), \quad (3.6)$$

where the $Y'_j(E_{k'})$ is the yield in the resulted energy (time) bin with the limits E_j, E_{j+n} .

3.3.6 Multiple scattering and neutron flux attenuation

For a precise measurement of the incident neutron flux that interacts with a finite size sample, two effects need to be accounted for. The first is the neutron attenuation in all materials after the fission chamber. This material includes the external wall of the fission chamber, the air, the sample container (if the case) and the sample itself. The neutrons may be removed from the beam through different reactions (e.g. capture or reaction with emission of charge particles and no neutrons as $(n,p),(n,\alpha)$). The second is the multiple scattering in the sample. This means that the neutron has a first interaction in the sample, loses some energy and than produces the $(n,xn\gamma)$ reaction of interest. The first interaction may be elastic scattering of even another $(n,xn\gamma)$ reaction, in which more than one neutron may cause this effect.

The two effects were determined simultaneously using the Monte Carlo code MCNP [73]. The geometry of the experimental setup was described in the input file of the code. The reaction rate in the sample for the full geometry is compared to the reaction rate when the materials in the beam following the fission chamber are absent (Fig. 3.12). The measured gamma-production cross-sections were introduced

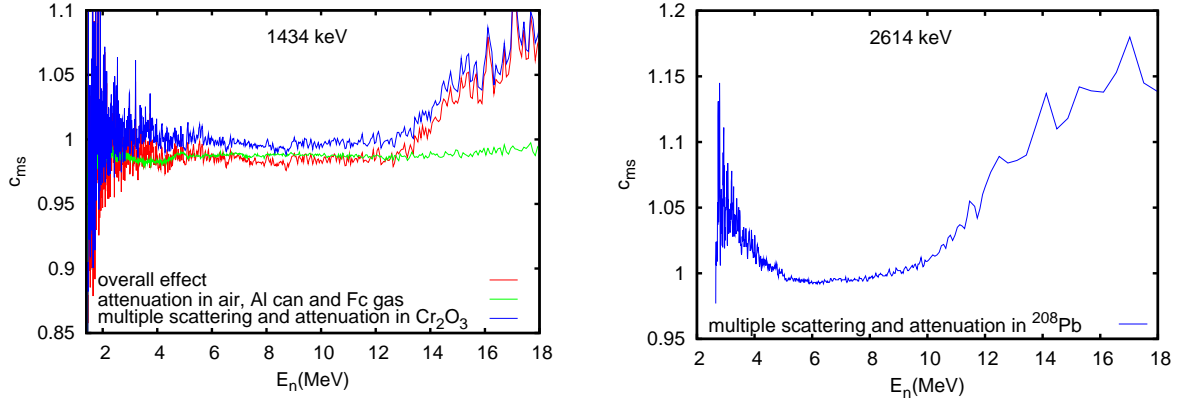


Figure 3.12: The neutron flux attenuation and multiple scattering correction for the 1434 keV transition of ^{52}Cr and for 2614 keV of ^{208}Pb .

as a dose card in the MCNP input file. To disentangle the two effects, an additional calculation was done with an empty sample only, in order to obtain the effect of the attenuation before the sample as a result of air, the fission chamber and the sample container.

From Fig. 3.12 one sees that the attenuation is about 2% independent of energy, whereas the multiple scattering effect in the sample varies between 2% and 15% depending on energy and on the sample. The multiple scattering and attenuation coefficient starts to increase above the $(n,2n)$ threshold in the sample, due to the multiplication of the neutron in this reaction.

3.3.7 Measurement uncertainties

The uncertainties of the parameters involved in the cross-section calculation will be given in the following. The atomic masses A with the corresponding uncertainties are taken from the online data bases [55]. The mass areal densities are known to better than 0.3% for both the sample and the ^{235}U from the fission chamber. The uncertainty of the fission chamber efficiency ϵ_{FC} is 1.6%. The beam diameter D_{beam} was measured with about 1% uncertainty. The $^{235}\text{U}(n,F)$ standard cross-section has an uncertainty smaller than 1% up to 10 MeV and is increasing to 1.5% at 20 MeV.

During different experiments with the fission chamber used here no changes in the neutron flux shape were observed. This allowed to apply a smoothing procedure on the fission chamber yield, $Y_{FC}(E_k)$, in order to reduce the statistical fluctuations. After the data smoothing the uncertainties of the $Y_{FC}(E_k)$ were smaller than 2% up to 10 MeV increasing up to 4% around 18 MeV.

The HPGe yield $Y_j(E_k)$ introduced the largest uncertainties. For the main γ -ray transitions, the HPGe yield uncertainty was about 5% below 10 MeV and increases up to about 15% around 18 MeV. For the weak γ -ray transitions the time-of-flight bins were grouped according to the Eq.3.6 in order to keep the total uncertainty in reasonable limits. The multiple scattering coefficient $c_{ms}(E_k)$ had a negligible statistical uncertainty from the MCNP calculation. A possible systematic uncertainty

that may come from the procedure used for the simulation was not evaluated.

The uncertainty of HPGe detectors efficiency, ϵ_i was less than 3% for almost all gamma rays below 1.4 MeV. Above 1.4 MeV the efficiency uncertainty increases up to 4-5%. The major experimental component in this uncertainty was the error on the calibration source activity, 1.5%, the rest was coming from the applied corrections. The statistical uncertainties from the efficiency measurement and from the MCNP simulations were less than 1%. The self-attenuation of the gamma ray and the effect of the finite extension of the sample are based completely on the MCNP simulations. Special effort was done to reduce any systematic error of these MCNP simulations describing as realistic as possible the geometry of the detectors and of the sample (see also [1]).

3.4 Conclusions

A new high resolution spectrometer was built at the GELINA facility for the measurement of gamma-ray production cross sections in the $(n, xn\gamma)$ reactions ($x=1, 2$ and 3) on the full energy range from the thresholds up to about 20 MeV. A neutron energy resolution of 1.1 keV at 1 MeV (36 keV at 10 MeV) and a total uncertainty of about 5% below 10 MeV (up to 15-20% at 20 MeV) was achieved for the main γ -ray transitions.

The $(n, n'\gamma)$ -technique was used with large volume HPGe detectors. Based on the level scheme of the nucleus, the total inelastic and the level inelastic cross-sections can be constructed up to about 4 MeV neutron energy (corresponding to the maximum excitation energy of an observed excited level). Above this energy the total inelastic cross-section constructed with the same procedure is only a lower limit for the exact value (Sec.2.1.2). This limit for the total inelastic cross-section may be very close to the real cross section, when there is no significant direct decay to the ground state, especially in the even-even nuclei. The cross-section normalization was done relatively to the standard ^{235}U fission cross-section.

The present setup is more suitable for the nuclei that emit γ -ray with energies above 500 keV and with low conversion coefficients. Any full converted transition (e.g. E0) and any isomer levels are not accessible with the present setup. Using the $n, n'\gamma$ technique the γ -ray angular distribution may be measured, but no information about the outgoing neutron angular distribution may be obtained.

Finally, one should mention that in the present experimental setup there is an important efficiency loss first due to the SRTR mode of operation (especially below 500 keV) and secondly due to the pile-up between the neutron induced events with an event from the GELINA gamma-flash. The latter represents 10 to 20% for every detector. One solution of both these problems is the use of *fast digitizers* * for the data acquisition. An alternative for the conventional acquisition system presented in this chapter will be presented in Chapter 4 where a completely independent

*Difference should be made between the fast digitizer described in the Chapter 4 and the fast time digitizer, FTD, (multi-hit time-to-digital converter) used with the conventional acquisition system (Sec.3.2.1)

58 *Experimental setup for the $(n,xn\gamma)$ cross-section measurements at GELINA*
acquisition system based on a *fast digitizer* will be described.

Chapter 4

Data acquisition system with a fast digitizer

The experimental setup described in the previous chapter was successfully used for $(n, xn\gamma)$ cross-section measurements. The major inconvenience of this experimental setup is the long time interval needed to achieve the described unprecedented performances. With four HPGe detectors about 500 hours of effective acquisition time are still needed. During such long acquisition periods changes in the setup settings may occur due to fluctuations in the ambient temperature or failure of different electronic modules.

Because of this, an increase in the detection efficiency, resulting in a smaller acquisition time, is desired. There are two solutions to increase the detection efficiency: to increase the number of detectors and to reduce the losses in the data acquisition system. The first solution is relatively expensive and the number of detectors was already increased from two (^{52}Cr measurement) to four. To gain another factor of two in the detection efficiency implies adding another 4 detectors.

The losses in the acquisition system can be reduced using a new acquisition system based on a fast digitizer. A DC440 fast digitizer from AcqirisTM was used. This chapter will describe the tests that were done for the evaluation of the performances of such a fast digitizer with large volume HPGe detectors. The main parameters that were monitored during the tests were the time and amplitude resolutions and the highest counting rate at which the dead time is still negligible. As a first step of the fast digitizer testing, data were taken with a start-stop experimental setup between a large volume HPGe detector and a plastic scintillator (Sec. 4.4.1). The results of applying different pulse processing algorithms on the same data set taken with the start-stop setup were compared. The pulse processing algorithm that gave the best results was implemented for an online data acquisition and then used for the cross-section measurements. The electronic scheme for the data acquisition system based on the fast digitizer will be given in Sec. 4.5.

The results obtained with the data acquisition based on the fast digitizer are given in Sec. 4.6. This section contains the final comparison between the differential gamma-production cross-sections measured in parallel with the two completely independent acquisition systems: conventional electronics and fast digitizer. The

last section of this chapter is dedicated to the conclusions on the data acquisition system with the fast digitizer.

4.1 The goal of a new acquisition system

In the data acquisition system based on the conventional electronics presented in Sec. 3.2 detected events are rejected in two ways:

- using the inhibit signal for the suppression of the gamma flash induced event and
- using the SRTR function of the CFD to obtain a good time resolution for the large volume HPGe detectors.

The SRTR function and the rejection of the gamma flash events were explained in detail in Sec. 2.2 and respectively Sec. 3.2.4. Only a summary of the problems will be recalled here.

The neutron bursts in which a gamma-flash induced event was detected were rejected to avoid a variable dead time in the acquisition system. When working in coincidence mode, the MMPM of the conventional acquisition system is not able to resolve two events that come separated in time by less than $14.4 \mu\text{s}$ ($8 \mu\text{s}$ coincidence window and $6.4 \mu\text{s}$ the conversion time of the ADC). In addition to this limitation, the spectroscopic amplifier gives a poor energy resolution in the case when two events are separated by less than about $18 \mu\text{s}$, if the shaping time is $6 \mu\text{s}$. At the average counting rates of this setup (6 neutron induced events per second) this two limitations affect only the neutron bursts that have a pile-up between a gamma flash and a neutron induced event. Solving the problem of these pile-ups increases the detection efficiency with 10-20% per detector, depending on the detector efficiency and on the detection angle.

Up to 40-60% detection efficiency is gained especially at low energies if the use of the SRTR function of the CFD is avoided without any deterioration of the time resolution. This represents the amount of rejected events from the tail of the time resolution spectrum with the CF function (see Fig. 3.5).

A solution for these two problems is a new data acquisition system based on a fast digitizer. The goal for the use of the fast digitizer was to gain detection efficiency as mentioned above and to have at least the same performance as the conventional acquisition system. An additional advantage of a fast digitizer is the simplicity of the experimental setup, because the number of used electronic modules is reduced significantly.

4.2 Working principle of a fast digitizer

A fast digitizer is a flash analog-to-digital converter that records samples of the input signal with a high repetition rate and transfers them for signal processing. Two properties define the performances of a fast digitizer: the number of bits for

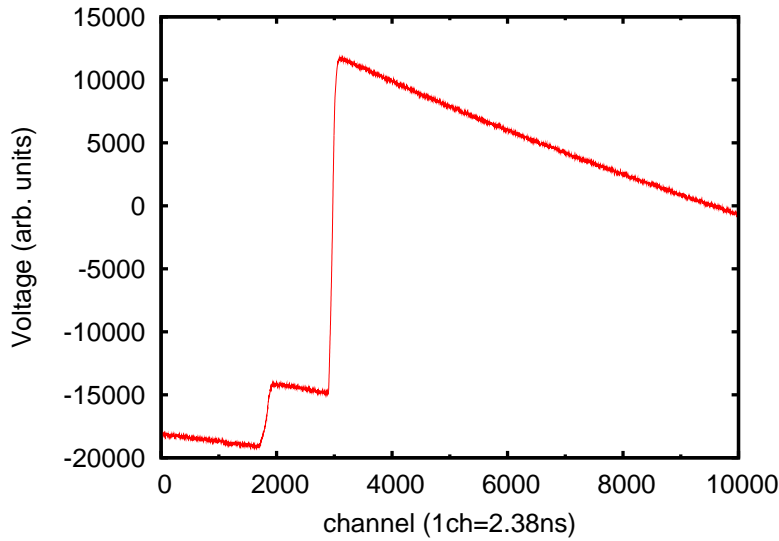


Figure 4.1: The HPGe preamplifier output recorded with the fast digitizer. The length of the signal is about $23.8 \mu\text{s}$ (10 000 samples). A pile-up of two pulses separated by about $2.5 \mu\text{s}$ can be seen. From such signal, a processing algorithm has to retrieve the starting point of every pulse (the time) and the pulse amplitude (the energy).

the amplitude and the sampling rate. The number of bits defines the amplitude resolution and the sampling rate defines the time resolution. An ideal digitizer should have both characteristics large enough such as the digitizer does not alter the performances of the detector. To have both high repetition rate and a large number of bits in one device represents a technological challenge. Nowadays the closest devices to the ideal fast digitizer have either up to 2 GSPS sampling rate but only 10 bits for the amplitude, or up to 14 bits for the amplitude but only about 100 MSPS sampling rate.

For the project described here, a DC440 digitizer from AcqirisTM was chosen. This has 420 MSPS maximum sampling rate that corresponds to a minimum sampling interval of about 2.38 ns and 12 bits for the amplitude. The full scale range of the inputs can have the following values: 250 mV, 500 mV, 1 V, 2 V, 5 V and 10 V. The input impedance is 50Ω . Every DC440 card has two input channels and a common external trigger input. This card has the trigger time interpolation function that allows a very precise determination of the trigger moment. In this way, the arrival time of the external trigger is determined within one sampling interval. The clock accuracy of the card is less than 0.2 ppm. The preamplifier output of the detector is given directly to one of the two independent input channels. An example of the digitized preamplifier output is given in Fig. 4.1. The DC440 module has no possibility of on-board signal processing and in consequence the full set of samples has to be transferred to the computer. There the signal is processed online or recorded on the disk. The digitizer system used here has 2 DC440 cards plugged in a CompactPCITM crate. The crate is connected to the computer through the

PCI bus.

An important limitation of the DC440 module is the transfer speed through the PCI bus (up to 100 MB/s). As it will be seen in the following sections, for the measurements at the 200 m flight path station, about 10 000 samples are needed to cover the neutron energy range of interest (400 keV up to 20 MeV). In the worst case when both cards have a trigger simultaneously, 40 000 samples have to be transferred. The transfer of these data can be done in slightly less than 1.25 ms which is the time interval between two consecutive neutron bursts. Moreover, the average counting rate is 6 neutron induced events per second and so no dead time should appear.

4.3 Digital algorithms for signal analysis

In this section the digital signal processing algorithms that were tested with the DC440 fast digitizer are described. These signal processing algorithms can be divided in timing algorithms that will give the starting time of the pulses and the amplitude algorithms that return the pulse amplitude, which is proportional with the deposited energy in the detector. In addition to these, some auxiliary algorithms will be introduced at the beginning of this section. These algorithms were used for the investigation of the noise and for pulse detection in a signal. A Timing Filter Amplifier (TFA) algorithm was used prior to the application of any timing algorithm to obtain an adequate pulse shape. Three timing algorithms will be discussed here, all three having well known analogs in conventional electronics ([82, 84, 89]. For the amplitude, only the *trapezoid* algorithm, that is specific to the digital signal processing, will be presented. Their recursive formulae and their parameters will be given.

4.3.1 Auxiliary algorithms

Signal noise analysis

The signal noise means the white noise in which every frequency component has the same amplitude. This noise has two sources. First, there is the noise introduced by the fast digitizer itself and this is clearly visible when nothing is connected to the input. Secondly there is the noise of the detector. When the output of the detector preamplifier is connected to the digitizer, the resulting noise band affects the amplitude resolution of the digitizer. This means that from the total number of bits available (12 in this case) some bits are used only to digitize the noise. In consequence every digitizer is characterized by the effective number of bits (ENOB) that is the difference between the total number of bits and the number of bits used for the noise digitization.

For the estimation of the noise intensity two conditions were tested. First, signals were recorded when nothing was coupled to the input (the baseline of the digitizer) and secondly the preamplifier output of the HPGe detector was connected.

Table 4.1: RMS_{*noise*} values with and without the detector coupled to the digitizer input. Two different detectors were used with different preamplifier gains. The full output scale is 4096 channels (12 bits) for 250 mV. The 420 MSPS sampling rate was used and N=3000 samples were averaged. When the HPGe detector is connected to the digitizer, the amplitude of the noise band is increased by a factor 5 for HPGe2.

input	preamp gain(mV/MeV)	RMS _{<i>noise</i>}	ENOB
empty	-	1.44 ± 0.06	9.7
HPGe1 b93061	92.3	5.75 ± 0.50	7.7
HPGe2 b04036	176	7.69 ± 0.50	7.3

The root mean square (RMS) value of the baseline signals was calculated in both cases. The following relation was used:

$$RMS_{noise} = \frac{1}{N+1} \sqrt{\sum_{k=0}^N (v_k - \bar{v})^2}, \quad (4.1)$$

where n is the number of samples used to calculate the average \bar{v} and v_k is the recorded voltage in the sample k . The effective number of bits (ENOB) was calculated with the relation [86]:

$$ENOB = N - \log_2(\sqrt{12} RMS_{noise}), \quad (4.2)$$

The results are summarized in table 4.1. The smallest input full scale range available for this module, 250 mV (± 125 mV) was used here. The test was done for two different HPGe detectors. The digitized output corresponded to 12-bits (4096 channels). It can be seen that the internal noise introduced by the digitizer itself is negligible compared with the detector noise.

Finding a pulse

For the first inspection of the recorded signal a recursive algorithm was used for finding the pulses that exceeded the noise level. Such algorithm has to be very fast to reduce to the minimum analysis time spent for the rejection of the signals without any pulse (zero-suppression). It has also to filter the signal noise to avoid false triggers. The straightforward method is to compare the average value of the signal after and before the pulse occurred. Two parameters are involved: the number of samples N over which the average is taken and the number of samples $2D + 1$ between the two averages:

$$o_k = \frac{1}{N} \sum_{i=1}^N (v_{k+i+D} - v_{k+i-N-D-1}), \quad (4.3)$$

Typical values used below for these parameters are $N=100$ samples and $D=10$ samples. A pulse is detected when the constructed signal o_k has a local maximum. The position of the local maximum can be used to define a region of interest were the

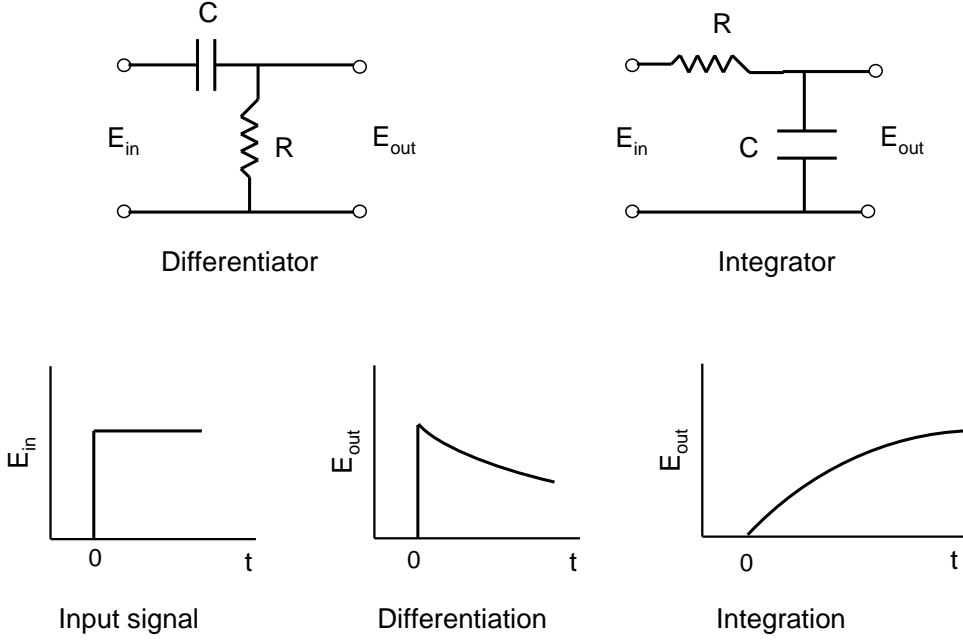


Figure 4.2: Analog shaping circuits (differentiator CR and integrator RC) and their response to a step input signal E_{in} .

starting time of the pulse can be searched with a better precision given by one of the timing algorithms explained below.

Digital Timing Filter Amplifier

To ensure that complete charge collection occurs and to minimize the ballistic deficit, the preamplifiers provide a quite long decay time, typically $50 \mu\text{s}$. For the pulse processing that follows it is desired that the long tail of the preamplifier signal is reduced, process called *pulse shaping*. In analog circuits the basic shaping circuits are the integrator (RC shaping) and the differentiator (CR shaping). The equivalent electronic schemes for the two circuits are given in Fig. 4.2.

The response function of a differentiator is:

$$\hat{E}_{out} = \frac{j\omega\tau}{1 + j\omega\tau} \hat{E}_{in} \simeq \hat{E}_{in} \cdot \begin{cases} 1 & , \omega\tau \ll 1, \\ 0 & , \omega\tau \gg 1. \end{cases} \quad (4.4)$$

where $\tau = RC$ is the decay constant of the circuit (Fig. 4.2), ω is the frequency and $j^2 = -1$. For a differentiator when the product $\omega\tau$ is small, the output voltage is proportional with the derivative of the input signal. If the differentiation conditions are not met (large $\omega\tau$) the input signal passes without alteration. The fast leading edge is not differentiated because τ is not small compared with the pulse rise time. The differentiator filters also the noise, the low frequencies are attenuated while the high frequencies pass only with little alteration. Consequently the differentiator is called *high-pass filter*.

The response function of an integrator is:

$$\hat{E}_{out} = \frac{1}{1 + j\omega\tau} \hat{E}_{in} \simeq \hat{E}_{in} \cdot \begin{cases} 1 & , \omega\tau \ll 1, \\ \frac{1}{j\omega\tau} & , \omega\tau \gg 1. \end{cases} \quad (4.5)$$

The integrator provide an output pulse proportional with the integral of the input for large values of $\omega\tau$. If the integration conditions are not met (small values for $\omega\tau$) again the input signal passes without alteration. Contrary to the differentiator, the integrator is a *low-pass filter* because only the low frequencies pass without alteration.

In Fig. 4.2 the response of the two shaping circuits is given for an input step-like signal. The output signals of single shaping circuits are not attractive and therefore their combination is used. This is the case of an analog shaping amplifiers that have a CR circuit followed by an amplification step and then by a RC circuit.

For the digital signal processing an equivalent of the analog timing filter amplifier (TFA) will be described here. Such algorithm is necessary prior to the use of the timing algorithms mainly to eliminate the signal offset $V_0(t)$ (see Eq. 2.12) and to filter the noise. Starting from the properties of the TFA, its response functions can be written as a product between the response function of a perfect amplifier, an integrator and a differentiator:

$$\hat{H}(\omega) = A \frac{1}{1 + j\omega\tau_1} \frac{j\omega\tau_2}{1 + j\omega\tau_2}, \quad (4.6)$$

where A is the amplification, τ_1 the integration time constant and τ_2 the differentiation time constant. ω is the input frequency. Eq. 4.6 can be written also as:

$$\hat{H}(\omega) = A \frac{\tau_2}{\tau_2 - \tau_1} \left[\frac{1}{1 + j\omega\tau_1} - \frac{1}{1 + j\omega\tau_2} \right] \quad (4.7)$$

Using the following integral

$$\frac{1}{\tau} \int_0^\infty e^{-t/\tau} e^{-j\omega t} dt = \frac{1}{1 + j\omega\tau}, \quad (4.8)$$

and making the convolution in the time domain, the response function of the TFA is:

$$H(t) = \begin{cases} A \frac{\tau_2}{\tau_2 - \tau_1} \left[\frac{1}{\tau_1} e^{-t/\tau_1} - \frac{1}{\tau_2} e^{-t/\tau_2} \right] & , t > 0 \\ 0 & , t \leq 0. \end{cases} \quad (4.9)$$

In the time domain, the output response $o(t)$ of the TFA for an input signal $v(t)$ is:

$$o(t) = (H * i)(t) = \int_{-\infty}^t v(x) H(t-x) dx = \int_0^\infty v(t-x) H(x) dx \quad (4.10)$$

For the digital signal that has a discrete representation with the sampling interval Δ , the output response $o(k\Delta)$ as a function of the input signal v_k is

$$o(k\Delta) = \sum_{l=0}^{\infty} v((k-l-1/2)\Delta) H((l+1/2)\Delta) \Delta \quad (4.11)$$

k is the index of the sample. The middle of the sampling interval Δ was considered. Shorter notation will be used: $o_k = o(k\Delta)$, $v_k = v((k-1/2)\Delta)$ and $H_l = H((l+1/2)\Delta)$. Finally, the discrete TFA output for a given input signal v_k can be written as:

$$o_k = A \frac{\tau_2}{\tau_2 - \tau_1} \left(\frac{\Delta}{\tau_1} e^{-\Delta/(2\tau_1)} o_k^{(1)} - \frac{\Delta}{\tau_2} e^{-\Delta/(2\tau_2)} o_k^{(2)} \right), \quad (4.12)$$

where

$$o_k^{(1,2)} = \sum_{l=0}^{\infty} (v_{k-l} e^{-l\Delta/\tau_{1,2}}) \quad (4.13)$$

Each factor $o_k^{1,2}$ can be written recursively:

$$o_{k+1}^{(1,2)} = v_k + e^{\Delta/\tau_{1,2}} o_k^{(1,2)}, \quad (4.14)$$

With the assumption that the input signal is constant before the first sample $k = 1$ is recorded, from Eq. 4.14 it results

$$o_1^{(1,2)} = v_1 \sum_{l=0}^{\infty} (e^{-\Delta/\tau_{1,2}})^l \approx v_1 \frac{e^{\Delta/(2\tau_{1,2})}}{\Delta/\tau_{1,2}}. \quad (4.15)$$

and therefore $o_1 = 0$. In this way the signal offset is reduced to zero. For the digital signal processing there is no need for the amplification, so $A = 1$.

4.3.2 Timing algorithms

Leading Edge Trigger

From the analog methods the Leading Edge Trigger (LET) is the simplest timing procedure. The method retrieves the time when the pulse crosses a fixed discrimination level (threshold). In the tests presented in this chapter, a TFA algorithm was applied on the raw signal before applying the LET algorithm. The time resolution of the leading edge trigger is affected by:

- *time jitter* that appears because of the pulses fluctuations around an average value (basically noise). The jitter is present even when the pulses have the same real starting time, same amplitude and rise time.
- *walk*. This is illustrated in Fig. 4.3 for two extreme cases. In both cases the pulses have the same true starting time. First case is when two pulses that have the same rise time but different amplitudes. The LET gives for the pulses 1 and 3 the different time values t_1 and t_3 even if the starting time is the

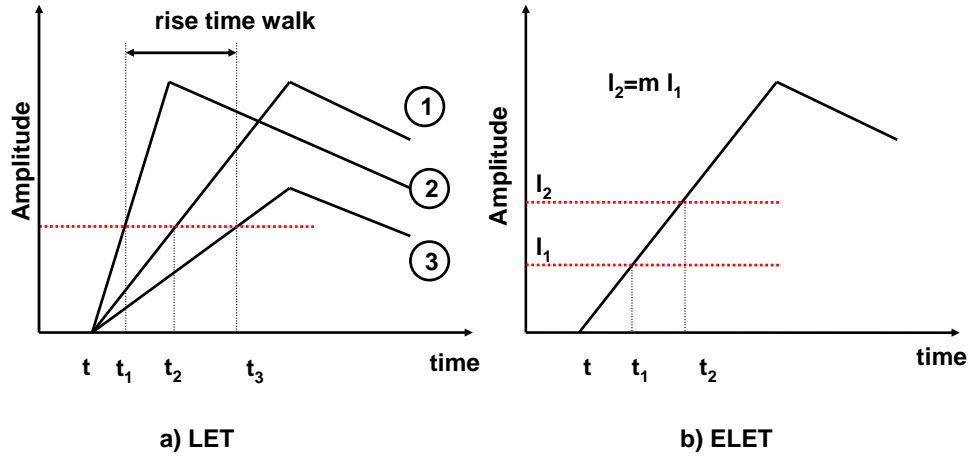


Figure 4.3: Schematic representation of two time pick-off methods: Leading Edge Trigger (LET) and Extrapolated Leading Edge Trigger (ELET). Generic pulses with linear rising edge were used. The rise time *walk* is illustrated for the leading edge trigger. The ELET method is almost *walk-free*. Both methods are affected by the pulse *jitter*.

same. The second extreme case is when the pulses have the same amplitude and different rise time (e.g. pulses 1 and 2). The LET gives the again different values for the time, t_1 and t_2 .

The leading edge trigger is working relatively well with pulses that have small dynamic range (constant rise time and almost the same amplitude). This is not the case of the large volume HPGe detectors where the pulse shape has large variations. To minimize the effect of the walk, the discrimination level (threshold) of the leading edge trigger has to be very low.

For a discrete signal the crossing time (t) of the leading edge threshold can be found even within one sampling interval. The equation used for the interpolation is:

$$t = k + \frac{l - v_k}{v_{k+1} - v_k}, \quad (4.16)$$

where the v_k is the signal amplitude and l is the value of the threshold. k is the sample index for which $v_k \leq l < v_{k+1}$.

Extrapolated Leading Edge Trigger

A procedure that is rather insensitive to the walk effect is the Extrapolated Leading Edge Trigger (ELET). This method is based on the approximation that the pulses have a linear shape in the first part of the rising edge. As long as this approximation is valid, the walk effect is negligible. In the tests presented in this chapter, a TFA algorithm was applied on the raw signal before applying the LET algorithm.

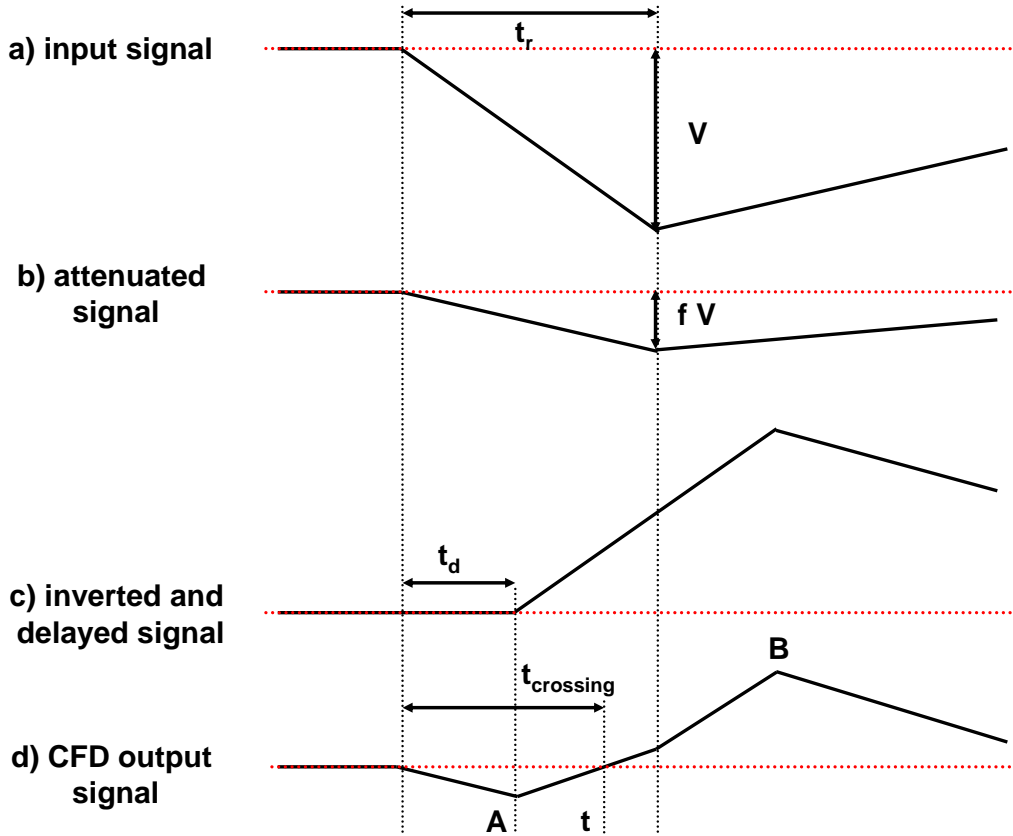


Figure 4.4: Schematic representation of the CFD timing methods. The output signal d) is the sum of the attenuated signal $b)$ and the inverted and delayed signal $c)$. The delay time t_d cannot be made too small because the minimum value in A has to be significantly outside the noise. As the ELET method, the CFD is *walk-free* for pulses with identical shape.

The trigger consists of a combination of two simple leading edge triggers, usually the second being an integer multiple of the first: $l_2 = ml_1$ (Fig. 4.3). Supposing the individual crossing times of the two thresholds are t_1 and t_2 and each is given by Eq. 4.16, then the extrapolated starting time of the pulse is:

$$t = \frac{mt_1 - t_2}{m - 1}. \quad (4.17)$$

The advantage of the digital signal processing over the analog electronics is that the ELET method is easier to apply. With analog electronics more complex setup is needed to make the extrapolation to the true starting time [83, 86].

Constant Fraction Discriminator

Another time pick-off method that is virtually walk-free for pulses that have the same rise time and a linear behavior in the first part of the rising edge is Constant Fraction Discrimination (CFD). Empirically, it was found that the Leading Edge Trigger method gives the best timing when the threshold is set at 10-20% from the

pulse amplitude. This observation led to the development of the CFD. The constant fraction discriminator gives the time when the pulse reaches a certain fraction f from the amplitude. The steps involved in the construction of a CFD signal are shown in Fig. 4.4.

The same input signal, a , is processed in two different ways. In the first case the initial signal is attenuated. In the second case the signal a is inverted and delayed with the delay t_d . The CFD output signal, d , is the sum of the signals b and c . The time is given by the crossing of the zero level and is independent on the pulse amplitude as long the pulses have the same shape.

A particular case of the general CFD method is the so called Amplitude and Rise Time Compensation (ARC) timing [86]. The ARC method uses by definition very short delays t_d such that the timing is given in the region where the rising edge of the pulse is still linear and the changes in the shape at longer time are avoided. The delay has to be long enough so that the initial part of the output signal is allowed to significantly exceed the noise level.

In the digital algorithm implemented in this work no difference will be made between the CFD and ARC methods. In the tests presented in this chapter, a TFA algorithm was applied on the raw signal before applying the CFD algorithm. For a discrete signal the recurrence to construct the output signal of the CFD is:

$$o_k = f v_{k-d} - v_k, \text{ where } k \geq d. \quad (4.18)$$

d is the delay in sampling intervals and f is the attenuation constant. v_k is the discrete signal produced with the TFA algorithm.

The advantage of a digital processing is that the zero crossing of the CFD output (see Fig. 4.4) can be searched backward, starting from the extreme point B , that is easily identified.

4.3.3 Pulse amplitude algorithm - trapezoid filter

Besides the starting time of the pulse, another pulse characteristic that has to be determined in common nuclear measurements is the amplitude. In conventional electronics the key element for pulse amplitude determination is the spectroscopic amplifier. This provides simultaneously the proper pulse amplification to match the requirements of the ADC that follows and the pulse shaping, reducing the long tail from the preamplifier. The most common shaping for the pulse amplitude is the Gaussian ($CR-(RC)^n$) shaping. Compared with the CR-RC shaping from a TFA, the Gaussian shaping provides a better signal-to-noise ratio. In the literature different other shaping procedures that give better amplitude resolution than the Gaussian shaping are mentioned: cusp-like, triangular and trapezoidal shaping (Fig. 4.5). These alternative shaping methods are more difficult to be implemented in the conventional electronics compared with the Gaussian shaping. Their advantages can be easily used in digital signal processing where the shaping parameters are the parameters of the analyzing software.

In choosing the most appropriate shaping method, a compromise between three general concepts has to be found: signal-to-noise ratio, pile-up of the pulses and

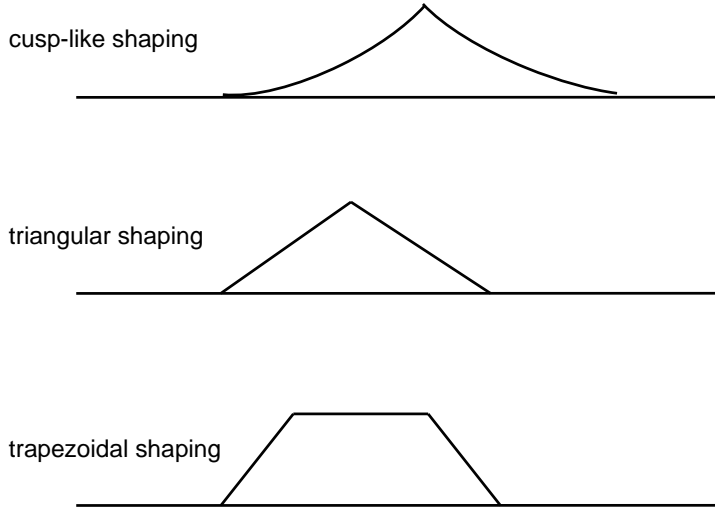


Figure 4.5: Three pulse shaping procedures that give a better amplitude resolution compared with the Gaussian shaping: cusp-like, triangular and trapezoidal shaping.

ballistic deficit. The best signal-to-noise ratio is given by the cusp-like shaping followed by the triangular shaping. To overcome the ballistic deficit a shaping with the flat-top comparable with the maximum rise time is needed. The trapezoidal shaping meets simultaneously good signal-to-noise ratio and good compensation for the ballistic deficit [88].

The basic function of the trapezoid algorithm is to convert the exponentially decaying signal from the preamplifier into a trapezoidal signal. This implies the convolution of the preamplifier signal (input signal v for the digitizer) with different time dependent functions. Several proposals for such methods can be found in the literature ([85, 87]), but the differences between them is only the order in which the convolutions are done. The algorithm described here was optimized also for a high speed calculation.

In the algorithm used here, two steps can be distinguished in the construction of the trapezoidal output signal. First the preamplifier signal is corrected for the finite decay time τ and converted into a step function. The trapezoid shape is then obtained applying the *pulse finding* algorithm described in Sec. 4.3.1. The demonstration of the recursive formulae used in the present work is given in the following. The starting point for this algorithm is the preamplifier output of a Ge detector given by the Eq. 2.12. In the discrete time scale the same equation can be written as:

$$v_k = v_0 - \frac{1}{c_e} e^{-\frac{k\Delta}{\tau}} \sum_{j=-\infty}^k i \left(\left[j - \frac{1}{2} \right] \Delta \right) e^{-\frac{(j+\frac{1}{2})\Delta}{\tau}}, \quad (4.19)$$

where v_k is the discrete representation of the preamplifier output voltage (digitizer input signal) for the sample k . Δ is the sampling interval and i is the current. For simplicity, $i_k = i((k - \frac{1}{2})\Delta)$. For two successive samples the following relation is

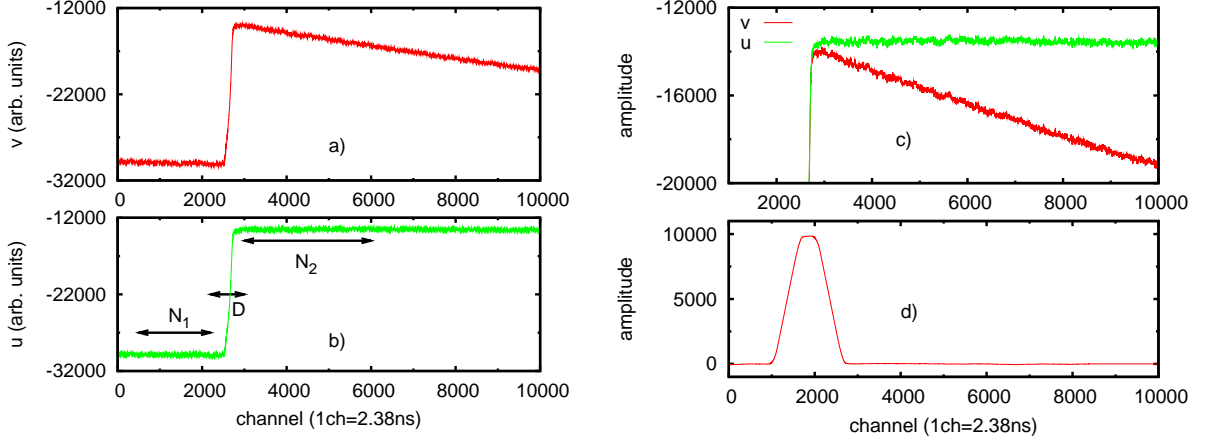


Figure 4.6: *a*: the preamplifier output as recorded with the digitizer (initial signal). *b*: the result of the recursive algorithm from the Eq. 4.22. *c*: the detailed comparison between *a*) and *b*) It can be seen that the *u* signal has a higher amplitude compared with the initial signal *v*. This is due to the correction for the ballistic deficit. *d*: The result of the complete trapezoid algorithm. To maximize the computing speed, only two averages on the *u* signal are done, one to the left of the starting time (on the interval N_1) and another to the right (on the interval N_2), after a maximum rise time. This average gives the maximum of the trapezoid.

valid:

$$(v_{k+1} - v_0)e^{\frac{\Delta}{2\tau}} - (v_k - v_0)e^{-\frac{\Delta}{2\tau}} = -\frac{\Delta}{c_e} i_k, \quad (4.20)$$

By analogy the same equation can be written if the decay time (τ) of the preamplifier would be very long ($\tau \rightarrow \infty$):

$$u_{k+1} - u_k = -\frac{\Delta}{c_e} i_k. \quad (4.21)$$

From Eq. 4.20 and 4.21 results:

$$u_{k+1} = u_k + (v_{k+1} - v_0)e^{\frac{\Delta t}{2\tau}} - (v_k - v_0)e^{-\frac{\Delta t}{2\tau}}. \quad (4.22)$$

with $u_0 = v_0$. The Eq. 4.22 transforms the initial signal from the output of an HPGe preamplifier with the decay constant τ in a signal similar to a step-like function (see Fig. 4.6). For the conversion of the exponentially decaying input signal into a step-like signal, only two parameters are needed: the signal offset v_0 and the decay time τ . These two parameters are determined prior to the application of the algorithm.

Making the transformation of the input signal v_k (affected by a finite τ) to a signal u_k (that correspond to an infinite τ) the correction for the ballistic deficit was implicitly included. This ballistic correction is valid in the approximation that the charge collection process takes place instantaneously in the middle of each sampling interval Δ . The real charge collection process is obviously continuous.

As the second step in the trapezoidal algorithm, on the obtained output signal u_k a pulse finding algorithm (Sec.4.3.1) is applied. The result is a trapezoidal pulse

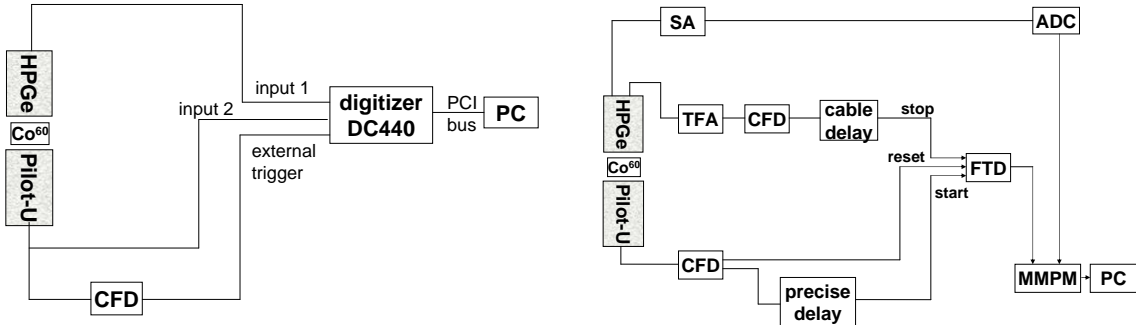


Figure 4.7: Two independent start-stop experimental setups for testing different signal processing algorithms: one with the DC440 digitizer (*Left*) and the other with conventional electronics (*Right*). Data were taken with both systems in identical conditions to have a precise comparison between their performances.

whose value of the flat-top gives the amplitude (Fig.4.6). To speed up the computing process and using the fact that the starting time, t , of the pulse was found already very precisely (e.g. with a CFD procedure), the pulse finding algorithm is reduced only to two averages: one before t and another one at a safe distance after t such as to allow to all pulses to reach the maximum amplitude (see Fig.4.6). This distance is the maximum rise time of the pulses. Another advantage of digital processing is that the number of channels (N) over which the average is made can be dynamically determined from the distance between two consecutive pulses in a signal. Even two different numbers of samples N_1 and N_2 can be used for the two averages to the left and to the right of the starting time (see also Fig. 4.6). For a reasonable amplitude resolution a minimum of 600 samples were needed for the averages N_1 and N_2 . The distance between the two averaging regions (D) has to be larger than the maximum collection time in the detector which can go up to 800 ns for a 100 % relative efficiency detector. In this way the full time interval between two consecutive pulses can be used to reduce the noise. It has to be noted that the full algorithm is based on the assumption that the exponential decay of the signal has a constant decay time τ . Deviations from this leads to limitations in the performances of the algorithm.

4.4 Results of the tested algorithms

4.4.1 Start-stop experimental setup for testing different algorithms

For testing the digitizer performances one aimed first to precisely compare its time and amplitude resolutions with the resolutions of the acquisition system based on the conventional electronics. For this purpose, two start-stop experimental arrangements were created: one with the fast digitizer and another with the conventional electronics described in Chapter. 3. The scheme of both setups is given in Fig. 4.7.

The same detectors and the same ^{60}Co source was used in both cases.

In the setup with the DC440 fast digitizer (Fig. 4.7 *Left*) the HPGe preamplifier output was given to one input channel of the digitizer and the split output of the plastic scintillator (Pilot-U) to the second channel from the same card. The common external trigger of the digitizer card was the output of the scintillator CFD. The plastic scintillator output was given to the second input channel only to have a check for the precision of the external trigger. For every external trigger, the digitizer recorded 10 000 samples that were saved in binary files on the computer hard-disk. The reference time in the recorded samples was the external trigger time. Data sets were taken with this setup changing the HPGe detectors or the full range scale of the digitizer input. On every data set, all the signal processing algorithms presented in the previous section were tested in order to establish the most suitable algorithm.

In the start-stop setup with conventional electronics (Fig. 4.7 *Right*) the start of the system was the plastic scintillator and the stop the delayed signal from the CFD of the HPGe detector. Spectra were recorded with both functions of the CFD module, SRTR and CF (see Sec. 3.2.3). The delay used for the output of the scintillator CFD had a precision of few picoseconds. This delay and the reset signal were needed for a proper functioning of the FTD (multi-hit time-to-digital converter). This start-stop setup was preferred to a classical start-stop setup with a TAC (Time-to-Amplitude Converter) because of the possibility to save simultaneously the time and the amplitude spectra and their coincidences.

4.4.2 Results of the timing algorithms

The first step in the signal processing was to apply a *pulse finding* algorithm (Sec .4.3.1) as a running filter to identify the number of pulses in every signal and to define regions of interest where the starting time of the pulses can be searched more precisely. The second step, common for all the timing procedures presented here, was the application of the Timing Filter Amplifier algorithm (Sec .4.3.2). On the resulted TFA signal the timing algorithms were applied. The obtained results are given in the following for a 104% relative efficiency detector (HPGe2).

Leading Edge Trigger

Fig. 4.8 shows the time spectra in the start-stop setup with the Leading Edge Trigger. The LET algorithm was applied on the output signal from a TFA algorithm with the integration time $\tau_1=10$ ns and differentiation time $\tau_2=200$ ns. The best time resolution of the 104% efficiency detector obtained with the Leading Edge Trigger was 18 ns. The time spectrum of the LET is characterized by a long tail to the right side of the peak. The FWHM of the time spectrum increases with the increase of the threshold l (Fig. 4.8 *Left*). This could be explained by the fact that for a higher threshold l the walk effect is larger. For a good performance of this algorithm a very low threshold l , immediately above the noise, was needed.

Keeping the very low threshold $l=15$ keV, but doing a selection on the amplitude (Fig. 4.8 *Right*) both the FWHM and the tail decrease for high energies. This

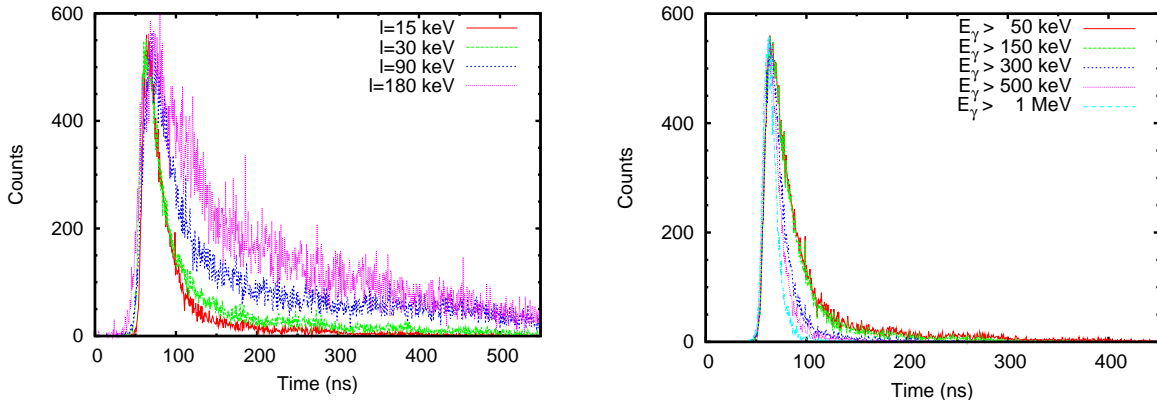


Figure 4.8: Results of LET algorithm. For the time spectra shown here the FWHM varied between 18 ns and 24 ns. *Left*: The threshold l was varied from immediately above the noise ($l=15$ keV) up to 90 keV. *Right*: The threshold $l=15$ keV was fixed and the pulse amplitude E_γ were selected. For higher pulse amplitude the peak tail decreases.

suggests that the high energy pulses have smaller variations in the rising edge.

Extrapolated Leading Edge Trigger

The Extrapolated Leading Edge Trigger (ELET) algorithm gives very good results as long the rising edge of the pulse is linear. The ELET algorithm was applied on the output signal from a TFA algorithm with the integration time $\tau_1=10$ ns and differentiation time $\tau_2=200$ ns. Two input parameters were varied for the ELET algorithm: the threshold l and the factor m that defines the second threshold. As it was expected from the tests with the LET, a very low threshold l produced the best results. For a fixed $l=15$ keV, the FWHM of the time spectrum decreases when the m is increased (Fig. 4.9 *Left*). This suggests that a larger difference between the two thresholds is needed to minimize the noise fluctuations of the signal (the time jitter). If the factor m is further increased, the tail on the left side of the peak increases because changes in the pulse shape appears. Fig. 4.9 *Right* shows that for the same $l=15$ keV and $m=2$, when the pulse amplitudes were selected the time resolution improved (smaller FWHM and smaller tails) for the high energy pulses. It results that the approximation of the rising edge linearity is more appropriate for high energy pulses.

Constant Fraction Trigger

When the CFD algorithm was applied two parameters were considered: the fraction f and the delay t_d . In addition, the parameters of the TFA algorithm (the integration time τ_1 , the differentiation time τ_2) were varied. The dependence on the TFA amplifier parameters is given in Fig. 4.10. The CFD parameters were kept constant: delay=31 ns and $f=0.25$. The time resolution deteriorates when the integration time τ_1 is increased (Fig. 4.10 *Left*). For large values of the integration time the

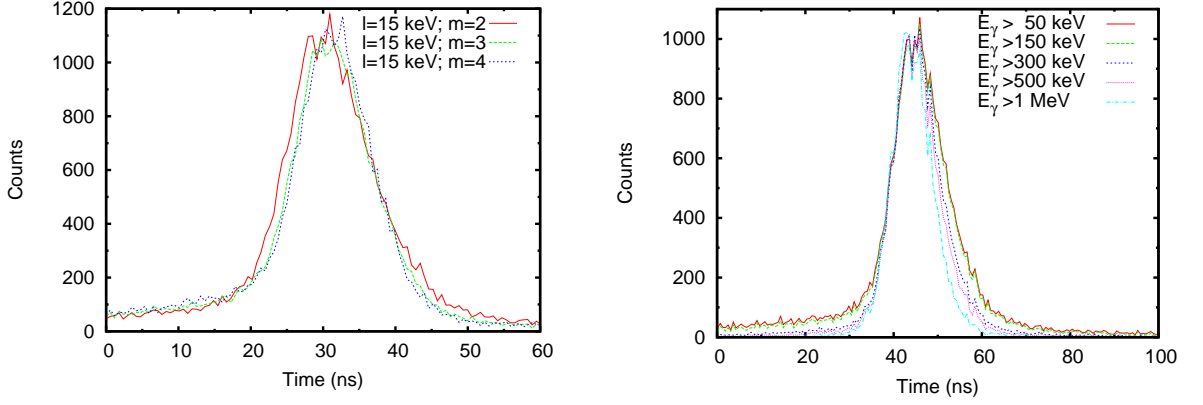


Figure 4.9: Results of using the ELET with a 104% relative efficiency detector. The FWHM of the ELET spectra was between 10 ns and 13 ns depending by the chosen parameters. *Left:* The threshold l was constant (as low as possible) and the factor m was varied. Further increase of m do not change significantly the time resolution spectrum. *Right:* The pulse amplitudes were selected for constant threshold $l=15 \text{ keV}$ and $m=2$.

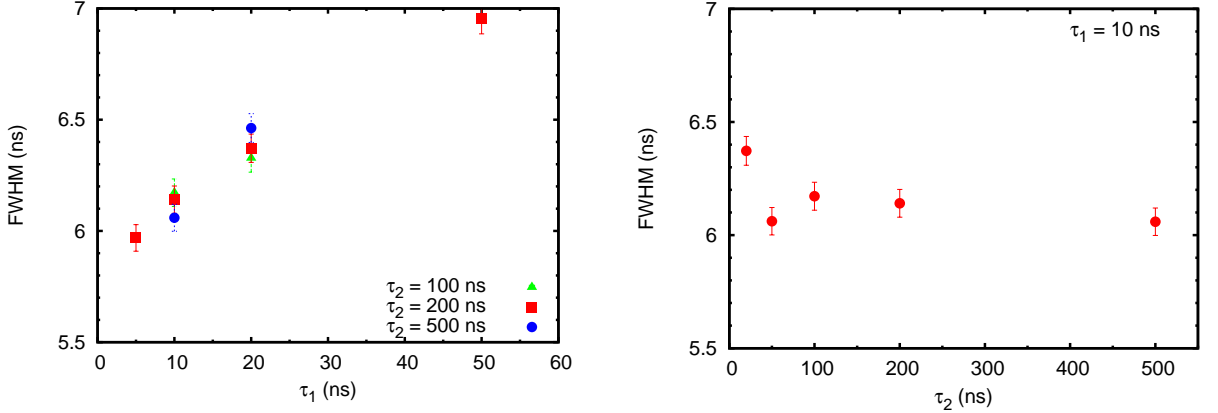


Figure 4.10: The dependence of the resolution of the CFD algorithm on TFA parameters differentiation and integration time. The CFD parameters were fixed: delay=31 ns and $f=0.25$. *Left:* The FWHM of the time spectrum increases when the TFA integration time is increased. *Right:* The time resolution remains almost constant for the variation of the differentiation time between 10 ns and 500 ns.

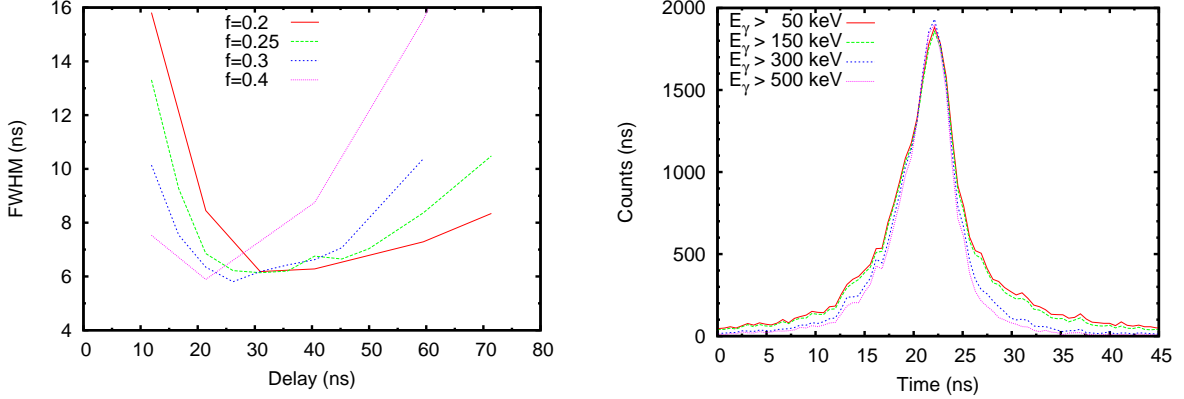


Figure 4.11: The TFA parameters were fixed: integration time $\tau_1=10$ ns and differentiation time $\tau_2=200$ ns. *Left:* The dependence of the CFD algorithm resolution on the fraction f and delay. A time resolution of 6.2 ns was obtained for different pairs of parameters (delay and f). *Right:* For the same delay=31 ns and the fraction $f=0.25$ the tails of the time peak were reduced selecting higher pulse amplitudes E_γ .

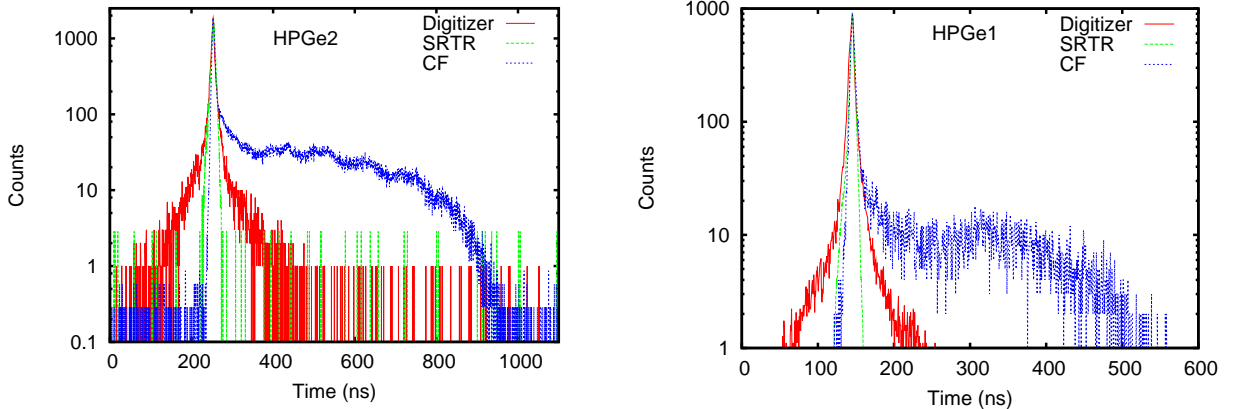


Figure 4.12: The comparison of the time resolution with the digitizer and conventional electronics. The two functions of the CFD module were used: Constant Fraction (CF) and Slow Rise Time Rejection (SRTR). The peaks were normalized to the same maximum. *Left:* the time resolution of the 104% relative efficiency detector. Almost the same FWHM=6.2 ns was obtained in all three cases. The tail of the spectrum was defined as all the pulses outside of one Full Width at Tenth Maximum (FWTM). The pulses in the tail amount to 55% from the full spectrum for the CF function and only 21% for the digitizer. *Right:* the time resolution of the 75.9% relative efficiency detector. The FWHM=5.8 ns was obtained for all cases. The pulses in the tail amount to 37% from the full spectrum for the CF function and only 22% for the digitizer.

signal is averaged over a longer time interval reducing the noise but simultaneously decreasing the slope of the rising edge of the pulse. Contrary, the time resolution is less dependent on the changes of the differentiation time τ_2 (Fig. 4.10 *Right*).

Fig. 4.11 *Left* shows the dependence of the time resolution on the fraction f and the delay used in the CFD algorithm. The parameters of the TFA algorithm were fixed: $\tau_1=10$ ns and $\tau_2=200$ ns. A time resolution of about 6.2 ns was observed, comparable with the value obtained with the conventional electronics. This resulted for different pairs of the two parameters, fraction and delay. When a delay of 31 ns and a fraction $f=0.25$ were used with a selection on the pulse amplitude (Fig. 4.11 *Right*) it was observed that the tail of the time spectrum decreased for high energy pulses. As for the case of the conventional electronics (Sec. 3.2.3) the time resolution is strongly dependent on the pulse amplitude.

Fig. 4.12 gives the comparison between the time resolution obtained with the digitizer and with the conventional electronics for two different detectors: 104% *Left* and 75.9% *Right*. Energies $E_\gamma \geq 150$ keV were selected in all these cases, both for the digitizer and for the conventional module. The fast digitizer gives the same FWHM as the conventional electronics for both detectors. Moreover the FWTM is almost the same for all three spectra. The difference is in the peak tail. The CF spectrum has a large tail that extends up to 400 ns for the smaller volume detector and up to 800 ns for the larger detector. The SRTR spectrum has no tail because all events in the tail are simply rejected at the expense of lower detection efficiency. The fast digitizer preserves the detection efficiency of the CF function and the tail is significantly reduced to about 21%.

4.4.3 Results of the amplitude algorithm

Prior to the application of the trapezoid algorithm (Sec. 4.3.3) it is necessary to determine the decay time, τ , of the preamplifier and the signal offset, v_0 . The decay time τ was determined from a least square fit of the decaying part of the pulse. The fit was done once for every detector, for a large number of pulses to assure a small statistical error. A Gaussian distribution was obtained for the decay time τ . The centroid of the distribution was taken. For the 104% relative efficiency detector $\tau=47.8$ μ s.

The signal offset v_0 (Sec. 4.3.3) was determined from the signals that have only one pulse and a horizontal behavior before the starting time of the pulse. The offset was determined as the signal average over the horizontal region before the pulse. The average was done over a sufficiently high number of samples to reduce the noise influence (3 000 samples in this case). Again a Gaussian distribution for the offset values was obtained when different signals were used for the determination. The distribution centroid was taken. During long acquisition periods small changes of the offset v_0 were observed for some detectors and periodical checks were needed.

Once the signal offset and the decay time τ were determined, the only parameter that can be varied in trapezoid algorithm (Sec. 4.3.3) is the number of samples N used for the average over the u_k signal. The dependence on the $N = N_1 = N_2$ of the energy resolution (FWHM) at the second line of the ^{60}Co spectrum is

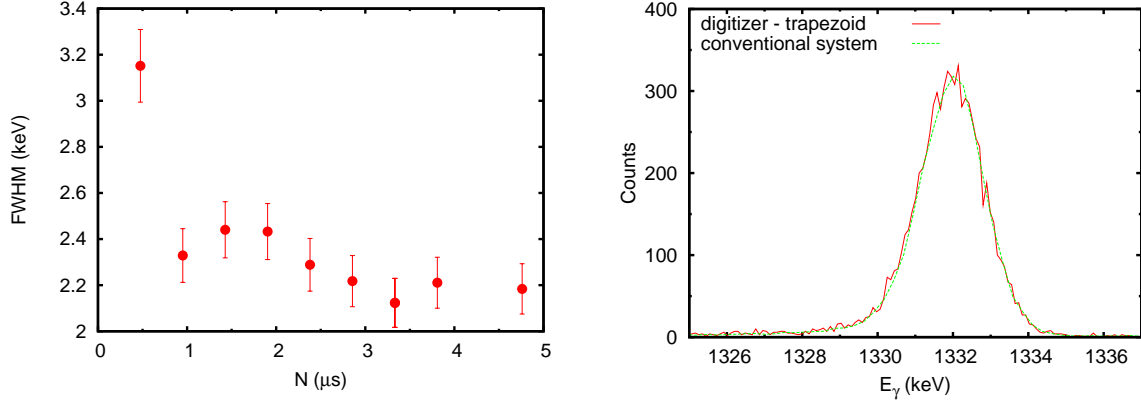


Figure 4.13: *Left:* The dependence of the energy resolution with the trapezoid algorithm on the number of sample $N = N_1 = N_2$ used for the average (Sec. 4.3.3). *Right:* The comparison of the energy resolution with the digitizer and with the conventional electronics. The 1.33 MeV peak of the ^{60}Co spectrum is shown. The FWHM=2.1 keV for both cases. For an easier comparison the two spectra were normalized to the same peak maximum and were calibrated in energy. This spectrum was obtained with $N = N_1 = N_2 = 3.3 \mu\text{s}$ and $D = 1.4 \mu\text{s}$.

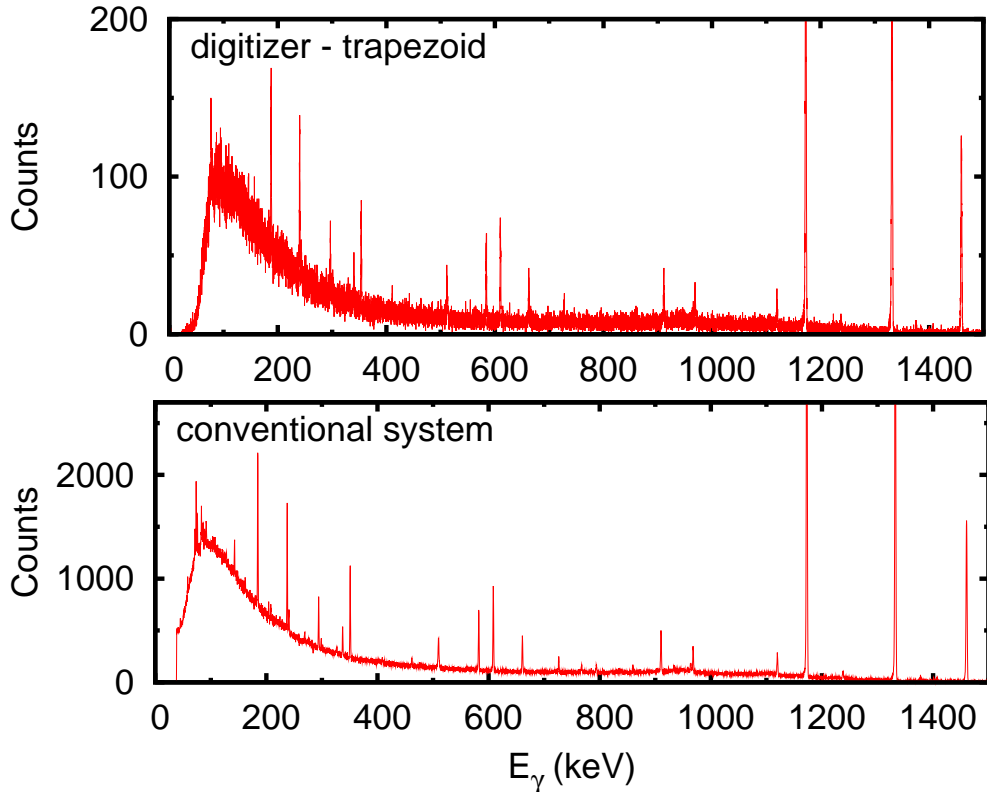


Figure 4.14: Comparison of the ^{60}Co amplitude spectra with the digitizer and with the conventional electronics. The *Counts* scale was expanded at low values for a better identification of the peaks in both spectra. Different acquisition times and different triggers for the acquisition systems were used for the two spectra.

Table 4.2: HPGe detector amplitude resolution for different full scale range of the digitizer.

full scale range (mV)	full scale range (keV)	FWHM (keV) at 1.33MeV
250	1513.7	2.13
500	3030.5	2.28
1000	6066.4	2.33

given in Fig.4.13 *Left*. The energy resolution improves when a larger number of samples (larger time interval) is used for the average and saturates around $3\ \mu\text{s}$ (1200 samples). A minimum of about $1\ \mu\text{s}$ is needed to still have a reasonable energy resolution, with a FWHM lower than 2.5 keV. The small oscillations in Fig.4.13 *Left* may come from the presence of a sinusoidal noise with a period of few hundreds of ns. The effect of such a noise disappears when a large number of samples N is used for average. A distance $(2D + 1) = 1.44\ \mu\text{s}$ (600 samples) was used between the two average regions. This distance was chosen to be higher than the maximum rise time of the pulses. As it can be seen from Fig. 4.12, the maximum rise time of the pulses in the 104% relative efficiency detector is about 800 ns. From this considerations a minimum of about $2.5\mu\text{s}$ spacing between two consecutive pulses is needed in the present trapezoid algorithm to preserve a reasonable amplitude resolution.

The advantage of determining first the starting time of the pulse and than the amplitude is that a variable number of samples N (and even $N_1 \neq N_2$, see Sec. 4.3.3) can be used for the average. These numbers N_1 and N_2 can be determined dynamically for every signal after the timing algorithm, as the maximum time interval between two consecutive pulses. For the online data acquisition, a minimum value of $1\ \mu\text{s}$ was imposed for N_1 and N_2 to preserve the good amplitude resolution. The dynamic determination of N can be useful for high counting rates.

Fig. 4.13 *Right* shows the comparison between the time resolution obtained with the digitizer and with the conventional system for the same detector. The fast digitizer gives the same resolution as the conventional system (FWHM=2.1 keV). The full ^{60}Co amplitude spectra obtained with the fast digitizer and with the conventional electronics are compared in Fig. 4.14. The following parameters were used for the digitizer spectrum from this figure: $N = N_1 = N_2 = 3.3\mu\text{s}$ and $D = 1.4\ \mu\text{s}$. All details of the conventional spectrum were reproduced by the fast digitizer.

In all of the amplitude tests that have been described in this section the minimum full scale range was used to cover the full amplitude spectrum of ^{60}Co . For investigating the effect of the digitizer's number of bits on the amplitude resolution of the detector, three different full scale ranges of the digitizer were used: 250 mV, 500 mV and 1 V. The amplitude resolutions obtained with the trapezoid algorithm for these three full scale ranges are given in Table. 4.2. A slight deterioration of the resolution was observed when the full scale range was increased. Reasonable amplitude resolutions were obtained even for the 1 V full scale range. From this work it can be concluded that a digitizer with 12 bits amplitude range is sufficient for used with Ge detectors at γ -ray energies below 10 MeV.

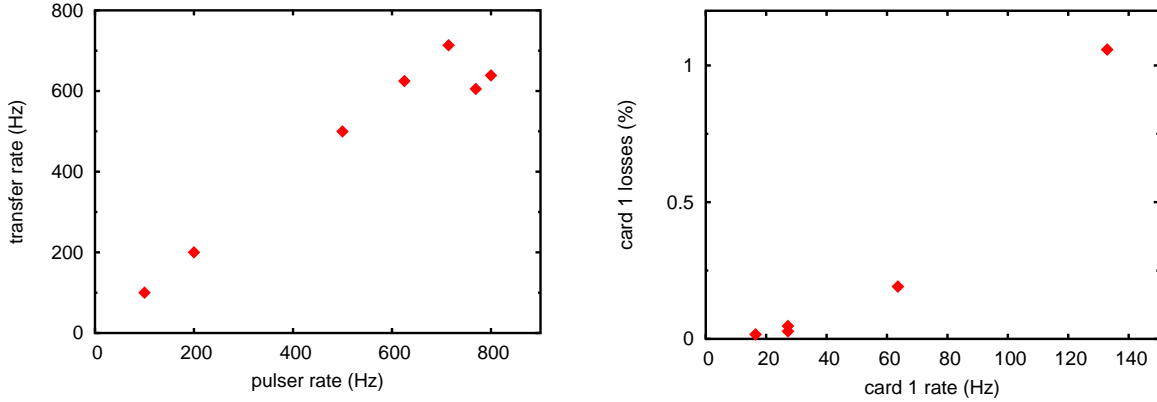


Figure 4.15: Rate tests for the Acqiris DC440 digitizer (2 cards connected to a common PC). *Left:* The transfer rate of the digitizer as a function of the frequency of a pulser connected to the external trigger input. *Right:* The digitizer external trigger was the signal of an 800 Hz pulser validated by the presence of a random signal (response of an HPGe detector to a calibration source) that comes with $23.8 \mu\text{s}$ after the pulser. Below 20 Hz average rate of such constructed external trigger the digitizer number of lost valid triggers is negligible.

4.4.4 Maximum counting rate

The fast digitizer samples continuously the signal, storing the data in a circular buffer. Once an external trigger occurs the acquisition is stopped and the data are transferred to the PC. The acquisition starts again immediately after the transfer process is finished. An online data analysis is preferred and this supposes that the transferred signals are stored temporally in the Random Access Memory (RAM) of the PC and analyzed while the digitizer waits for a new external trigger. Only the starting time of the pulse and the amplitude value are stored on the PC hard-disk. The acquisition and data transfer from the digitizer have a higher priority than the analysis procedure.

The following test was made for the efficiency of the data transfer as a function of the acquisition rate was made. A pulser gave the external trigger of the digitizer with a fixed frequency and the number of the transferred signals was counted for a long enough time. The number of external triggers was counted simultaneously with an external counter. Every signal had 10 000 samples ($23.8 \mu\text{s}$) and both digitizer cards triggered simultaneously. The data from 4 input channels were transferred for every trigger. From Fig. 4.15 it can be seen that the digitizer starts to lose signals when the pulser frequency exceeds about 750 Hz. At this frequency the dependence of the transfer rate as a function of the pulser rate becomes non-linear. This is due to a possible conflict between the two cards of the digitizer connected to the same PC when the cards trigger simultaneously. To avoid this limitation in the transfer rate of the digitizer two solutions are available. The first one is to record less than 10 000 samples for every channel. The second solution is to reduce the trigger rate to the rate of the neutron induced events, that in average is 6 s^{-1} for every detector.

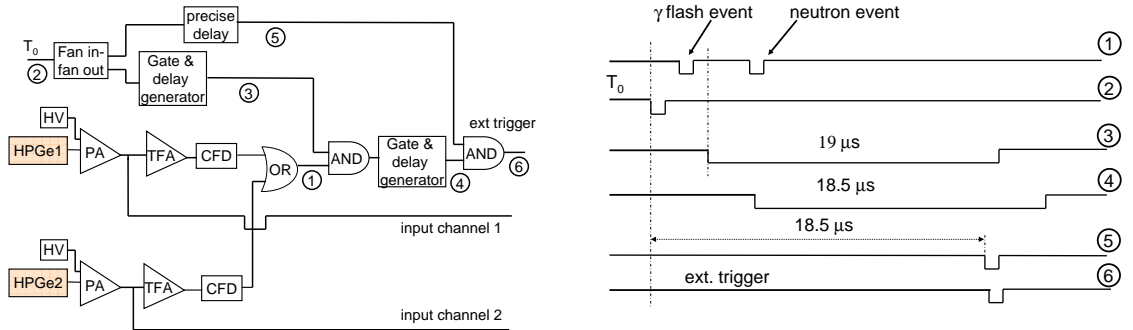


Figure 4.16: The t.o.f. setup based on the fast digitizer Acqiris DC440. One card of the digitizer accommodated two HPGe detectors. Conventional electronic modules were still used to reduce the counting rate to the neutron induced counting rate (about 6 counts/s in average). The corresponding timing of the signals is given in the left panel. The external trigger is the delayed t_0 signal

The second solution it was used in the electronic setup for the $(n, xn\gamma)$ cross-sections measurement at 200 m flight path station (Sec. 4.5).

In a second test, the external trigger was a signal of a pulser with 800 Hz frequency that was validated by the presence of an output signal of an HPGe detector that sees a radioactive source. The HPGe detector output has to be within $23.8 \mu s$ after the pulser signal. The distance between the radioactive source and the detector was decreased to increase the average rate of the external trigger. The losses in the card were defined as the difference between the number of signals counted by the external counter and the number of signals transferred in the digitizer. Fig. 4.15 shows the dependence of the losses in the card versus the external trigger rate. At external trigger rates below 20 Hz the losses are less than 0.1% and that suggest that the DC440 fast digitizer can be used in the actual inelastic scattering cross-section measurement at GELINA, the dead time of a setup based on the digitizer being negligible. In conclusion, working with 4 large volume HPGe detectors connected simultaneously to this digitizer is possible at 800 Hz repetition rate of the accelerator with no dead time as long as the external trigger rate for each card is relatively small (about 20 Hz). The dead time should not be neglected at rates greater than 100 Hz.

4.5 Electronic scheme for the t.o.f. measurement with the digitizer

For the measurement of the neutron inelastic scattering cross-section with the digitizer, the electronic setup of Fig. 4.16 was used. The purpose of the conventional electronic modules was only to reduce the counting rate to the rate of the neutron induced events, i.e. avoid triggering by the γ -flash. For this, an external trigger was constructed to select only the events that are generated within about $19 \mu s$ after the

arrival of the gamma flash. This time range allows the detection of the neutrons from about 500 keV up to 20 MeV. The trigger is the t_0 signal from the accelerator validated by the presence of a neutron induced signal in one of the two HPGe detectors connected to one card. Using fast logic coincidence units and a very precise delay unit, the precision of the t_0 signal is preserved for the external trigger.

For every external trigger, the digitizer card records 10 000 samples and transfers them to the PC where the signals are processed online. On the disk were recorded the amplitude and the time of the pulse. An additional flag that gives the number of pulses in every signal was recorded to check the consistency of the recorded data.

For a while, this new data acquisition system based on the fast digitizer was used in parallel with the data acquisition system based on the conventional electronics described in Sec. 3.2. This is the case for the measurements with two samples: ^{208}Pb and ^{206}Pb . The output signals of all the four detectors of the setup were split to be connected to the digitizer and to the conventional acquisition system.

4.6 Results of the $(n,xn\gamma)$ cross-section measurement with the digitizer

In this section the results of the $(n,xn\gamma)$ cross-section measurements with the data acquisition system based on the fast digitizer are presented. Firstly, the results of efficiency determination for the digitizer will be given. Then the integral amplitude and time-of-flight spectra are shown for the cross-sections measurement with the setup at 200 m flight path station. The comparison of the differential gamma production cross-section measured in parallel with the two completely independent data acquisition systems (with conventional electronics and with the fast digitizer) is given.

4.6.1 Absolute efficiency calibration of the fast digitizer

With the setup described in the Sec. 4.5 the absolute efficiency of the acquisition system was measured with the same calibration sources as described in Chapter 3. The ratio between the detection efficiency of the digitizer and the *detector efficiency* measured with the setup based on the conventional electronics is given in Fig. 4.17 for two different detectors. For both detectors a higher detection efficiency can be observed for the digitizer. For HPGe1, the digitizer was more efficient with about 1.5% and for HPGe4 only with about 0.8%. This small difference between the two acquisition systems was explained by the fact the conventional spectroscopic amplifier has a larger resolving time compared with the digitizer. With a shaping time of $6 \mu\text{s}$, the spectroscopic amplifier needs about $18 \mu\text{s}$ between two successive pulses to resolve the pulses without an amplitude resolution deterioration. The resolving time of the digitizer is about $2.5 \mu\text{s}$. This is supported by the observation that when a smaller shaping time is used for the spectroscopic amplifier the efficiency ratio become closer to unity (see Fig. 4.17).

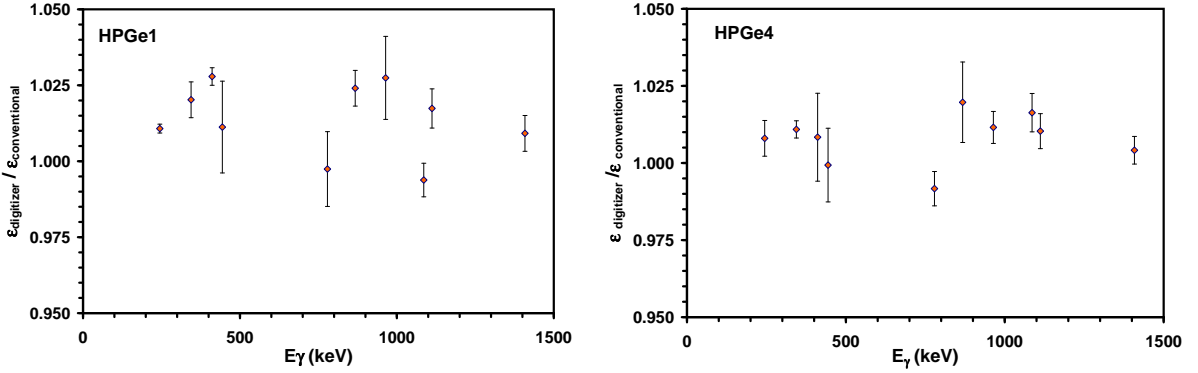


Figure 4.17: The ratio between the absolute efficiency measured with the fast digitizer and the *detector efficiency* (as defined in Sec. 3.2.5) measured with the acquisition system based on the conventional electronics. This ratio is given for two different detectors. The shaping time of the spectroscopic amplifier was 6 μs for HPGe1 and 4 μs for HPGe4.

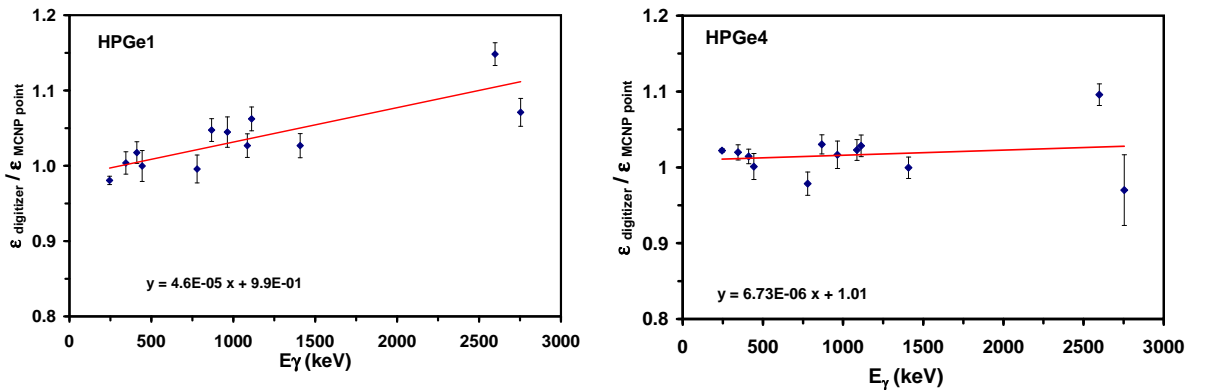


Figure 4.18: The ratio between the measured *detector efficiencies* with the digitizer and the simulated *detector efficiencies* with the MCNP and with a point-like source. This ratio reflects also the agreement between the experimental results and the MCNP simulations.

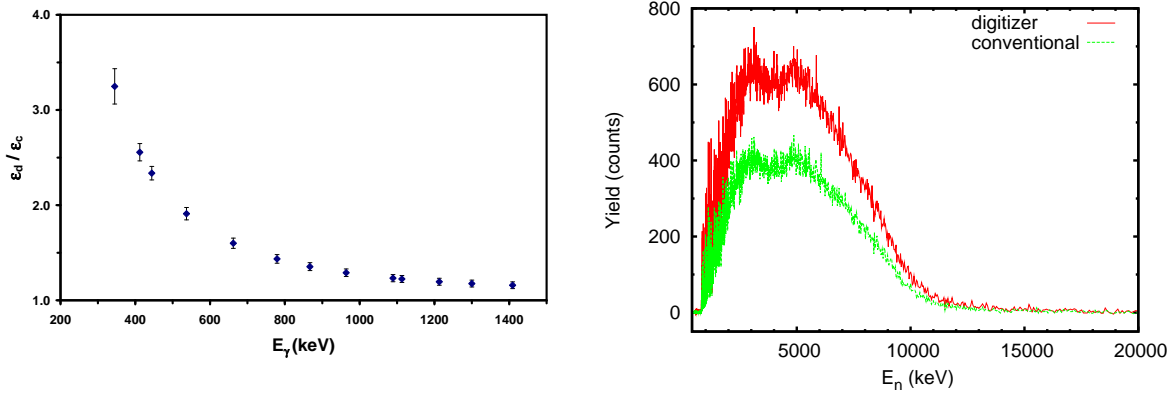


Figure 4.19: *Left:* Detection efficiency comparison between the digitizer and the conventional acquisition system. *Right:* The yield of the HPGe2 for the 803 keV transition in the ^{206}Pb measurement. The comparison between the yield obtained with the digitizer and with the conventional acquisition system is shown. The acquisition time was the same in both cases.

The applied corrections for the efficiency were explained for the conventional system in Chapter 3. For the digitizer the absolute efficiency is only corrected for the γ -ray self-attenuation and extended volume source effect. No losses due to the use of the SRTR function appear in the digitizer. The final absolute efficiency for the cross-sections measurement with the fast digitizer can be written as:

$$\epsilon_d = \epsilon_{MCNP\,extended} \frac{\epsilon_{digitizer}}{\epsilon_{MCNP\,point}}. \quad (4.23)$$

The linear fit of the ratio $\frac{\epsilon_{digitizer}}{\epsilon_{MCNP\,point}}$ was used to reduce the uncertainties due to the individual fluctuations. This ratio and the corresponding linear fit are given in Fig. 4.18 for the detectors HPGe1 and HPGe4 for the ^{208}Pb measurement. These two detectors are the extreme cases for the agreement between the measured *detector efficiency* with the digitizer and the simulated efficiencies with MCNP with the point-like source.

Fig. 4.19 *Left* shows the ratio between the efficiency of the acquisition system with the fast digitizer (ϵ_d) and the efficiency of the acquisition system with the conventional electronics (ϵ_c). The two efficiencies are calculated with Eq. 4.23 and respectively Eq. 3.4. These two sets of efficiencies were used for the cross-section calculation with the ^{206}Pb sample and include all the corrections. It can be seen that the acquisition system based on the fast digitizer has a much higher efficiency, especially at low energies (3 times higher at 350 keV). The difference between the two systems is reduced to 15% at 1.4 MeV. This difference in efficiency is reflected in a better statistics for the fast digitizer. In Fig. 4.19 *Right* the yield of the main gamma peak from the ^{206}Pb nucleus (803 keV) is shown as a function of the neutron energy for the two acquisition systems. The data were recorded in parallel for the same time interval. For this γ -ray peak 40% was gained in the efficiency using the fast digitizer.

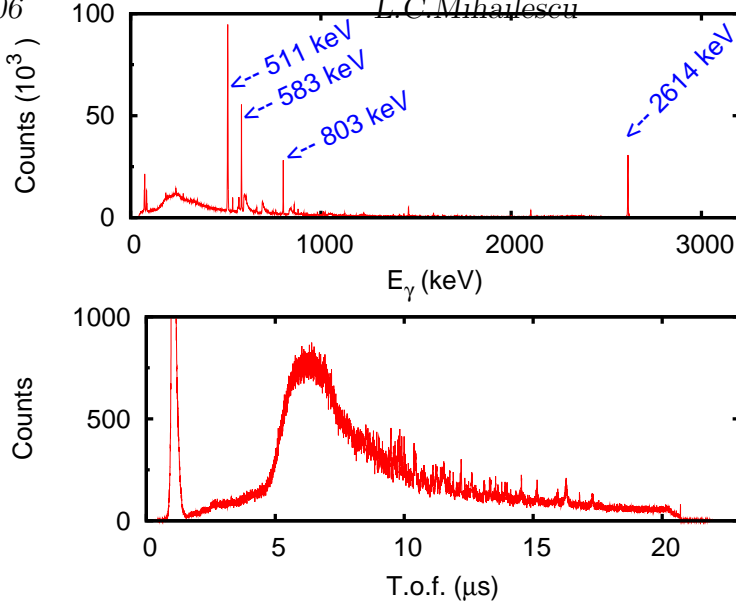


Figure 4.20: Typical examples of the integral amplitude and t.o.f. spectra for the ^{208}Pb measurement with the digitizer. *Above:* Amplitude spectrum *Below:* T.o.f. spectrum.

4.6.2 Amplitude and t.o.f. spectra

Examples of the integral amplitude and time-of-flight spectra for the ^{208}Pb cross-sections measurement are shown in Fig. 4.20. The amplitude spectrum was integrated over the full neutron energy range, from 500 keV up to 25 MeV. The main γ -ray peaks from the ^{208}Pb nucleus are of 2614 keV and 583 keV. The 803 keV peak is from the ^{206}Pb nucleus and resulted from the $(n, xn\gamma)$ reactions on different Pb isotopes in the sample.

In the t.o.f. spectrum, the gamma flash peak can be easily distinguished at low values of the t.o.f. spectrum. This peak resulted only from the signals that had a pile-up between the gamma-flash induced events and the neutron induced events. In the data acquisition system based on the conventional electronics all these events were rejected using the inhibit signal.

4.6.3 Differential gamma production cross-section

In parallel with the data from the conventional acquisition system, the data from the acquisition system based on the fast digitizer were analyzed and the differential gamma production cross-sections were compared. Here, only few examples of the gamma-production cross-sections are shown. Fig. 4.21 presents the differential gamma production cross-section for the 2614 keV and 583 keV transitions from ^{208}Pb nucleus. The measurement angles were 110° and respectively 150° . The two results of completely independent acquisition systems (but same detectors) agree well within the stated uncertainties. The magnitudes of the uncertainties are given as generic error bars at 6 MeV and at 15 MeV.

The neutron energy resolution of the two acquisition systems can be compared

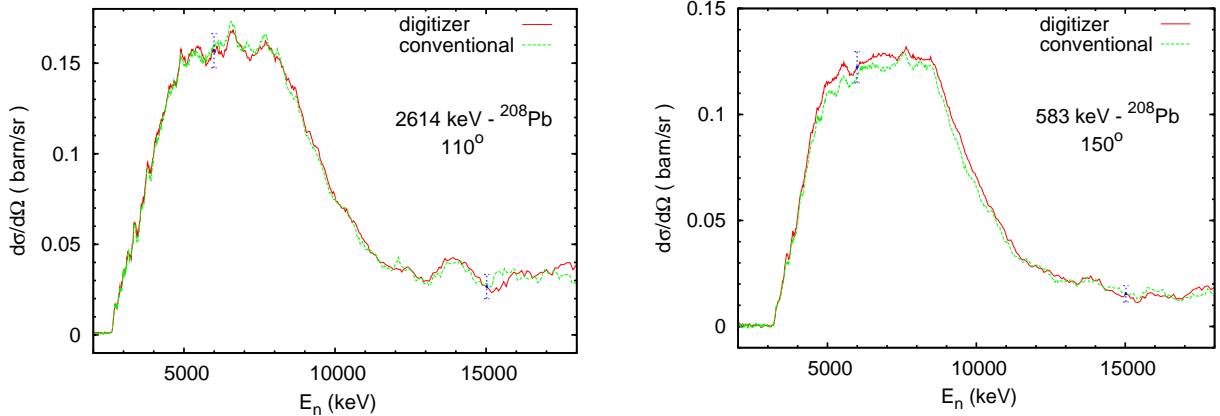


Figure 4.21: Comparison of the differential gamma production cross-sections obtained with the fast digitizer and with the conventional electronics for ^{208}Pb . Both excitation functions were smoothed with a running average filter only for an easier comparison. *Left:* Differential gamma production cross-section at 110° for the main transition of ^{208}Pb nucleus (2614 keV). *Right:* Differential gamma production cross-section at 150° for the second transition of ^{208}Pb nucleus (583 keV).

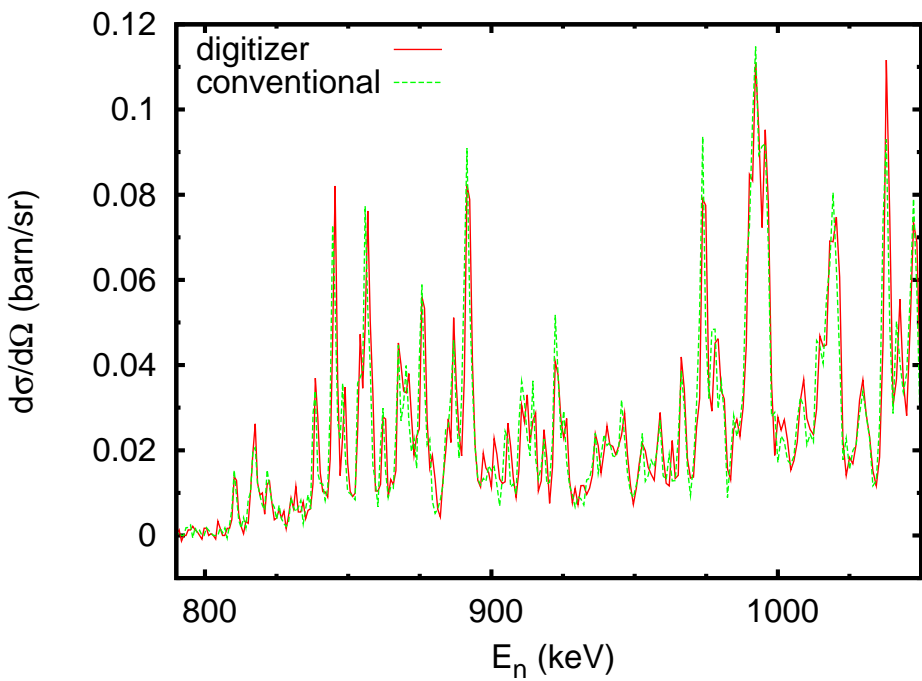


Figure 4.22: High resolution differential gamma production cross-sections obtained for the 803 keV transition from ^{206}Pb with the fast digitizer and with the conventional acquisition system.

when resonance structures are visible. This is the case for the main transition of ^{206}Pb (803 keV) at neutron energies immediately above the inelastic threshold. The resonance structures in the differential gamma production cross-section of the 803 keV transition are shown in Fig. 4.22 for the two acquisition systems. The data were recorded in parallel with the same detector (HPGe2) at 150° . The two systems provide almost the same result. The small difference in the resonance amplitude may be the effect of the tail in the time resolution spectrum of the digitizer (see Fig.4.12). This small difference does not outweigh the higher efficiency of the digitizer.

4.7 Conclusions

A new data acquisition system based on a fast digitizer was created to increase the detection efficiency in the $(n, xn\gamma)$ cross-section measurements with the experimental setup at 200 m flight path station. In a first stage, tests were made to investigate of the possibility using a 12-bits and 420 MSPS fast digitizer with large volume HPGe detectors. These tests involved the comparison of time and amplitude resolutions obtained with the fast digitizer and with the conventional electronics. Different signal processing algorithms were tested offline on the same sets of raw signals (as recorded from the output of the preamplifier) to establish the most suitable one for the online acquisition. The trapezoid algorithm for the amplitude and the CFD algorithm for the timing were preferred for the online signal processing. With the fast digitizer the amplitude and time resolutions were identical with the results obtained with the conventional electronics. The advantages of the fast digitizer are firstly the fact that the time spectrum of the digitizer has a much smaller tail than the CF function of the CFD module and secondly that the minimum resolving time of trapezoid algorithm is only $2.5 \mu\text{s}$, much smaller than the one of the spectroscopic amplifier.

The results of the tests concluded that the 12-bits and 420 MSPS fast digitizer can be used successfully with large volume HPGe detectors for low counting rates as it is the case for the $(n, xn\gamma)$ setup at the 200 m flight path station at GELINA. Substantially higher counting rates can be accommodated by a fast digitizer if an on-board data processing would be possible, e.g. if the digitizer has on-board Field Programmable Gate Array (FPGA) that can be used for a complete signal processing. The on-board signal processing would simplify even further the electronic scheme given in Sec. 4.5, avoiding the use of any conventional electronic module for the external validation.

The differential gamma production cross-sections obtained with the data acquisition system based on the fast digitizer and with the data acquisition system based on the conventional electronics were compared for two sets of measurements, with ^{208}Pb and ^{206}Pb samples. The two acquisition systems give the same result for the differential gamma production cross-sections and the advantage of the fast digitizer is a higher detection efficiency, that increases from 15% at 1.4 MeV up to 300% at 350 keV. The increase in the efficiency of the fast digitizer has two sources:

- the digitizer resolves the pile-up of the neutron induced events with the gamma-

flash induced events. 10%-20% efficiency is gained in this way for every detector.

- the digitizer does not reject the pulses with a slow rise time and has the same efficiency as the CF function of the conventional CFD module. The tail of the time resolution spectrum is significantly reduced for the digitizer compared with the analog CF module.

Chapter 5

Results and discussion

The present chapter focuses on the results of the cross-sections measurements of the five nuclei that were investigated: ^{52}Cr , ^{209}Bi and $^{206,207,208}\text{Pb}$. The data were taken with the experimental setup described in Chapter 3. The results shown in this chapter were obtained only with the data acquisition based on the conventional electronics.

For the ^{207}Pb and ^{208}Pb nuclei, the samples were enriched only to 92.40% and respectively 88.11%. Therefore, corrections for the isotopic composition and mixing of the $(n, xn\gamma)$ ($x=1,2,3$) reactions on different isotopes were needed. These corrections were done iteratively using the cross-sections measured here. All the other corrections mentioned in Chapter 3 were applied, unless mentioned otherwise.

5.1 ^{52}Cr neutron inelastic scattering and $(n,2n)$ cross-sections

5.1.1 Introduction

The majority of the experiments that measured the neutron inelastic cross-section of ^{52}Cr involved the $(n, n'\gamma)$ -technique (Refs. [93, 96, 98–102, 145, 147]). The (n, n') -technique was used in the experiments performed by Olsson *et al.* [94] at 21 MeV and by Korzh *et al.* [97] at energies below 3 MeV.

The only measurement that covered the full energy range from the inelastic threshold up to about 14 MeV was done by Voss *et al.* [99]. Except this, all the measurements were done either at low neutron energies, from the inelastic threshold up to about 4 MeV, or around 14 MeV.

Using Ge(Li) detectors, different experiments measured the cross-sections of maximum 12 γ -ray transitions. The best neutron energy resolution was obtained by Voss *et al.* [99], 2.2 keV at 1 MeV and 70 keV at 10 MeV. This was the first work that showed the presence of the resonance structures in the neutron inelastic cross-sections at low energies. However a systematic difference in normalization was observed between the data of Voss *et al.* and the other data.

In the experiment described in this work, 12 γ -ray transitions from the $^{52}\text{Cr}(n, n'\gamma)^{52}\text{Cr}$

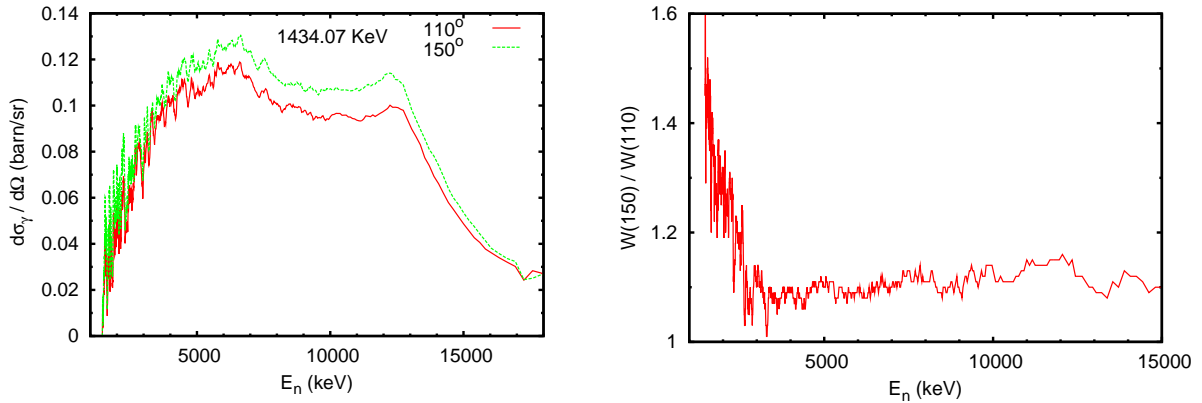


Figure 5.1: *Left:* Differential gamma production cross-section for the 1434.07 keV transition from ^{52}Cr at 110° and 150° . The data were smoothed with a moving average window for an easier comparison. The width of the window was 88 ns. *Right:* The ratio between the angular distribution at 150° and 110° for the 1434.07 keV. The angular distribution is defined by the relation $W(\theta) = \frac{4\pi}{\sigma} \frac{d\sigma}{d\Omega}(\theta)$. The data were smoothed with the same filter as on the *Left*.

reaction were observed. The highest measured excited level has an energy of 3.77 MeV. A simplified level scheme of ^{52}Cr is given in Fig. 2.1 where the γ -rays for which the gamma production cross-sections were determined are marked. At least one γ -ray was observed from the decay of every excited level up to 3.77 MeV excitation energy. This allowed to obtain the exact values of the total inelastic and level cross-section up to 3.77 MeV. For the level of 3.472 MeV two transitions (704.6 keV and 2038.0 keV) were observed and the γ -ray branching ratios were deduced.

For the $^{52}\text{Cr}(n,2n\gamma)^{51}\text{Cr}$ reaction channel, two γ -ray transitions were observed, 749.07 keV and 1164.4 keV, that decay from the first and respectively third excited level to the ground state. Only one measurement of the gamma production cross-section from the $(n,2n)$ reaction on ^{52}Cr was found in the literature (Ref. [93]). There, the gamma production cross-section was measured for the same two γ -ray transitions at 14.6 MeV.

5.1.2 Gamma production cross-sections

The differential gamma production cross-sections at two angles 110° and 150° are the primary measured quantities in the present experiment. From these, the integral gamma production cross-section was obtained using the Gauss quadrature procedure. The equations used to calculate the differential and the integral gamma production cross-sections were given in Sec. 3.3.1.

1434.97 keV

The differential gamma production cross-section for the main transition of ^{52}Cr , 1434.07 keV, is given in Fig. 5.1 *Left*. The data were smoothed with a moving

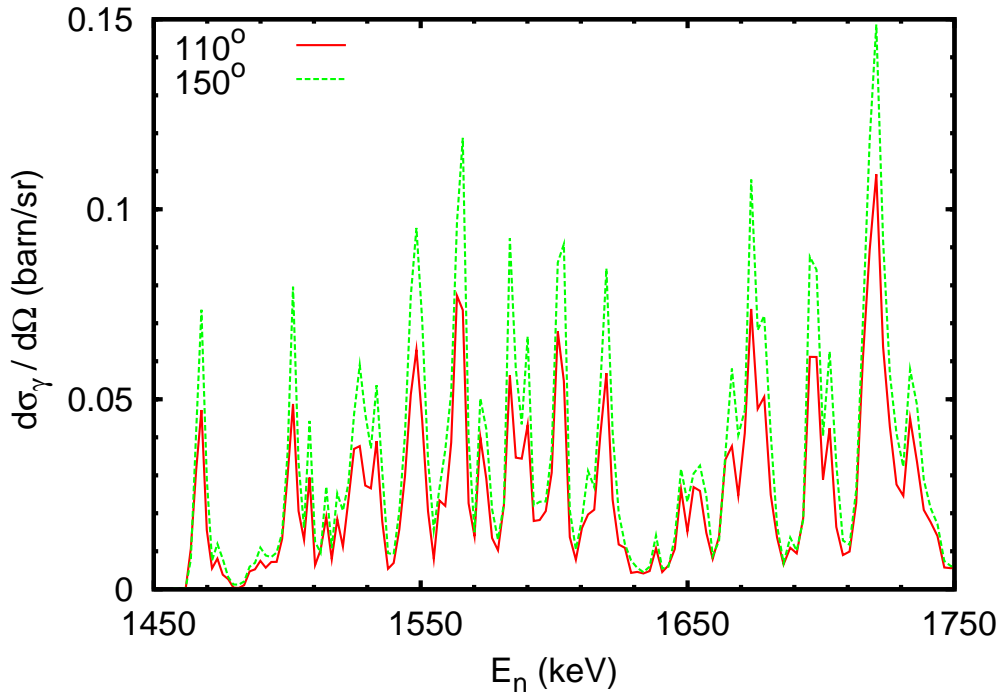


Figure 5.2: The differential gamma production cross-section of the 1434.07 keV transition with the full energy resolution of this experiment at 150° and 110° . In this energy interval, a total uncertainty of 6% was obtained for both indicated angles.

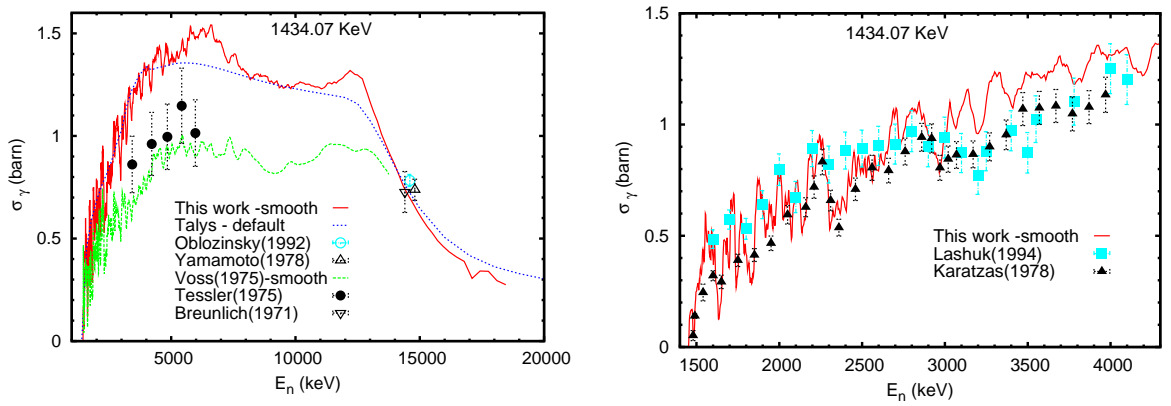


Figure 5.3: Integral gamma production cross-section for the 1434.07 keV transition in ^{52}Cr . *Left:* Full energy scale from the threshold up to 18 MeV. *Right:* A detailed plot at low neutron energies.

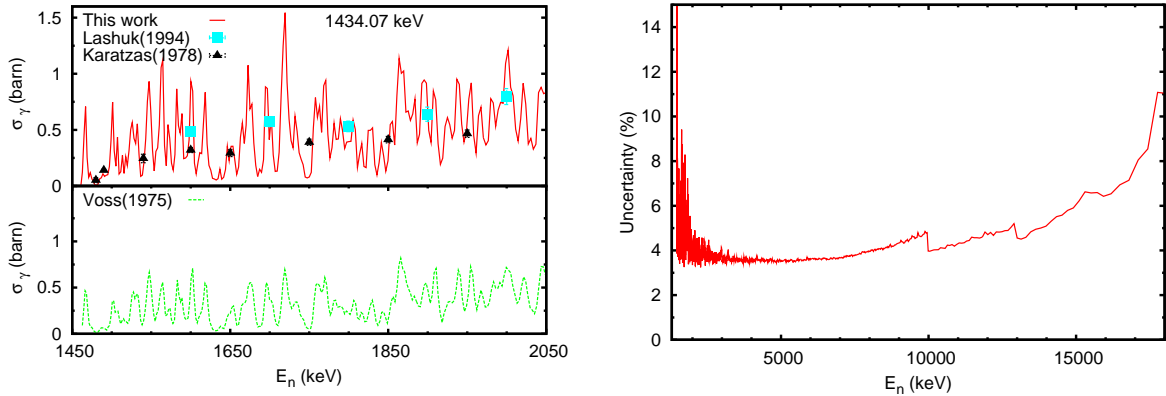


Figure 5.4: *Left:* Integral gamma production cross-section for the 1434.07 keV transition in ^{52}Cr with the full energy resolution. The present data are compared with the results of Voss *et al.* [99]. *Right:* The total uncertainty of the integral gamma production cross-section for the 1434.07 keV transition

average window filter only for a better comparison. The width of the window was 11 energy bins (88 ns time-of-flight). Fig. 5.1 *Right* shows the ratio between the differential gamma production at 150° and 110° as a function of neutron energy. This ratio is equal to the ratio of the angular distributions $W(\theta)$ at the two angles. The value predicted by the Eq. 2.17 for a stretched $E2$ γ -ray transition from an initial level 2^+ to a level 0^+ is 1.61. It can be seen that the value of this ratio immediately above the threshold is in very good agreement with the theoretical prediction for an $E2$ transition. With the increase of the neutron energy the ratio $W(150)/W(110)$ decreases, becoming constant and different from unity at about 2.5 MeV neutron energy. This may be a consequence of the fact that at 2.4 MeV the second excited level starts to be populated and the angular distribution of the 1434 keV transition is affected by the feeding from this level.

Fig. 5.2 shows the differential gamma production cross-sections of the 1434.07 keV transition with the full energy resolution of this experiment. The high neutron energy resolution of the setup allowed the observation of the resonance structures at low energies above the inelastic threshold.

The integral gamma production cross-section obtained by integrating the differential cross-sections through the Gauss quadrature is given in Fig. 5.3. At 14 MeV the present results agree well with the other measurements. A significant difference can be observed in the comparison with the data of Tessler *et al.* [130] and Voss *et al.* [99]. These data are lower than the present ones. The normalization of the present data is supported by the good agreement with the recent data of Karatzas *et al.* [96] and Lashuk *et al.* [130] at low energies (Fig. 5.3 *Right* and Fig. 5.4 *Left*). Despite the difference in the normalization with the Voss results (difference mentioned first time in Ref. [96]) the same resonance structures are observed (Fig. 5.4 *Left*). The net advantage of the present results is a factor 2 gained in the neutron energy resolution, 1.1 keV at 1 MeV for the present results, compared with 2.2 keV in the experiment of Voss *et al.*

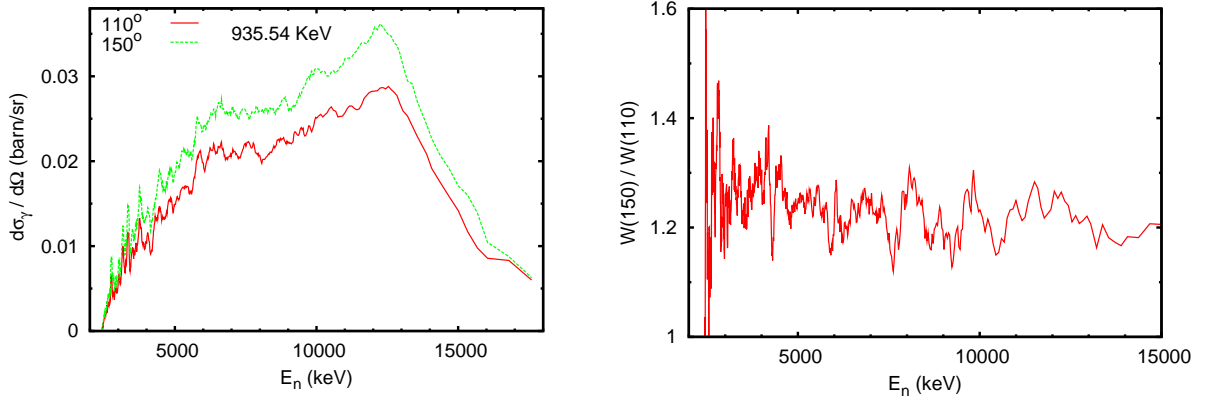


Figure 5.5: *Left:* Differential gamma production cross-section for the 935.54 keV transition in ^{52}Cr at 110° and 150° . *Right:* The ratio between angular distributions at 150° and 110° . The data were smoothed with a moving average window for an easier comparison in both panels.

The calculation done with the Talys code, that used the default input parameters, describe well the present data except for the two broad peaks at 6 MeV and respectively 12.5 MeV. At these energies the Talys calculations are below the present experimental values.

The total uncertainty of the integral gamma production cross-section for the 1434.07 keV is given in Fig. 5.4 *Right*. Below 10 MeV neutron energy, the total uncertainty was less than 5%. With the increase of the neutron energy, the total uncertainty increased up to 10% at 18 MeV because of the statistical uncertainty that became the dominant component. The large fluctuations in the total uncertainty at energies immediately above the inelastic threshold are due to the observed resonance structures (between two consecutive resonances a small number of counts was recorded). The steps in the total uncertainty at 10 MeV and about 13 MeV are due to the grouping of few energy bins to keep a reasonable statistical uncertainty. This procedure was explained in Sec. 3.3.5.

935.54 keV

The 935.54 keV γ -ray transition that decays from the second excited level at 2.369 MeV to the first excited level at 1.434 MeV has the same multipolarity as the 1434.07 keV transition (E2). The differential gamma production cross-sections at the two angles 150° and 110° and their ratio is given in Fig. 5.5. The ratio between the angular distributions at the two angles does not show a clear neutron energy dependence as in the case of the 1434.07 keV transition, maybe because of the feeding from the higher excited levels.

The integral gamma production cross-section for the 935.54 keV is given in Fig. 5.6. Within the stated uncertainties the present data agree very well with the experimental data at 14 MeV and with the results of Karatzas *et al.* [96] and Lashuk *et al.* [130] at low energies. As in the case of the 1434.07 keV transition, the

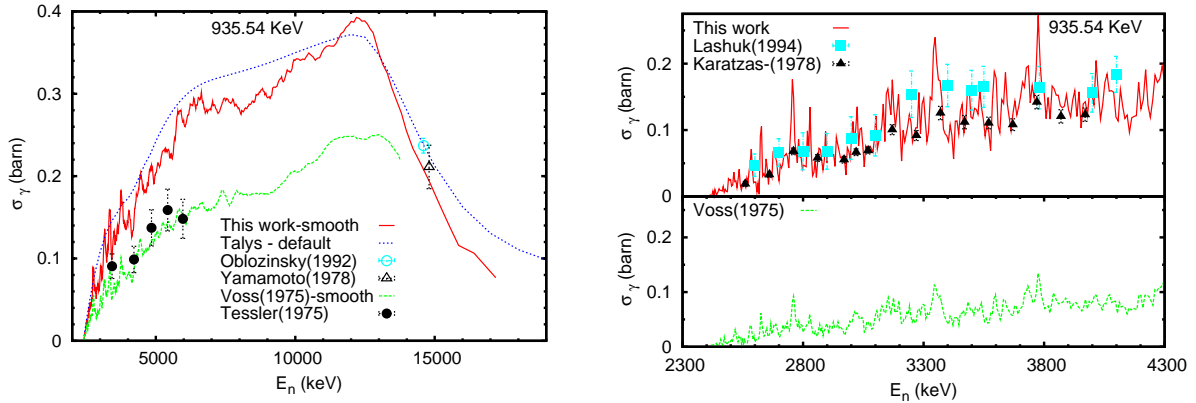


Figure 5.6: Integral gamma production cross-section for the 935.54 keV transition in ^{52}Cr . *Left*: Full energy scale from the threshold up to 18 MeV. *Right*: A detailed plot at low neutron energies.

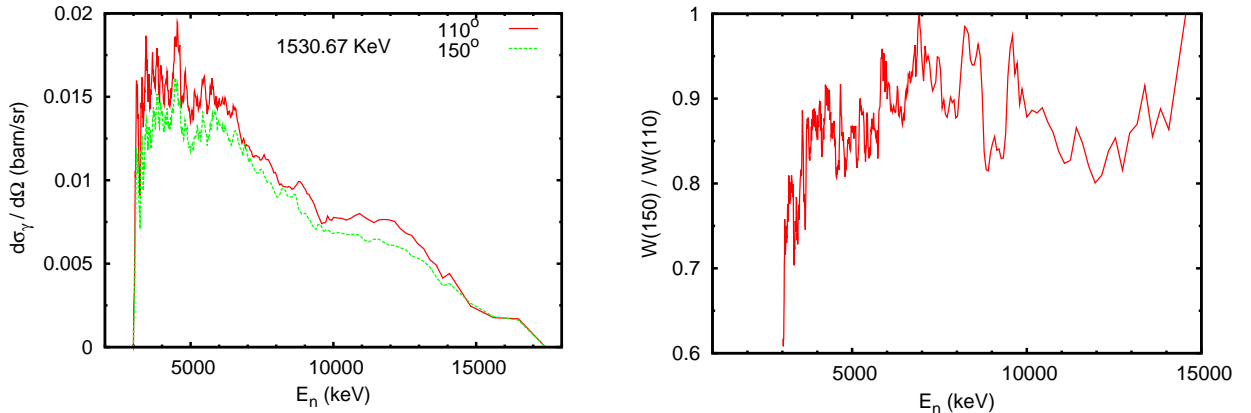


Figure 5.7: *Left*: Differential gamma production cross-section for the 1530.67 keV transition in ^{52}Cr at 110° and 150° . *Right*: The ratio between angular distributions at 150° and 110° . The data were smoothed with a moving average window for an easier comparison in both panels.

same difference in the amplitude can be observed between the present data and the data of Voss *et al.* [99]. Also for this transition, 935.54 keV, some small resonance structures can be observed below 4 MeV (Fig. 5.6 *Right*).

The Talys calculation describes reasonably the present experimental integral gamma production cross-section for the 935.54 keV transition on the full energy range, from the threshold (2.41 keV) up to 18 MeV. The calculation is higher than the measured values with about 15% around 8 MeV neutron energy (Fig. 5.6). The same difference can be observed at energies above 14 MeV.

1530.67 keV

A different example of γ -ray angular distribution is given in Fig. 5.7 for the 1530.67 keV transition ($M1+E2$). This γ -ray results from the decay of the 5th excited level, at

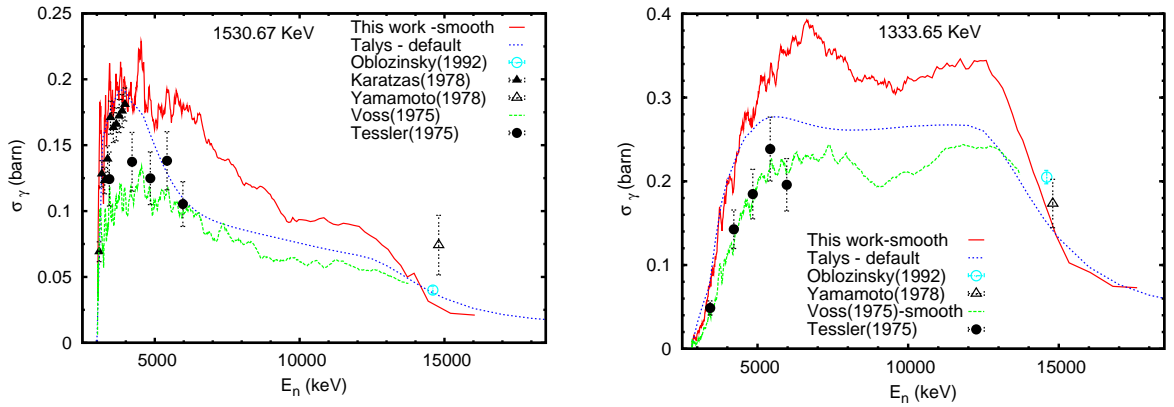


Figure 5.8: Integral gamma production cross-section for the 1530.67 keV and 1333.65 keV transitions in ^{52}Cr .

2964.78 keV. For this transition the ratio between angular distribution at 150° and 110° is smaller than unity. From Eq. 2.19, from an M1+E2 transition with a mixing ratio $\delta = -6.25$ (Ref. [131]), as given in the evaluated level scheme, the predicted value of the ratio $W(150)/W(110) = 0.76$, above the threshold. This value agrees well with the experimental ratio shown in Fig. 5.7 Right. The ratio $W(150)/W(110)$ has a small increase above the threshold and then becomes constant.

The integral gamma production cross-section of the 1530.67 keV is given in Fig. 5.8. Different from the case of the first two gamma transitions, the Talys code calculation underestimates the integral gamma production cross-section in the energy range between 5 MeV and 13 MeV.

The transitions from higher lying levels

The integral gamma production cross-section for 9 other γ -ray transitions that were observed are shown in Figs. 5.8 and 5.9. In general, good agreement can be noted between the present data and the data of Karatzas *et al.* at low energies and the data of Oblozinsky *et al.* at 14.6 MeV. For the transitions for which Voss *et al.* data were available a systematic difference in the normalization can be observed as in the case of the main transitions. This difference in the normalization is energy dependent and may come from the determination of the response function of the scintillator used by Voss *et al.* for the neutron flux measurement. Despite the difference in the normalization, the shape of the integral gamma production cross-section is similar the same in the case of present data and Voss *et al.* data. The data of Tessler *et al.* [130] are systematically lower.

The Talys code calculation describes fairly well the experimental cross-section of the 704.6 keV and 744.23 keV transitions on the full energy range. For the other measured transitions the agreement with the calculation is good at incident energies below about 4-5 MeV. However, it underestimates the present experimental data in the energy interval between 4 MeV and 14 MeV for the following transitions: 647.53 keV, 1246.28 keV, 1333.65 keV, 1727.53 keV and 2038.0 keV. In the case of the

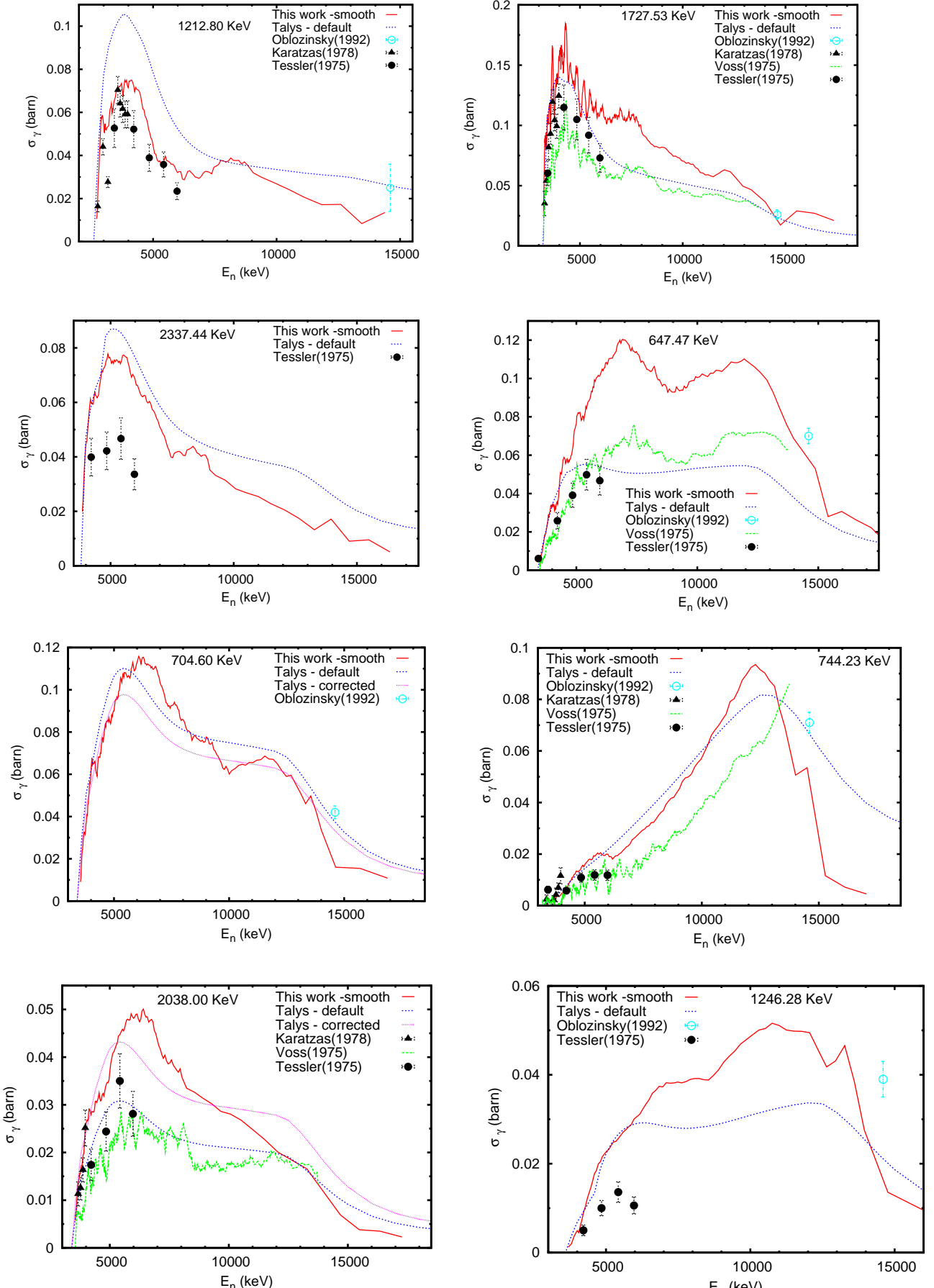


Figure 5.9: Integral gamma production cross-section for transition that decay from higher excited levels of ^{52}Cr . For the 704.60 keV and 2038.00 keV transitions from the level at 3472.24 keV the production cross-sections were corrected for the ob-

1212.8 keV and 2337.44 keV the Talys calculations are higher than the experimental values.

Branching ratio for the level at 3472 keV

The excited level of 3472.24 keV was the only level from which two γ -ray transitions were observed with sufficient statistics to build the gamma production cross-sections. According to the adopted level scheme the transitions by which the level decays are 704.6 keV and 2038.0 keV. Within the uncertainties, the thresholds of the gamma production cross-section for these two transitions were the same. The ratio between their gamma production cross-sections is constant as a function of the neutron energy, bringing an additional support to the gamma ray identification. The relative gamma intensities found in this experiment are 100% for 704.6 keV and $44.2 \pm 12\%$ for 2038.0 keV. This relative intensity for the 2038.0 keV transition is two times higher than the adopted value (Ref. [131]). On the other hand Karatzas *et al.* [96] found a relative intensity of 66, with about 50% higher than the present value. The effect of the difference between the measured and the evaluated branching ratio on the gamma production cross-section is shown in Fig. 5.9. The gamma production cross-section. With the new measured values for the branching ratios (the "corrected" curve in Fig. 5.9) the calculation describes slightly better the production cross-section of the 2038.00 keV transition. For the 704.60 keV transition the difference between the measured production cross-section and the Talys calculation becomes larger around 6 MeV and smaller at energies above 10 MeV.

(n,2n) gamma production cross-sections

The relatively high threshold of the $^{52}\text{Cr}(n,2n)^{51}\text{Cr}$ reaction (12.27 MeV) and the low neutron flux at high energies resulted in poor statistics for the gamma ray peaks from the (n,2n) channel. Fig. 5.10 shows the amplitude spectrum of the detector at 150° integrated over the neutron energies from just below the (n,2n) threshold up to 20 MeV. This procedure allowed an easier identification of the ^{51}Cr peaks. Only two transitions, 749.06 keV and 1164.4 keV, were observed with enough statistics to construct the gamma production cross-sections. The transition of 27.8 keV from the decay of the second excited level was not observed in this experiment because of its very low energy, below the thresholds of the electronics. Another limitation for this transition is its internal conversion factor of 0.905 [131]. The 603.5 keV and 1480.3 keV transitions were too weak to be separated from the background with a reasonable statistical error.

The resulting gamma production cross-sections for the two transitions from ^{51}Cr are shown in Fig. 5.11. The observed reaction threshold for each transition is the same as the calculated one and this fact confirms the correct identification of the gamma rays. The $^{52}\text{Cr}(n,2n)^{51}\text{Cr}$ gamma production cross-section presented here were not corrected for the neutron attenuation and multiple scattering. For the (n,2n) cross-sections the multiple scattering is expected to be negligible and the attenuation correction with the ^{52}Cr sample is of the order of 1.5 %-2 %. The total uncertainty for the derived (n,2n) gamma production cross-section was around

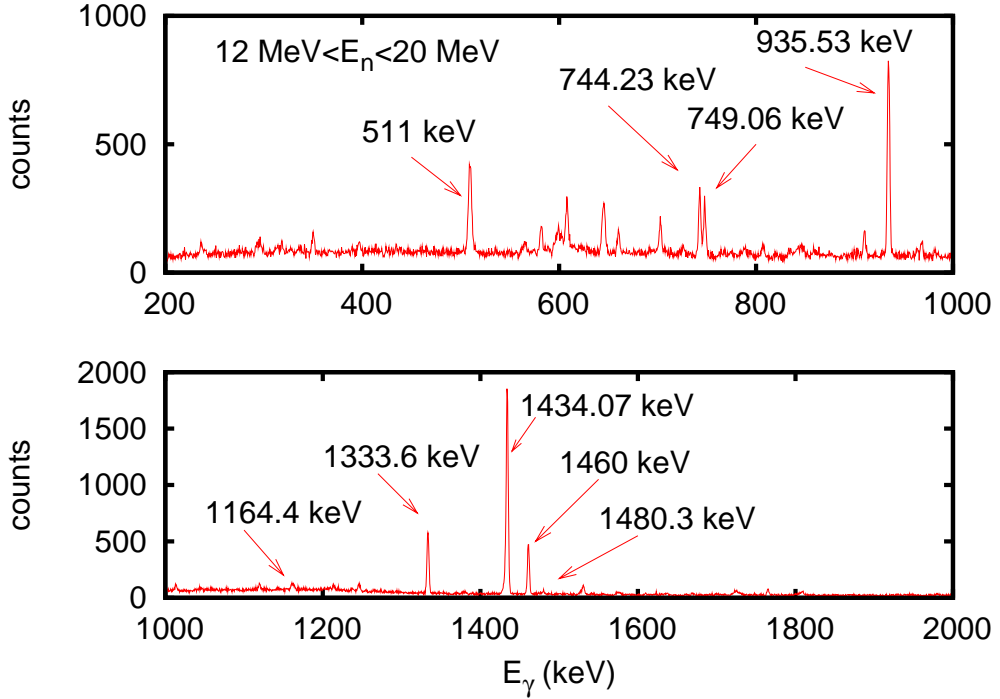


Figure 5.10: HPGe yield integrated over neutron energies between 12 MeV and 20 MeV. The 749 keV and 1164 keV peaks from the $^{52}\text{Cr}(\text{n},2\text{n})^{51}\text{Cr}$ reaction are better observed with such a selection on the neutron energy.

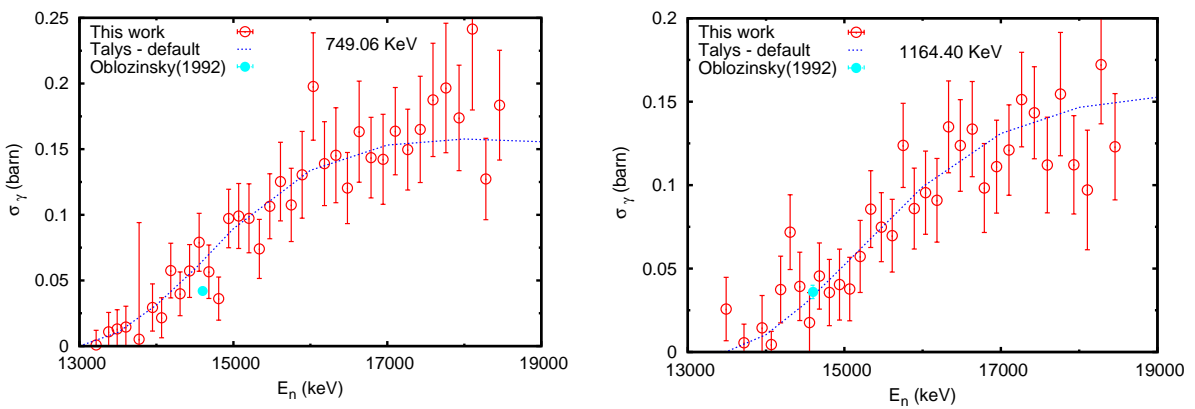


Figure 5.11: $^{52}\text{Cr}(\text{n},2\text{n})^{51}\text{Cr}$ gamma production cross-section

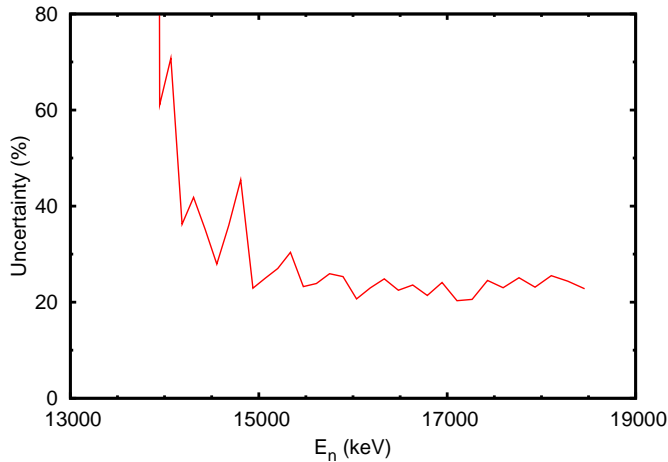


Figure 5.12: Total uncertainty for the gamma production cross-section of the 749 keV transition from the $^{52}\text{Cr}(n,2n)^{51}\text{Cr}$ reaction.

25% (Fig. 5.12). Higher values for the total relative uncertainty were obtained immediately above the threshold because of the poor statistics. The neutron energy resolution ranged between 120 keV immediately above the threshold and 180 keV at 18 MeV. The present data agree very well with the Talys calculation and with the measurement of Oblozinsky *et al.* [93] at 14.6 MeV.

5.1.3 Total inelastic and level cross-sections

Total neutron inelastic cross-section

The total inelastic cross-section was obtained as described in Sec. 2.1.2 using the integral gamma production cross-sections. Up to 3.771 MeV excitation energy, only four transitions contribute to the total inelastic cross-section: 1434.07 keV, 1530.67 keV, 1727.53 keV and 2337.44 keV (see also Fig. 2.1). According to the adopted level scheme, the next excited level above 3771 keV that decays directly to the ground state is at 3951.2 keV. This leads to the conclusion that the total inelastic cross-section shown here (Fig. 5.13) is exact up to about 4.0 MeV neutron energy; above this value it has to be considered as a lower limit. In the case of the ^{52}Cr , the majority of the excited levels decay through the first excited level so this limit is very close to the exact value.

For a better comparison of the total cross-section with the existing data in Fig. 5.13 *Left* the present data were smoothed. The inset of Fig. 5.13 *Left* represents the total uncertainty for the total inelastic cross-section. Because the 1434.07 keV transition is the dominant component in the construction of the total inelastic cross-sections, the uncertainty of the total inelastic cross-section is very similar to the uncertainty of the 1434.07 keV transition. At the extremities of the energy interval the total uncertainty is dominated by the statistical fluctuations. The steps in the uncertainty at 10 MeV and 13 MeV are due to the grouping together of few energy bins.

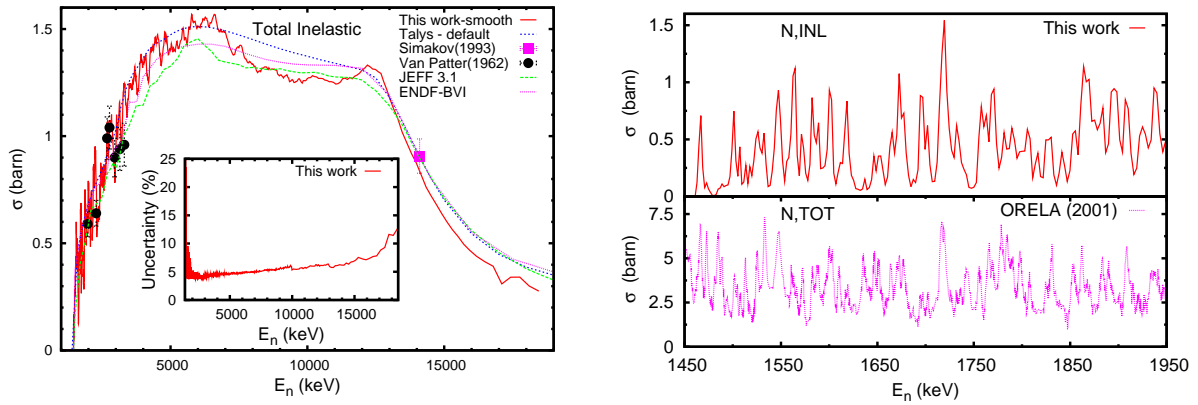


Figure 5.13: Total inelastic cross-section of ^{52}Cr . *Left:* Comparison with other experimental data, with the evaluations of the libraries JEFF 3.1, and ENDF/B-VI and with the Talys calculation. The corresponding total uncertainty is given as inset. *Right:* Comparison of the full resolution total inelastic cross-section with the total neutron cross-section measured at ORELA *et al.* [105]

The total inelastic cross-section agrees very well with the experimental data of Van Patter *et al.* [102] at low energies and that of Simakov *et al.* [130] at 14 MeV. The evaluated cross-sections, ENDF/B-VI and JEFF 3.1, are very close to the present data except above 14 MeV where the evaluations are slightly higher.

Despite the fact that the Talys calculation underestimates almost all the gamma production cross-sections that contribute to the total inelastic cross-section, the latter is well described in the whole energy range.

In Fig.5.13 *Right*, the full resolution total inelastic cross-section is compared with the total neutron cross-section measured in a transmission experiment at ORELA [105]. Despite the poorer resolution of the inelastic measurement compared with the transmission measurement, many structures are common to both data sets. At the same time one observes clearly that the resonances in the inelastic cross-section is not a fixed fraction of the resonances in the total neutron cross-section. This is in accord with the random nature of the partial widths.

Level 1434.09 keV

The cross-section of the first excited level is given in Fig. 5.14 together with the corresponding total uncertainty. As described in Sec. 2.1.2, this cross-section was obtained subtracting from the gamma production cross-section of the 1434.07 keV transition the contributions of the following transitions: 935.54 keV, 1212.80 keV, 1333.65 keV, 1530.67 keV, 744.23 keV, 647.47 keV, 2038.0 keV, 1246.28 keV and 2337.44 keV. From the evaluated level scheme, the next level that decays directly to the 1434.09 keV level has an energy of 4563.0 keV. From this it results that the constructed cross-section of the 1434.09 keV level is exact up to about 4.5 MeV neutron energy.

The present cross-section for the 1434.09 keV level agrees very well with the data

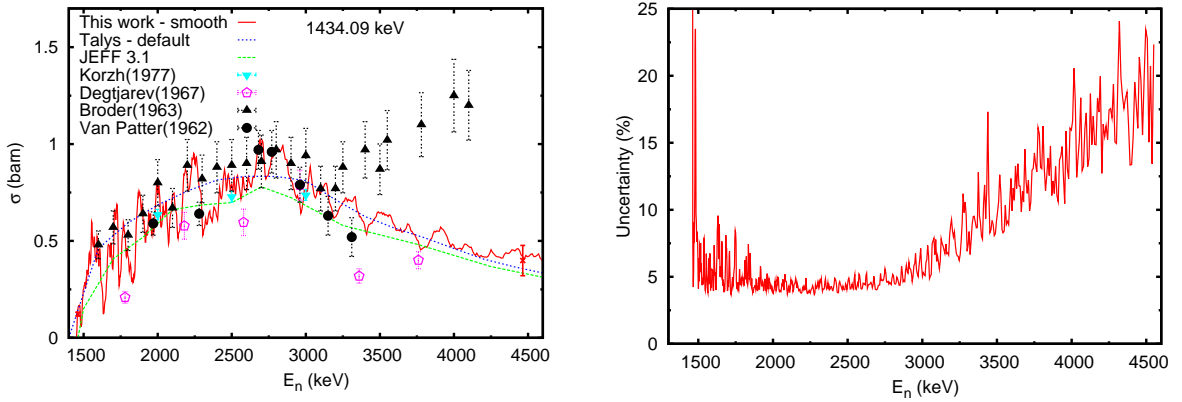


Figure 5.14: Cross-section of the 1434.09 keV level (*Left*) and its corresponding total uncertainty (*Right*).

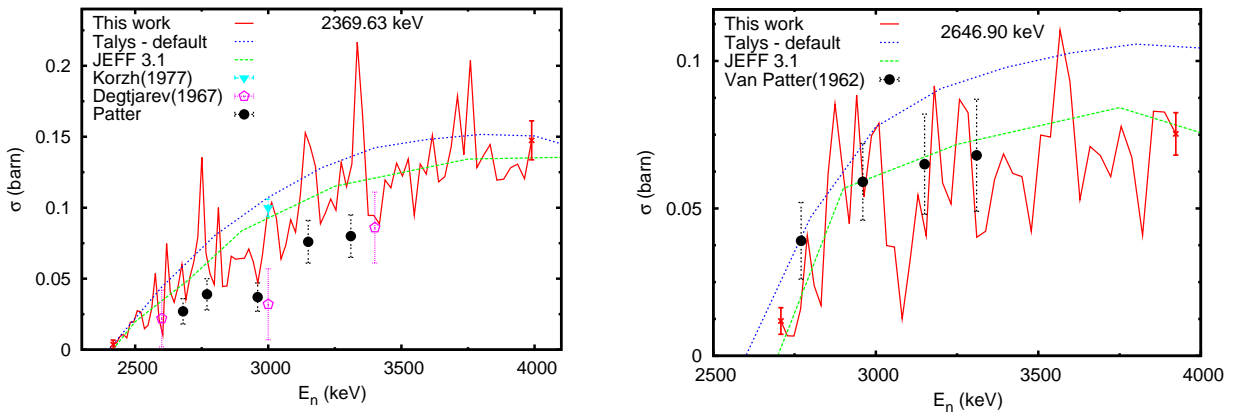


Figure 5.15: Cross-section of the 2369.63 keV (*Left*) and 2646.9 keV (*Right*) levels. Generic uncertainty bars are given at the extremities of the energy range for the graphs with a continuum line.

of Van Patter *et al.* [102] and Korzh *et al.* [97]. The results of Degtjarev *et al.* [101] are below the present values. The level cross-section given by Broder *et al.* [130] is significantly higher above 3.2 MeV, maybe because of an insufficient correction for the feeding from the higher excited levels. The evaluated data, JEFF 3.1, and the Talys calculation match very well the present results. For the Talys calculation, the good agreement with the measured data in the case of the level cross-sections can be understood also from the good agreement of almost all the gamma production cross-sections at energies below 4-5 MeV.

The total uncertainty for the cross-section of the 1434.09 keV level increases with the neutron energy up to about 20% at 4.5 MeV. The larger uncertainty for this level cross-section is due to the fact that 9 different γ -ray transitions feed this excited level.

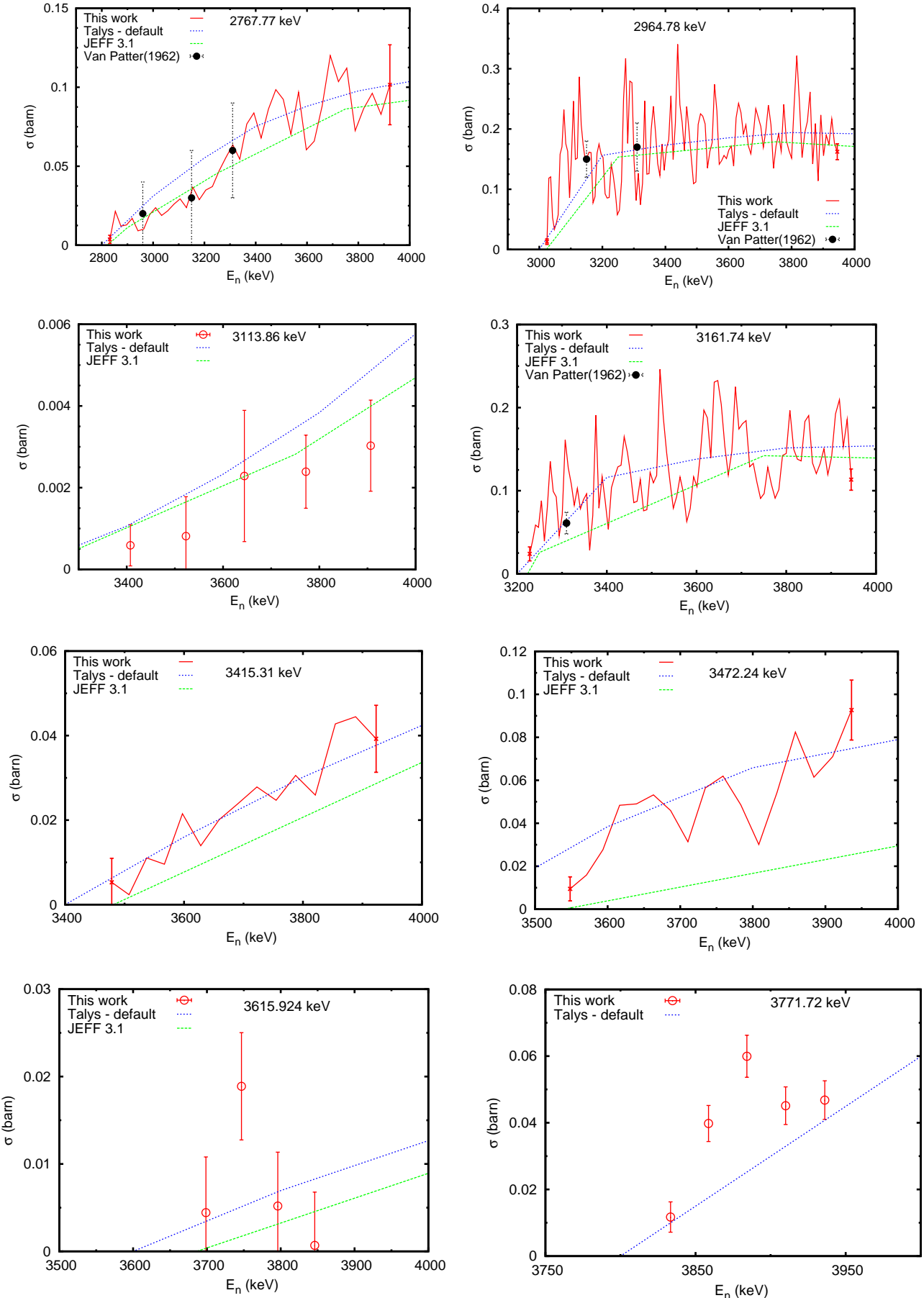


Figure 5.16: Cross-section of the higher energy levels. Generic uncertainty bars are given at the extremities of the energy range for the graphs with a continuum line.

Levels with higher excitation energy

The cross-sections for the excited levels up to 3771 keV are given in Figs. 5.15 and 5.16. All these cross-sections were constructed only up to about 4 MeV. Generic uncertainty bars were plotted on the graphs at the extremities of the energy range. Where other experimental data exist, a good agreement with the present data was found.

In general the default calculation of Talys describes well the level cross-sections presented here. For the levels at 2646.9 keV and at 3113.86 keV, the calculation given slightly higher results above 3 MeV and respectively 3.5 MeV. For the level at 3771.7 keV, the calculation is slightly lower, but still at the limits of the error bars.

The same general good agreement was found with the evaluated cross-section from the JEFF 3.1 library. Fine tuning of evaluated data are still possible.

5.1.4 Conclusions

Using a highly enriched sample of ^{52}Cr , 12 γ -ray transitions from the inelastic scattering channel and two γ -ray transitions from the $(n,2n)$ reaction channel were observed. For all these transitions the differential gamma production cross-section at two angles, 110° and 150° , were measured from the threshold up to about 18 MeV. The integral gamma production cross-sections were obtained for the same energy range. Levels were observed up to maximum excitation energy of 3771 keV.

The inelastic total and level cross-sections were constructed based on the evaluated level scheme of ^{52}Cr and using the integral gamma production cross-sections. Above 4 MeV neutron energy, the total inelastic cross-section presented here is only a lower limit but is close to the exact value. The same 4 MeV represents the maximum neutron energy up to which the level cross-sections were given.

Neutron energy resolutions of 1.12 keV at 1 MeV up to 35 keV at 10 MeV were obtained for the main transitions and for the total inelastic scattering cross-section. The total uncertainty on the gamma production cross-section of the main transition and on the total inelastic scattering cross-section was smaller than 5% up to 10 MeV and less than 10% up to 18 MeV.

Comparing with the previous experiments, the set of cross-sections measured in the present experiment for ^{52}Cr have the advantage of covering the full energy range from the threshold up to about 18 MeV in only one run, reducing significantly the systematic uncertainties. Moreover the present results have a better neutron energy resolution and smaller total uncertainties than the existing experimental data. The cross-sections measured here may improve the further evaluations.

In general, the Talys code calculation with the default input parameters describes relatively well the measured cross-sections presented here. The gamma production cross-sections are described well at energies below about 4 MeV, but significant differences with the measured data are visible above this energy. The total inelastic cross-section is better described by the default Talys calculation on the full energy range. This is valid despite the fact that the gamma production cross-sections of the transitions that go directly to the ground state are underesti-

mated by the calculation. These γ -rays are 1434.07 keV, 1530.67 keV, 1727.53 keV and 2337.44 keV. Anyway, the calculation gives higher values for the total inelastic cross-section around 9 MeV and above 14 MeV. These differences are higher than the given uncertainties. The good agreement of the calculated level cross-section with the measured values can be understood also from the good agreement of almost all the gamma production cross-sections at energies below 4-5 MeV.

The large cross-sections data set that was obtained in this experiment for the neutron inelastic scattering and (n,2n) reaction on ^{52}Cr can be used as benchmark for the nuclear codes and in future evaluations. As it can be seen from the comparisons presented here, further fine tuning can be done for the Talys code, especially for a better description of the gamma production cross-sections. The evaluated cross-sections can be also improved.

5.2 ^{209}Bi neutron inelastic scattering and (n,2n) cross-sections

5.2.1 Introduction

The majority of experiments that measured the inelastic cross-sections used the (n,n')-technique [106–108, 110–114, 116, 117, 119–122, 124, 125, 141, 148]. In all these experiments, the cross-section for only two excited levels (896 keV and 1608 keV) were measured. In some cases the cross-sections were measured for two other groups of levels at about 2 MeV and respectively 3 MeV. Due to the relatively low energy resolution of the neutron detectors it was not possible to observe the individual levels from these groups.

Only 3 data sets of gamma production cross-sections measured with the (n,xn γ)-technique were found (Lashuk *et al.* [130], Dickens *et al.* [161] and Sherrer *et al.* [123]).

The majority of the above mentioned measurements was done with low energy neutrons, from the inelastic threshold up to about 4 MeV. Several point data were found in the literature for the total inelastic cross-section at 6 MeV, 14 MeV and 21 MeV. Moreover, the discrepancies between all existing data are rather important.

In the present experiment, due to the high energy resolution of the HPGe detectors, a very good identification of the ^{209}Bi γ -rays in a complex spectrum was possible. In consequence the gamma production cross-sections were measured for 39 transitions from the threshold up to about 20 MeV. The observed γ -rays are shown in the simplified level scheme of ^{209}Bi from Fig. 5.18. As an example, the gamma-ray spectrum recorded with one of the HPGe detectors is shown in Fig. 5.17. The most intense γ -rays in the spectrum are marked. The highest excitation energy of an observed level was 3.80 MeV. Up to 2.91 MeV excitation energy, at least one γ -ray was observed for every excited level. Above this energy some levels were not observed. As described in Sec. 2.1.2 the total inelastic cross-section was constructed up to about 20 MeV neutron energy. The cross-sections of the levels below 3.5 MeV excitation energy were constructed as well.

For the (n,2n) reaction channel no gamma production cross-section data were found in the literature. All experiments for the (n,2n) reaction on ^{209}Bi measured the total (n,2n) cross-sections. In Refs. [127–129], large volume liquid scintillator detectors (Gd or Cd-loaded) were used to count the outgoing neutrons. In the present experiment, 8 γ -rays were observed from the $^{209}\text{Bi}(n,2n)^{208}\text{Bi}$ reaction. The gamma production cross-section of these was obtained from the thresholds up to about 20 MeV.

5.2.2 Gamma production cross-sections

The integral gamma production cross-section was obtained using the Gauss quadrature for the angle integration of the differential cross-sections. In the case of ^{209}Bi , the inelastic gamma production cross-section tends to decrease significantly above 10 MeV neutron energy. Because of this and of the fact that the neutron flux at GELINA decreases exponentially at this energies, poor statistics was obtained

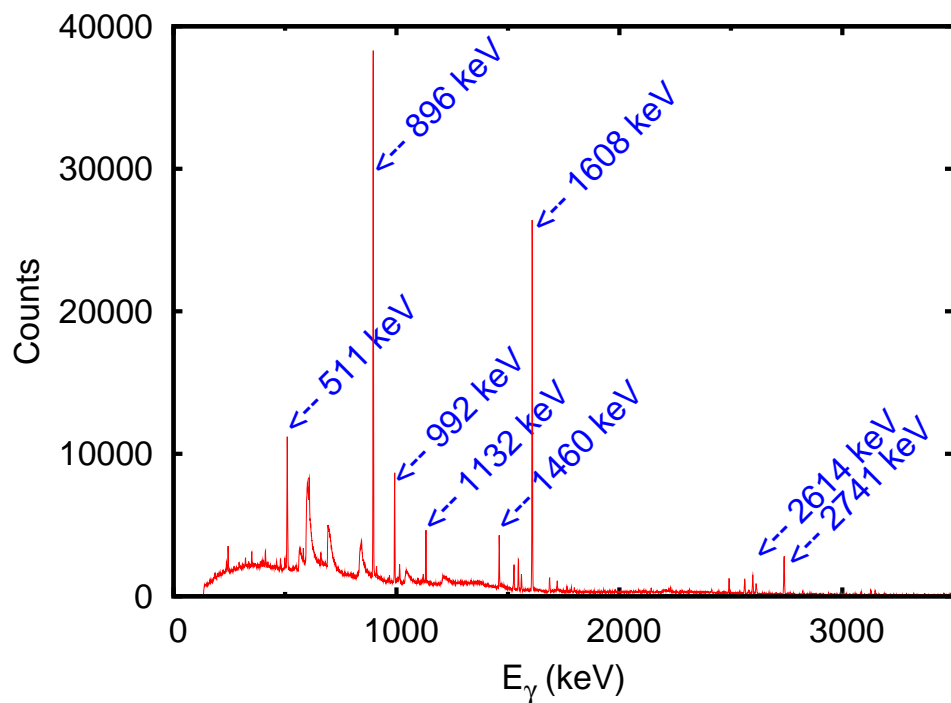


Figure 5.17: The γ -ray spectrum of an HPGe detector with the ^{209}Bi sample. The spectrum was integrated over the neutron energies from 800 keV up to about 25 MeV. The main γ -ray peaks from the inelastic scattering on the ^{209}Bi sample are clearly visible.

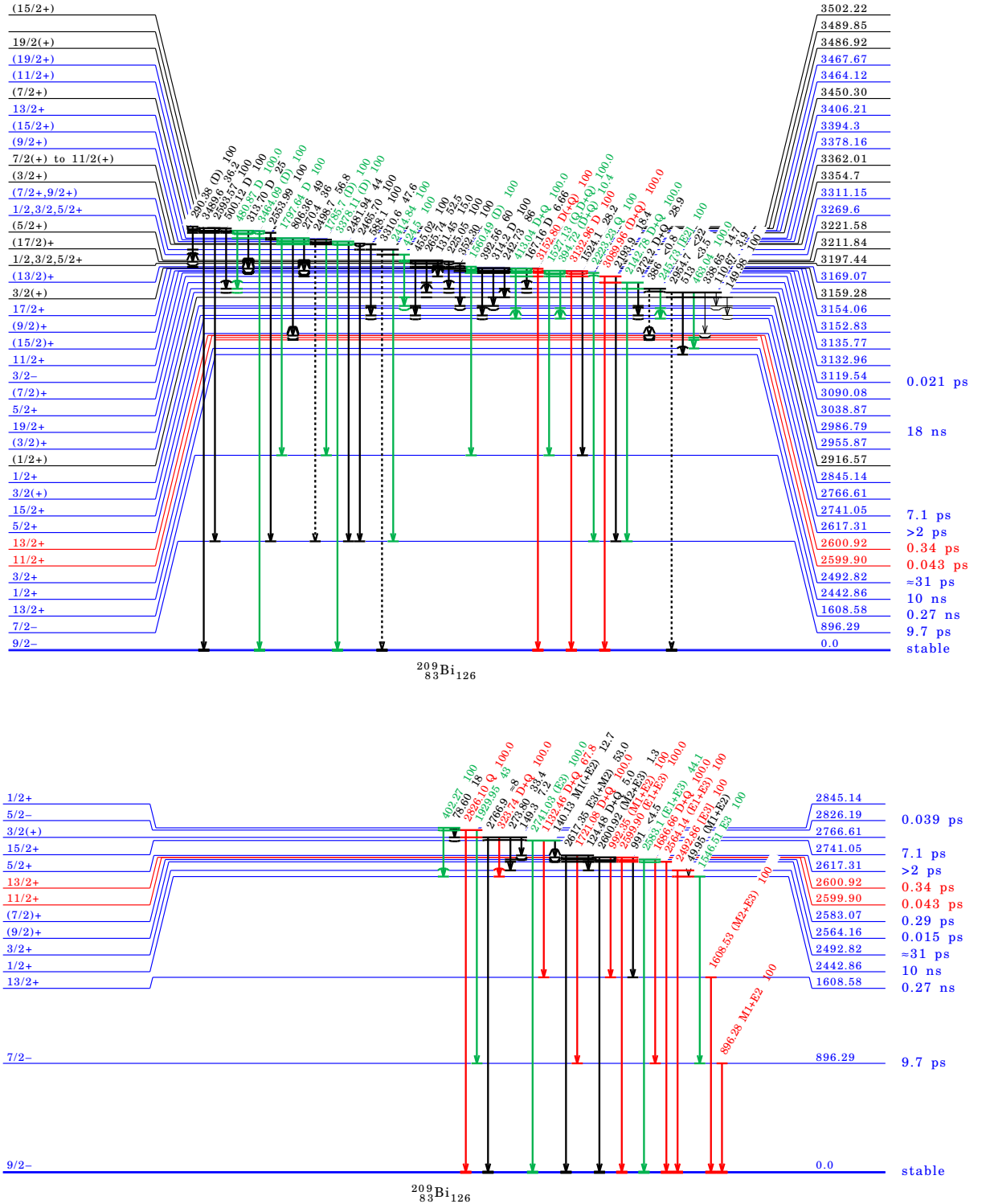


Figure 5.18: Simplified level scheme of ^{209}Bi *et al.* [131]. The gamma production cross-sections of the transitions drawn with colors were measured in the present experiment. The "red" γ -rays were used to construct the total inelastic cross-section. The excited levels drawn with black were not observed. The two levels very close to each other at 2600 keV were marked with red (see the text for details). Other five transitions from levels above 3.46 MeV were not drawn in this scheme for sake of simplicity: 808.0 keV, 2678.8 keV, 2705.42 keV, 2887.3 keV and 2904.5 keV.

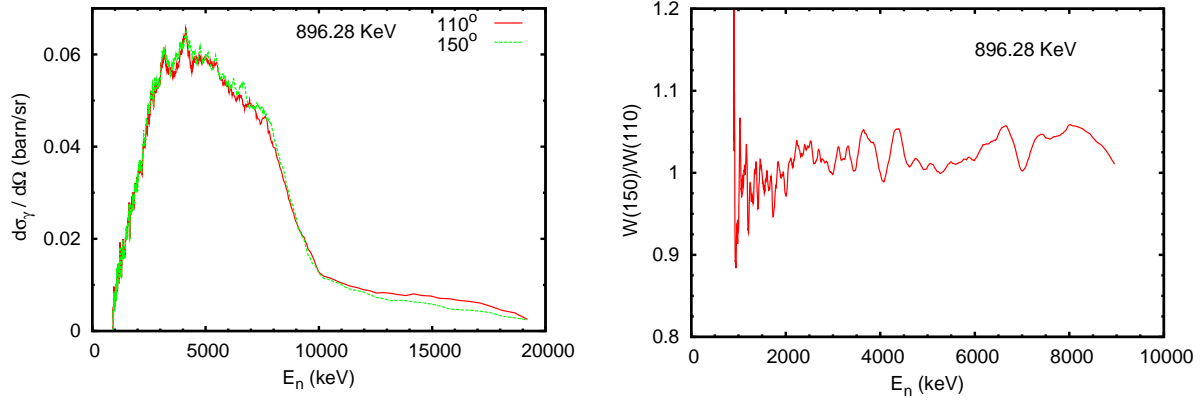


Figure 5.19: Differential gamma production cross-section for the 896.28 keV transition in ^{209}Bi . *Left:* Smoothed curves from the threshold up to 20 MeV at two angles, 110 and 150 degrees. *Right:* The ratio between the angular distribution $W(\theta) = \frac{4\pi}{\sigma} \frac{d\sigma}{d\Omega}(\theta)$ at 150 and 110 degrees.

for some γ -ray transitions at energies above 10 MeV. For very weak transitions the gamma production cross-section were measured only below 10 MeV. In the following will be presented the results for the gamma production cross-sections of all observed γ -rays.

896.28 keV

The main transition in ^{209}Bi has a mixed multipolarity of M1+ E2 with a mixing ratio equal to -0.70 [131]. The differential gamma production cross-section is shown in Fig. 5.19 for the two angles of measurement, 110° and 150°. No significant angle dependence was observed for this transition. The dependence of the ratio between the angular distribution $W(\theta)$ at 150° and at 110° is shown in Fig. 5.19 *Right*.

Fig. 5.20 shows the integral gamma production cross-section of the 896.28 keV transition. Above 9 MeV neutron energy a γ -ray transition of 895.9 keV from the reaction $^{209}\text{Bi}(n,2n)^{208}\text{Bi}$ is produced. The two γ -ray peaks cannot be separated and the cross-section of the inelastic transition may be overestimated above 9 MeV (see also the $(n,2n)$ cross-sections). The green curve in Fig. 5.20 represents the sum of the gamma production cross-sections calculated with Talys for the two transitions, 896.28 keV from ^{209}Bi and 895.9 keV from ^{208}Bi . At energies above 9 MeV (the threshold of the 895.9 keV transition), the present measured data are close to this sum of the calculated cross-sections (green curve). The calculation performed with the Talys code with the default parameters describes well the measured data below 2.5 MeV. In the energy range between 2.5 MeV and 9 MeV the calculation underestimates significantly the measured gamma production cross-section.

The present results are in good agreement with the data of Lashuk *et al.* [130] up to about 2.5 MeV (see also Fig. 5.21). Above this energy, the Lashuk *et al.* data are slightly lower. The data point of Dickens *et al.* [161] at 5.4 MeV is about 20 % lower.

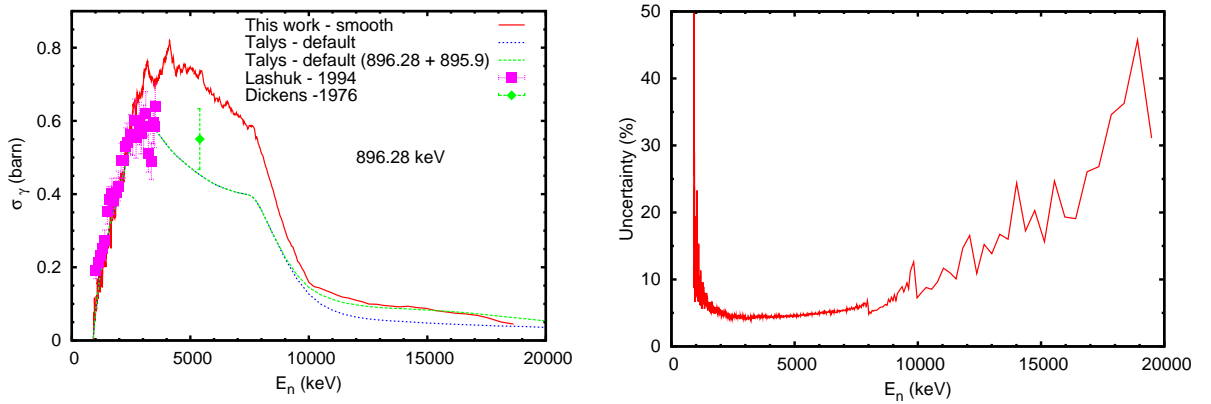


Figure 5.20: *Left:* Integral gamma production cross-section for the 896.28 keV transition in ^{209}Bi . Full energy scale from threshold up to 20 MeV. The data were smoothed with an averaging moving window filter for an easier comparison with other data. *Right:* Total uncertainty of the integral gamma production cross-section for the 896.28 keV transition in ^{209}Bi .

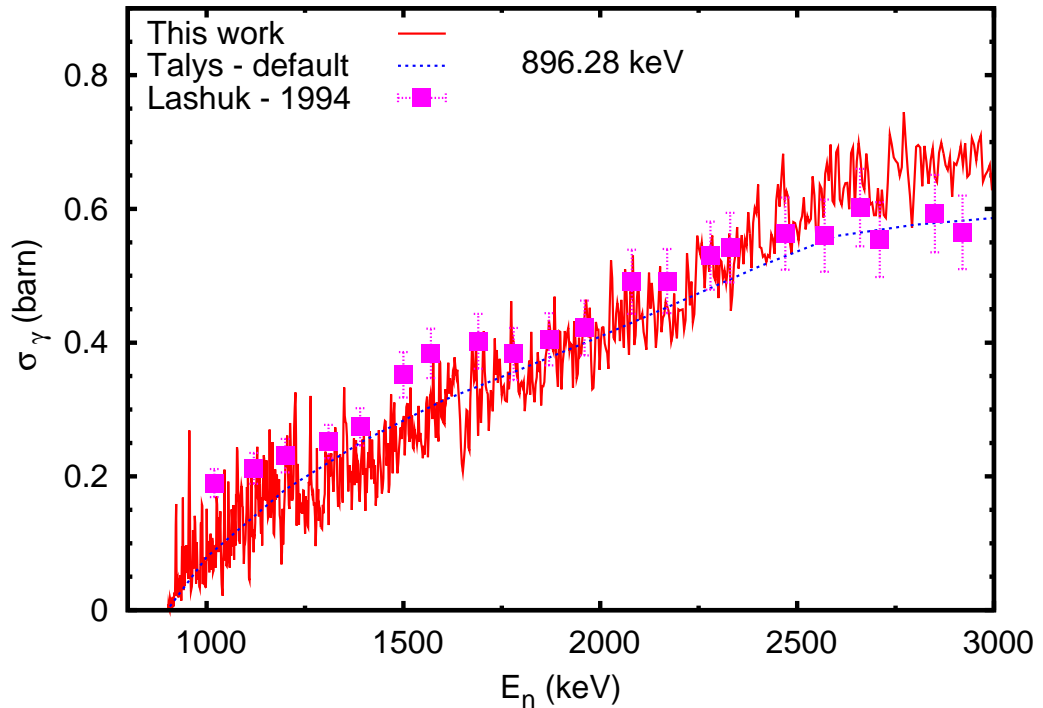


Figure 5.21: High resolution integral gamma production cross-section for the 896.28 keV transition in ^{209}Bi .

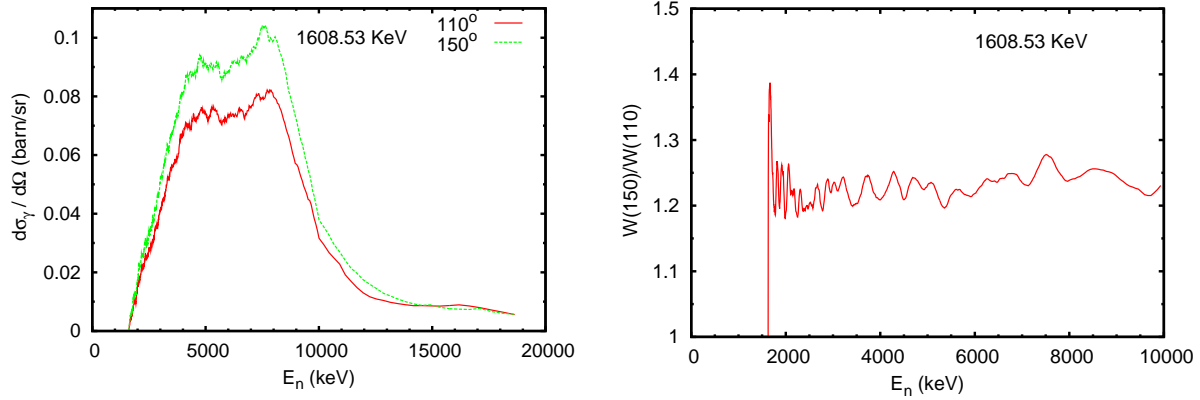


Figure 5.22: Differential gamma production cross-section for the 1608.53 keV transition in ^{209}Bi . *Left:* Smoothed curves from the threshold up to 20 MeV at two angles, 110 and 150 degrees. *Right:* The ratio between the angular distribution $W(\theta)$ at 150 and 110 degrees.

The gamma production cross-section with the high energy resolution is given in Fig. 5.21 for neutron energies up to 3 MeV. Because of the high level density in the compound nucleus ^{210}Bi , no significant resonance structures were observed in the neutron inelastic cross-section of ^{209}Bi at low energies.

The total uncertainty for the integral gamma production cross-section of the main transition in ^{209}Bi is given in Fig. 5.20 *Right*. At low energies, because of the slow rise of the cross-section, large uncertainties were obtained. At the extremities of the energy range the statistical uncertainty is the major component in the total uncertainty. Starting from 8 MeV neutron energy, few energy bins were grouped to reduce the statistical uncertainties. This procedure caused the steps in the uncertainty plot at 8 MeV and 10 MeV. In this way it was obtained a total uncertainty of about 5% below 10 MeV and a maximum of 40% at 18 MeV.

1608.53 keV

According to the evaluated level scheme, the second transition in ^{209}Bi , 1608.53 keV, has a mixed multipolarity of $M2 + E3$ with a mixing ratio $\delta = 0.33$ [131]. In the present experiment, significant angle dependence was observed for the differential gamma production cross-section of this transition (Fig. 5.22). The energy dependence of the ratio between the angular distributions $W(\theta)$ at 150° and at 110° is shown in Fig. 5.22 *Right*.

The integral gamma production cross-section of the 1608.53 keV transition compared with existing experimental data is given in Fig. 5.23. The measurement of Sherrer *et al.* [123] at 3.2 MeV is in good agreement with the present results. Below 3.0 MeV the data of Lashuk *et al.* [130] are slightly above the present results. With the increase of the neutron energy they become lower than the present data. No experimental data were found in the literature for energies higher than 5.4 MeV.

In general, for the 1608.53 keV transition the Talys calculation with the default

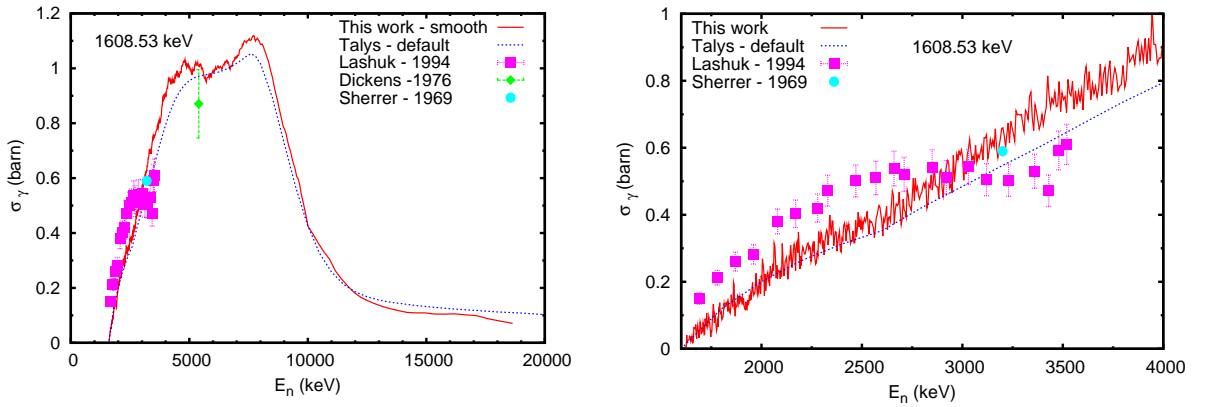


Figure 5.23: Integral gamma production cross-section for the 1608.53 keV transition in ^{209}Bi . *Left:* Full energy scale from threshold up to 20 MeV. The data were smoothed with an averaging moving window filter for an easier comparison with other data. *Right:* Detailed plot with the full energy resolution.

parameters describes well the experimental data in the full energy range, from the threshold up to 19 MeV (Fig. 5.23). In the middle energy range, between 4 MeV and 9 MeV, the calculation is still lower than the measured data. The difference is more evident at the two broad peaks at 5 MeV and 8 MeV.

Fig. 5.23*Right* shows the low energy part of the integral gamma production cross-section of the 1608.53 keV transition. As in the case of the 896.28 keV transition, no clear resonance structure was observed for the 1608.53 keV transition above the threshold.

1546.51 keV

The 1546.51 keV γ -ray is an electric octupole transition that decays from the third excited level ($1/2^+$) to the first one ($7/2^-$). The measured angular distribution does not show a large anisotropy between the 110° and 150° angles (Fig. 5.24). The energy dependence of the ratio between the angular distribution $W(\theta)$ at 150° and 110° is given in Fig. 5.24 *Right*.

The corresponding integral gamma production cross-section is shown in Fig. 5.25 *Left*. The measured point at 5.4 MeV from Ref. [161] is much lower than the present values. The default calculation with Talys underestimates significantly the measured data except the extremities of the energy interval. Just above the threshold and around 10 MeV, the calculation is close to the measured data.

The transitions from higher lying levels

The integral gamma production cross-section for 36 other transitions from the decay of higher lying levels in ^{209}Bi is given in Figs. 5.25, 5.26, 5.27, 5.28, 5.29 and 5.30. For some of these transitions, measured data with Ge(Li) detectors at 5.4 MeV are available from Ref. [161]. In general with the increase of the excitation energy, the gamma production cross-section decreases. The weakest γ -ray transitions that were

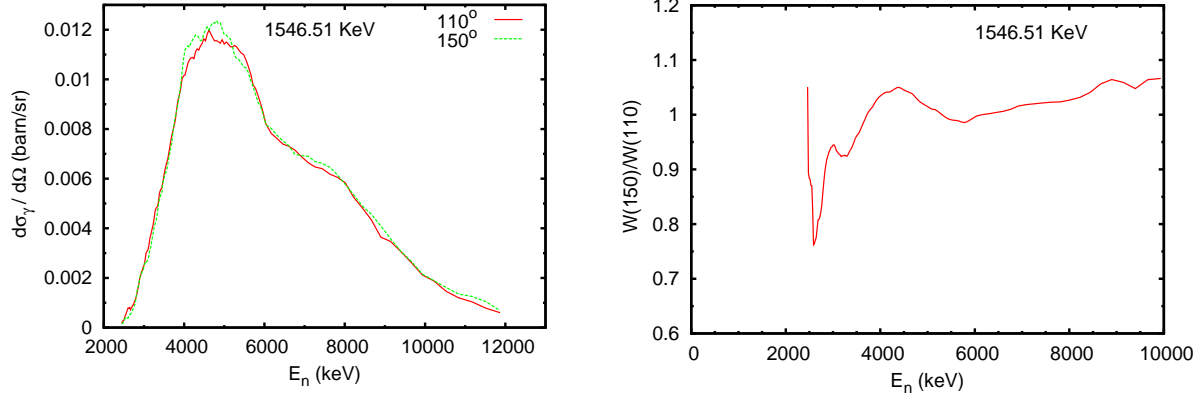


Figure 5.24: Differential gamma production cross-section for the 1546.51 keV transition in ^{209}Bi . *Left:* Smoothed curves from the threshold up to 12 MeV at two angles, 110 and 150 degrees. *Right:* The ratio between the angular distribution $W(\theta)$ at 150 and 110 degrees.

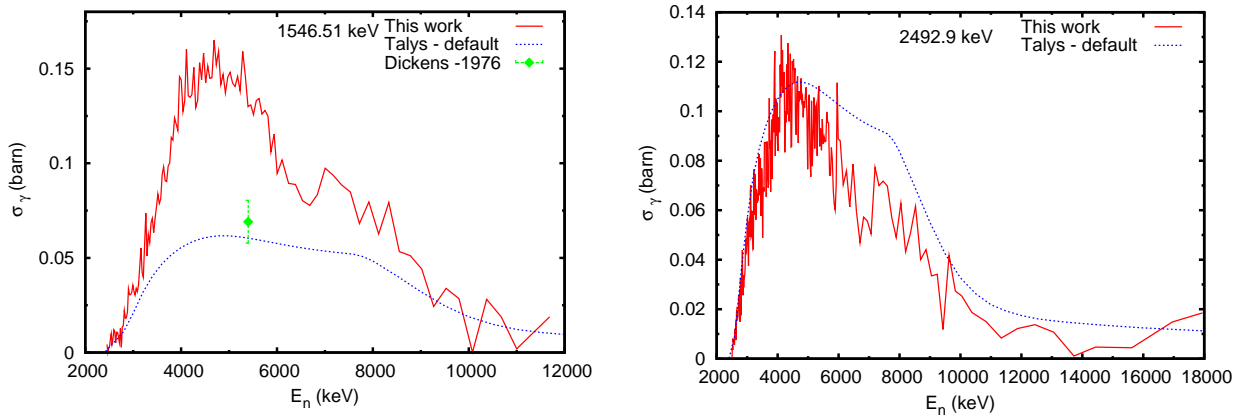


Figure 5.25: The integral gamma production cross-section for the 1546.51 keV and 2492.9 keV transitions in ^{209}Bi with the full neutron energy resolution. The measurement of the 1546.51 keV was limited to 12 MeV because of the small counting rate at this energies.

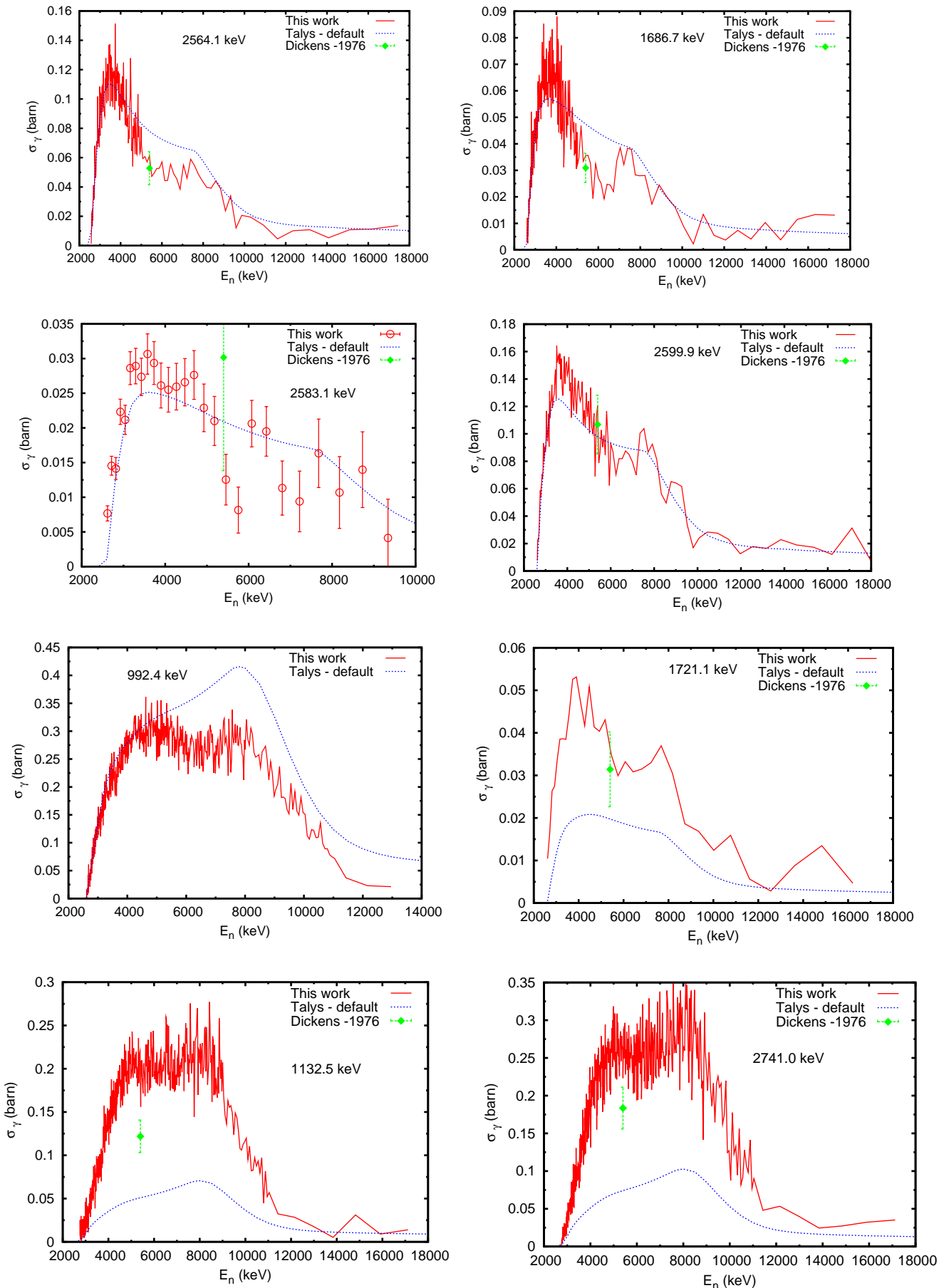


Figure 5.26: Integral gamma production cross-section for the transitions from higher lying levels in ^{209}Bi

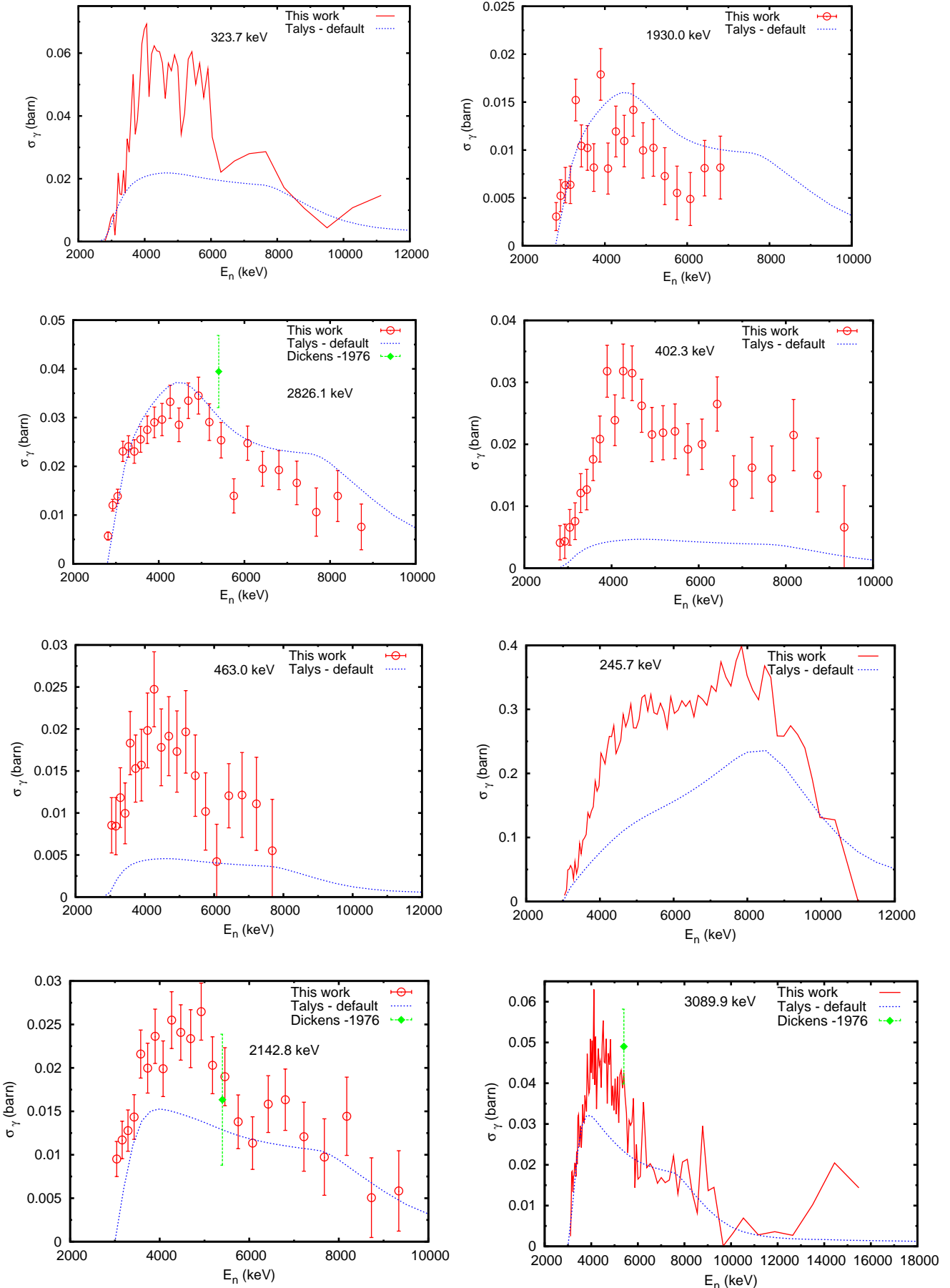


Figure 5.27: Integral gamma production cross-section for the transitions from higher lying levels in ^{209}Bi

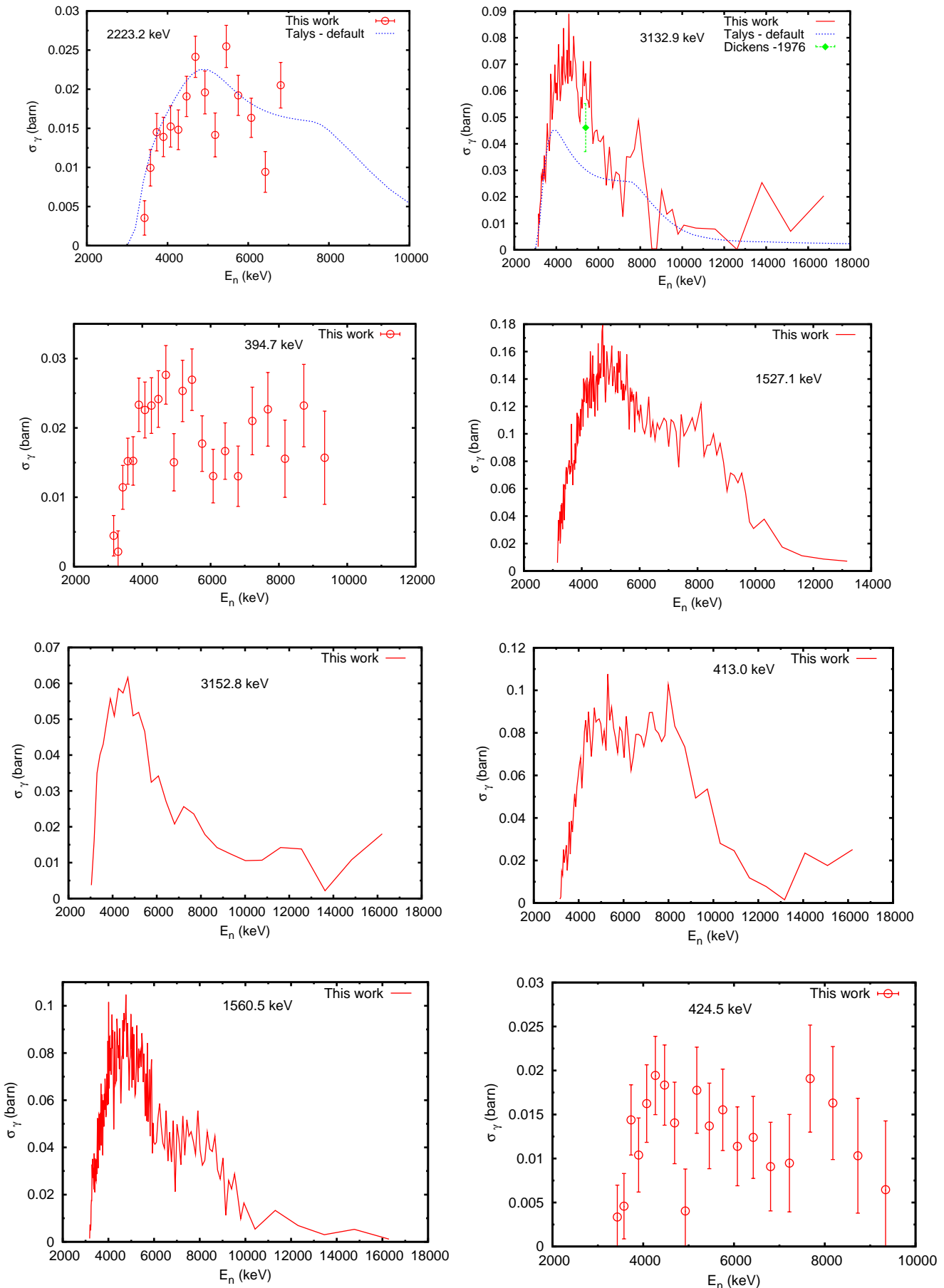


Figure 5.28: Integral gamma production cross-section for the transitions from higher lying levels in ^{209}Bi

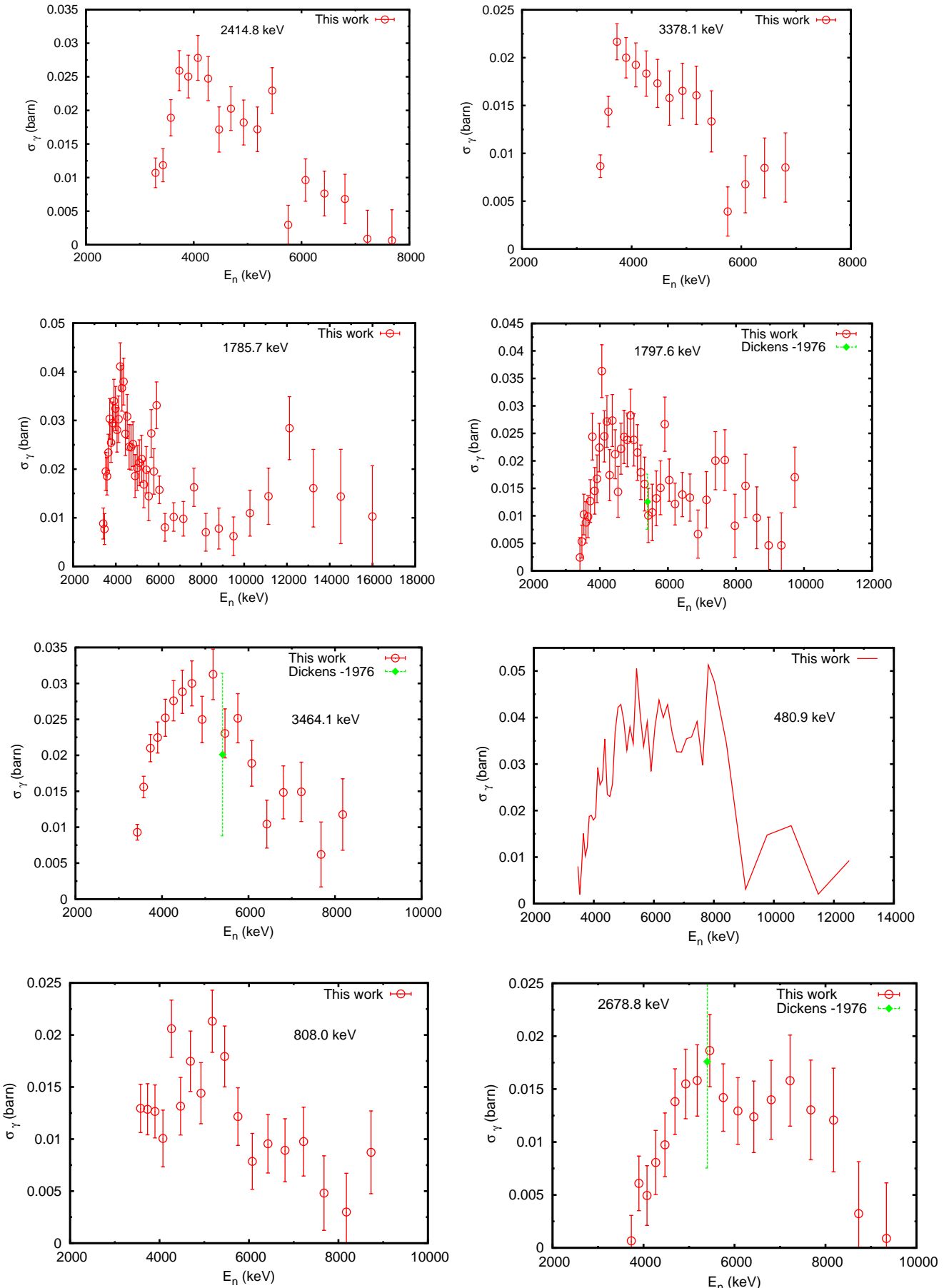


Figure 5.29: Integral gamma production cross-section for the transitions from higher lying levels in ^{209}Bi

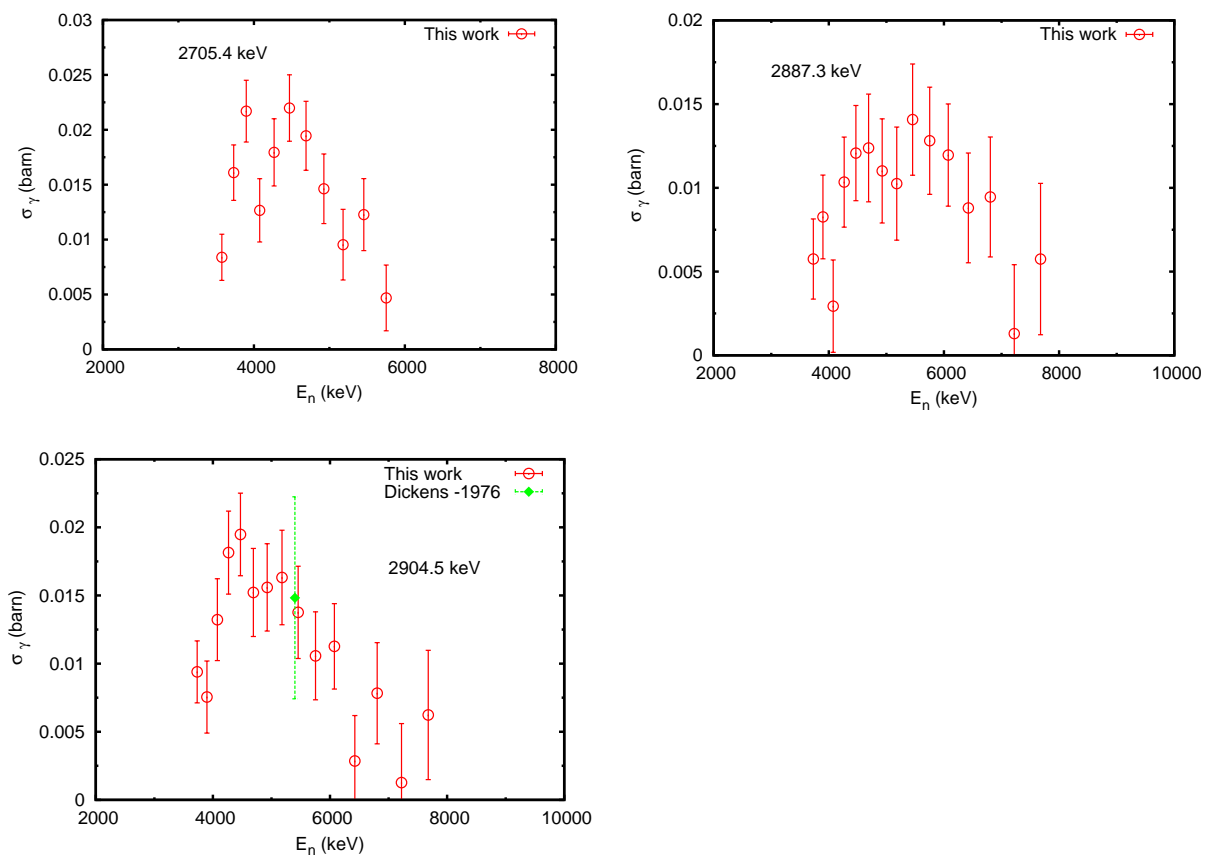


Figure 5.30: Integral gamma production cross-section for the transitions from higher lying levels in ^{209}Bi

observed have energies of 1930.95 keV and 2887.3 keV. These γ -rays have a maximum cross-section of about 15 mb around 4 MeV. Low neutron energy resolution was used in order to achieve a total uncertainty of about 30%. Because of their small cross-sections these transitions were measured only up to 8 MeV. For these transitions point-like data were used in the graphs. The most intense transitions from the higher lying levels have the energies of 992.4 keV and 2741.0 keV. In the maximum, these transitions reach a cross-section of about 300 mb, almost a factor three less than the cross-section of the 1608.53 keV transition.

In the present measurement some difficulties arose for the transitions from the very close lying levels at 2599.90 keV and at 2600.92 keV (see Fig. 5.18). The level at 2599.90 keV decays through a γ -ray of 2599.90 keV to the ground state and through a 991 keV γ -ray to the level at 1608.58 keV. From the evaluated level scheme, the intensity of the 991 keV transition is smaller than 4.5% from the intensity of the 2599.90 keV transition. The level at 2600.92 keV decays through the transitions of 992.35 keV and 2600.92 keV. The latter one is only 1.3% from the intensity of the 992.35 keV transition. Because of the small branching ratios of the 991 keV and 2600.92 keV transitions, it was assumed that in the present measurement the observed peaks in the γ -ray spectra are due to the transitions at 992.35 keV and respectively 2599.90 keV. In conclusion, the gamma-production cross-sections given in Fig. 5.26 for the 992.35 keV and 2599.90 keV transitions contain negligible contributions from the 2600.92 keV and respectively the 991 keV transitions.

Gamma production cross-sections calculated with the Talys code were available for the transitions that decay from levels up to 3.13 MeV excitation energy. In general, the Talys calculation provides good description of the experimental data at low energies, below about 4 MeV. This general good agreement for the gamma production cross-section at low energies is reflected in a reasonable description of the level cross-section (see below).

On the full energy range, the Talys calculation with the default parameters describes reasonable the measured data for transitions as 2492.9 keV, 2564.1 keV, 1686.7 keV, 2583.1 keV, 2599.9 keV, 2826.1 keV, 1929.95 keV and 2223.2 keV. In the case of the 992.4 keV transitions, Talys calculations overestimate the experimental data above 5 MeV. For the other transitions the Talys calculation predicts significantly lower cross-sections. It should be noted that for the transition from the level at 2741 keV (1132.5 keV and 2741 keV) the calculation is lower than the measured data even just above the threshold (see Fig. 5.26).

Where available, the measured points of Dickens *et al.* [161] at 5.4 MeV agree generally well with the present data. For the 1132.5 keV and 2741 keV transitions (Fig. 5.26) the Dickens *et al.* data are lower than the present values.

Branching ratios

In the case of 5 excited levels of ^{209}Bi , two γ -rays from the decay of each level were observed (Table. 5.1). These allowed the determination of the corresponding branching ratios of the levels. For every level, the branching ratios were determined from the integral cross-sections of the two transitions over the full neutron energy

Table 5.1: Branching ratios for levels in ^{209}Bi nucleus and the corresponding absolute uncertainties. The present results are compared with the values from the evaluated level scheme.

E_{level} (keV)	E_γ	Present results		ENSDF	
		Intensity	Uncertainty	Intensity	Uncertainty
2583.07	1686.66	100	-	100.0	1.3
	2583.1	46.8	1.8	44.1	1.3
2741.05	1132.46	77.1	3.5	67.8	0.6
	2741.03	100	-	100.0	0.6
2826.19	1929.95	37.1	1.9	43	5
	2826.10	100	-	100.0	1.2
3135.77	394.72	17.5	2.3	10.4	0.4
	1527.13	100	-	100	2.1
3575.00	808.0	100	-	100	40
	2678.8	112.7	7.2	58	4

interval. Integrating over a large neutron energy interval the statistical uncertainty was reduced. For additional check, the branching ratio as a function of the neutron energy was found to be constant within the statistical fluctuations. The observed threshold for every of these transitions was the same as the calculated one. These represent additional support in the γ -ray identification.

The new values of the branching ratios were compared in Table 5.1 with the values from the evaluated level scheme *et al.* [131]. Within the uncertainties the branching ratios for the levels at 2583.07 keV and 2826.19 keV agree with the evaluated values from Ref. [131] (see Table 5.1). Higher intensities were found for the γ -rays of 394.72 keV, 1132.46 keV and 2678.8 keV. Moreover, the intensity of the 2678.8 keV transition was found to be higher than the intensity of the 808.0 keV.

Using the new value for the branching ratio 1132.46 keV transition in the Talys calculation would not improve significantly the agreement between the calculation and the measurement (Fig. 5.26). As mentioned in the section above, the calculation underestimates the measurements with about a factor 4 in the middle energy range, while the new value of the branching ratio is higher only with about a factor 0.14.

$(n,2n)$ gamma production cross-sections

For an easier identification of the gamma rays from the $(n,2n)$ reaction channel on ^{208}Bi , the amplitude spectrum of the HPGe detectors was constructed integrating the neutron energies from 7.4 MeV up to 25 MeV (Fig. 5.32); the $(n,2n)$ threshold is 7.495 MeV. The main γ -ray peaks from the $^{209}\text{Bi}(n,2n)^{208}\text{Bi}$ reaction are clearly visible. The γ -rays that decay from the first and second excited levels were not observed in this experiment (Fig. 5.31). The 63.5 keV transition from the first excited level in ^{208}Bi to the ground state has a very low energy, below the physical thresholds in the electronic setup. This transition is also internally converted ($\alpha =$

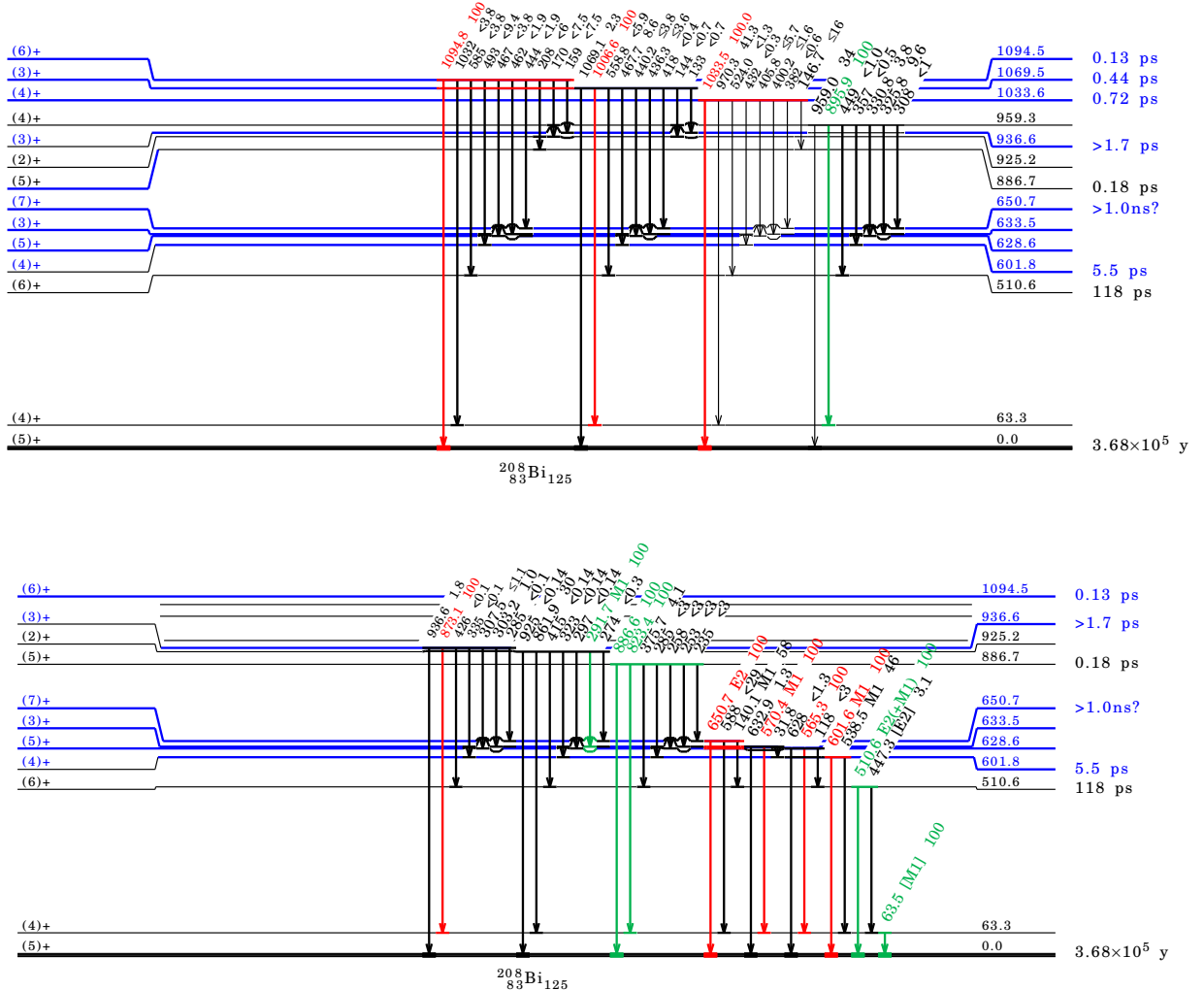


Figure 5.31: Simplified level scheme of ^{208}Bi *et al.* [131]. The gamma production cross-section of the transitions drawn in "red" was measured in the present experiment. The γ -rays drawn in "green" have intensity 100 and were not observed because of their low energy or because of the increased background around these peaks.

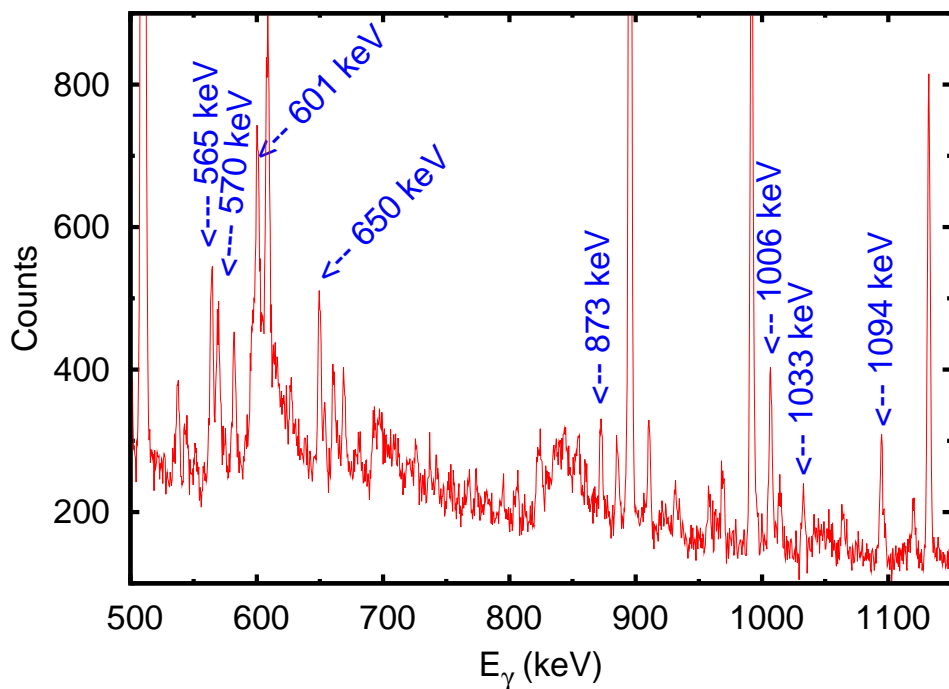


Figure 5.32: The $(n,2n)$ γ -ray spectrum of an HPGe detector with the ^{209}Bi sample. The spectrum was integrated over the neutron energies from 7.4 MeV (just below the $(n,2n)$ threshold) up to about 25 MeV. The main γ -ray peaks from the $^{209}\text{Bi}(n,2n)^{208}\text{Bi}$ reaction are clearly visible.

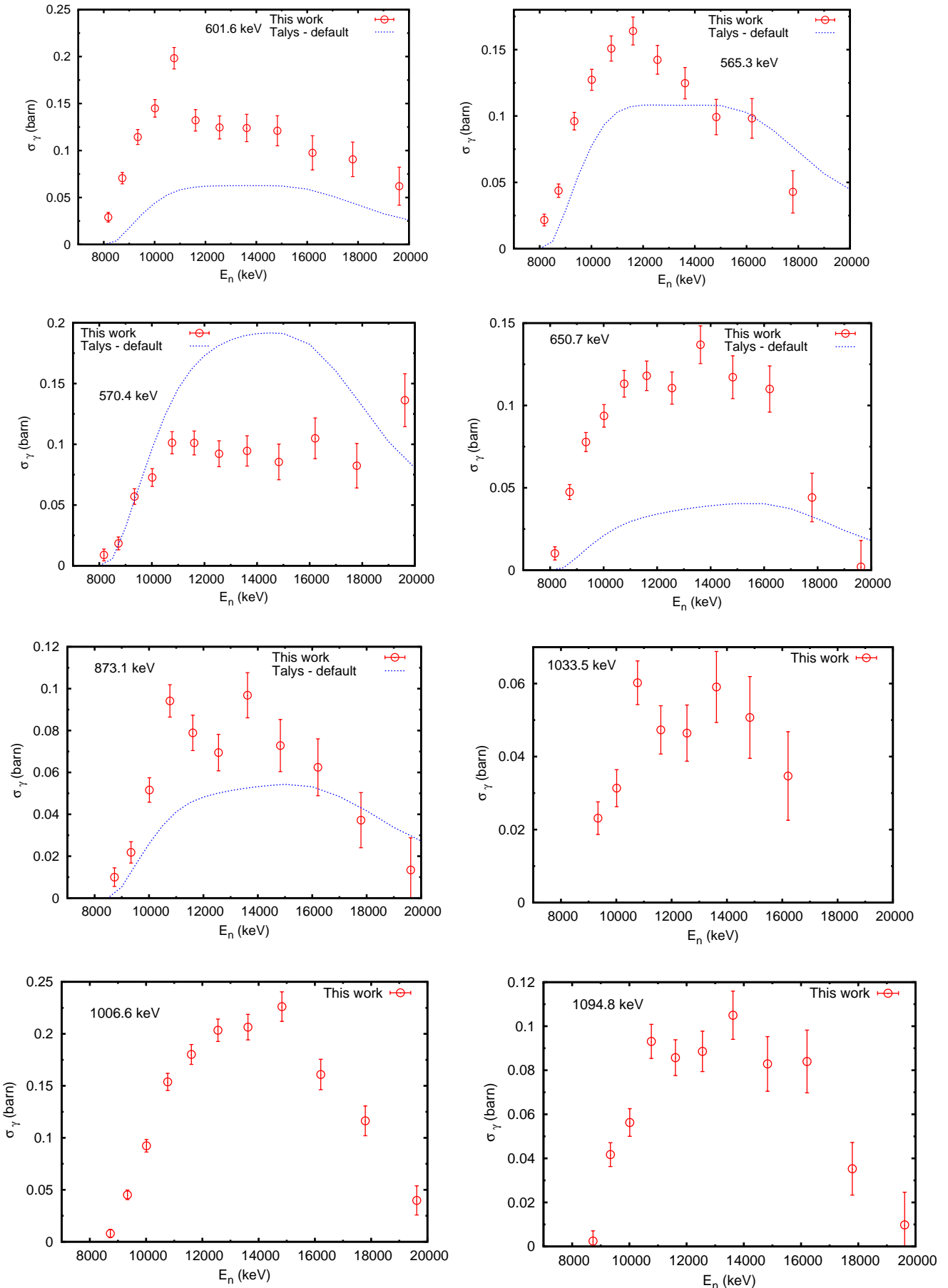


Figure 5.33: Integral gamma production cross-section for the transitions from the $^{209}\text{Bi}(n,2n)^{208}\text{Bi}$ reaction.

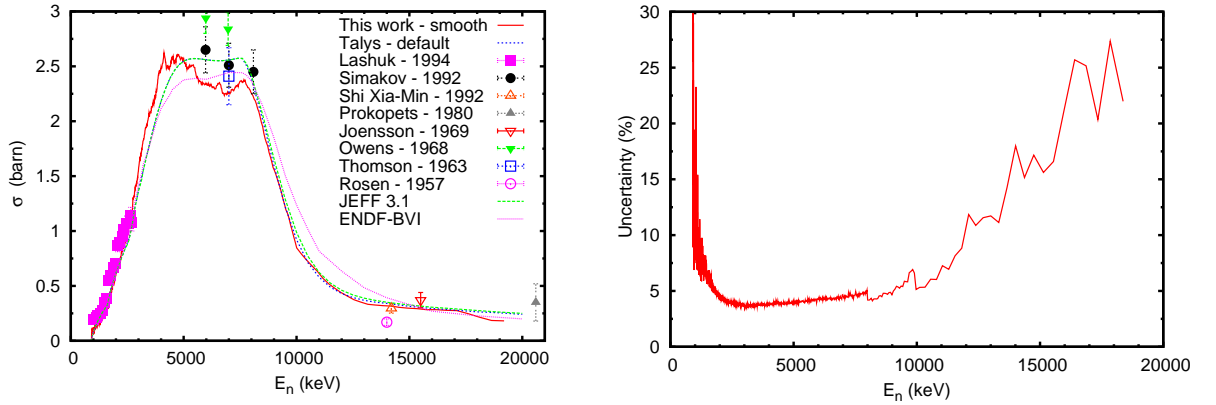


Figure 5.34: *Left:* Smooth curve for the total inelastic gamma production cross-section of ^{209}Bi from the threshold up to 20 MeV. *Right:* The corresponding total uncertainty.

7.52 Ref. [131]). The second excited level decays through a 510.6 keV γ -ray that cannot be distinguished from the 511 keV transition of the background.

Starting from the third excited level, the gamma production cross-section of 8 γ -rays from the $^{209}\text{Bi}(n,2n)^{208}\text{Bi}$ reaction were measured for the first time, from the threshold up to 20 MeV. The measured cross-sections are given in Fig. 5.33. A neutron energy resolution of 0.55 MeV at 9 MeV up to 1.8 MeV at 20 MeV was used.

The transition of 895.9 keV from the decay of the level at 959.3 keV was not identified in the spectrum because it has the same energy as the main transition in the inelastic channel. From the cross-sections of the neighboring transitions 873.1 keV and 1033.5 keV and the Talys calculation it can be estimated that the 895.9 keV transition has a maximum cross-section of about 35 mb at 12 MeV. This may produce an overestimation of the measured gamma production cross-sections of the 896.28 keV transition from the inelastic channel with about 50% around 15 MeV (Fig. 5.20). The $^{209}\text{Bi}(n,2n)^{208}\text{Bi}$ gamma production cross-section presented here were not corrected for the neutron attenuation and multiple scattering. For the $(n,2n)$ cross-sections the multiple scattering is expected to be negligible and the attenuation correction with the ^{209}Bi sample is of the order of 1.5 %-2 %.

From Fig. 5.33, the agreement of the default calculation of the Talys code with the experimental data is very poor. Differences of a factor 3 can be observed between the calculation and the experimental data.

5.2.3 Total inelastic and level cross-section

Total neutron inelastic cross-section

The total inelastic cross-section (Fig. 5.34) was constructed based on the evaluated level scheme of ^{209}Bi using the integral gamma production cross-sections. The following transitions were used for the total inelastic cross-section (see also Fig. 5.18): 896.28 keV, 1608.53 keV, 2492.9 keV, 2564.1 keV, 1686.7 keV, 2599.9 keV,

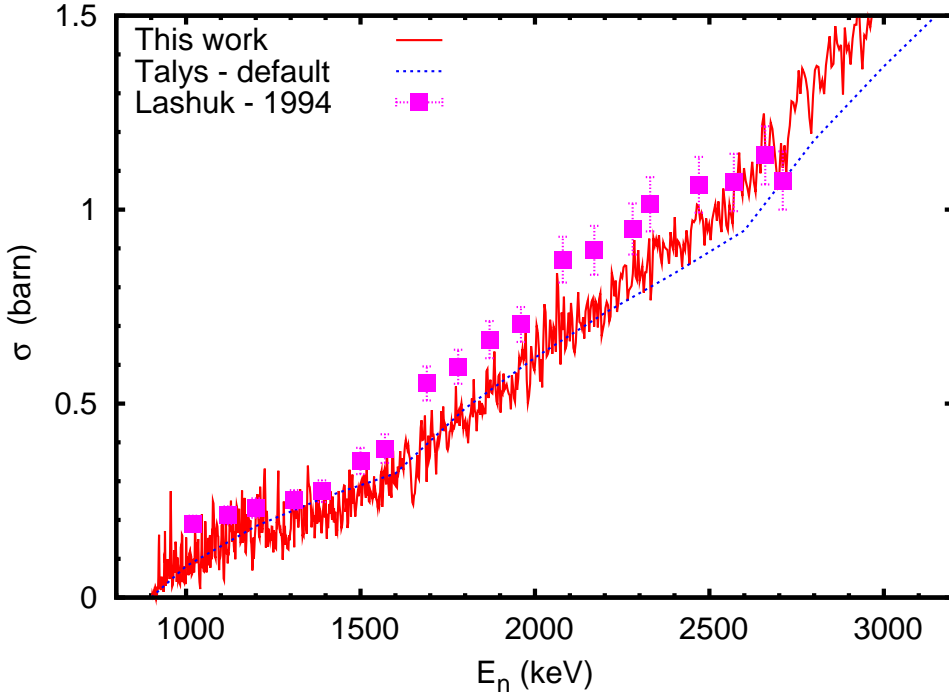


Figure 5.35: High resolution data for the total inelastic gamma production cross-section of ^{209}Bi .

992.4 keV, 1721.1 keV, 1132.5 keV, 323.74 keV, 2826.1 keV, 3089.9 keV, 3132.9 keV and 3152.8 keV. Using these transitions, the total inelastic cross-section given here (Fig. 5.34) is exact up to 3.3 MeV neutron energy and above this energy has to be considered a lower limit.

The relative total uncertainty of the total inelastic cross-section is given in Fig. 5.34. It has high values just above the inelastic threshold and at high energies. This is due to the poor statistics at these energies. In the middle energy range, the total uncertainty is less than 5 %.

Figs. 5.34 and 5.35 shows the comparison between the present results for the total inelastic cross-section and the existing data from the literature. Below 2.7 MeV the data of Lashuk *et al.* [130] agree well with the present values. Four different measurements were found in the databases between 14 MeV and 21 MeV. The data of Shi Xia Min *et al.* [130], Joensson *et al.* [130], Prokopets *et al.* [130] agree well with the present measurement. The point data of Rosen *et al.* [130] is lower than the present data.

Around 7 MeV neutron energy, all the existing measurements (Simakov *et al.* [130], Owens *et al.* [114] and Thomson *et al.* [141]) give higher values for the total inelastic cross-section than the present experiment. In the present experiment the contribution to the total inelastic cross-section of all the transitions that decay directly to the ground state from levels with an energy higher than 3.3 MeV was neglected. In ^{209}Bi such transitions may have a non-negligible contribution. Moreover, in the ^{209}Bi nucleus it was found (Ref. [132]) that there is a strength concentration around 6 MeV, that decay with a significant branching ratio directly to the ground state.

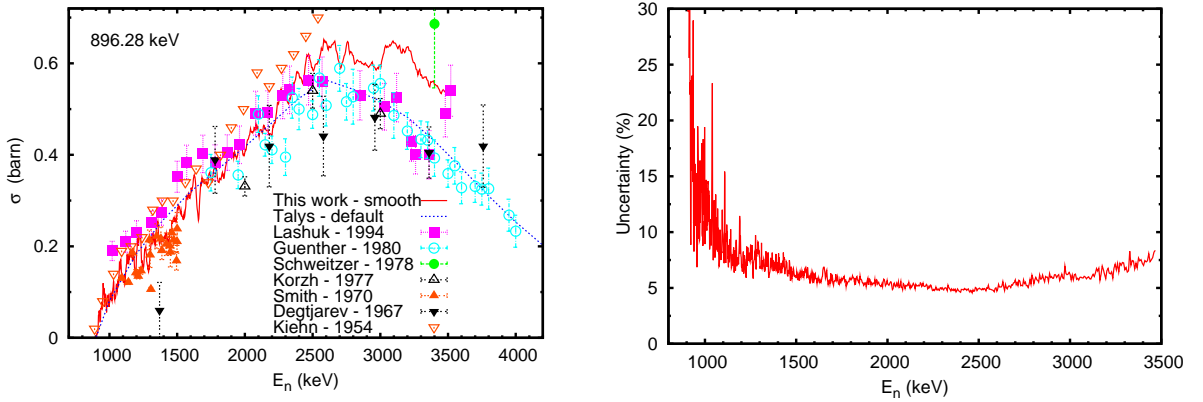


Figure 5.36: *Left:* Cross-section of 896.29 keV excited level in ^{209}Bi . *Right:* The corresponding total uncertainty.

Such transitions, that were not observed in the present experiment, may increase the present total inelastic cross-section around 6 MeV. All the existing measurements around 7 MeV used the (n,n')-technique, that is not sensitive to the missed γ -ray transitions.

The Talys calculation describes well the total inelastic cross-section at energies below 3 MeV and at energies above 7 MeV. Between 3 MeV and 5 MeV the Talys calculation underestimates the present data. This is in contradiction with the fact that the present data for the total inelastic cross-section are a lower limit above 3.3 MeV. Between 5 MeV and 7 MeV the Talys calculation is higher than the present measurements and is in a better agreement with the Simakov *et al.* [130] results.

The evaluated total inelastic cross-sections from ENDF/B-VI and JEFF 3.1 are shown in Fig. 5.34. The JEFF 3.1 evaluation coincides with the default Talys calculation. The ENDF/B-VI evaluation differs from the JEFF 3.1 evaluation for the energies between about 4 MeV and 8 MeV. In this region, the ENDF/B-VI evaluation is lower.

Level 896.29 keV

The following γ -rays were used to construct the cross-section of the level at 896.29 keV: 896.28 keV, 1546.51 keV, 1686.7 keV, 1721.1 keV, 1929.95 keV, 2142.8 keV, 3089.9 keV and 1785.7 keV. The obtained results are shown in Fig. 5.36. This cross-section is exact up to 3.1 MeV neutron energy. In the energy region 3.1 MeV and 3.5 MeV the cross-section presented here is an upper limit to the exact value. This limit is a very good approximation to the exact value because only 2 very weak transitions were neglected. The total uncertainty for the 896 keV level cross-section is given in Fig. 5.36 *Right* and ranges between 15% just above the inelastic threshold and about 7% at 3.5 MeV.

Below 2.5 MeV, the present results for the cross-section of the level at 896.28 keV are between the scattered values given by different experiments found in the liter-

ature (Fig. 5.36). Above 2.5 MeV the present results are higher than the values given by Guenther *et al.* [108] experiment. The Guenther *et al.* experiment used the (n,n')-technique and its data were normalized to the H(n,n) standard cross-section. The level cross-section were the primary measured quantities in the Guenther *et al.* experiment. Still, the difference between the two data sets is too large to be explained by the fact that above 3.1 MeV the present data are an upper limit for the level cross-section. Anyway, the existing data around 3.5 MeV (Lashuk *et al.*, Schweitzer *et al.* and Guenther *et al.*) are very scattered.

The default Talys calculation describes well the present data up to about 2.5 MeV. Above this energy, the calculation follows the Guenther *et al.* [108] data. The JEFF 3.1 evaluated level cross-section is not plotted in Fig. 5.36 because it coincides with the default Talys calculation.

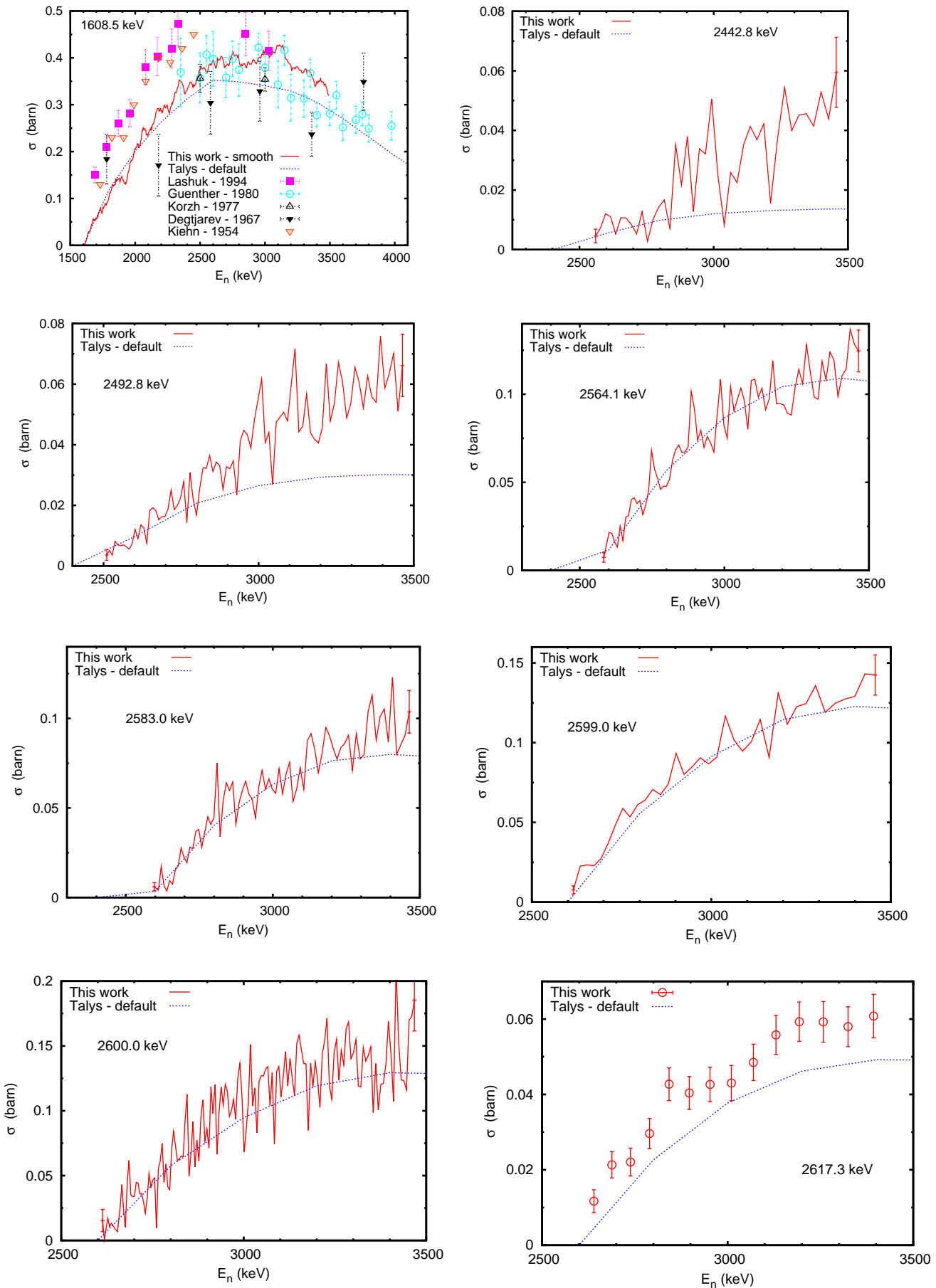
Levels with higher excitation energy

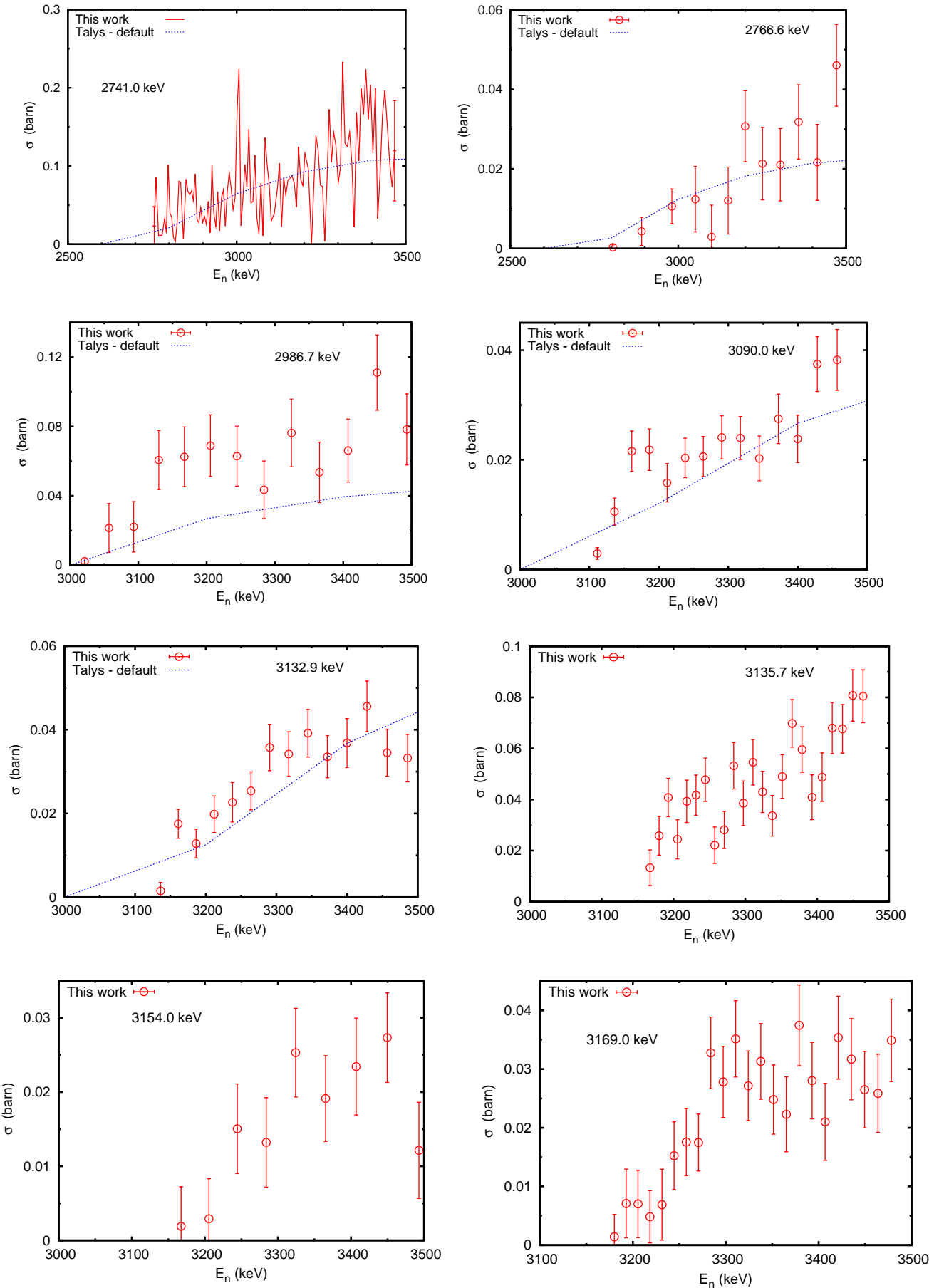
The cross-sections of the other excited levels up to 3.16 MeV excitation energy are shown in Figs. 5.37 and 5.38. Except for the second excited level, at 1608.5 keV, no experimental cross-sections were found for the other levels. In the case of the 1608.5 keV level, the data presented here, Fig. 5.37, are exact up to 3.5 MeV. All the transitions that feed the 1608.5 keV up to an excitation energy of 3.4 MeV were used to construct the level cross-section of this level.

For the level at 1608.5 keV, the data of Lashuk *et al.* [130] and Kiehn *et al.* [145] are higher than the present results. Contrary, the data of Guenther *et al.* [108] above 2.3 MeV are slightly lower than the present data as in the case of the 896.28 keV level. The Talys calculation follows the Guenther *et al.* data above 2.3 MeV.

For the other excited level given in Figs. 5.37 and 5.38, the Talys calculation was available for excitation energies up to 3132 keV. Where available, the Talys calculation with the default parameters describes relatively well the level cross-sections below 3.15 MeV. This agreement was expected already from the comparison of the gamma production cross-section with the Talys calculation. In both cases, level cross-sections and gamma production cross-sections, the agreement with the Talys calculation is generally good at low energies.

Above 3.15 MeV, the calculation is lower for levels as 2442.8 keV, 2492.8 keV and 2617.3 keV. Of course, above the 3.1 MeV neutron energy, the present results for the level cross-section may be affected by the excited levels that were not observed here. Above 3154 keV, some excited levels were not observed in the present measurement. The difference with the Talys calculation may be consistent with the fact that the feeding from some levels above 3154 keV excitation energy was neglected. It should be noted that in the case of the ^{209}Bi , the JEFF 3.1 evaluation of the level cross-section coincides with the Talys calculation with the default input parameters. Therefore the JEFF 3.1 evaluation was not plotted here for the level cross-sections as in the case of the ^{52}Cr nucleus.

Figure 5.37: Cross-section of levels with higher excited energy in ^{209}Bi .

Figure 5.38: Cross-section of levels with higher excited energy in ^{209}Bi .

5.2.4 Conclusions

The neutron inelastic and $(n,2n)$ gamma production cross-sections of ^{209}Bi were measured with an unprecedented neutron energy resolution and total uncertainty. Many of these gamma production cross-sections were measured for the first time; only the inelastic cross-sections of the 896.28 keV and 1608.53 keV had been measured and only at energies below 5 MeV. No gamma production cross-section data were found in the literature for the $^{209}\text{Bi}(n,2n)^{208}\text{Bi}$ reaction. In the present experiment, the gamma production cross-sections were measured for 39 inelastic γ -rays and for 8 γ -rays from the $(n,2n)$ reaction. Neutron energy resolutions of 1.12 keV at 1 MeV up to 35 keV at 10 MeV were obtained for the main transitions and for the total inelastic scattering cross-sections. In the ^{209}Bi nucleus, no clear resonance structure were observed in the inelastic cross-sections at low neutron energies, just above the inelastic threshold. For the $(n,2n)$ transitions, a neutron energy resolution of 0.55 MeV at 9 MeV up to 1.8 MeV at 20 MeV was used. With this resolution, the present experiment covered the full energy range from the threshold up to about 20 MeV in only one run avoiding systematic errors.

Using the evaluated level scheme of ^{209}Bi and the gamma production cross-sections, the total inelastic cross-section was obtained from the threshold up to about 20 MeV. The total inelastic cross-section presented here is exact up to 3.3 MeV and is a lower limit above this energy. The cross-sections of the excited level were constructed from the thresholds up to about 3.5 MeV.

The present results were compared with the available experimental data from the databases and with the Talys calculation with the default parameters. Relatively good agreement was found with the few existing experimental data. The Talys calculation with the default input parameters describes well the gamma production cross-section and the level cross-sections at energies below 3.1 MeV. Above this energy, the Talys calculation describes relatively well the 1608.53 keV transition in ^{209}Bi but not the first transition that is underestimated (these two transitions have comparable cross-sections). In general, for the rest of the transitions the agreement is rather poor. The total inelastic cross-section calculated with Talys agree well with the present measurement at below 3 MeV and above 7 MeV. Clear differences are visible in the intermediate energy region. Further tuning of the code parameters may be possible, starting from the description of the gamma production cross-section on the full energy range. The gamma production cross-sections are the primary measured quantities and are not affected by the excited levels that were not observed in this experiment.

The present measurement with the ^{209}Bi sample produced a large amount of precise neutron inelastic and $(n,2n)$ cross-sections. These new data can be used in the new evaluations of the neutron cross-sections and as benchmark for the nuclear codes.

5.3 ^{206}Pb neutron inelastic scattering and (n,2n) cross-sections

5.3.1 Introduction

The neutron inelastic scattering cross-sections on ^{206}Pb had been measured using both the (n,n')-technique and the (n,n' γ)-technique. With the first technique (Refs. [134, 139–141, 143, 148]) the measurements were done at few energies between 2 MeV and 8 MeV with best neutron energy resolution of 30 keV. The majority of these experiments measured only the differential cross-sections for few excited levels. The experiments presented in Refs. [135, 142, 145, 147, 149] used the (n,n' γ)-technique. Except Refs. [135, 147] where Ge(Li) detectors were used for the γ -ray detection, the other experiments used NaI detectors. Most of the previous experiments used radiogenic samples with only about 88% of ^{206}Pb .

For the ^{206}Pb nucleus, there are two major limitations in the use of the (n,n' γ) technique. The first one is the presence of an E0 transition from the second excited level at 1165 keV with the spin and parity 0^+ (Fig. 5.39). This transition is fully converted internally and is not observed by the HPGe detectors. The second limitation is represented by the existence of an isomer at 2200.14 keV with a life time of 125 μs . The γ -rays from the decay of this isomer (516.18 keV and 202.44 keV) are delayed and not observed in the prompt spectrum. Because the life time of this level is 10 times smaller than the time interval between two consecutive neutron bursts, the level decays almost completely between two bursts. Therefore the isomer level does not spoil the neutron energy resolution of the γ -rays that are fed by the γ -rays from the isomer. In practice, no measurable yield was detected below the inelastic threshold of the 880.98 keV γ -ray that is fed by the 516.18 keV γ -ray from the isomer (Fig. 5.39).

In the present measurement at least one γ -ray was observed from the decay of the levels up to 2196.7 keV (see Fig. 5.39). Above this excitation energy, some levels were not observed. The maximum energy of an observed level was 3562.84 keV. In total, the gamma production cross-section was measured for 23 γ -rays from the threshold up to about 20 MeV neutron energy. The γ -ray peak at 1588 keV is due to two different transitions in ^{206}Pb , emitted from the levels at 2391.32 keV and 2929.06 keV. Therefore, the measured gamma-production cross-section presented here is the sum of the two gamma production cross-sections.

The only (n,2n) cross-sections measurements on ^{206}Pb were performed using the activation technique (Ref. [137]). Such measurements provide only the total (n,2n) cross-sections. In the present experiment, two γ -rays from the $^{206}\text{Pb}(n,2n)^{205}\text{Pb}$ reaction were observed: 573.88 keV and 703.44 keV. No γ -rays from the first two excited levels of the ^{205}Pb nucleus were observed because of their low energy.

5.3.2 Gamma production cross-sections

Fig. 5.40 shows an example of the amplitude spectrum obtained with the HPGe detectors and the ^{206}Pb sample. The main peaks from the $^{206}\text{Pb}(n,n'\gamma)^{206}\text{Pb}$ reaction

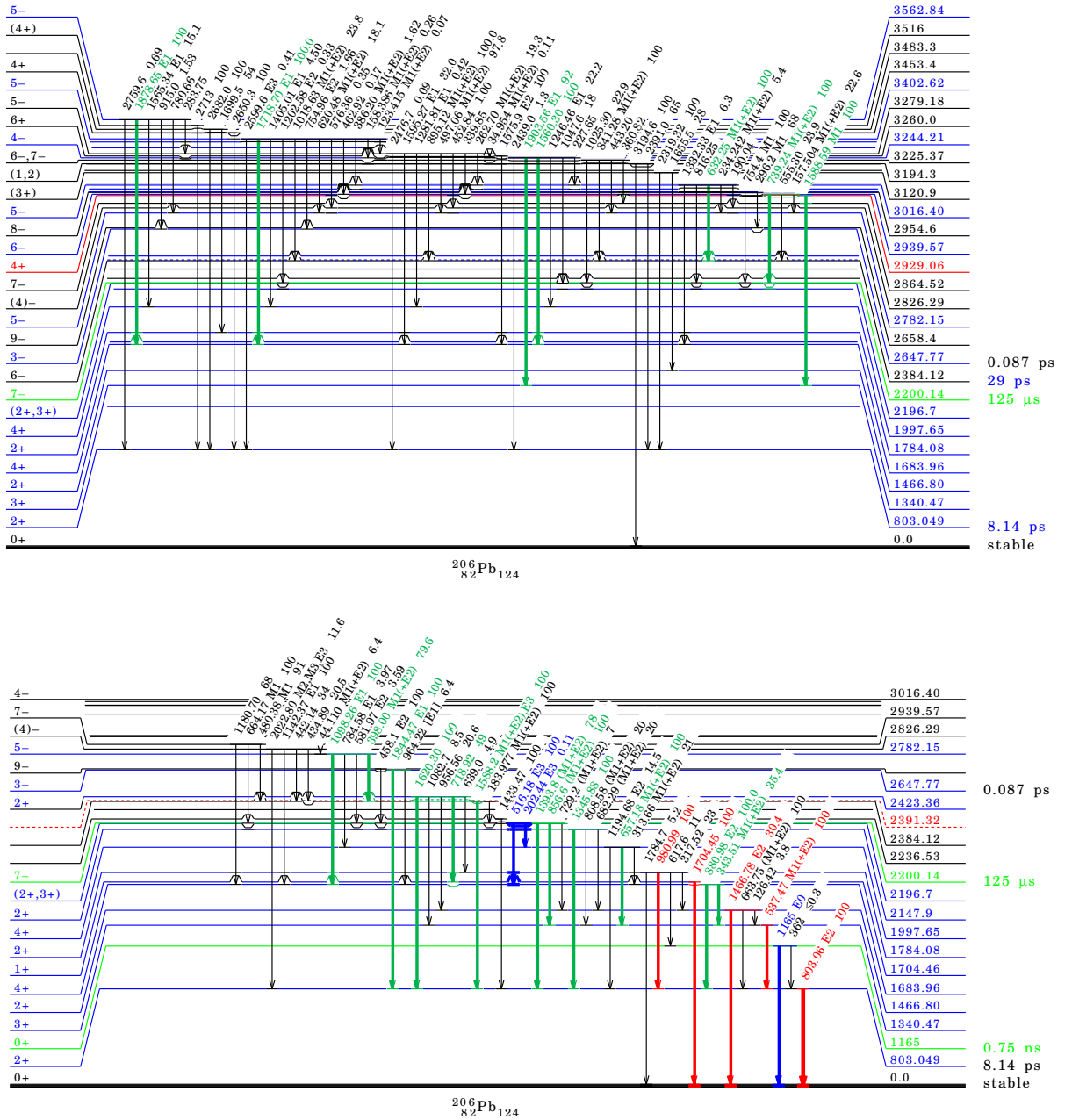


Figure 5.39: Simplified level scheme of ^{206}Pb *et al.* [131]. The gamma production cross-section of the transitions drawn with colors was measured in the present experiment. The "red" γ -rays were used to construct the total inelastic cross-section. The excited levels drawn with black were not observed. The two levels at 2391.32 keV and at 2929.06 keV decay through γ -rays of about same energy: 1588.2 keV and 1588.59 keV (see the text for details).

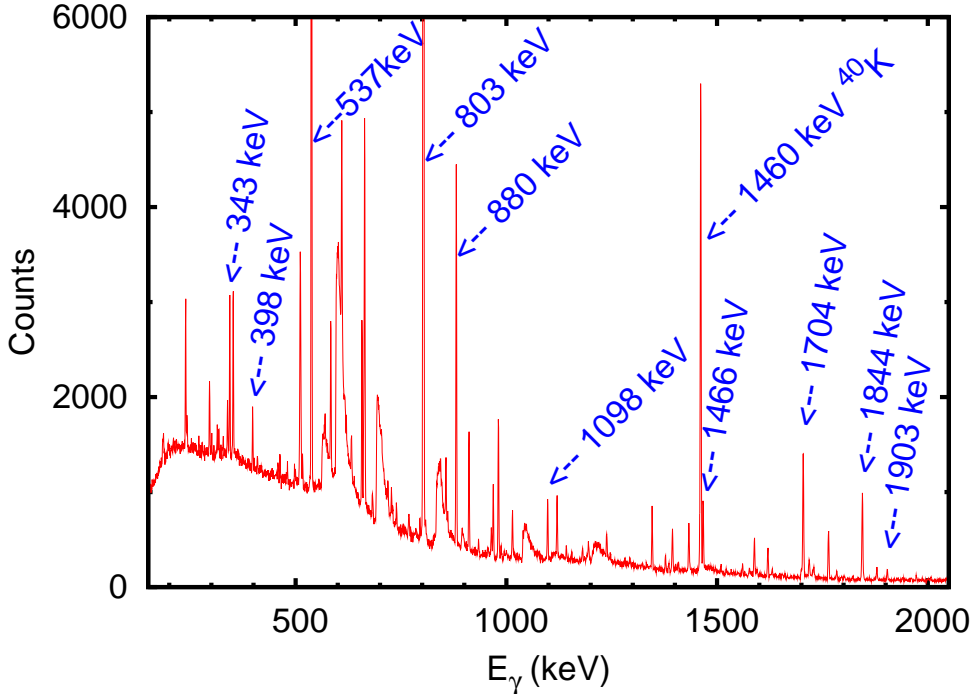


Figure 5.40: The γ -ray spectrum of a HPGe detector with the ^{206}Pb sample (99.8% enrichment). The spectrum was integrated over the neutron energies from 800 keV up to about 25 MeV. The main γ -ray peaks from the inelastic scattering on the ^{206}Pb sample are clearly visible.

are marked. The integral gamma production cross-sections of the observed γ -ray will be presented in the following. For the two most intense transitions the differential gamma-productions are shown as well.

803.06 keV

In the ^{206}Pb nucleus the transition from the first excited level to the ground state is by far the most intense in the spectrum. As in all other even-even nuclei that we studied, the majority of the excited states decay through the first excited level. For these nuclei, the gamma production cross-section of the main transition is a good approximation for the total inelastic cross-section.

The 803.06 keV γ -ray is an E2 transition from the initial level 2^+ to the ground state 0^+ . A clear angle dependence of the differential gamma production cross-section was observed (Fig. 5.41). The ratio between the angular distribution $W(\theta)$ ($W(\theta) = \frac{4\pi}{\sigma} \frac{d\sigma}{d\Omega}(\theta)$) at 150° and 110° has its maximum just above the inelastic threshold and it decreases at higher energies. From the Eq. 2.17, the value for this ratio at the threshold is 1.61, which is in a good agreement with the experimental value.

As in the case of the ^{52}Cr nucleus, well defined resonance structures were observed for ^{206}Pb . The resonance structures in the differential and the integral gamma production cross-sections are shown in Fig. 5.42. The observation of these resonances was possible due to the very good neutron energy resolution of 1.1 keV at 1 MeV of

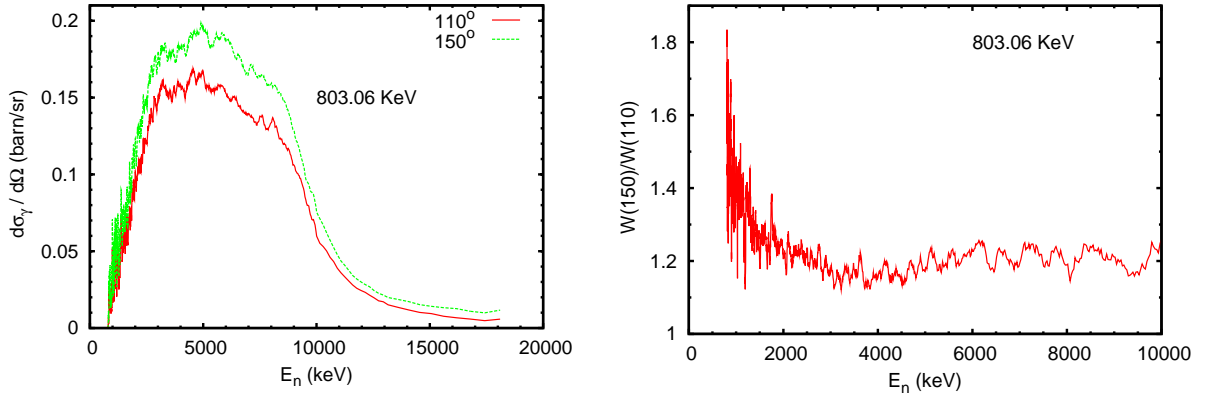


Figure 5.41: Differential gamma production cross-section for the 803.06 keV transition in ^{206}Pb . *Left:* Smoothed curves from the threshold up to 20 MeV at two angles, 110 and 150 degrees. *Right:* The ratio between the angular distribution $W(\theta) = \frac{4\pi}{\sigma} \frac{d\sigma}{d\Omega}(\theta)$ at 150 and 110 degrees.

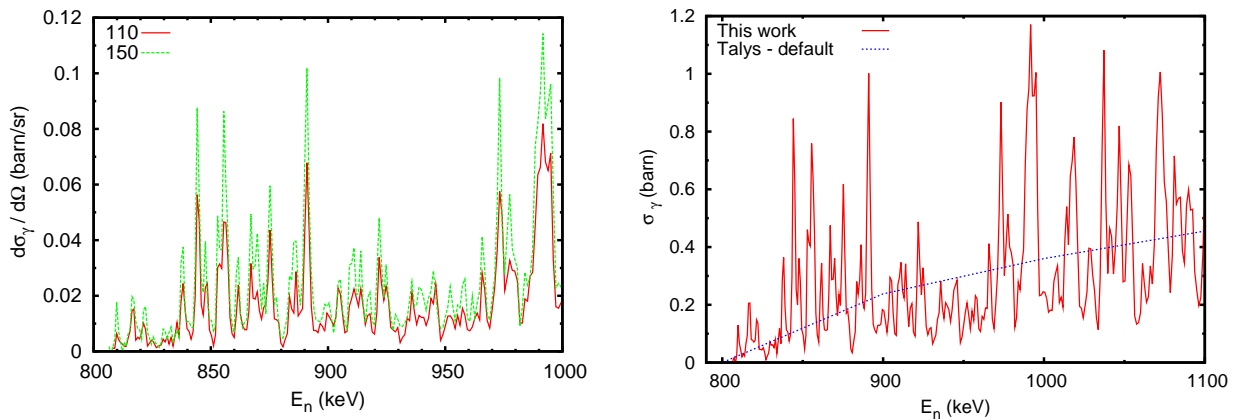


Figure 5.42: Full resolution gamma production cross-section for the 803.06 keV transition in ^{206}Pb . *Left:* Differential gamma production cross-section at 110° and 150° . *Right:* Integral gamma production cross-section compared with Talys calculation.

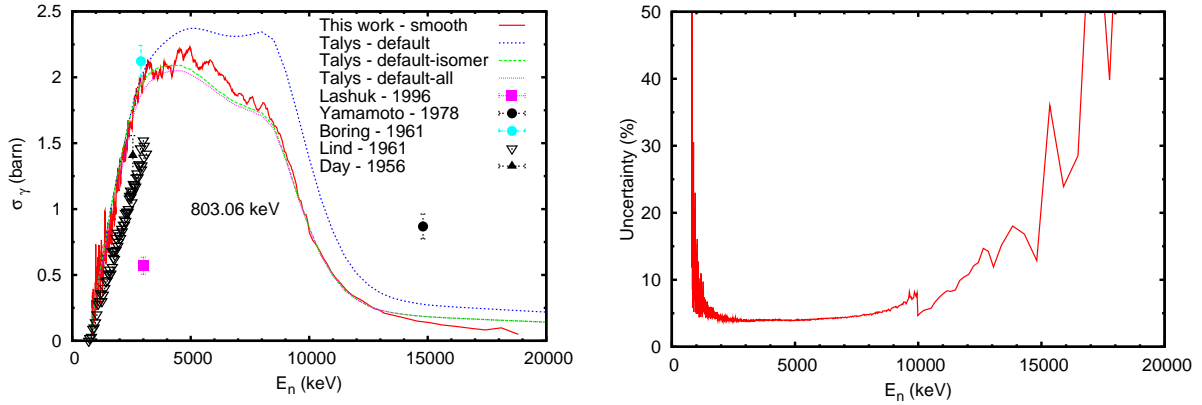


Figure 5.43: *Left:* Integral gamma production cross-section for the 803.06 keV transition in ^{206}Pb . Full energy scale from threshold up to 20 MeV. The data were smoothed with an averaging moving window filter for an easier comparison with other data. *Right:* The corresponding total uncertainty.

the present experiment.

Fig. 5.43 shows the integral gamma production cross-section of the 803.06 keV transition from the inelastic threshold up to 20 MeV. The present data were smoothed with an averaging moving window filter for an easier comparison with the other data. The width of the filter was 11 energy bins, which is equivalent to 88 ns time-of-flight. Only few experimental data points were found in the literature for the integral gamma production cross-section. Large discrepancies with these point data are observed. The difference with the measured values of Day *et al.* [149] increases with the increase of the incident neutron energy. The two data points of Lashuk *et al.* [?] and Yamamoto *et al.* [147] are very different compared with the present results: the first one lower and the second one, at about 15 MeV is higher. The point value of Boring *et al.* [142] agrees well with the present values at about 3 MeV.

In the case of the ^{206}Pb nucleus, for a proper comparison with the experimental data, two corrections were needed for the gamma production cross-section of the 803.06 keV given by the Talys calculation. The first one regards the presence of the isomer level at 2200.14 keV. The Talys code neglects the long life time of the isomer level and the γ -rays from the isomer are considered as prompt transitions. For the comparison with the present measurement, the cross-section of the γ -rays that decay from the isomer (516.18 keV and 202.44 keV) has to be subtracted from the cross-section of all the γ -rays that are fed by the isomer.

The second correction regards the presence of the E0 transition. The Talys code attributes the full decay strength of the 0^+ level, at 1165 keV, to the 362 keV transition that feeds the first excited level. This is contrary to the information in the evaluated level scheme *et al.* [131], where the 362 keV transition has negligible intensity (less than 0.3%). Because of this, the calculated gamma production cross-section of the 362 keV transition has to be subtracted from the calculated gamma production cross-section of the 803.06 keV in order to make a correct comparison.

The total uncertainty of the integral gamma production cross-section of the

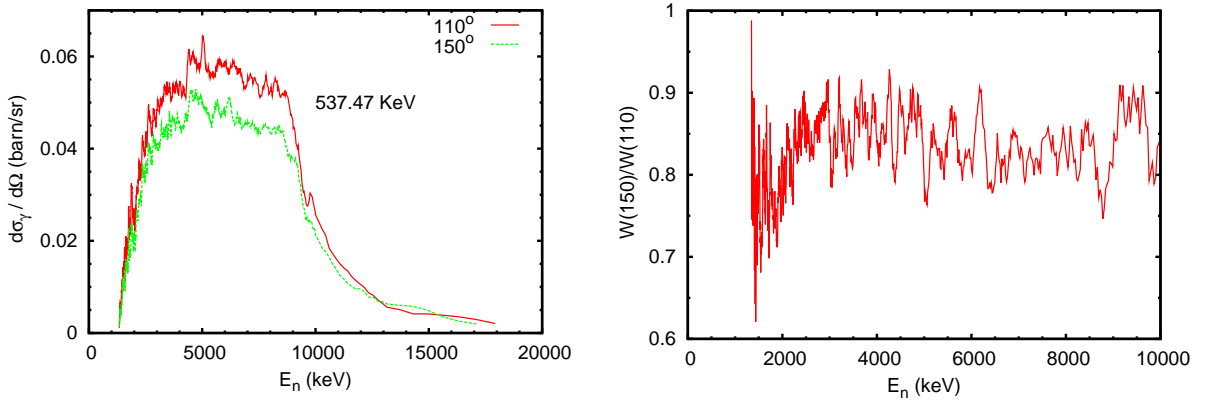


Figure 5.44: Differential gamma production cross-section for the 537.47 keV transition in ^{206}Pb . *Left:* Smoothed curves from the threshold up to 20 MeV at two angles, 110° and 150° . *Right:* The ratio between the angular distribution $W(\theta)$ at 150° and 110° .

803.06 keV γ -ray is shown in Fig. 5.43 *Right*. A total uncertainty of about 5% was obtained below about 9 MeV with a continuous increase above this energy. The increase of the uncertainties at the extremities of the measurement interval is due to the low counting rate (small cross-sections and lower neutron flux at high energies).

After the corrections for the decay from the isomeric level and from the 0^+ level, the default calculation with the Talys code describes well the present measurements in the full energy range (Fig. 5.43). In this figure are given two corrected Talys calculations. The first one includes only the correction for the isomeric level. The second one, denoted "default-all" includes both corrections, for the isomer and for the 0^+ excited level. The effect of the $E0$ transition is small compared with the correction for the isomer.

Despite the general good agreement with the measurement, still there are two differences to be noticed in this comparison. Around 6 MeV neutron energy, the default calculation with Talys after all the corrections is lower than the present measurement. The same can be observed above 15 MeV. These differences between the calculation and the present measured data are of about two time the standard deviation of the measurement.

537.47 keV

Fig. 5.44 shows the differential gamma production cross-section of the 537.47 keV transition from ^{206}Pb . This transition has an angle dependence of an M1+E2. The ratio between the angular distribution $W(\theta)$ at 150° and 110° is given in the right panel of Fig. 5.44. This ratio is almost constant with the neutron energy.

The angle integrated gamma production cross-section is given in Fig. 5.45 from the threshold up to about 20 MeV. The left panel of this figure shows the smoothed data. The experimental data of Lashuk *et al.* [130], Day *et al.* [149] and Lind *et al.* [130] are relatively close to the present results. The other two measurements

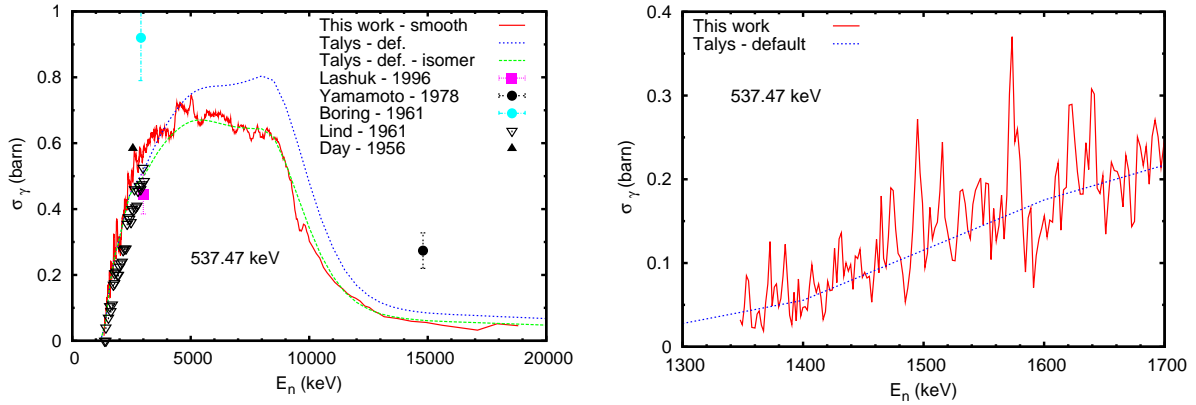


Figure 5.45: *Left:* Integral gamma production cross-section for the 537.47 keV transition in ^{206}Pb . Full energy scale from threshold up to 20 MeV. The data were smoothed with an averaging moving window filter. *Right:* Full energy resolution data.

(Boring *et al.* [142] and Yamamoto *et al.* [147]) are considerably higher. The Talys calculation corrected for the isomer describes well the experimental data. A small difference can still be observed between 3 MeV and 5 MeV neutron energy. Even if the 537.47 keV transition decays from the third excited level, some resonance structures are still visible up to 1.7 MeV (Fig. 5.45 *Right*).

The transitions from higher lying levels

Figs. 5.46, 5.47 and 5.48 show the integral gamma production cross-section for the transitions from excited levels above 1466.80 keV. Up to 2196.7 keV excitation energy, at least one γ -ray was observed to decay from every level. Above this energy some levels were not observed.

The gamma production cross-section given for the 1588 keV is a sum of the gamma production cross-sections of two transitions of 1588.2 keV and 1588.59 keV that decay from the levels at 2391.32 keV and respectively at 2929.06 keV. In absence of any coincidence measurement between the γ -rays, the two γ -ray could not be distinguished with the present experimental setup.

The most intense γ -ray from the level at 1466.80 keV (663.75 keV) was not measured in the present experiment because of a background peak at about the same energy. Below the threshold of the 663.75 keV transition the yield of the HPGe detectors was different from zero and was not constant in neutron energy.

Only the measurements of Yamamoto *et al.* [147] for the 880.98 keV transition and Lind *et al.* [130] for the 1704.45 keV were found in the literature (see Fig. 5.46). The Yamamoto *et al.* value for the gamma production cross-section of the 880.98 keV is much higher than the present results. The data of Lind *et al.* for the 1704.45 keV agree well with the present measurement up to about 2.5 MeV. Above this energy, the Lind *et al.* data are higher.

The Talys calculation was done with the default input parameters. The cor-

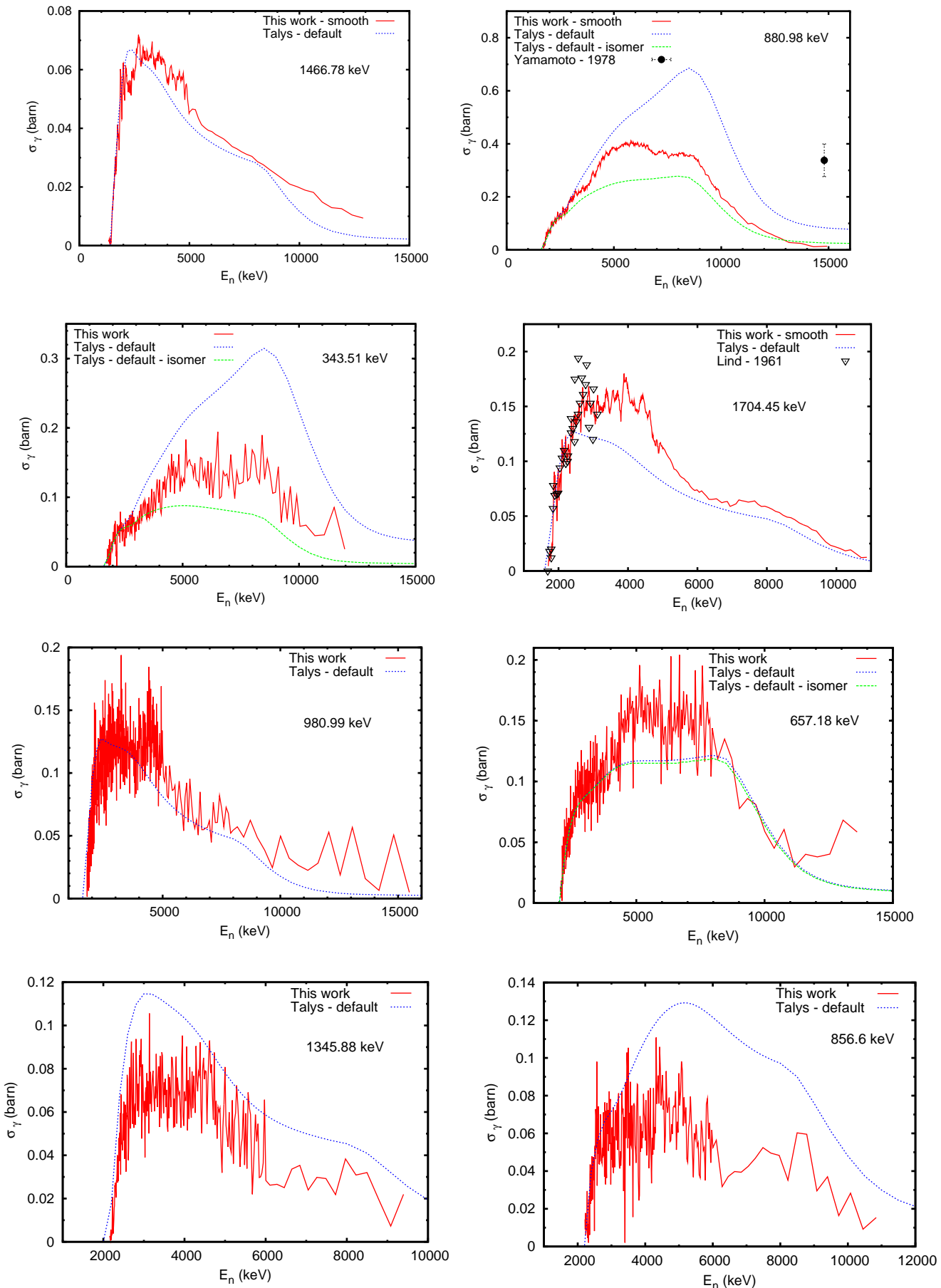


Figure 5.46: Integral gamma production cross-section for the transitions from higher lying levels in ^{206}Pb .

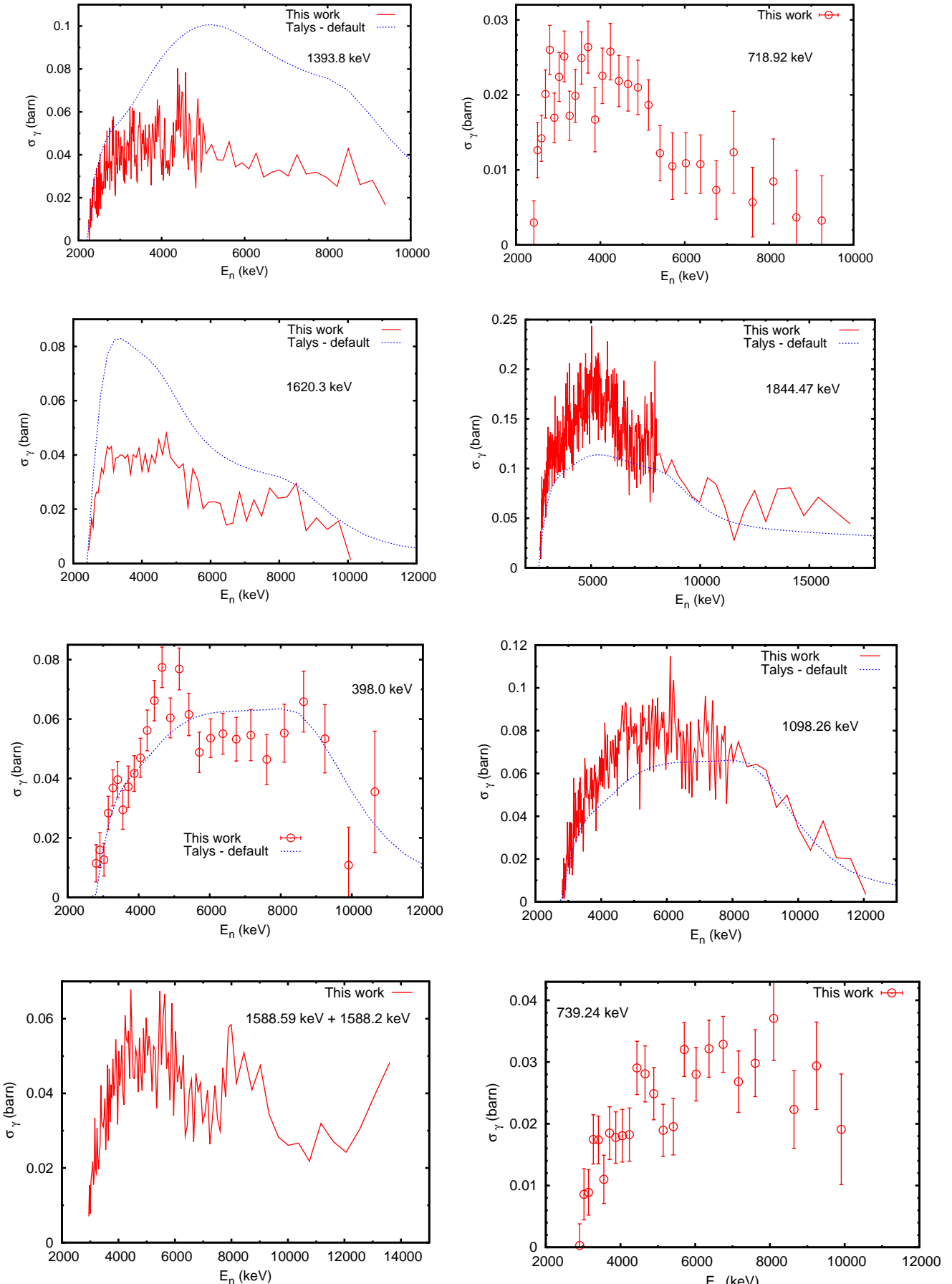


Figure 5.47: Integral gamma production cross-section for the transitions from higher lying levels in ^{206}Pb . The gamma production cross-section given for the 1588 keV is a sum of the gamma production cross-sections of two transitions of 1588.2 keV and

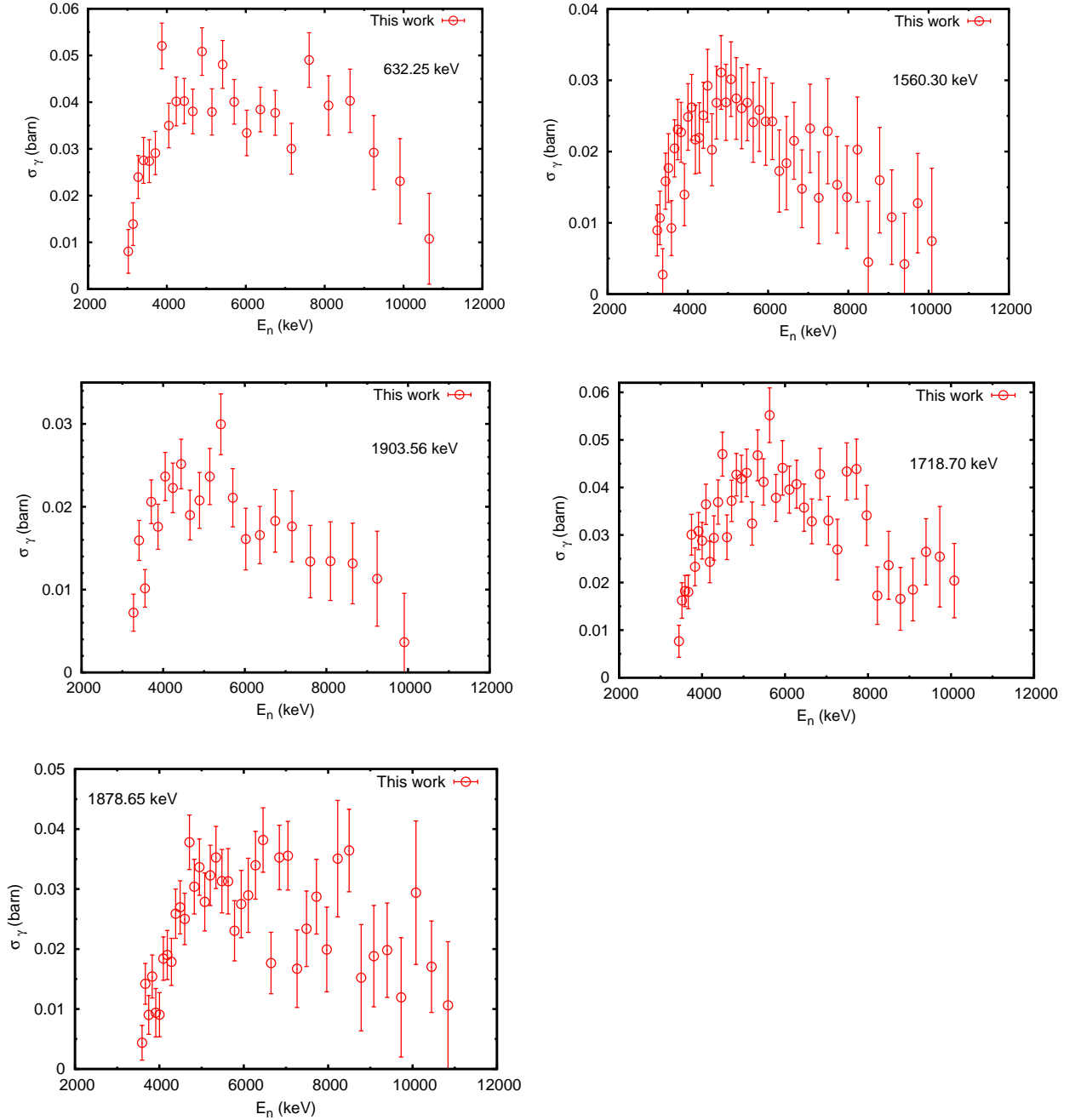


Figure 5.48: Integral gamma production cross-section for the transitions from higher lying levels in ^{206}Pb . The feeding from the isomer was subtracted from the production cross-sections of the 343.51 keV, 657.18 keV and 880.98 keV transition. The experimental cross-sections contain only the prompt decay of the nucleus while the calculation includes also the cross-section of the delayed γ -rays from the isomer.

Table 5.2: Branching ratios for levels in ^{206}Pb nucleus and the corresponding absolute uncertainties. The present results are compared with the values from the evaluated level scheme *et al.* [131].

E_{level} (keV)	E_γ	Present results		ENSDF	
		Intensity	Uncertainty	Intensity	Uncertainty
1683.96	343.51	36.6	0.9	35.4	0.5
	880.98	100	-	100.0	1.0
2196.70	856.6	100	-	100.0	-
	1393.8	67.4	1.8	78	5
2423.36	718.92	47.6	1.6	49.0	2
	1620.30	100	-	100.0	4
2782.15	398.00	88.0	2.2	79.6	0.7
	1098.26	100	-	100.0	11
3244.21	1560.30	100	-	100	5
	1903.56	86.3	3.8	92	4

reactions for the decay from the isomer were done where it was required and both corrected and uncorrected Talys calculations are shown. This correction was done for the following transitions: 343.51 keV, 657.18 keV and 880.98 keV. The production cross-section of the γ -ray from the isomer was subtracted from the production cross-section of γ -rays from above, using the appropriate branching ratios. For the γ -rays from levels above the excitation energy of 2.78 MeV no calculated gamma production cross-sections were available.

The default calculation with Talys describes reasonably transitions as 1466.78 keV, 343.51 keV and 980.99 keV. Significant discrepancies appear for other transitions as 880.98 keV and 856 keV. No systematic difference was observed between the calculation and the experimental data; the discrepancies with the calculation are in both senses, overestimation and underestimation.

Branching ratios

In 5 different cases, two γ -rays from the decay of the same excited level in ^{206}Pb were observed with enough statistics to construct the gamma production cross-sections. For these levels it was possible to deduce the ratio between the γ -ray intensities (branching ratios). These ratios were calculated from the integrated gamma production cross-sections over the full neutron energy range. An identical energy range was used for the integration of two γ -rays from the same level. The measured thresholds of these γ -rays agree with the calculated ones. As additional verification of the γ -ray identification, within the uncertainties, the present measured branching ratios are constant as a function of the neutron energy. The results for the branching ratios are given in Table. 5.4. The present results agree within the uncertainties with the evaluated values [131] for the levels at 1683.96 keV, 2423.36 keV and 3244.21 keV. For the 1393.8 keV γ -ray it was found a higher relative intensity. For the 398.0 keV,

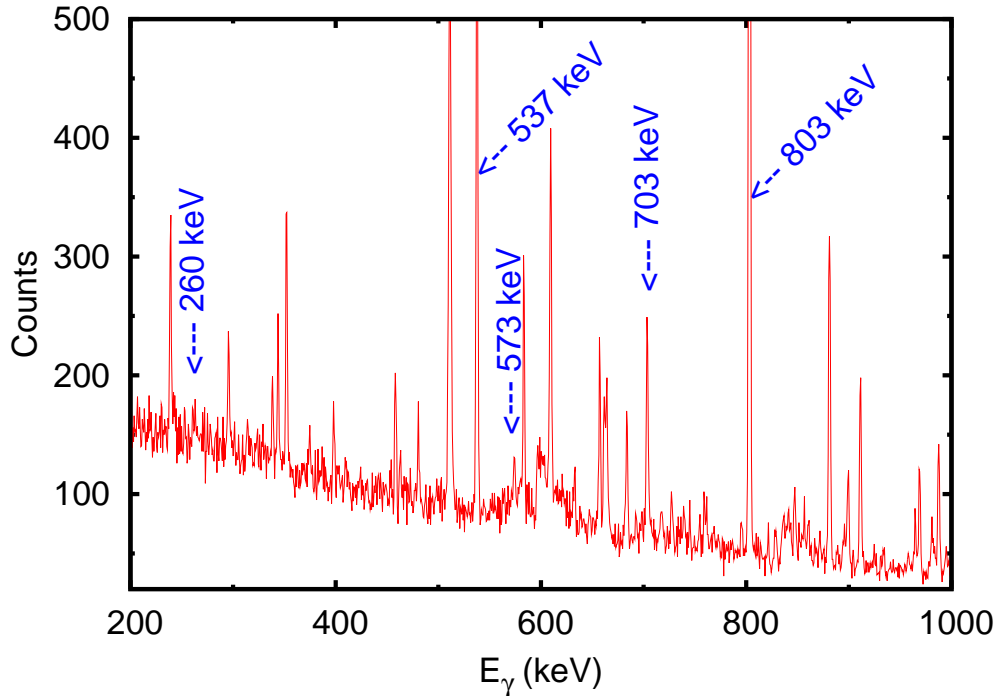


Figure 5.49: γ -rays spectrum with the ^{206}Pb sample (99.8% enrichment) integrated over neutron energies above 8.12 MeV up to about 25 MeV. The 573.88 keV and 703.44 keV γ -ray peaks from the $^{206}\text{Pb}(n,2n)^{205}\text{Pb}$ reaction are seen well in such a spectrum. The position of 260.5 keV γ -ray peak is indicated but such peak is not clearly defined in this spectrum.

the present value of the branching ratio is lower than the evaluated one.

$(n,2n)$ gamma production cross-sections

The threshold of the $(n,2n)$ reaction on ^{206}Pb is at 8.125 MeV. The γ -rays spectrum with the ^{206}Pb sample integrated over neutron energies above the $(n,2n)$ threshold is given in Fig. 5.49. Two γ -ray from the ^{205}Pb nucleus were observed: 573.88 keV and 703.44 keV. The γ -rays from the decay of the first two excited levels in ^{205}Pb were not observed because of their low energy (2.3 keV and 260.5 keV) and the increased background in that energy region. The fact that the 260.48 keV γ -ray was not clearly observed may be also due to its conversion coefficient of 0.61 [131].

The gamma production cross-section of the 573.88 keV and 703.44 keV transitions is given in Fig. 5.50. The observed experimental threshold of the two $(n,2n)$ transitions is the same as the calculated one. At 10 MeV neutron energy, an energy resolution of 150 keV was obtained for the 703.44 keV transition and 360 keV for the 573.88 keV. The Talys calculation underestimates the gamma production cross-section of the 573.88 keV transition and overestimates it in the case of the 703.44 keV transition.

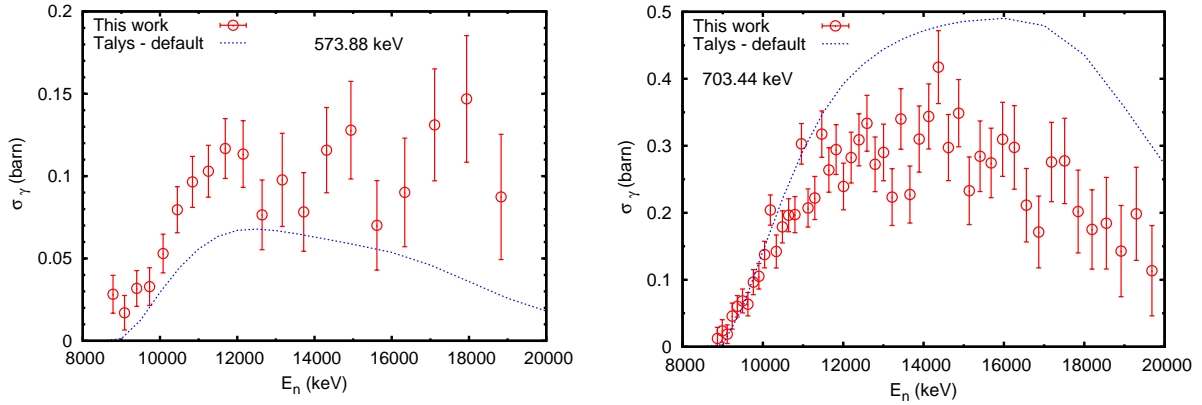


Figure 5.50: Integral production cross-section for the γ -rays from the $^{206}\text{Pb}(n,2n)^{205}\text{Pb}$ reaction.

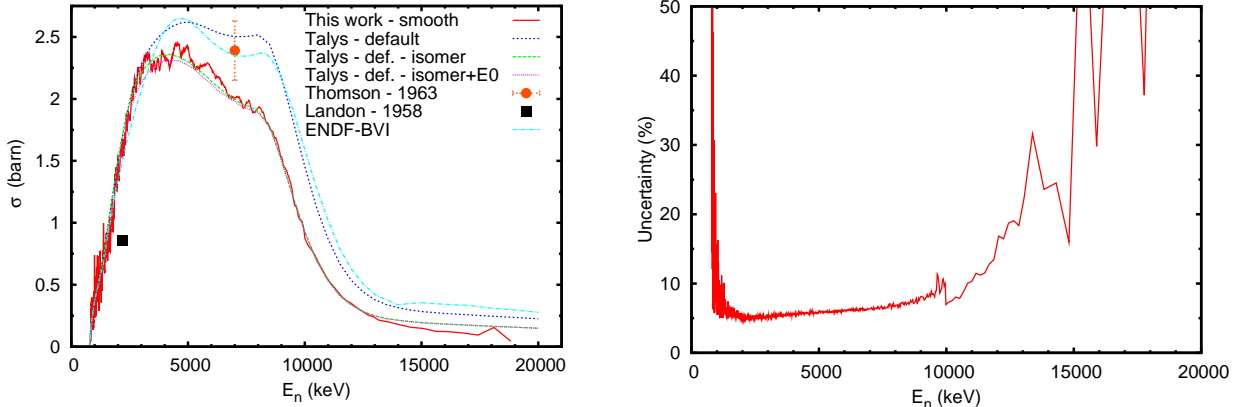


Figure 5.51: *Left:* Smooth data for the total neutron inelastic cross-section of ^{206}Pb on full energy range up to 20 MeV. *Right:* Total uncertainty of the total inelastic cross-sections.

5.3.3 Total inelastic and level cross-sections

The total inelastic and level cross-sections were constructed as described in Sec. 2.1.2 using the integral gamma production cross-sections and the evaluated level scheme of ^{206}Pb . The results for these quantities will be presented in the following.

Total neutron inelastic cross-section

For the construction of the total inelastic cross-section, the following γ -rays were used: 803.06 keV, 1466.78 keV and 980.99 keV (see Fig. 5.39). The total inelastic cross-section so constructed does not include the contribution of the isomeric level and the 0^+ level. According to the level scheme of ^{206}Pb , the first level that decays directly to the ground state and was not observed in the present experiment is at 3194.3 keV. This means that up to this energy the total inelastic cross-section presented here is exact up to the contribution of the isomeric level and of the 0^+

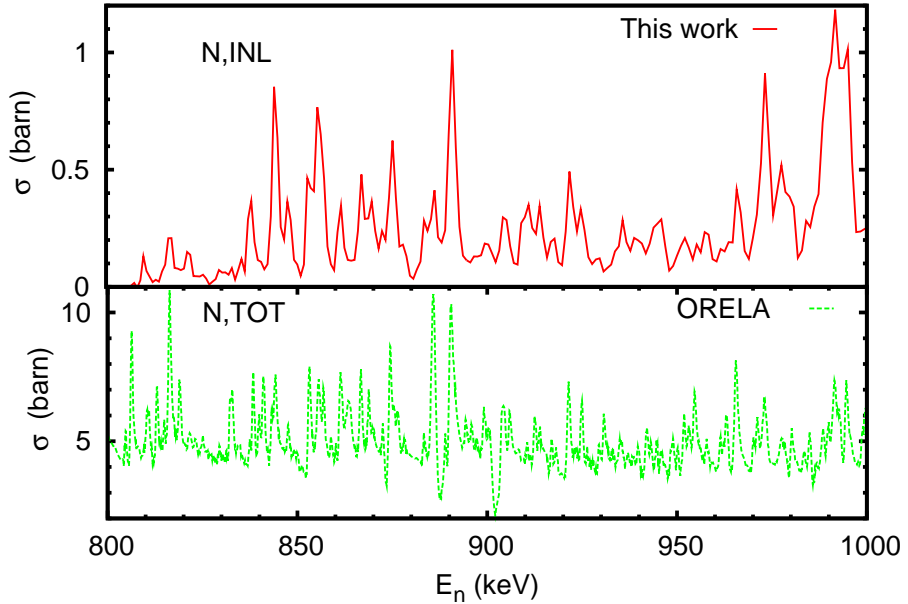


Figure 5.52: Full resolution total inelastic cross-section compared with the neutron total cross-section measured at ORELA *et al.* [?]

level. Above 3.2 MeV the present curve is a lower limit to the total inelastic cross-section. This limit is a very close to the exact value for the even-even nucleus of ^{206}Pb . In this case the total inelastic cross-section is determined mainly by the gamma production cross-section of the main transition.

The energy resolution was 1.1 keV at 1 MeV and 35 keV at 10 MeV. The result is shown in Fig. 5.51 together with the corresponding total uncertainty. The total relative uncertainty is around 5 % at about 2 MeV and increases slowly for higher energies. The large values of the relative total uncertainty at the extremities of the energy interval are due to the poor statistics.

Two experimental points for the total inelastic cross-sections were found in the literature (Ref. [141] and [143]). Both these points differ from the present measurement. The Landon [143] data point at about 3 MeV is lower than the present results and the data point of Thomson [141] at about 7 MeV is higher. The Talys calculation with the default parameters describes very well the present results after the correction for the isomer and for the E0 transition (Sec. 5.3.2). Fig. 5.51 *Left* shows three different curves for the Talys calculation with the default parameters. The curve denoted "def.-isomer" represents the default calculation from which it was subtracted the isomer contribution. The curve denoted "def.-isomer+E0" is corrected for both, the isomer and the 0^+ level. It can be seen that the contribution due to the 0^+ level is very small compared with the contribution of the isomer.

The ENDF-BVI evaluation (Fig. 5.51) gives higher values for the total inelastic cross-section because it includes the contribution of the isomer level. The JEFF 3.1 evaluation was not plotted here because it coincides with the Talys calculation.

Fig. 5.52 shows the total inelastic cross-section below 1 MeV compared with the

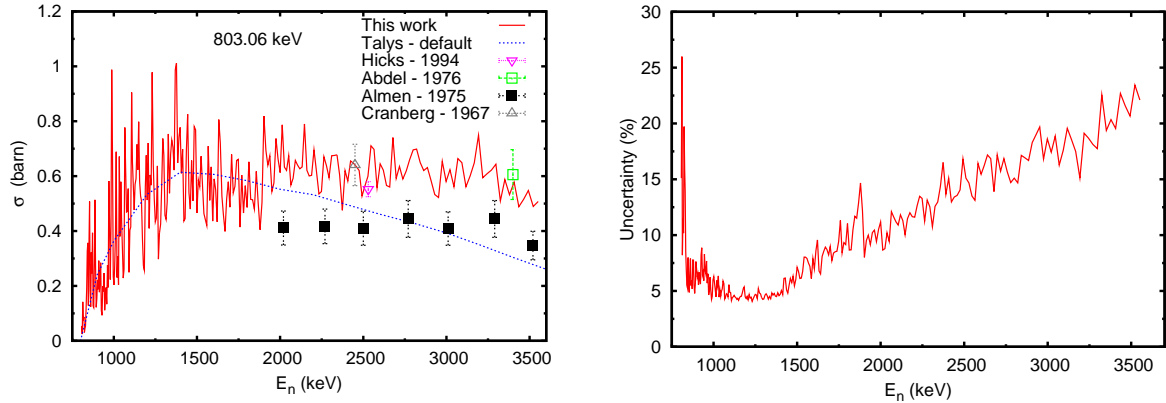


Figure 5.53: *Left:* The cross-section of the 803.06 keV level in ^{206}Pb . *Right:* The corresponding total uncertainty.

total neutron cross-section measured at ORELA in a transmission experiment *et al.* [146]. Despite the poorer neutron energy resolution of the present experiment, many of the resonances from the total cross-section are seen also in the total inelastic cross-section. Differences in the relative intensity between different resonances in the inelastic and in the total cross-section may be observed. As an example, the resonances at about 890 keV have almost the same intensity in the total cross-section. In the inelastic cross-section the resonance at 892 keV has higher intensity than the resonance at 886 keV.

Level 803.05 keV

The cross-section of the first excited level is given in Fig. 5.53. The first level not observed here which decays to the 803.06 keV level is at 2236.53 keV. Therefore, the cross-section given here for the 803.06 keV level is exact up to 2.2 MeV. Above this energy, the curve given in Fig. 5.53 *Left* is an upper limit for the 803.06 keV level cross-section. The relative uncertainty is given in Fig. 5.53 *Right* for the cross-section of the level at 803.05 keV.

The Talys calculation with the default input parameters describes well the cross-section of the level at 803.06 keV up to about 2 MeV. Above this energy, the calculation gives lower values. Part of this difference may come from the fact that the feeding from levels that were not observed above 2236 keV excitation energy was neglected.

The existing experimental data for this level cross-section are somewhat contradictory. The values given by the experiments of Hicks *et al.* [134], Abdel *et al.* [130] and Cranberg *et al.* [148] agree with the present results. The data of Almen *et al.* [130] are lower, but just at the limit of one standard deviation of the two experiments.

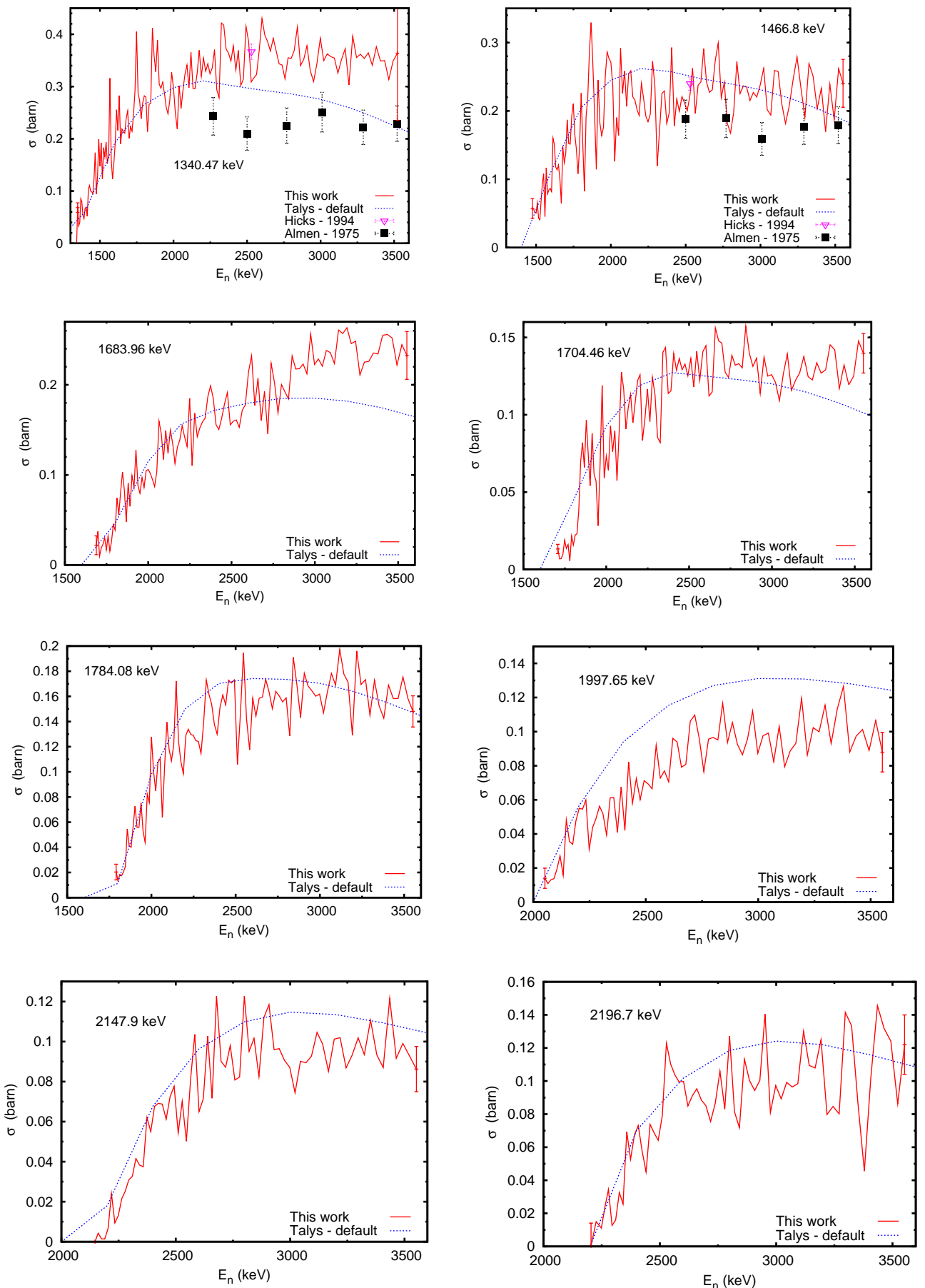


Figure 5.54: The cross-section of the excited levels above 1.3 MeV in ^{206}Pb . Generic error bars are plotted at the extremities of the energy interval.

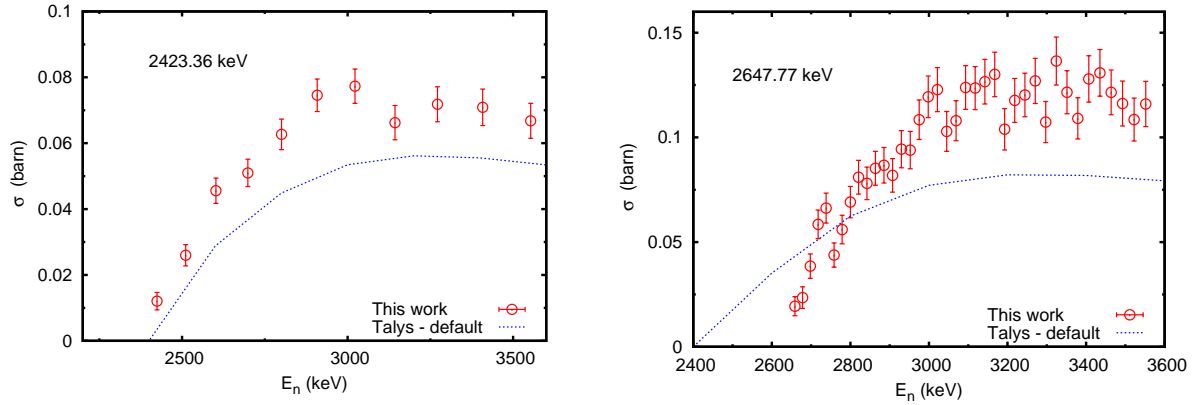


Figure 5.55: The cross-section of the excited levels above 1.3 MeV in ^{206}Pb .

Levels with higher excitation energy

The cross-sections of the levels with excitation energy between 1340.47 keV and 2647.77 keV are given in Figs. 5.54 and 5.55. These cross-sections were given only up to about 3.5 MeV neutron energy, because 3.56 MeV is the highest excited level observed in this experiment.

Above 2.2 MeV excitation energy some excited levels were not observed. Because of this, above 2.2 MeV neutron energy, the level cross-sections presented here are upper limits to the exact values. The difference to the exact values reflects the intensity of the excited levels not observed in this experiment. The cross-section of these levels has to be weak such as the transitions that decay from them to have a cross-section of less than 20 mb, which is the approximate observation limit of the present measurement. Generic error bars are plotted at the extremities of the energy interval for every level cross-section.

Previous experimental data were found only for the levels at 1340.47 keV and at 1466.8 keV. The data of Almen *et al.* [130] are lower than the present results. The values of Hicks *et al.* [134] at about 2.5 MeV are in good agreement with the present one.

The Talys calculation with the default input parameters is plotted together with the present results (Figs. 5.54 and 5.55). No correction of the calculated curves was needed for the level cross-sections for the presence of the isomer and the 0^+ level.

Below 2.5 MeV neutron energy, the agreement between the calculation and the present measurement is good for the majority of the levels presented here. Above 2.5 MeV, the calculation gives lower values than the present measurement for the levels at 1340.47 keV, 1683.96 KeV, 1704.46 keV, 2423.36 keV and 2647.77 keV. These differences are in accord to the approximation of the lower limit above 2.5 MeV for the present measurement. For the level at 1997.65 keV, the calculation gives higher values than the measurement. This is a contradiction of the lower limit approximation. For the other levels presented here the calculation describes relatively well the measurement also above 2.5 MeV.

It has to be noted that the Talys calculation with the default input parameters

coincides with the JEFF 3.1 evaluation for the level cross-sections.

5.3.4 Conclusions

A highly enriched sample with 99.8 % of ^{206}Pb was used for the measurement of the gamma production cross-sections from the $^{206}\text{Pb}(\text{n},\text{n}'\gamma)^{206}\text{Pb}$ and from the $^{206}\text{Pb}(\text{n},2\text{n})^{205}\text{Pb}$ reactions. The gamma production cross-section was measured for 23 γ -rays from the inelastic scattering reaction and two γ -rays from the ($\text{n},2\text{n}$) reaction. Up to 2.2 MeV excitation energy, at least one γ -ray was observed from the decay of every excited level. Between 2.2 MeV and 3.56 MeV only several other levels were observed. For five excited levels, two γ -rays were observed from the decay of each of these levels. The branching ratios were deduced for these levels.

The most intense transitions from the inelastic reaction were measured with an unprecedented neutron energy resolution of 1.1 keV at 1 MeV (35 keV at 10 MeV) on the full energy range from the threshold up to about 20 MeV, in only one run. The best neutron energy achieved for the γ -rays from the ($\text{n},2\text{n}$) reaction was 150 keV at 10 MeV neutron energy (equivalent to 32 ns time-of-flight bins). For the weak transitions in the ^{206}Pb nucleus, the neutron energy of the measurement was limited to about 10 MeV.

In the ^{206}Pb neutron inelastic and ($\text{n},2\text{n}$) reaction cross-sections with the ($\text{n},\text{xn}\gamma$)-technique there are two limitations: the isomeric level at 2200.14 keV and the 0^+ level at 1165 keV that decays to the ground state level through a E0 transition. The γ -rays from the decay of the isomer and the E0 transitions do not appear in the prompt γ -ray spectrum. Therefore, the cross-sections measured in the present experiment do not include the contributions from the isomer level at 2.2 MeV and from the 0^+ level at 1165 keV.

Based on the level scheme of ^{206}Pb , the total inelastic and the level cross-sections were constructed. The total inelastic cross-section presented here is exact up to 3.2 MeV with the exception of the contribution of the isomer and of the 0^+ level. Above 3.2 MeV, the levels that decay directly to the ground state were not observed and because of this the present total inelastic cross-section is a lower limit. This limit is expected to be very close to the total inelastic cross-section as long high lying states decay predominantly to the first few excited states.

The level cross-sections given here are exact up to 2.2 keV. Above 2.2 keV some excited levels were not observed and their decay to the studied levels was neglected. The level cross-sections presented here were not affected by the presence of the isomer and the 0^+ level.

A total uncertainty for the total inelastic cross-section of 5% was achieved below 9 MeV neutron energy. Higher uncertainties were obtained just above the inelastic threshold and at high neutron energies because of the smaller counting rate.

Due to the high neutron energy resolution of the present experiment, below 2 MeV it was possible to observe resonance structures in the gamma production cross-section and in the total inelastic cross-section. These resonance structures were compared with the resonances observed in the transmission experiments found in the literature.

The measured cross-section were compared with the existing data found in the literature and with the Talys calculation with the default parameters. A small amount of previously measured data were found and in general poor agreement was observed with these data.

For a correct comparison of the measured cross-sections in this experiment with the Talys calculation, the later was corrected for the contributions of the isomer and 0^+ level. For the gamma production cross-section of the two most intense γ -rays in ^{206}Pb , the corrected Talys calculation with the default input parameters is in a general good agreement with the measured data on the full energy range. For the other γ -rays the measured production cross-sections agree well with the corrected Talys calculation at low neutron energies. Differences appear above 3.5 MeV. The total inelastic cross-section without the contribution of the isomer and the 0^+ level agree generally well with the corrected Talys calculation on the full energy range, from the inelastic threshold up to about 20 MeV.

The present measurement provided a large amount of cross-section data for the neutron inelastic and $(n,2n)$ reactions. The improvement brought by this new experiment to the neutron inelastic and $(n,2n)$ reactions cross-section consists of the very good neutron energy resolution, the very good total uncertainty and the large number of observed γ -rays. Such cross-section can be used in the further neutron data evaluations and as benchmark for the nuclear codes.

5.4 ^{207}Pb neutron inelastic scattering and (n,2n) cross-sections

5.4.1 Introduction

Few experimental data exist for the ^{207}Pb neutron inelastic and (n,2n) cross-sections. Three measurements were done with (n,n'γ)-technique (Lashuk *et al.* [130], Yamamoto *et al.* [147] and Day *et al.* [149]). From these experiments only Lashuk *et al.* [130] and Yamamoto *et al.* [147] used the advantage of the Ge(Li) detectors for the γ-ray identification in the spectrum. The (n,n')-technique was used by Cranberg *et al.* [148], Abdel *et al.* [130] and Almen *et al.* [130]. The first author measured only the differential level cross-sections.

The production cross-section of the main γ-ray in the $^{207}\text{Pb}(\text{n},\text{2n})^{206}\text{Pb}$ reaction was measured by Vonach *et al.* [152]. In the experiment of Vonach *et al.* [152] the (n,n'γ) reaction was not analyzed because of the overlap of the low energy neutrons from consecutive bursts.

As in the case of ^{206}Pb nucleus, ^{207}Pb has an isomer at relatively low excitation energy, 1633.36 MeV (Fig. 5.56). The isomer in ^{207}Pb has a life time of 0.806 s which is much larger than the period between two consecutive bursts at GELINA (1.25 ms). In these conditions it was found that the prompt decay of the isomer level is negligible. Therefore the cross-sections measured in the present experiment do not include any contribution from the isomer. For a proper comparison with the default Talys calculation, the theoretical cross-sections for some γ-rays and for the total inelastic cross-section have to be corrected for the contribution of the isomer.

From the five samples studied in this work, the ^{207}Pb sample was the first case where the sample enrichment was only 92.40 % and the concentrations of the impurities of ^{206}Pb and ^{208}Pb isotopes could not be neglected. Therefore, additional corrections for the (n,xnγ) reactions on different isotopes were needed. Table. 5.3 shows how the residual nuclei (γ-ray peaks) were produced with the present ^{207}Pb sample. The threshold of the γ-ray production is indicated as well. As an example, Fig. 5.57 shows the yield of the 803.06 keV transition from the ^{206}Pb residual nucleus. This γ-ray peak resulted mainly from the $^{207}\text{Pb}(\text{n},\text{2n}\gamma)^{206}\text{Pb}$ reaction, but

Table 5.3: Corrections for the isotopic composition of ^{207}Pb sample. The residual nuclei ^{207}Pb and ^{206}Pb can be produced in different reactions on the 92.4 % enriched sample. The threshold is given for the γ-ray production in different reactions.

residual nucleus	reaction	content in the sample	threshold (MeV)
^{207}Pb	$^{207}\text{Pb}(\text{n},\text{n}'\gamma)^{207}\text{Pb}$	92.40 %	0.572
	$^{208}\text{Pb}(\text{n},\text{2n}\gamma)^{207}\text{Pb}$	5.48 %	7.975
^{206}Pb	$^{206}\text{Pb}(\text{n},\text{n}'\gamma)^{206}\text{Pb}$	2.16 %	0.806
	$^{207}\text{Pb}(\text{n},\text{2n}\gamma)^{206}\text{Pb}$	92.40 %	7.57
	$^{208}\text{Pb}(\text{n},\text{3n}\gamma)^{206}\text{Pb}$	5.48 %	14.98

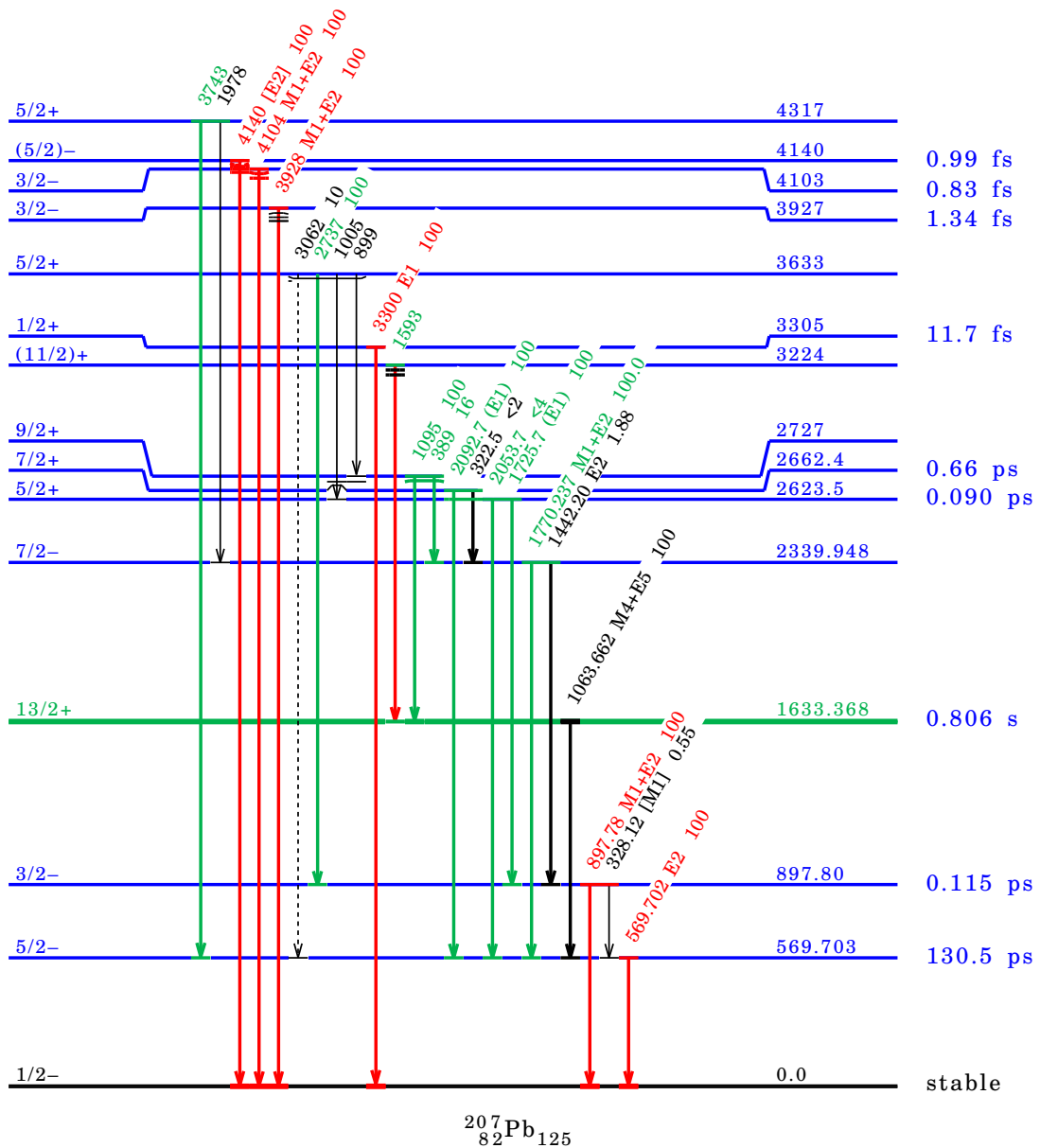


Figure 5.56: Simplified evaluated level scheme of ^{207}Pb [131]. The gamma production cross-section of the transitions drawn with colors was measured in the present experiment. The "red" γ -rays were used to construct the total inelastic cross-section. The isomer level at 1633.36 keV was not observed in the present experiment.

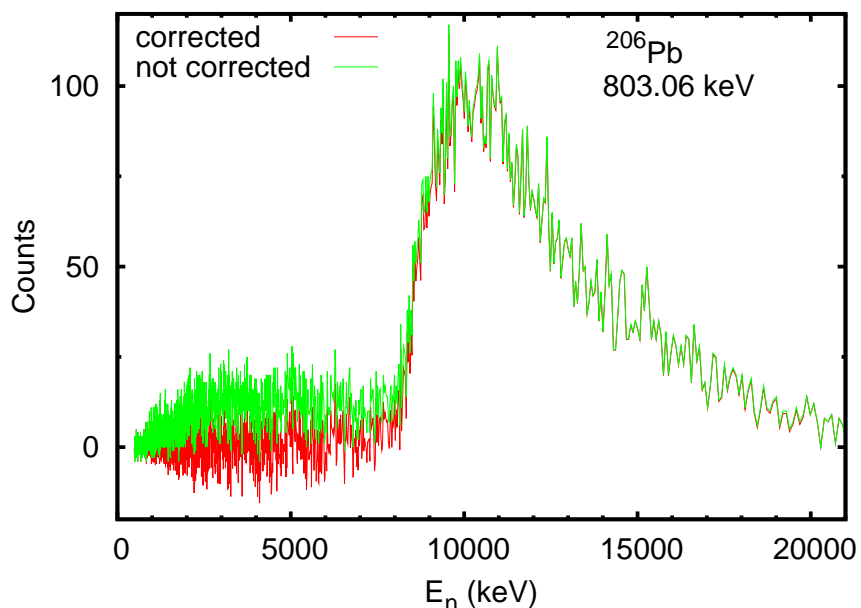


Figure 5.57: 803.06 keV γ -ray yield from the ^{207}Pb sample before and after the correction for the isotopic composition of the sample. As shown in Table. 5.3 these peak is produced in three different reactions. After the correction for the $^{206}\text{Pb}(n,n'\gamma)^{206}\text{Pb}$ reaction the average background below the $(n,2n)$ threshold equals zero. The correction for the $^{208}\text{Pb}(n,3n)^{206}\text{Pb}$ above 14.98 MeV was almost negligible.

clear evidence for the other two reactions is visible: the inelastic scattering reaction below 7 MeV and the ($n,3n\gamma$) reaction above 15 MeV. The corrections for the ($n,xn\gamma$) reaction on ^{207}Pb sample were done using the measured cross-sections presented in this work.

In the present measurement the gamma production cross-section was measured for 15 γ -rays from the $^{207}\text{Pb}(n,n'\gamma)^{207}\text{Pb}$ reaction (see Fig. 5.56) and four γ -rays from $^{207}\text{Pb}(n,n'\gamma)^{207}\text{Pb}$ reaction. The maximum energy of an observed excited level in ^{207}Pb was 4317 keV. In Fig. 5.56, the observed γ -rays are drawn with colors. Based on the evaluated level scheme, the total inelastic and the level cross-section were constructed.

5.4.2 Gamma production cross-sections

Fig. 5.58 shows the γ -ray spectrum recorded with the HPGe detector at 150° . The spectrum was integrated over the neutron energy from just below the inelastic threshold up to 25 MeV. The most intense peaks in the spectrum are by far the peaks at 569.70 keV and 897.78 keV. The gamma production cross-section for all the measured transitions will be given in the following. The differential gamma production cross-section will be shown as an example for the 569.70 keV and 897.78 keV transitions. The angle integration was done using the Gauss quadrature described in Sec. 2.3.3.

569.70 keV

The 569.70 keV is the most intense transition in the ^{207}Pb spectrum. The differential gamma production of this transition is shown in Fig. 5.59 for the two angles: 110° and 150° . The typical angular distribution for an E2 transition is observed. The ratio between the angular distribution $W(\theta)$ at 150° and 110° is given in Fig. 5.59 *Right*. No clear energy dependence of this ratio was observed.

The very good neutron energy resolution of the present experiment allowed the observation of the resonance structures in the gamma production cross-section between the inelastic threshold and about 2.5 MeV. The full resolution data for the differential and the angle integrated gamma production cross-section is shown in Fig. 5.60.

The angle integrated gamma production cross-section on the full energy range from the threshold up to 20 MeV is given in Fig. 5.61. The present data were smoothed with moving average filter only for an easier comparison with the other data. The width of the filter was 11 neutron energy bins (equivalent of 88 ns time-of-flight). The neutron energy resolution of this cross-section was 1.1 keV at 1 MeV and 35 keV at 10 MeV.

A total uncertainty of about 5 % was obtained between 2 MeV and 7 MeV (Fig. 5.61 *Right*). Above 7 MeV the statistical uncertainty starts to increase due to the small counting rate and becomes the dominant component in the total uncertainty. To reduce the total uncertainty, few energy bins were grouped together at the expense of lower energy resolution. This grouping procedure produced the steps

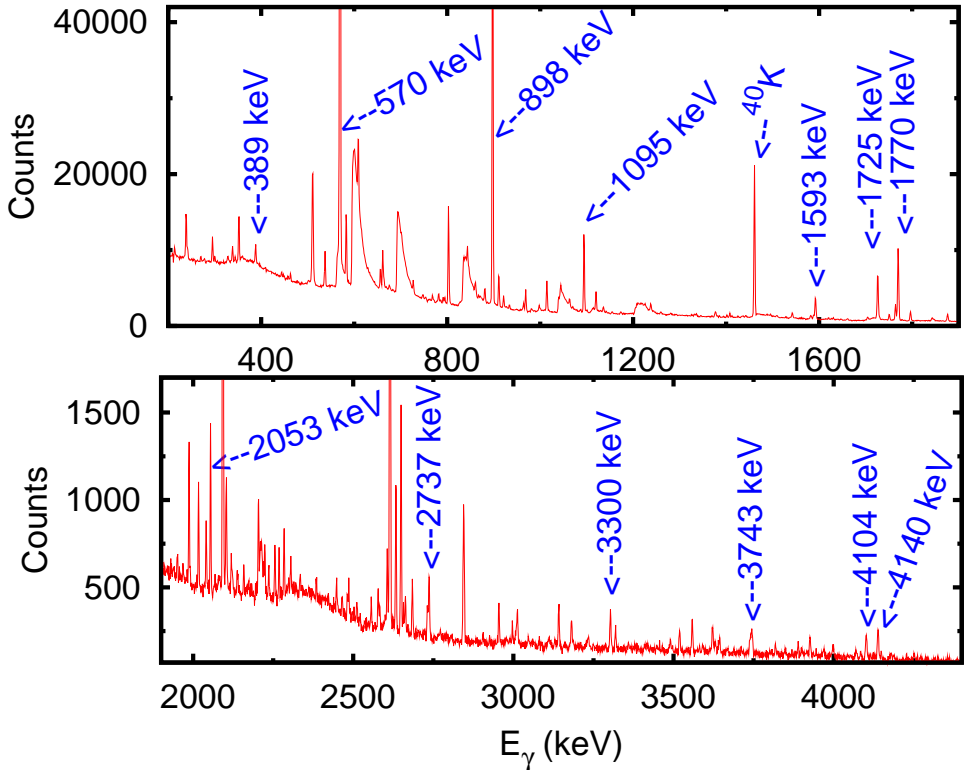


Figure 5.58: The γ -ray spectrum of an HPGe detector with the ^{207}Pb sample (92.40% enrichment). The spectrum was integrated over the neutron energies from 500 keV up to about 25 MeV. The main γ -ray peaks from the inelastic scattering on the ^{207}Pb sample are clearly visible. The small counting rate of the experiment is suggested by the high intensity of the 1460 keV peak from ^{40}K .

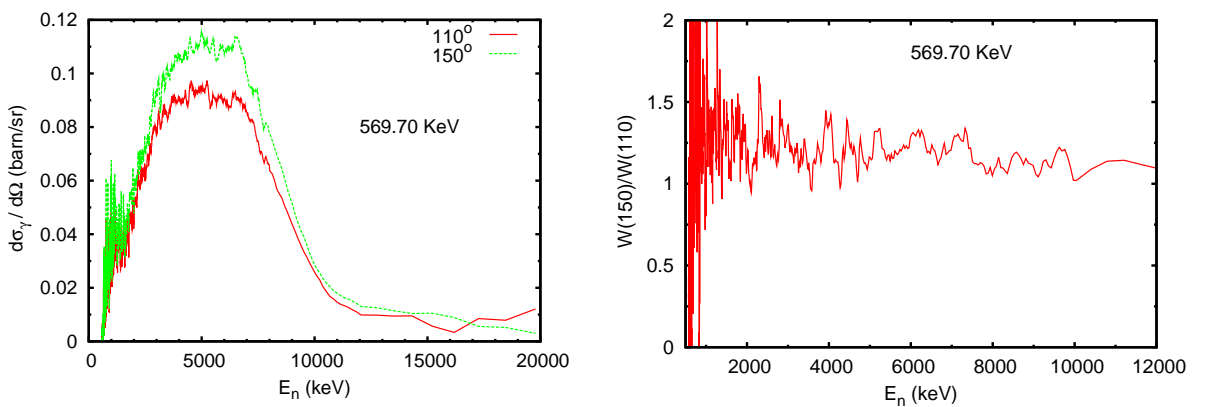


Figure 5.59: Differential gamma production cross-section for the 569.7 keV transition in ^{206}Pb . *Left:* Smoothed curves from the threshold up to 20 MeV at two angles, 110 and 150 degrees. *Right:* The ratio between the angular distribution $W(\theta) = \frac{4\pi}{\sigma} \frac{d\sigma}{d\Omega}(\theta)$ at 150 and 110 degrees.

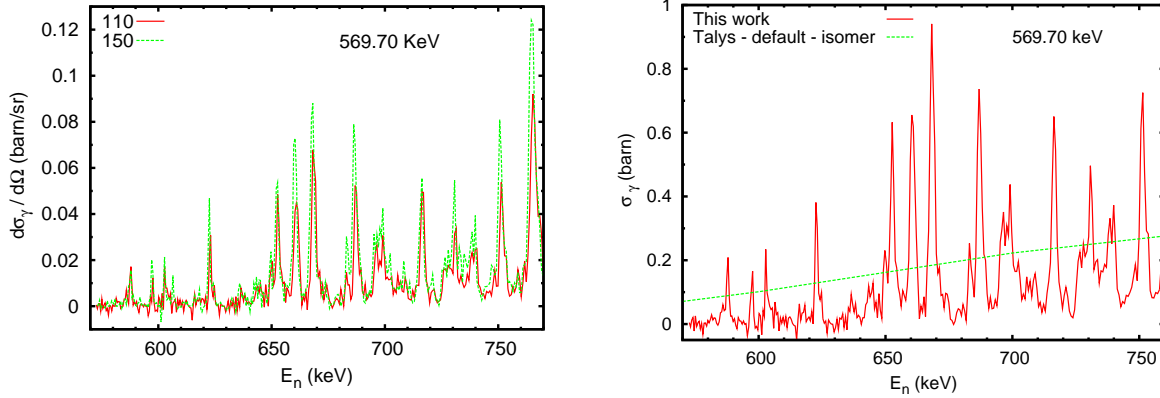


Figure 5.60: Full resolution gamma production cross-section for the 569.7 keV transition in ^{207}Pb . *Left:* Differential gamma production cross-section at 110° and 150° . *Right:* Integral gamma production cross-section compared with Talys calculation.

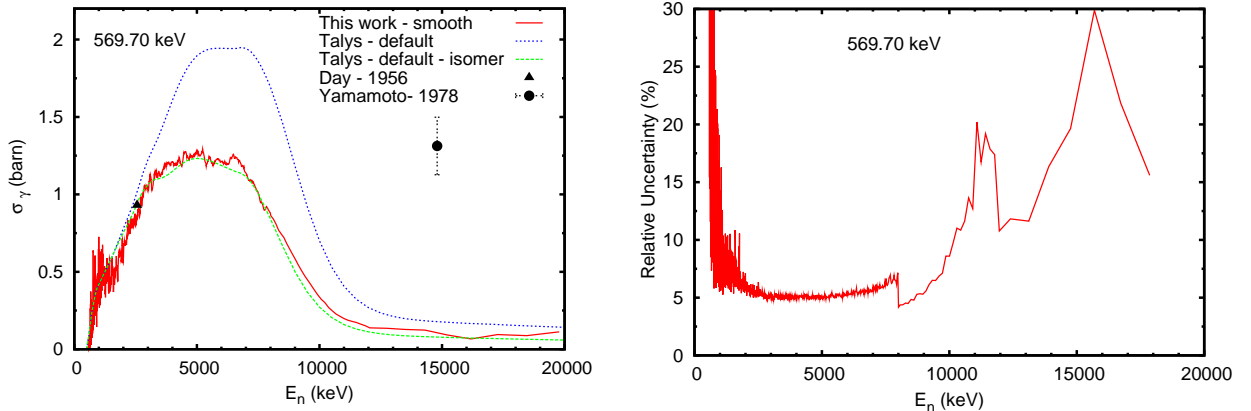


Figure 5.61: *Left:* Integral gamma production cross-section for the 569.7 keV transition in ^{207}Pb . Full energy scale from threshold up to 20 MeV. The data were smoothed with an averaging moving window filter for an easier comparison with other data. *Right:* The corresponding total uncertainty.

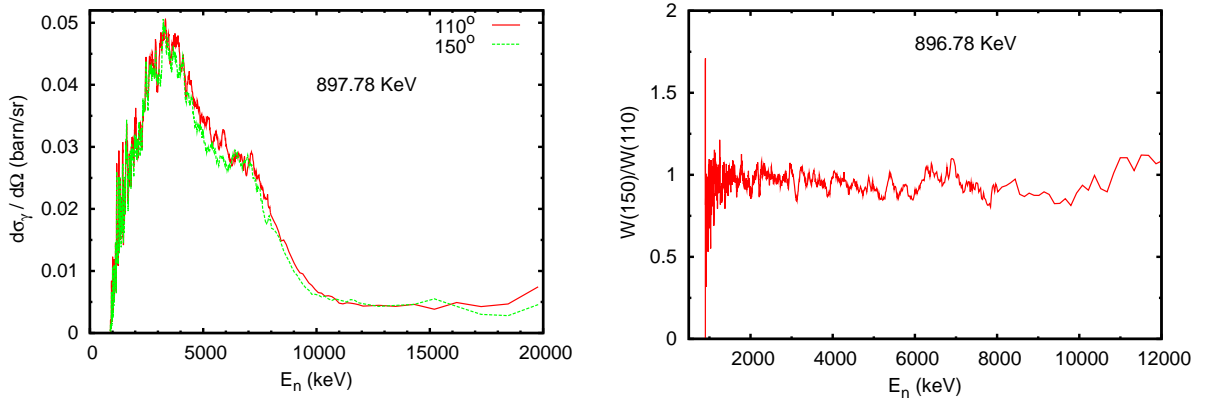


Figure 5.62: Differential gamma production cross-section for the 897.78 keV transition in ^{207}Pb . *Left:* Smoothed curves from the threshold up to 20 MeV at two angles, 110° and 150° . *Right:* The ratio between the angular distribution $W(\theta)$ at 150° and 110° .

in the uncertainty plot (Fig. 5.61 *Right*).

Only two measured points were found in the literature. The Yamamoto *et al.* [147] data are very high compared with the present results. The Day *et al.* [149] point at low energies agrees well with the present results.

For the comparison with the present experimental data, the Talys calculation with the default input parameters was corrected for the isomer level. The isomer level at 1633.37 keV decays directly to the first excited level. The Talys code neglects the long decay time of the isomer and considers the 1063.66 keV transition as a prompt γ -ray (Fig. 5.56). The calculated gamma production cross-section of the 1063.66 keV transition was subtracted from the calculated gamma production cross-section of the 569.702 keV transition. Fig. 5.61 shows both, the isomer corrected and the uncorrected Talys calculated curves. After the isomer correction, the calculation describes well the measured data on the full energy range.

897.78 keV

The 897.78 keV γ -ray from the decay of the second excited state to the ground state is an M1+E2 transition. Almost no angle dependence was observed for this transition (Fig. 5.62). This can be also observed from the ratio between the differential gamma production cross-sections at the two angles, which equals unity.

Fig. 5.63 gives the integral gamma production cross-section from the threshold (901 keV) up to 20 MeV. The same neutron energy resolution was used as in the case of the 569.70 keV transition. The resonance structures above the threshold are visible well for this transition up to about 2 MeV.

The point of Day *et al.* [149] at about 3 MeV is slightly higher than the present measurement. As in the case of the main transition, the value from the measurement of Yamamoto *et al.* [147] is higher. For the 897.78 keV transition no correction of the Talys calculation is needed for the decay of the isomer, because there is no

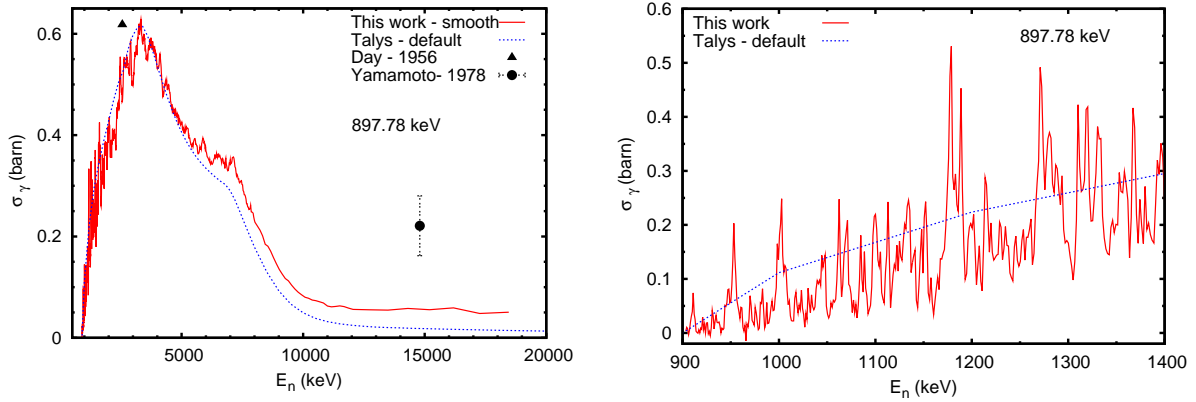


Figure 5.63: *Left:* Integral gamma production cross-section for the 897.78 keV transition in ^{207}Pb . Full energy scale from threshold up to 20 MeV. The data were smoothed with an averaging moving window filter. *Right:* Full energy resolution data.

decay from the isomer to the 897.80 keV level. The calculation describes well the gamma production cross-section of this transition up to 6 MeV. Above this energy the calculation is lower.

The transitions from higher lying levels

The gamma production cross-section of other γ -ray transitions from higher excited levels are shown in Figs. 5.64 and 5.65. For the weak transitions the gamma production cross-sections were measured only up to 8 MeV and with a poor energy resolution. In the case of the 3928 keV transition only four points were obtained.

Previous experimental data were found in Ref. [147] only for the 1770.24 keV and for the 1095 keV transitions. These points of Yamamoto *et al.* are very high compare with the present results for both transitions.

The Talys code with the default parameters calculates the gamma production cross-sections only up to the 3.3 MeV excitation energy. For the 2053.7 keV transition the Talys code contains a branching ratio equals zero, while the evaluated value from Ref. [131] is less than 4. Higher value was found from the present experiment (see next section). Using the branching ratio measured in this experiment it was possible to estimate the cross-section of the 2053.7 keV transition from the cross-section of the 1725.7 keV transition. This estimation is shown with in Fig. 5.64 with green. With the new branching ratio, the calculated values for the 1725.7 keV transition decrease.

The Talys calculation describes well the gamma production cross-section of the 2092.7 keV on the full energy range. After the correction for the new value of the branching ratio, the calculation is still close to the experimental data. At energies below 3 MeV the calculation is in good agreement with the measurement for all transitions except for the 1593 keV. At energies above 3 MeV, the calculation is higher for the 1770.24 keV and 3300 keV and lower for the 1095 keV and 389 keV.

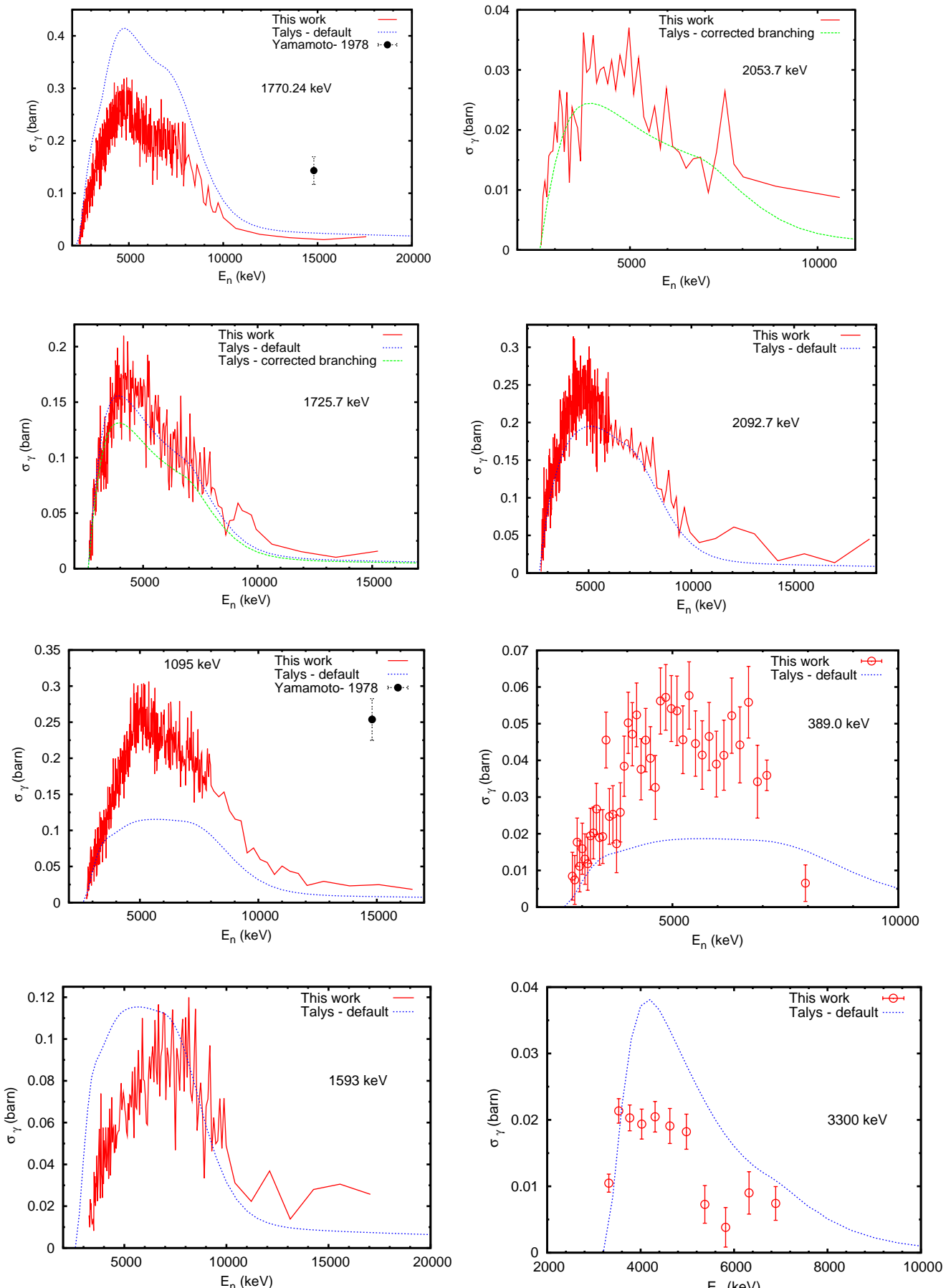


Figure 5.64: Integral gamma production cross-section for the transitions from higher lying levels in ^{207}Pb . New intensity ratio was found for the γ -rays of energy 1725.7 keV and 2053.7 keV. Using this new value, a calculated curve can be de-

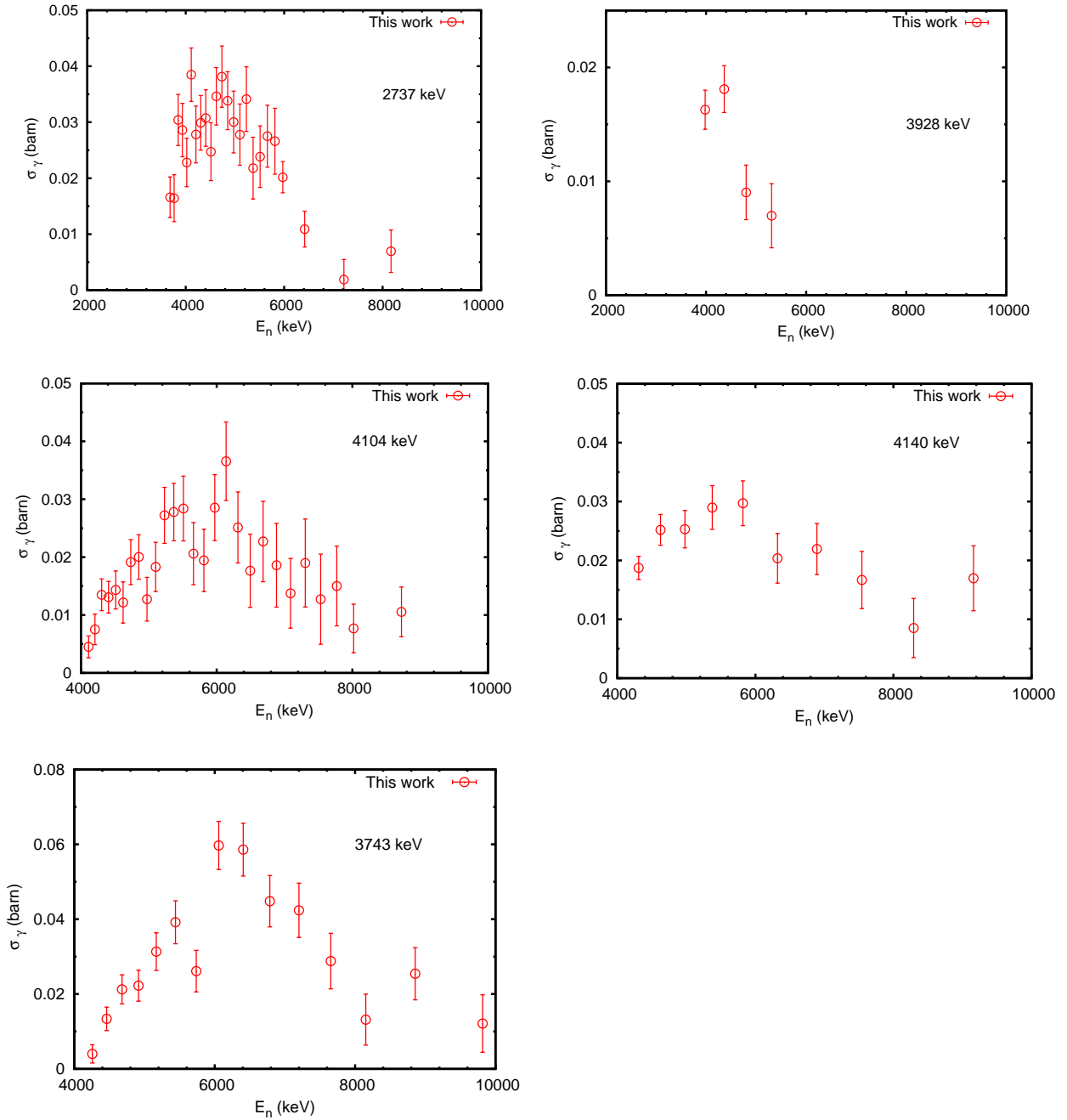


Figure 5.65: Integral gamma production cross-section for the transitions from higher lying levels in ^{207}Pb .

Table 5.4: Branching ratios for levels in ^{207}Pb nucleus and the corresponding absolute uncertainties. The present results are compared with the values from the evaluated level scheme [131].

E_{level} (keV)	E_{γ}	Present results		ENSDF	
		Intensity	Uncertainty	Intensity	Uncertainty
2623.5	1725.7	100	-	100	-
	2053.7	18.6	3.4	<4	-
2727	389	21.1	4.7	16	-
	1095	100	-	100	-

Branching ratios

For each of the levels at 2623.5 keV and 2727 keV excitation energy two γ -rays were observed (Fig. 5.56). From the integral gamma production cross-sections of this transitions (Fig. 5.64) the relative intensities (branching ratios) were deduced. These ratios were calculated from the gamma production cross-sections integrated over the same interval of neutron energy. Within the statistical fluctuations, the branching ratios of the two levels are constant with the neutron energy. The same threshold was observed for the γ -rays from the decay of every excited level. These two observation are an additional support for the correct identification of the γ -rays in the spectrum.

In Table. 5.4, the present branching ratios were compared with the evaluated values [131]. The present value for branching ratio of the 2053.7 keV transition is higher than the evaluated value. For the transitions from the level at 2727 keV the present values agree with the evaluated [131] values within the uncertainties.

(n,2n) gamma production cross-sections

For an identification of the γ -rays from the $^{207}\text{Pb}(n,2n)^{206}\text{Pb}$ reaction, the gamma ray spectrum was integrated over the neutron energies from about 7 MeV up to 25 MeV (Fig. 5.66). Four γ -rays from the (n,2n) reaction were observed. These peaks have contributions from the other (n,xn) reactions of different Pb isotopes in the sample as described in Table. 5.3. Only the cross-section of the 803.06 keV transition was corrected for the contribution from $^{208}\text{Pb}(n,3n)^{206}\text{Pb}$ reaction and that correction was very small (see Fig. 5.57). No correction was applied for the neutron attenuation and multiple scattering in the ^{207}Pb sample for these (n,2n) cross-sections.

At energies above 7 MeV the peak intensities of the 803.06 keV from the (n,2n) reaction and of the 897.78 keV from the (n,n'γ) reaction are comparable. Fig. 5.67 shows the gamma production cross-section for the four transitions observed in the $^{207}\text{Pb}(n,2n)^{206}\text{Pb}$ reaction. In the case of the 803.06 keV transition, the data of Vonach *et al.* [152] are slightly above the present results. For the other three transitions there is no other experimental data.

The energy resolution for the 803.06 keV was 35 keV at 10 MeV up to 200 keV

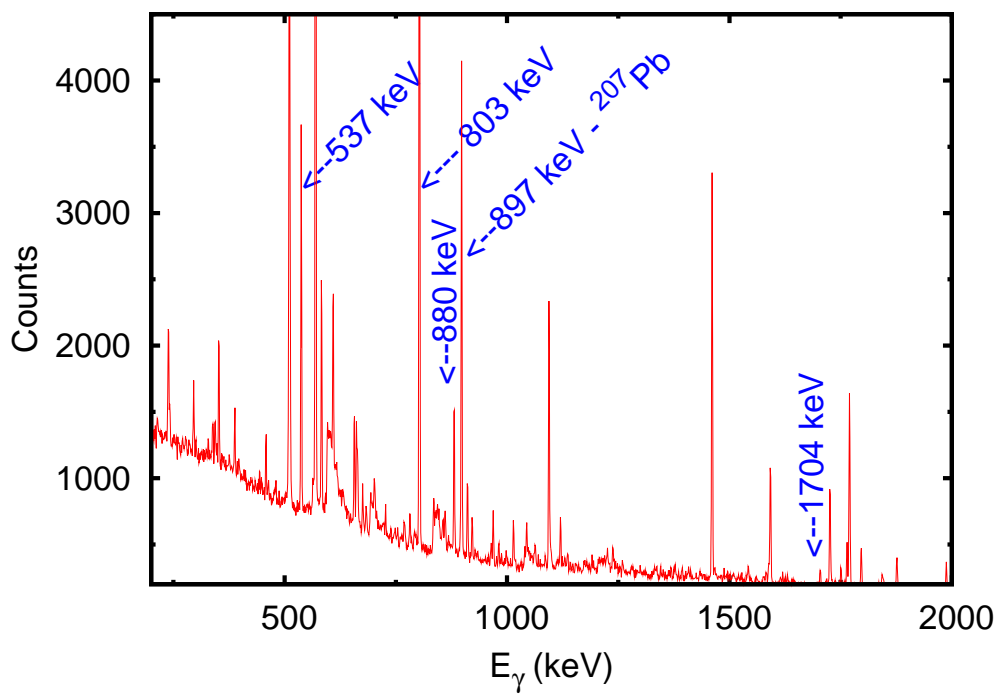


Figure 5.66: γ -rays spectrum for the ^{207}Pb measurement (92.4 keV% enriched sample) integrated over neutron energies from 6.7 MeV to about 25 MeV. The 803.06 keV and 537.47 keV γ -ray peaks from the $^{207}\text{Pb}(n,2n)^{206}\text{Pb}$ reaction are seen well in such a spectrum.

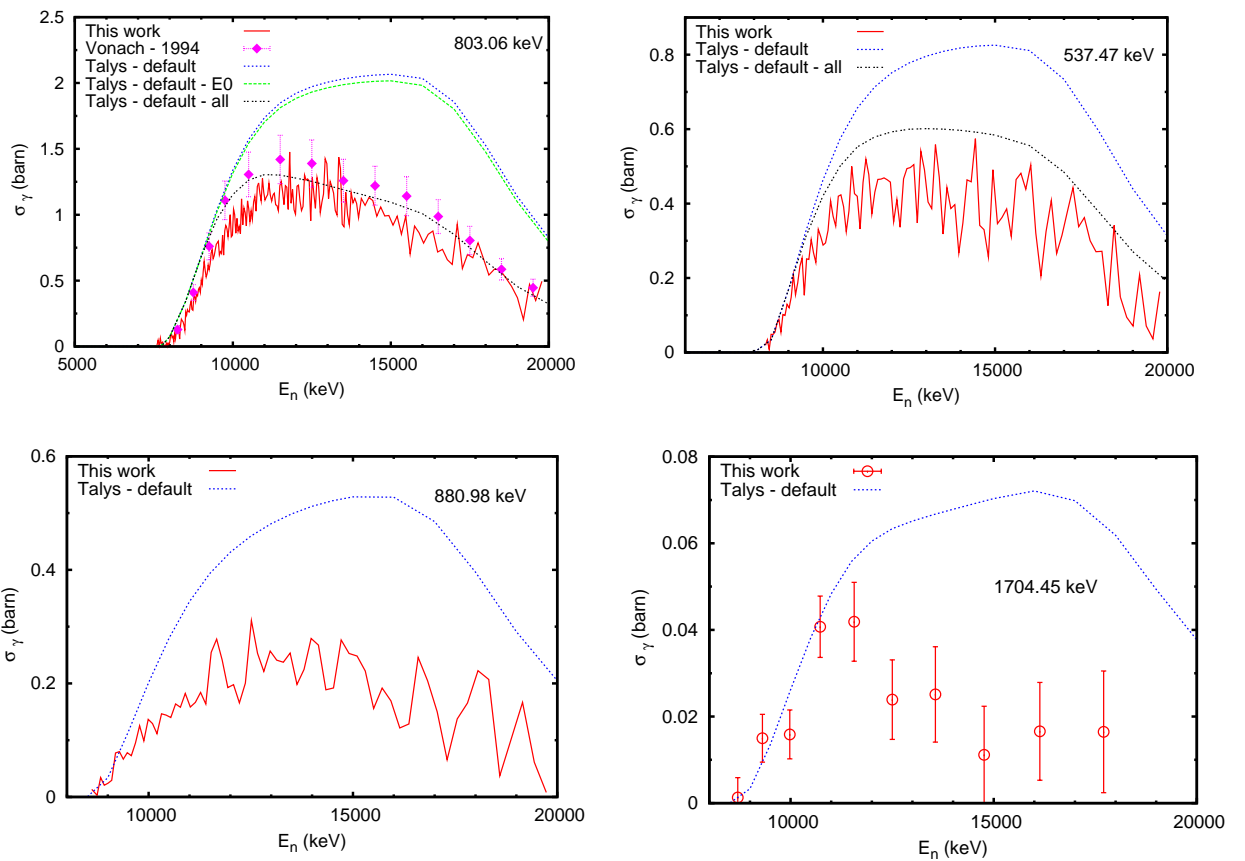


Figure 5.67: Integral production cross-section for the γ -rays from the $^{207}\text{Pb}(n,2n)^{206}\text{Pb}$ reaction.

at 19.5 MeV. A minimum of 8 % total uncertainty around 10 MeV was achieved. For the other three transitions a lower neutron energy resolution was used.

The (n,2n) cross-section measurement for ^{207}Pb is limited by the presence of the 0^+ level at 1165 keV and an isomer at 2200.14 keV in the residual nucleus of ^{206}Pb . The γ -rays from the decay of the isomer and the E0 transition were not observed in the prompt γ -ray spectrum. The measured gamma production cross-sections from the $^{207}\text{Pb}(n,2n)^{206}\text{Pb}$ reaction do not contain any contribution from the isomer and from 0^+ level. For a correct comparison with the present measurement, the Talys calculation with the input parameters has to be corrected for the isomer and for the E0 transition. This means that the calculated gamma production cross-sections of the γ -rays from the isomer have to be subtracted from the calculated gamma production cross-section of the transition that is fed by the isomer or by the 0^+ level.

After the correction for both the E0 transition and the isomer in ^{206}Pb , the Talys calculation is close to the present measurement for the 803.06 keV transition and 537.47 keV (Fig. 5.67). The differences that remained after the corrections for the isomer and for the E0 transition are at the limit of the uncertainty bars. After the isomer correction, the calculation gives lower cross-sections for the 880.98 keV transition, above 10 MeV. Above this energy the calculation gives negligible values while the measurements gives cross-sections of the order of 200 mb. The 1704.45 keV transition is not affected by the presence of the isomer in the level scheme of ^{207}Pb .

5.4.3 Total inelastic and level cross-sections

The angle integrated gamma production cross-sections and the evaluated level scheme of ^{207}Pb were used to construct the total inelastic and the level cross-sections as described in Sec. 2.1.2. These will be given in the following.

Total neutron inelastic cross-section

The total inelastic cross-section excluding the cross-section leading to the isomer was constructed using the production cross-section of the following transitions: 569.70 keV, 897.78 keV, 3300 keV, 3928 keV, 4104 keV and 4140 keV. All these γ -rays are drawn with "red" in Fig. 5.56. The total inelastic cross-section without the isomer contribution (Fig. 5.68) is exact up to about 4.1 MeV which is the highest energy of an observed excited level that decays directly to the ground state. Above 4.1 MeV, the present result is a lower limit for the total inelastic cross-section, excluding the isomer contribution.

The 569.7 keV and 897.78 keV transitions are the major components in the total neutron inelastic cross-section. The cross-section of all the other transitions is much smaller. Therefore, the same neutron energy resolution was obtained as in the case of the 569.7 keV gamma-production cross-section: 1.1 keV at 1 MeV and 35 keV at 10 MeV. A total uncertainty smaller than 8 % was obtained below 10 MeV (Fig. 5.68 *Right*). Higher uncertainties were obtained at the higher energies due to the low counting rate. The same observation is valid at low energies were

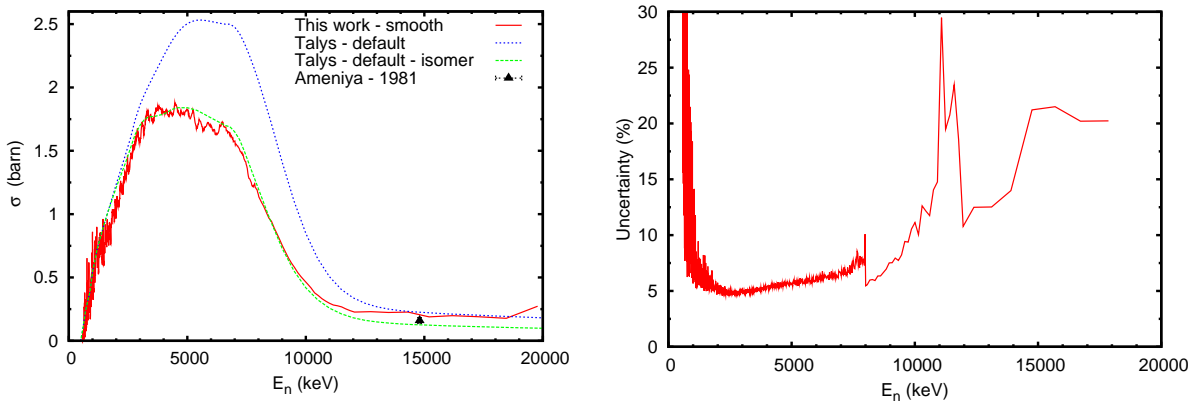


Figure 5.68: *Left:* Smooth data for the total neutron inelastic cross-section of ^{207}Pb on full energy range up to 20 MeV. *Right:* Total uncertainty of the total inelastic cross-sections.

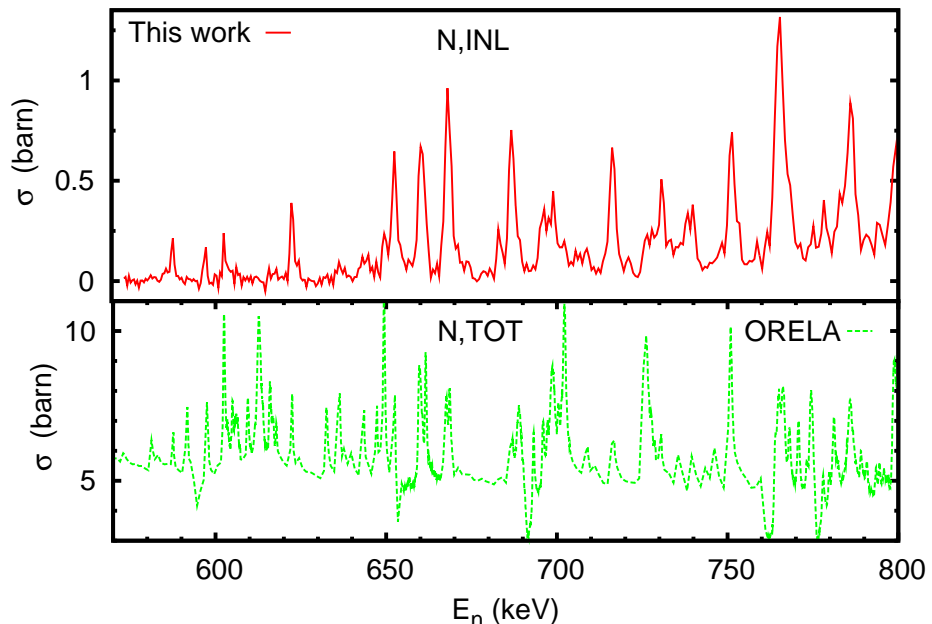


Figure 5.69: Full resolution total inelastic cross-section compared with the neutron total cross-section measured at ORELA [151]

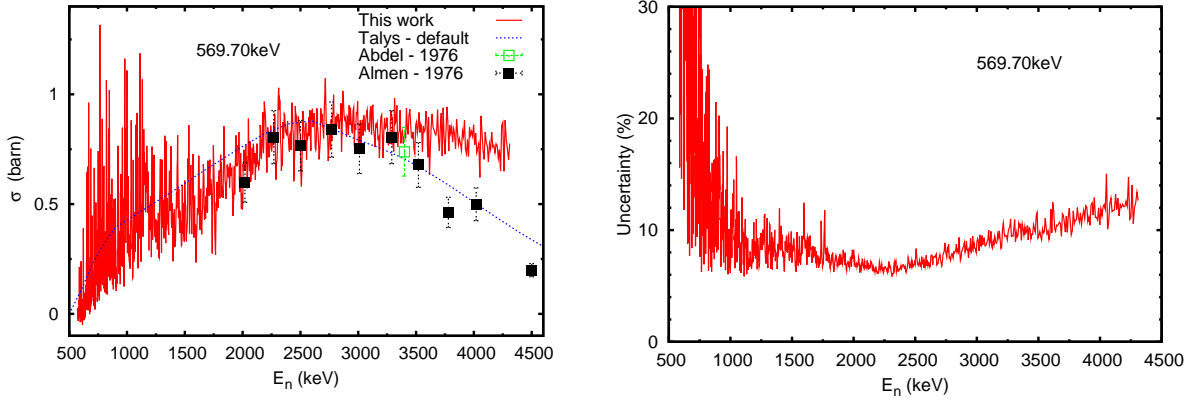


Figure 5.70: *Left:* The cross-section of the 569.7 keV level in ^{207}Pb . *Right:* The corresponding total uncertainty.

the counting rate was very small between the resonances (Fig. 5.69). The steps in the relative total uncertainty from Fig. 5.68 *Right* are due to the grouping of few neutron energy bins in one bin to reduce the statistical fluctuations. This grouping procedure was explained in Sec. 3.3.5.

In Fig. 5.69 the full resolution data for the total inelastic cross-section is compared with the neutron total cross-section measured in a transmission experiment at ORELA [151]. Many resonances from the total cross-section are observed also in the inelastic cross-section, but still with a poorer neutron energy resolution. It can be observed that the relative intensity of different resonances is different in the inelastic channel than in the total cross-section. For example, in the inelastic reaction, the resonance at 750 keV has smaller amplitude than the resonance at 765 keV (Fig. 5.69). The intensity is reversed in the total cross-section.

Only one experimental point was found in the literature for the total inelastic cross-section at 14.7 MeV (Ameniya *et al.* [130]). This point agrees well with the present measurement (Fig. 5.68).

For a correct comparison with the present experimental data, the Talys calculation with the default input parameters has to be corrected for the contribution of the isomer to the total inelastic cross-section. Fig. 5.68 shows both Talys curves, corrected and uncorrected for the contribution of the isomer level. After the correction for the isomer level in ^{207}Pb at 1633 keV, the calculation describes generally well the measured cross-section on the full energy range. The difference between the calculation and the measurement at energies above 12 MeV is within the given uncertainties of the present measurement.

Level 569.703 keV

The cross-section of the level at 569.7 keV in ^{207}Pb (Fig. 5.70) is exact up to about 4.1 MeV, the maximum observed excitation energy. The following γ -rays were used for this level cross-sections: 569.702 keV, 897.78 keV, 1770.237 keV, 1725.7 keV, 2092.7 keV and 2737.0 keV. Fig. 5.70 *Right* shows the relative total uncertainty of

the cross-section of the level at 569.70 keV. This is around 8 % in the middle of the energy range and increases up to 12 % at 4.1 MeV. The large relative uncertainty at low energies, just above the threshold are the results of the statistical fluctuations and the poor statistics between the resonances.

The present results agree well with both the experimental existing data and with the Talys calculation up to about 3.5 MeV. Above this energy the calculation and the results of Almen *et al.* [130] are lower. The Abdel *et al.* [?] data point at about 3.4 MeV agrees within the error bars with the present measurement.

Levels with higher excitation energy

Besides the level at 569.7 keV, the cross-section was constructed for the excited levels with energy up to 3.633 MeV (Fig. 5.71). The level cross-sections are not affected by the presence of the isomeric level at 1633.37 keV in ^{207}Pb and are exact up to 4.3 MeV incident neutron energy. This is valid because the maximum energy of an observed excited level was 4.3 MeV.

Previous experimental data were found only for the second excited level at 897.80 keV (Fig. 5.71). The data of Almen *et al.* [130] agree with the present results within the uncertainties. The point of Abdel *et al.* [130] is about a factor 2 higher than the present data.

The Talys calculation with the default input parameters describes well the measured data for the level at 2623.5 keV and only at energies below 3.5 MeV for the levels at 2662.4 keV and 2727.0 keV. Above this energy, the calculation gives lower values for the level cross-sections. For the level at 2339.94 keV, a slightly different shape is given by the calculation. For the 3633.0 keV no default calculation was available.

5.4.4 Conclusions

For ^{207}Pb , the gamma production cross-section was measured for 15 γ -rays from neutron inelastic scattering and 4 γ -rays from the (n,2n) reaction. For two excited levels in ^{207}Pb , two γ -rays from the decay of every level were observed. The branching ratios were deduced for these γ -rays.

In the present experiment only the prompt γ -rays were detected and the measured cross-sections do not include the feeding from the isomer level at 1633 keV. Similar, the measured (n,2n) gamma production cross-sections do not include the contribution from the isomer at 2200 keV and from the E0 transition in the residual nucleus of ^{206}Pb . Because the sample was enriched only to 92.4 %, a correction was needed for the (n,xn) reactions on different isotopes.

The gamma production cross-section of the intense γ -rays and the total inelastic cross-sections were measured over the full energy range from the threshold up to about 20 MeV with a neutron energy resolution of 1.1 keV at 1 MeV (35 keV at 10 MeV). The total uncertainty of the gamma production cross-section of the 569.702 keV transition was about 5 % in the middle of the energy range, increasing

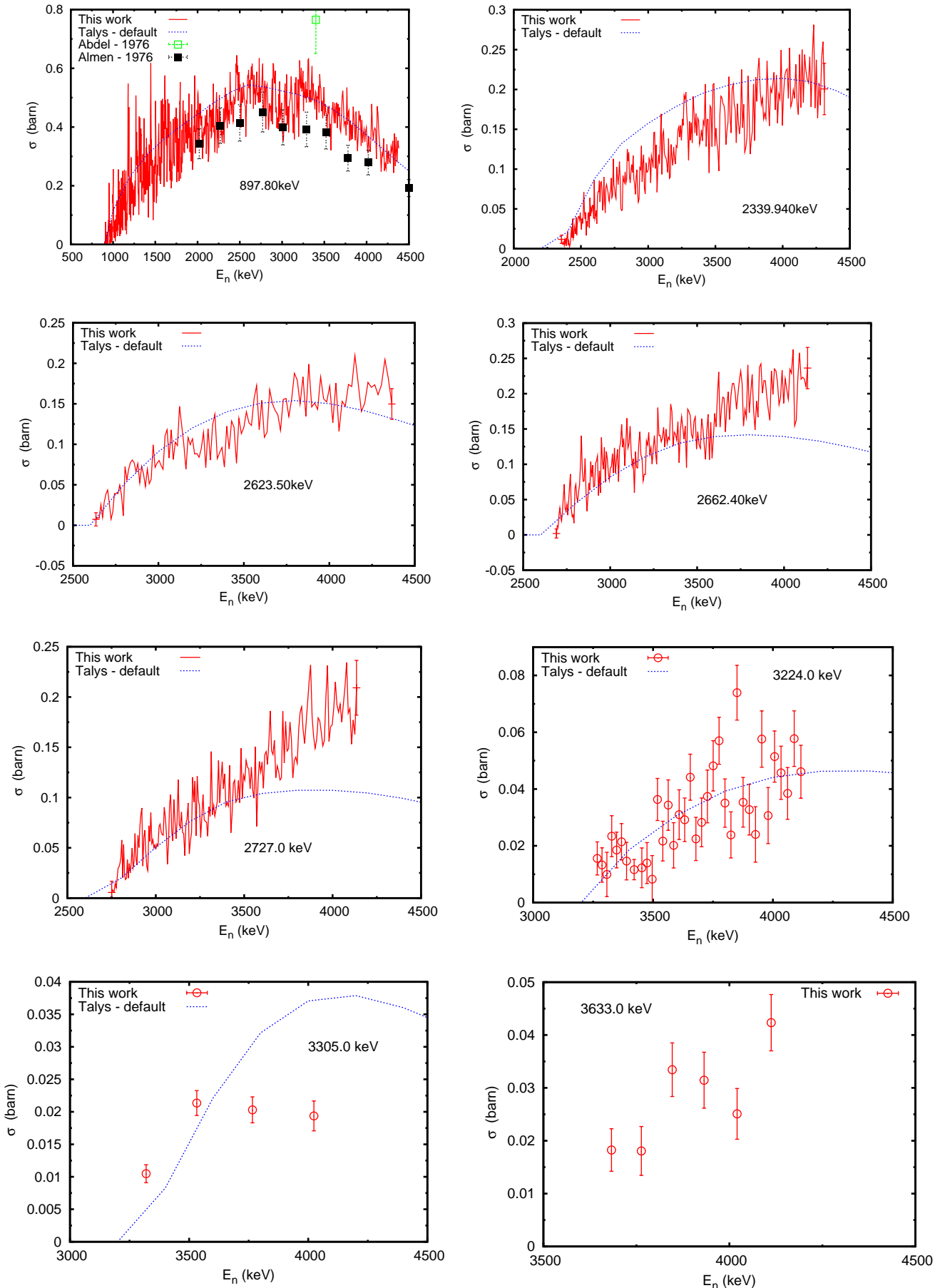


Figure 5.71: The cross-section of the excited levels above 570 keV in ^{207}Pb .

at the extremities because of the statistical fluctuations. Uncertainties below 25% at the maximum of the cross-section were obtained for the other γ -rays.

The total neutron inelastic scattering cross-section and the level cross-sections were constructed based on the evaluated level scheme of ^{207}Pb and using the measured integral gamma production cross-sections. The transitions of 569.70 keV and 897.78 keV had the largest contribution to the total inelastic cross-section.

Due to the unprecedented neutron energy resolution of the experimental setup at GELINA, well defined resonance structures were observed for the 569.702 keV and for the 897.78 keV γ -rays below about 2.5 MeV. These resonances in the inelastic cross-sections were compared with the resonances in the total neutron cross-sections from the literature.

Few experimental data were available for the comparison with the present results. The disagreement with some previous measured data may be explained by the use of the detectors with poor resolution (NaI detectors), the use of natural Pb sample or improper multiple scattering correction.

The present measured data were compared also with the Talys calculation with the default input parameters. The Talys calculation had to be corrected for the contribution of the isomer level in ^{207}Pb . Corrections for the E0 transition and for the isomer level in ^{206}Pb nucleus were needed for a correct comparison in the case of the (n,2n) gamma production cross-sections. In the case of ^{207}Pb the code describes relatively well the production cross-sections of the most intense γ -rays. For the other γ -rays the agreement is good only at low neutron energies. Significant differences are observed at energies above 3 MeV. This general good agreement of the gamma production cross-section at low neutron energy may explain also the relative good agreement between the calculation and the present measurement for the level cross-sections.

For the (n,2n) cross-sections, after the correction for the isomer level in the residual nucleus ^{206}Pb , the calculation gives comparable values for the most intense transition. Large difference were observed for the other 3 measured transition from the (n,2n) reaction on ^{207}Pb .

In conclusion, a large amount of precise neutron inelastic and (n,2n) reaction cross-section data were produced in only one run, from the threshold up to about 20 MeV. These data can be used in future neutron data evaluations and as benchmark for the nuclear codes.

5.5 ^{208}Pb neutron inelastic scattering, (n,2n) and (n,3n) cross-sections

5.5.1 Introduction

The ^{208}Pb nucleus was studied by different authors using both techniques described in Sec. 2.1((n,n')-technique and (n,xn γ)-technique). Experiments like Towle *et al.* [163], Almen *et al.* [130], Finlay *et al.* [157] and Bainum *et al.* [160] use the (n,n')-technique. All these experiments were able to identify only few neutron energy groups. Moreover Finlay *et al.* [157] and Bainum *et al.* [160] measured only the differential level cross-sections.

The (n,n' γ)-technique was used in experiments from Refs. [152–156, 161]. All these experiments used germanium detectors (Ge(Li) or HPGe). In the experiment of Dickens *et al.* [161] a large number of γ -rays from ^{208}Pb were identified and their production cross-section was measured at 6 energies between 4.9 MeV and 8 MeV. The measurement was done with a Ge(Li) detector placed at 55° and 125° . The maximum observed excitation energy was about 6.6 MeV. Only the transition from the first excited state to the ground state was measured in the experiment of Vonach *et al.* [152] for the neutron inelastic, (n,2n) and (n,3n) reactions on ^{208}Pb . The measurement was done with the HPGe detectors at 125° , from the threshold up to 200 MeV neutron energy. The normalization of the Vonach data was done relative to the measurement of Hlavac *et al.* [154] at 14.7 MeV. At its turn the Hlavac measurement was normalized to the gamma production cross-section of the 1434 keV transition in $^{52}\text{Cr}(n,n'\gamma)^{52}\text{Cr}$ reaction. In Refs. [155, 156] the γ -rays were measured from the decay of levels around 5.5 MeV excitation energy.

As in the case of the ^{207}Pb measurement, corrections for the isotopic composition of the sample were needed for the ^{208}Pb sample. The studied residual nuclei (^{208}Pb , ^{207}Pb and ^{206}Pb) were produced in different (n,xn γ) reaction on the isotopes present in the sample. In Table. 5.5 is shown how the γ -ray peaks are produced in the ^{208}Pb sample with only 88.1 % enrichment. All the (n,2n) and (n,3n) production cross-sections measured here were corrected for the contribution of different isotopes.

In the present measurement 29 γ -rays were observed from the inelastic scattering

Table 5.5: Corrections for the isotopic composition of ^{208}Pb sample results. The threshold is given for the γ -ray production in different reactions.

residual nucleus	reaction	content in the sample	threshold (MeV)
^{208}Pb	$^{208}\text{Pb}(n,n'\gamma)^{208}\text{Pb}$	88.11 %	2.63
^{207}Pb	$^{208}\text{Pb}(n,2n\gamma)^{207}\text{Pb}$	88.11 %	7.98
	$^{207}\text{Pb}(n,n'\gamma)^{207}\text{Pb}$	0.89 %	0.57
^{206}Pb	$^{208}\text{Pb}(n,3n\gamma)^{206}\text{Pb}$	88.11 %	14.98
	$^{207}\text{Pb}(n,2n\gamma)^{206}\text{Pb}$	0.89 %	7.57
	$^{206}\text{Pb}(n,n'\gamma)^{206}\text{Pb}$	10.99 %	0.81

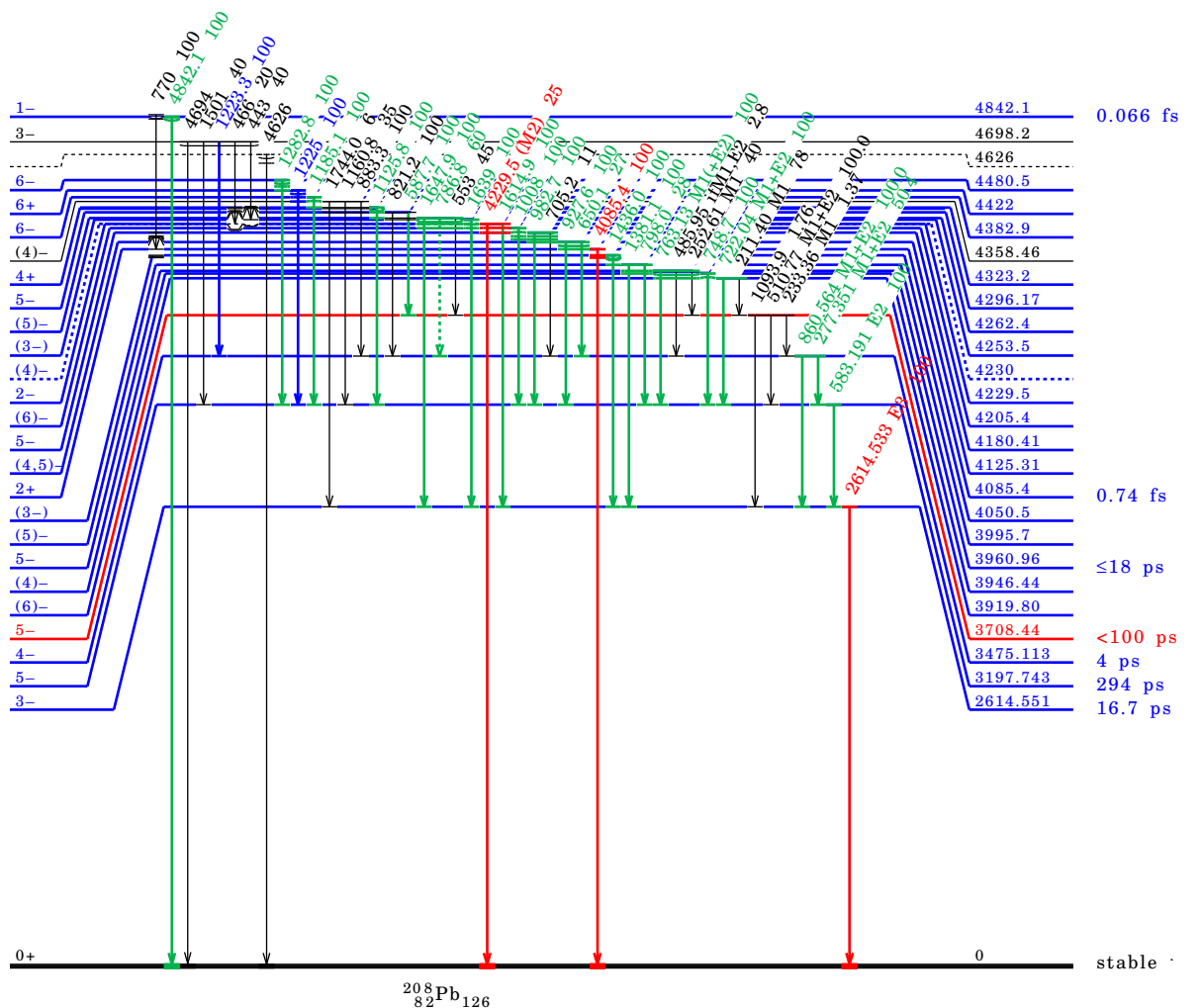


Figure 5.72: Simplified evaluated level scheme of ^{208}Pb [131]. The gamma production cross-section of the transitions drawn with colors was measured in the present experiment. The "red" γ -rays were used to construct the total inelastic cross-section. The level at 3708.44 keV was not observed because it decays through a 510.36 keV γ -ray that could not be distinguished from the 511 keV in the background.

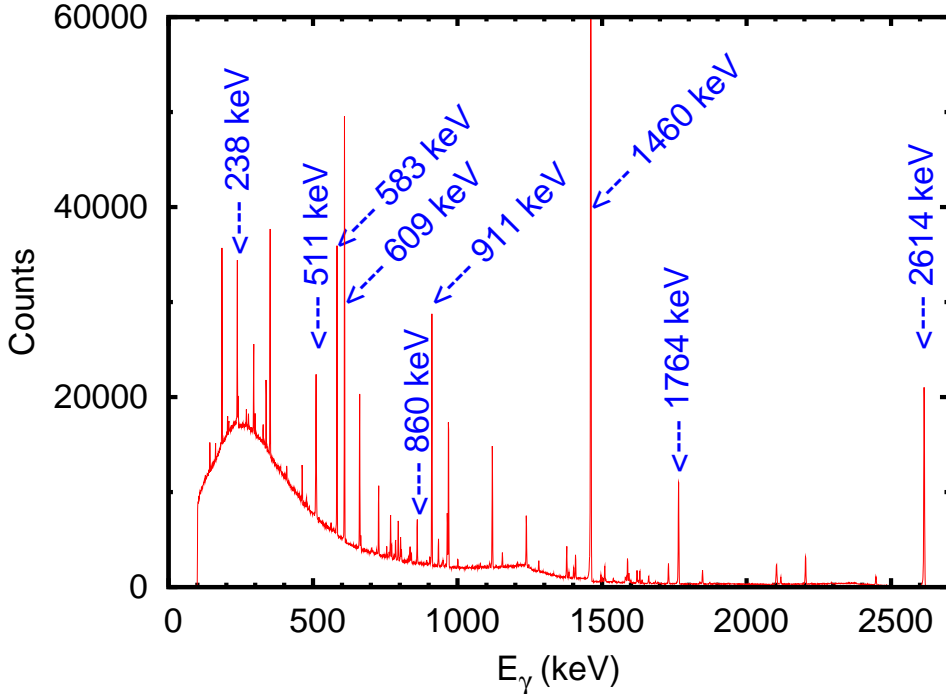


Figure 5.73: Background spectrum with the ^{208}Pb sample in position and no neutron beam. The 2614.5 keV, 583.19 keV and 860.56 keV peaks from ^{208}Pb are present in the background.

on ^{208}Pb , 5 γ -rays from the ($n,2n$) reaction and one γ -ray from the ($n,3n$) reaction. The maximum observed excitation energy in the inelastic scattering was 5563 keV. Up to 4323 keV at least one γ -ray was observed to decay from every excited level. The level at 3708.44 keV was not observed because it decays through a 510.36 keV γ -ray that could not be distinguished from the 511 keV in the background.

The total inelastic and the level cross-sections were constructed using the level scheme of ^{208}Pb and the measured integral gamma production cross-sections. The detailed results for ^{208}Pb nucleus are given in the following.

5.5.2 Gamma production cross-sections

The ^{208}Pb sample used in the present experiment had radiogenic origin. Therefore a slightly increased radioactivity was observed from the sample and a higher background was measured with the sample in position, especially at energies below 500 keV. The background spectrum measured with one of the HPGe detector is shown in Fig. 5.73 as an example. Different from the other 4 nuclei presented in this work, the main γ -ray peaks of ^{208}Pb are always present in a background spectrum. All these ^{208}Pb transitions from the background result from the decay of the parent nucleus ^{208}Tl . The most intense γ -rays from the natural decay of ^{208}Tl and their relative intensities are: 2614.533 keV (99.16 %), 583.191 keV (84.5 %), 510.77 keV (22.6 %), 860.564 keV (12.42 %), 277.35 keV (6.31 %) and 763.13 keV (1.81 %).

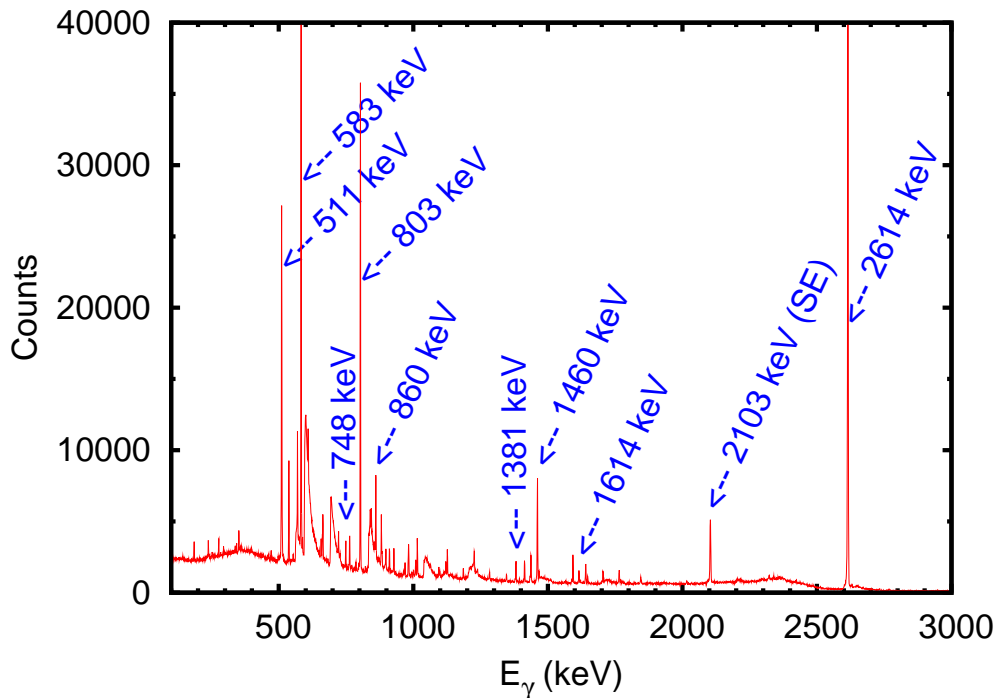


Figure 5.74: The γ -ray spectrum of an HPGe detector with the ^{208}Pb sample (88.11% enrichment). The spectrum was integrated over the neutron energies from 500 keV up to about 25 MeV. The main γ -ray peaks from the inelastic scattering on the ^{208}Pb sample are clearly visible. The small counting rate of the experiment is suggested by the high intensity of the 1460 keV peak from ^{40}K . The 2103 keV is the single escape peak from the 2614 keV γ -ray.

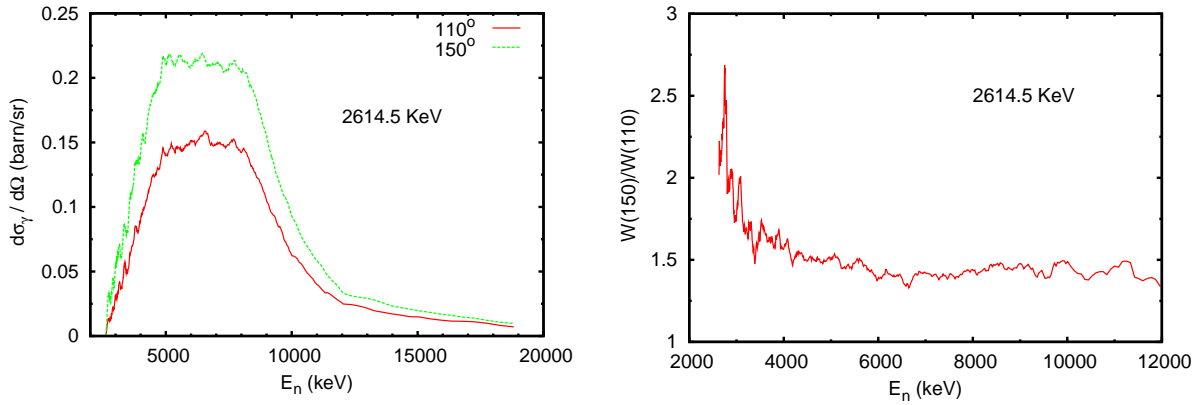


Figure 5.75: Differential gamma production cross-section for the 2614.5 keV transition in ^{208}Pb . *Left:* Smoothed curves from the threshold up to 20 MeV at two angles, 110 and 150 degrees. *Right:* The ratio between the angular distribution $W(\theta)$ at 150 and 110 degrees.

The presence of the ^{208}Pb peaks in the natural background resulted in an average HPGe yield different from zero below the thresholds in the $^{208}\text{Pb}(n,n'\gamma)^{208}\text{Pb}$ reaction. Such effect was observed only for three γ -rays: 2614.5 keV, 583.19 keV and 860.56 keV. The 510.77 keV transition was not measured at all in this experiment because these γ -ray peak coincides with the 511 keV peak from the background. The other γ -ray peaks from the decay of ^{208}Tl nucleus were not observed in the background measurement with the sample in position because of their low intensity. For the 2614.5 keV, 583.19 keV and 860.56 keV transitions the prompt γ -ray yield was corrected for the natural background measured in an independent run of 48 hours and normalized to the acquisition time. After the correction, the average HPGe yield equals zero below the reaction threshold.

The angle integrated production cross-section for the γ -rays from the $(n,xn\gamma)$ ($x=1,2,3$) reaction on ^{208}Pb are given in the following. The angle integration was done with the Gauss quadrature procedure described in Sec. 2.3.3. The differential gamma production cross-section at the two measurement angles 110° and 150° is given only for two transitions as example.

2614.5 keV

Fig. 5.75 shows the differential production cross-section for the 2614.5 keV transition at two angles 110° and 150°. For this transition one can observe a significant angular distribution. The ratio between the angular distribution ($W(\theta) = \frac{4\pi}{\sigma} \frac{d\sigma}{d\Omega}(\theta)$) at 150° and 110° (Fig. 5.75 *Right*) has a maximum at the inelastic threshold and decreases at high energies where become almost constant, equal to 1.5. According to the theoretical predictions for an E3 transition from the 3⁻ level to 0⁺ level(Eq. 2.17), the ratio between the angular distribution at 150° and 110° equals 2.59 just above the threshold. This prediction is in good agreement with the observed value.

Fig. 5.76 shows the full neutron energy resolution data for the differential and for

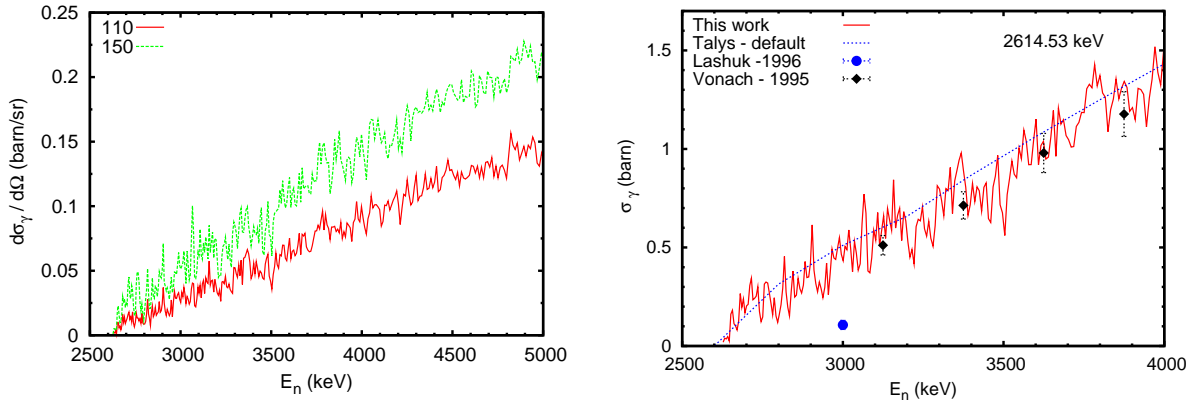


Figure 5.76: Full resolution gamma production cross-section for the 2614.5 keV transition in ^{208}Pb . *Left:* Differential gamma production cross-section at 110° and 150° . *Right:* Integral gamma production cross-section compared with Talys calculation.

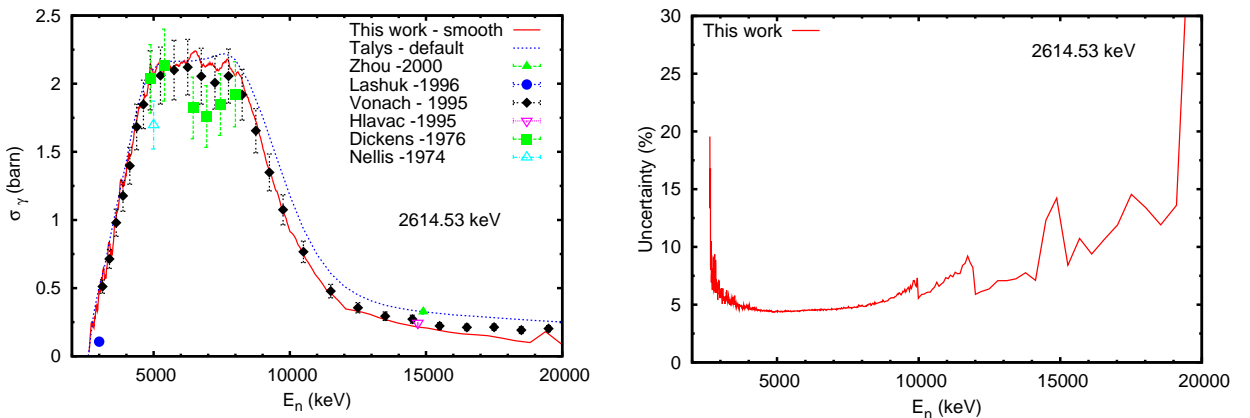


Figure 5.77: *Left:* Integral gamma production cross-section for the 2614.5 keV transition in ^{208}Pb . Full energy scale from threshold up to 20 MeV. The data were smoothed with an averaging moving window filter for an easier comparison with other data. *Right:* The corresponding total uncertainty.

the integral gamma production cross-section of the 2614.5 keV transition. No clear resonance structures were observed for the ^{208}Pb nucleus, despite de good neutron energy resolution that was used.

The integral gamma production cross-section on full energy range from the inelastic threshold up to 20 MeV is given in Fig. 5.77. The smoothed curve is given here to allow an easier comparison with the other data. The present data were obtained with a neutron energy resolution of 1.1 keV at 1 MeV (35 keV at 10 MeV). The corresponding total uncertainty is shown in the *Right* panel of Fig. 5.77. The total uncertainty is around 5 % below 8 MeV and increases up to 15 % at about 20 MeV. The increase in the total uncertainty above 8 MeV is due to the statistical fluctuations. The same observation is valid just above the inelastic threshold where the cross-section increases slowly and consequently the statistics is poor. The steps at 10 MeV and 12 MeV in the relative total uncertainty are the result of the grouping of few neutron energy bins in one bin to improve the statistical uncertainty. The grouping procedure was described in Sec. 3.3.5.

A detailed measurement of the gamma production cross-section of the 2614.5 keV transition had been done by Vonach *et al.* [152]. The present results agree well with the data of Vonach *et al.*. In the experiment of Vonach *et al.* the γ -ray detection was done at 125° with respect to the beam direction. The integral gamma production cross-section was calculated multiplying the differential gamma production cross-section at 125° with 4π . For the angular distribution of the 2614.5 keV as given by Eq. 2.17, the angle integration method used by Vonach *et al.* should underestimate the integral cross-section with about 17 % just above the inelastic threshold compared with the Gauss quadrature used in the present work (Sec. 2.3.3). With the increase of the neutron energy, the difference between the two integration procedures should diminish to about 10 % because of the decrease in the anisotropy (see also Fig. 5.75 *Right*). Such difference between the two data sets is not observed in Fig. 5.77.

The point measurement of Lashuk *et al.* [130] at 3 MeV and the measurement of Zhou *et al.* [153] at 14.7 MeV are lower and respectively higher than the present results. The Hlavach *et al.* [154] measured point at 14.7 MeV agrees well with the present measurement. The Dickens *et al.* [161] points at 4.9 MeV and 5.4 MeV agree well with the present measurement, while the other four points between 6.4 MeV and 8 MeV are lower. The Nellis *et al.* [162] point at 5 MeV is also lower than the present data.

The Talys calculation with the default parameters agrees well with the measured data up to about 7 MeV. Above this energy, the calculation is slightly higher. No correction was needed to the calculation for the comparison with the present measured data.

583.19 keV

Fig. 5.78 gives the differential gamma production cross-section for the second transition in ^{208}Pb nucleus. The typical angle dependence of an E2 transition is observed. The ratio of the differential cross-section at the two angles 150° and 110° has the

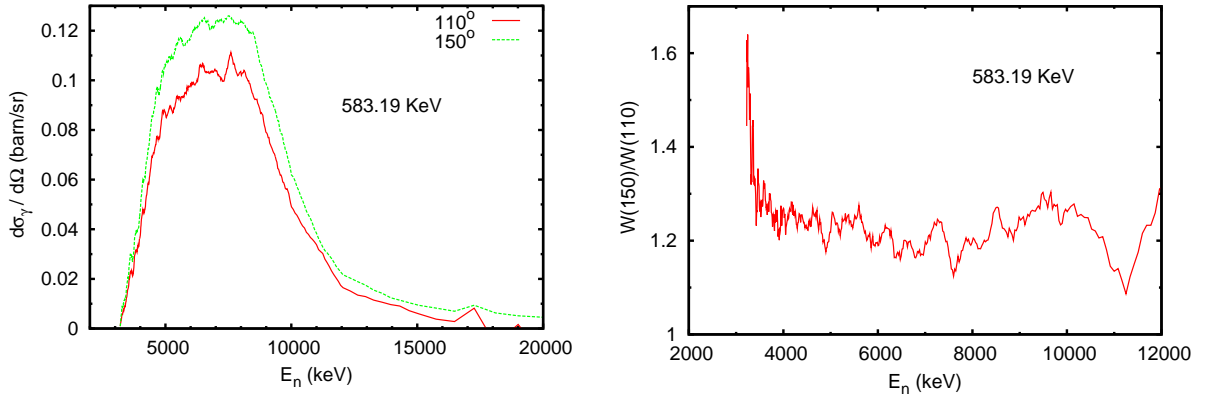


Figure 5.78: Differential gamma production cross-section for the 583.19 keV transition in ^{208}Pb . *Left:* Smoothed curves from the threshold up to 20 MeV at two angles, 110° and 150° . *Right:* The ratio between the angular distribution $W(\theta)$ at 150° and 110° .

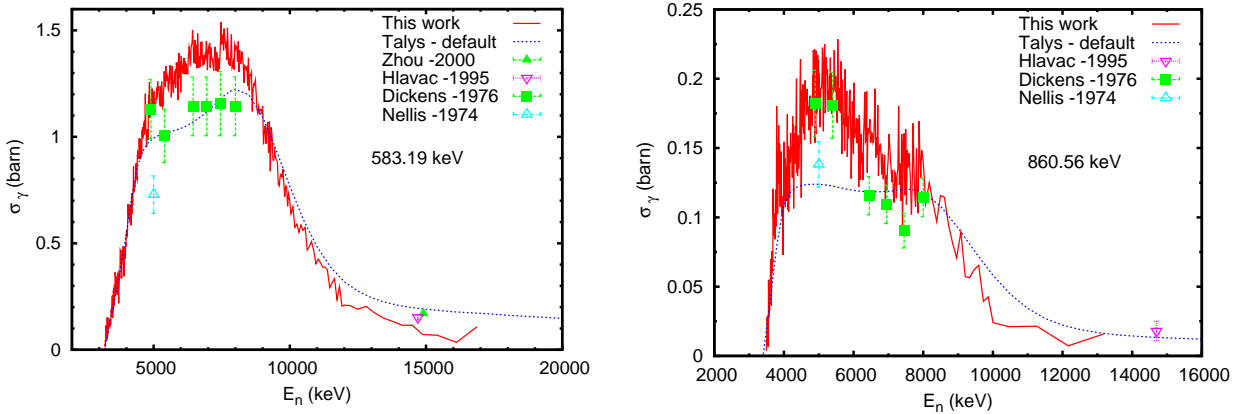


Figure 5.79: Integral gamma production cross-section for ^{208}Pb . Full energy scale from threshold up to 20 MeV. *Left:* 583.19 keV transition .*Right:* 860.56 keV transition.

maximum value at the threshold and become almost constant, equal to 1.2, above 4 MeV. The behavior of this E2 transition from a 4^+ level to a 2^+ level is similar with the energy dependence of the angular distribution for the other measured E2 transitions in ^{52}Cr and ^{206}Pb .

The integral gamma production cross-section of the 583.19 keV transition is given in Fig. 5.79. For this transition the production cross-section was measured from the threshold, 3.2 MeV, up to 17 MeV. The previous measurements of Zhou *et al.* [153] and Hlavac *et al.* [154] gave slightly higher values for the integral gamma production cross-section. The Dickens *et al.* [161] point at 4.9 MeV agrees with present measurements. The other points of Dickens *et al.* are lower. The Nellis *et al.* [162] point at 5 MeV is also lower.

The Talys calculation with the default parameters agrees well with the measurements up to 5 MeV and between 9 MeV and 12 MeV. The calculation underestimates the integral cross-section with about 25 % in the energy range between 5 MeV and 9 MeV. At high energies, above 12 MeV the calculation predicts higher values.

The transitions from higher lying levels

The integral production cross-section for other 27 γ -rays from the neutron inelastic scattering on ^{208}Pb nucleus are given in Figs. 5.79 *Right*, 5.80, 5.81, 5.82, 5.83. The 2948 keV transition decays from the maximum observed excited level at 5563 keV. The level at 3708.44 keV was not observed because it decays through a 510.36 keV γ -ray. Above 4480.5 keV some excited levels were not observed, maybe because of their low cross-section.

The cross-section of the majority of these transitions was measured only up to about 10 MeV incident neutron energy. Above this energy the statistics was not sufficient for a precise measurement; the γ -ray peaks were not clearly visible from the background even after grouping several energy bins.

The production cross-section of the observed transitions from levels higher than 3.4 MeV had maximum values between 15 mb and 200 mb. At the extremities of the measurement energy interval the cross-sections are much lower.

In general the data of Hlavac *et al.* [154] and the data of Dickens *et al.* [161] agree well with the value that can be extrapolated from the present measurement (Fig. 5.79 *Right*).

The Talys code calculates the production cross-section of the γ -rays that decay from levels up to 4229 keV. Where calculation is available, there is no systematic difference between the present measurement and the calculation. Some gamma production cross-sections are well described by the calculation (722 keV, 1436 keV or 1008 keV). In the case of the 860 keV, 748 keV and 763 keV the difference to the measured values is not negligible.

Branching ratios

In ^{208}Pb nucleus, five were the cases where two γ -rays that decay from the same excited level were observed. For these levels the ratios between the γ -ray intensity (branching ratios) were measured. The intensity ratio was calculated as the ratio

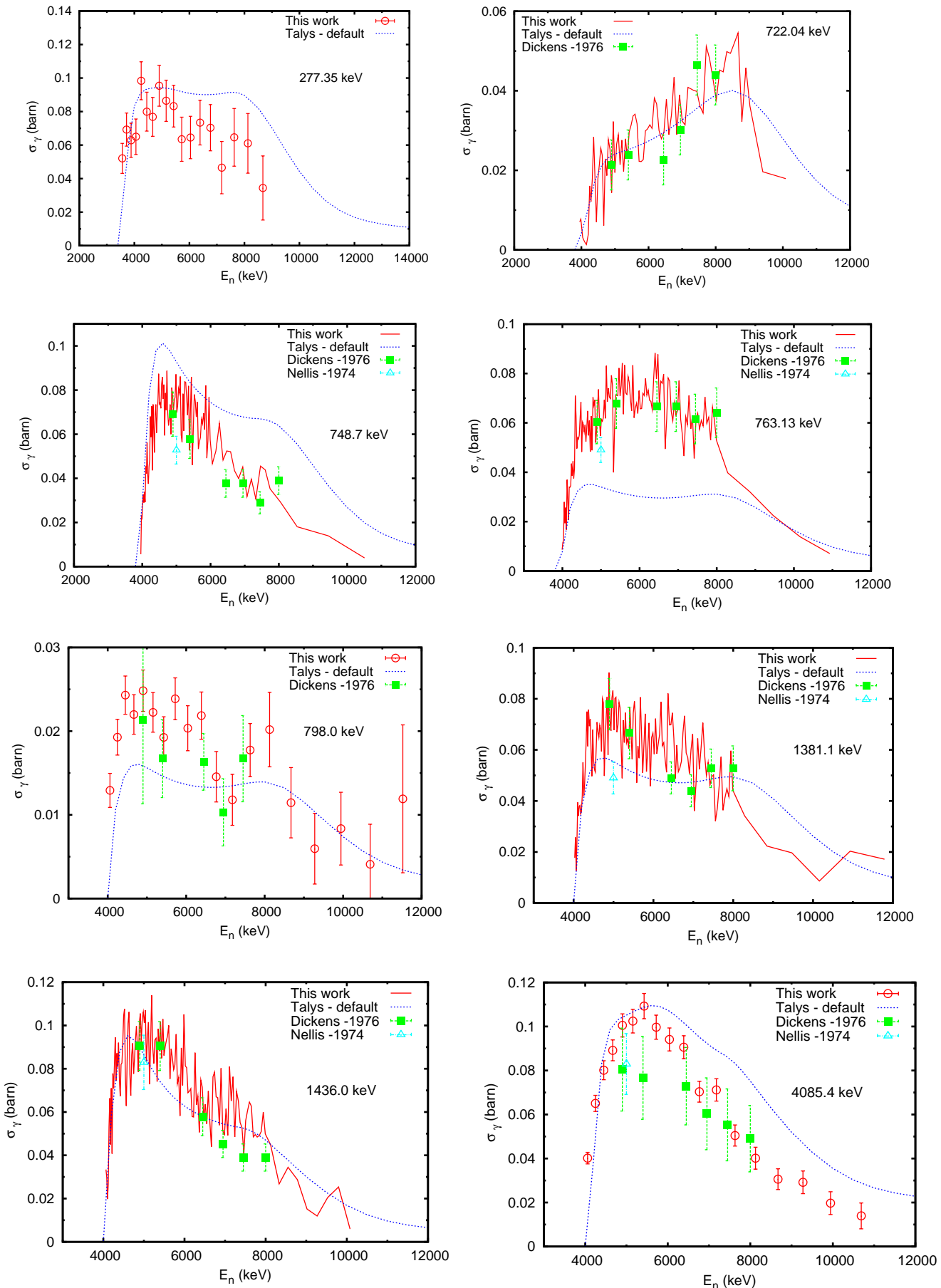


Figure 5.80: Integral gamma production cross-section for the transitions from higher lying levels in ^{208}Pb .

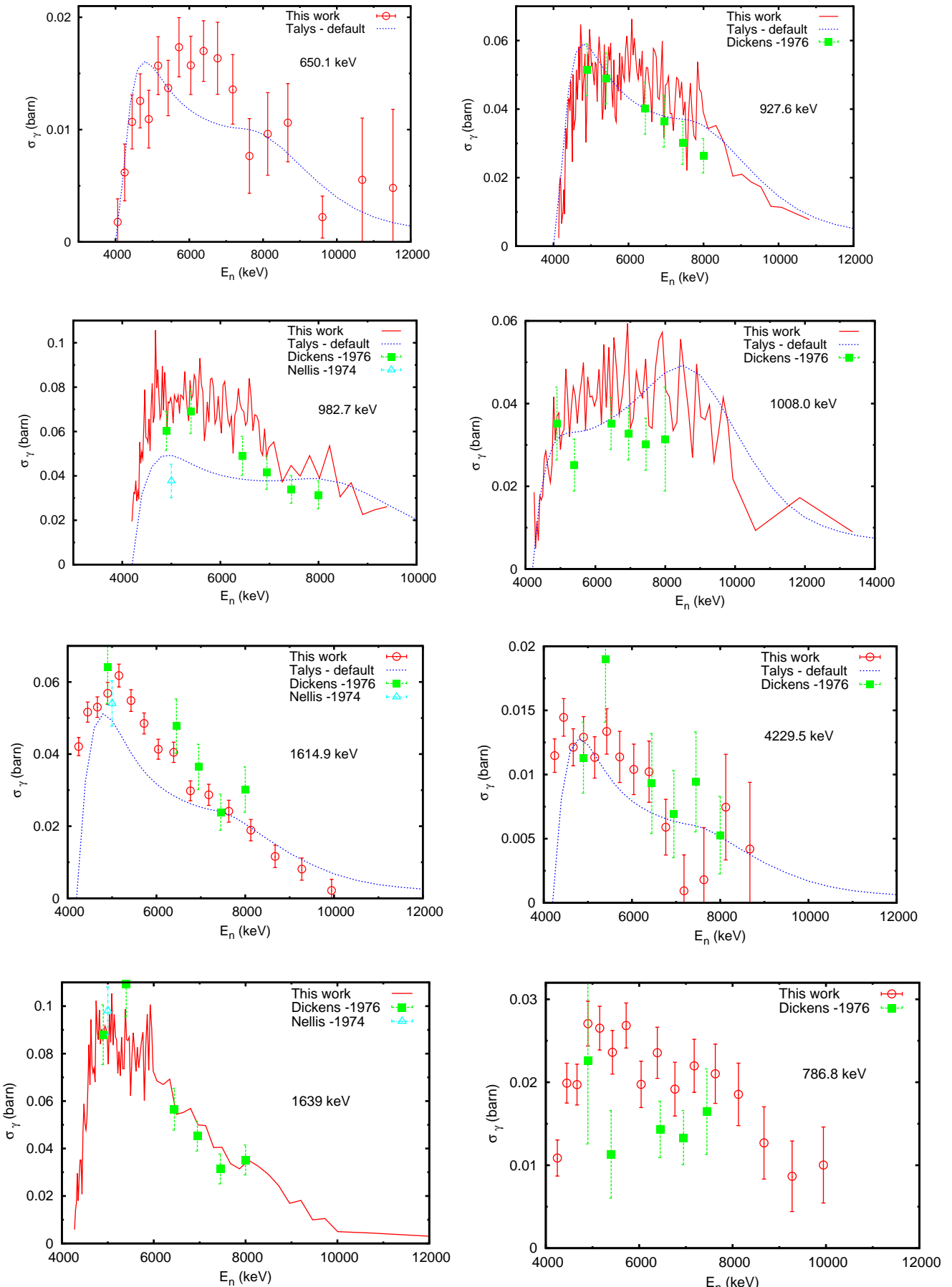


Figure 5.81: Integral gamma production cross-section for the transitions from higher lying levels in ^{208}Pb .

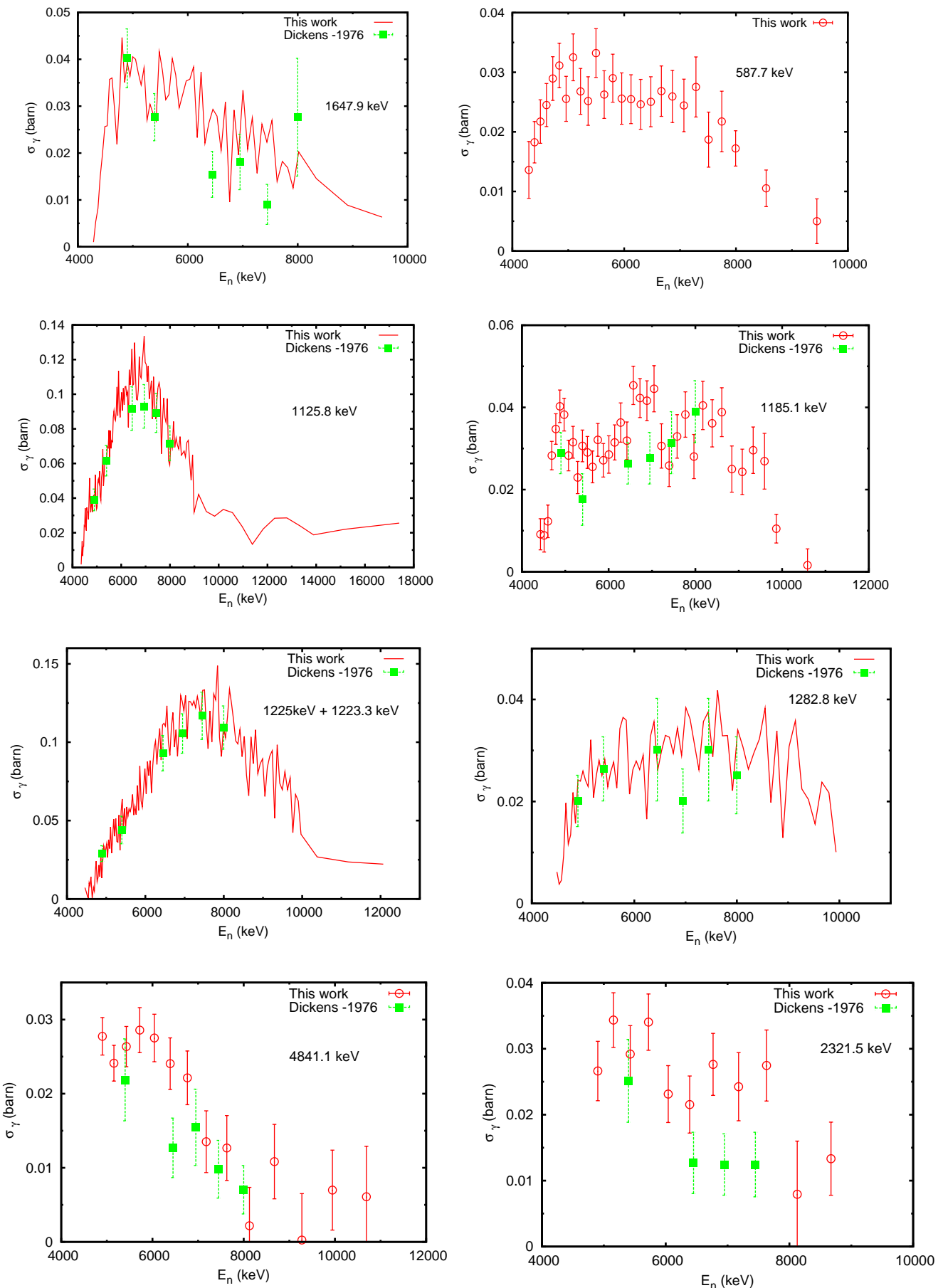


Figure 5.82: Integral gamma production cross-section for the transitions from higher lying levels in ^{208}Pb .

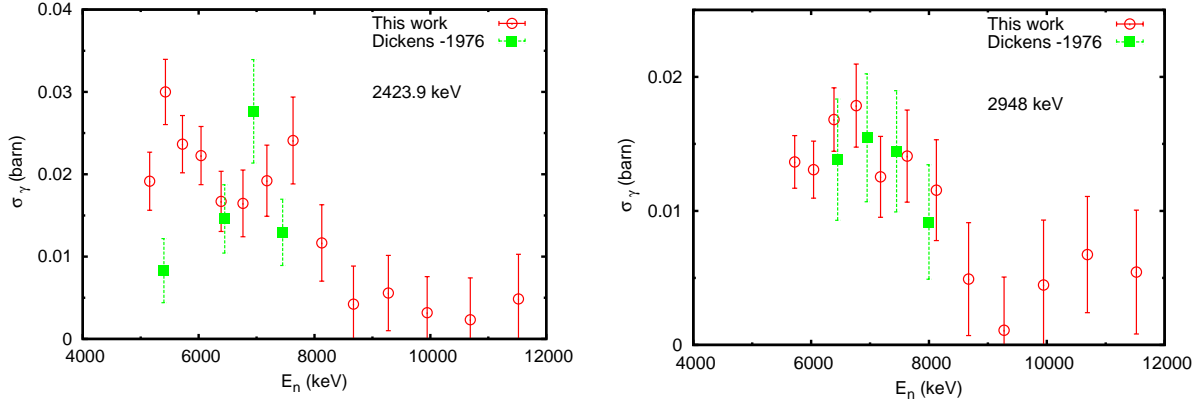


Figure 5.83: Integral gamma production cross-section for the transitions from higher lying levels in ^{208}Pb .

Table 5.6: Branching ratios for levels in ^{208}Pb nucleus and the corresponding absolute uncertainties. The present results are compared with the values from the evaluated level scheme [131].

E_{level} (keV)	E_γ	Present results		ENSDF	
		Intensity	Uncertainty	Intensity	Uncertainty
3475.113	277.35	45.0	7.5	50.4	1.6
	860.564	100	-	100	1.1
3995.7	798.0	32.7	4.9	28.0	4
	1381.1	100	-	100	-
4125.31	650.1	29.6	5.2	27	4
	927.6	100	-	100	-
4229.5	1614.9	100	-	100	-
	4229.5	22.4	2.8	25	6
4262.4	786.8	81.0	14.6	60	13
	1647.9	100	-	100	-

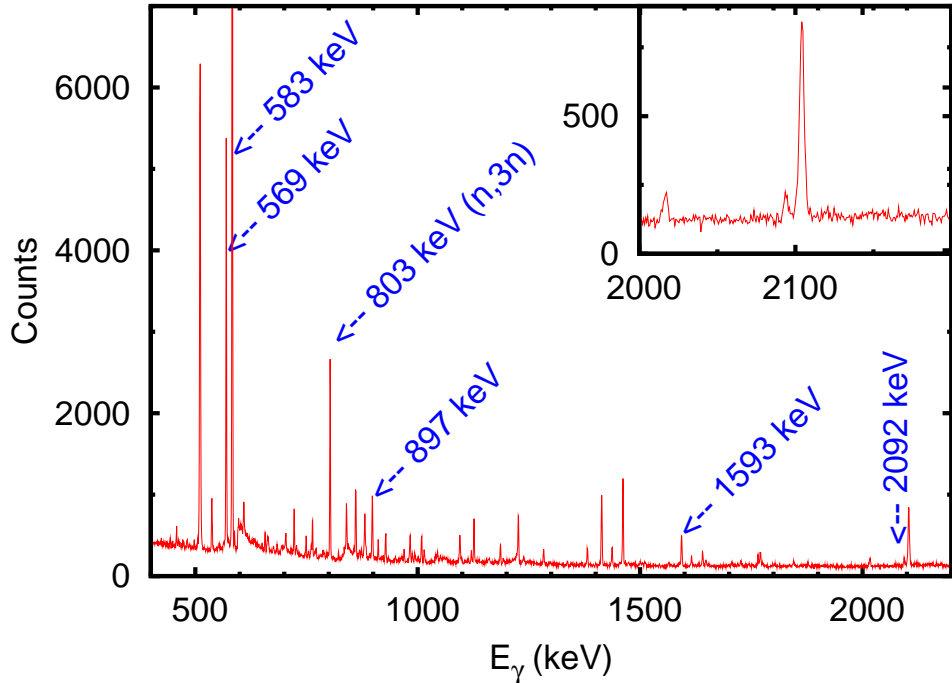


Figure 5.84: γ -ray spectrum with the ^{208}Pb sample (88.1 keV% enrichment) integrated over neutron energies above 7.4 MeV up to about 25 MeV. The 569 keV, 897 keV, 1770 keV, 1593 keV and 2092 keV peaks resulted mainly from the $^{208}\text{Pb}(n,2n\gamma)^{207}\text{Pb}$ reaction. The 803 keV peak was produced in the $^{208}\text{Pb}(n,3n\gamma)^{206}\text{Pb}$ reaction. A zoom of the spectrum around 2092 keV peak is shown as inset.

between the integrated gamma production cross-sections over the full measured neutron energy range. As additional check in the support of the correct γ -ray identification, the branching ratio was observed to be constant with the neutron energy. The same threshold was observed for the γ -rays from the decay of the same excited level.

The resulted branching ratios are given in Table. 5.6. The present values for the branching ratios agree with the evaluated values within the uncertainties. The large uncertainties of the present measurement are due the poor statistics of the less intense transitions from every level.

$(n,2n)$ and $(n,3n)$ gamma production cross-sections

Fig. 5.84 shows the γ -ray spectrum with the ^{208}Pb sample integrated over the neutron energies from 7.4 MeV up to about 25 MeV. In this spectrum were observed 5 γ -rays from the ^{207}Pb nucleus and one γ -ray from the ^{206}Pb nucleus. These γ -ray peaks resulted mainly from the $(n,2n)$ and respectively $(n,3n)$ reactions on ^{208}Pb nucleus. As shown in Table. 5.5, these γ -ray peaks have contributions from other (n,xn) ($x=1,2,3$) reactions on the Pb isotopes present in the sample.

The $(n,2n)$ and $(n,3n)$ cross-sections presented here were corrected for the iso-

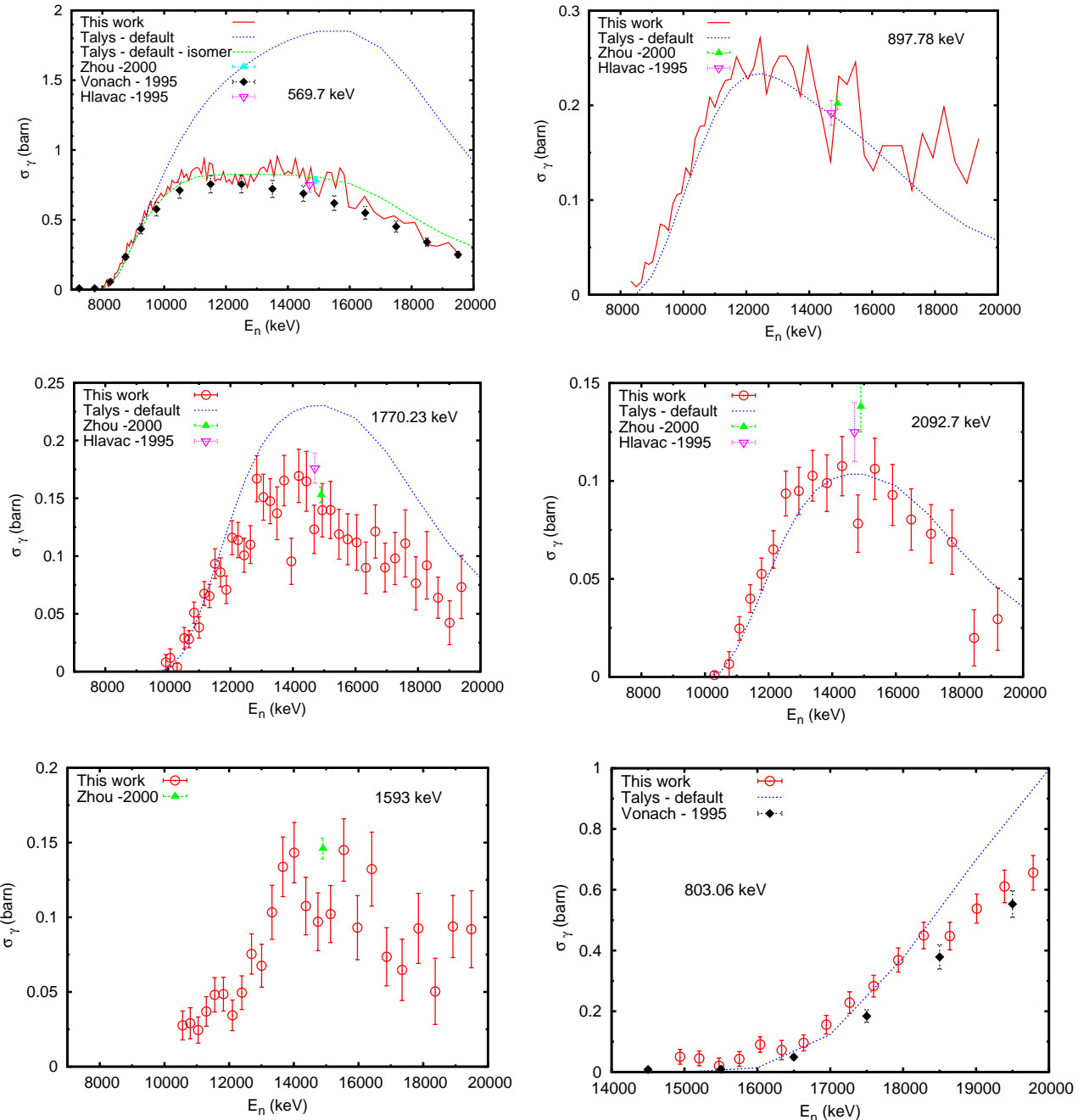


Figure 5.85: Integral cross-section of the γ -rays from the $(n,2n)$ and $(n,3n)$ reactions on ^{208}Pb .

topic composition of the sample. The gamma production cross-sections of ^{206}Pb and ^{207}Pb nuclei measured in this work were used for this correction. The (n,2n) gamma production cross-section shown in Fig. 5.85 were corrected for the neutron attenuation and multiple scattering in the ^{208}Pb sample. This correction coefficient is almost constant in neutron energy and is about 0.985 for the 569.7 keV (see Sec. 3.3.6). The neutron attenuation has the dominant contribution for this coefficient in the (n,2n) reaction. The (n,3n) gamma production cross-section was not corrected for the neutron attenuation and multiple scattering in the sample.

Fig. 5.85 shows the resulted (n,2n) cross-sections on ^{208}Pb nucleus. The 1593 keV γ -ray peak coincides with the double escape peak of the most intense transition from the spectrum, 2614.5 keV. Because of this, the HPGe yield for the 1593 keV peak was different from zero below the $^{208}\text{Pb}(n,2n)$ threshold even after the correction for the isotopic composition. Above 9 MeV neutron energy, the yield due to the double escape peak decreased significantly becoming close to zero and therefore its contribution in the (n,2n) cross-section was neglected. The threshold of the 1593 keV transition from the $^{208}\text{Pb}(n,2n)$ reaction is at 10.5 MeV.

For the 569.7 keV the best neutron energy resolution was obtained: 50 keV at 8 MeV up to 350 keV at 18 MeV. For the same transition a total uncertainty that increases from about 6 % at 10 MeV up to 15 % at 20 MeV was obtained. The lowest neutron energy resolution was obtained for the 2092.7 keV transition, 320 keV at 10 MeV. The total uncertainty for the 2092.7 keV transition had a minimum of about 15 % around 13 MeV.

As in the case of inelastic scattering, a detailed measurement of the $^{208}\text{Pb}(n,2n)$ cross-section had been done by Vonach *et al.* [152] from the threshold up to 200 MeV. Two other measurements of Zhou *et al.* [153] and Hlavac *et al.* [154] were done around 14 MeV. The agreement of all experimental data is very good. The Talys calculation describes very well the present measurements for the 569.7 keV and 897.78 keV. For the 1770.2 keV the calculation gives higher values above 12 MeV.

The (n,3n) cross-section on ^{208}Pb is given in Fig. 5.85 for the 803.06 keV transition. The neutron energy resolution used for this cross-section was 260 keV at 15 MeV up to 350 keV at 18 MeV. The total uncertainty range from 50 % just above the threshold down to 9 % at 20 MeV. The present values agree well with the measurement of Vonach *et al.* [152] on the full energy range and only up to 18.5 MeV with the default Talys calculation. The production cross-section of the 803.06 keV γ -ray from the $^{208}\text{Pb}(n,3n)^{206}\text{Pb}$ reaction was not corrected for the neutron attenuation and multiple scattering. Anyway this correction is expected to be less than 2 %.

5.5.3 Total inelastic and level cross-sections

The total inelastic and the level cross-sections were constructed using the integral gamma production cross-sections and the evaluated level scheme of the ^{208}Pb nucleus as described in Sec. 2.1.2. The obtained results are given in the following.

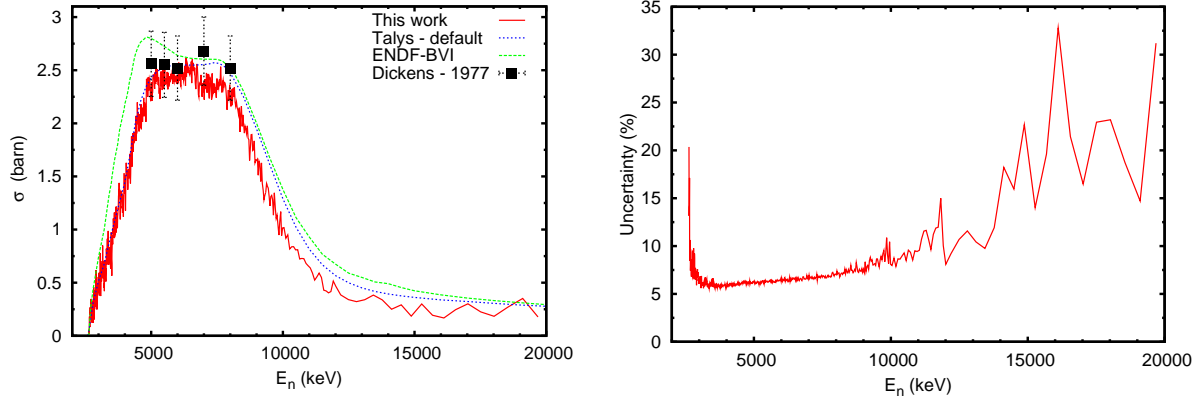


Figure 5.86: *Left:* Smooth data for the total neutron inelastic cross-section of ^{208}Pb on full energy range up to 20 MeV. *Right:* Total uncertainty of the total inelastic cross-sections.

Total neutron inelastic cross-section

The total inelastic neutron cross-section was constructed using the gamma production of the following 3 γ -rays: 2614.5 keV, 4085.4 keV and 4229.5 keV (see also Fig. 5.72). The result is given in Fig. 5.86. The total neutron inelastic cross-section constructed here is not affected by the fact that the level at 3708.44 keV was not observed. The missed transition of 510.77 KeV from the fourth excited level does not contribute directly to the total inelastic cross-section. The total neutron inelastic cross-section was obtained with a neutron energy resolution of 1.1 keV at 1 MeV (35 keV at 10 MeV). The corresponding total uncertainty has a minimum value of 5% at energies around 4 MeV and increases up to about 20 MeV.

The total inelastic cross-section presented here is exact up to 4.5 MeV because the level at 4626 keV is the first level that decays directly to the ground state and was not observed (Fig. 5.72). Above this energy, the present total inelastic cross-section is only a lower limit. For the ^{208}Pb nucleus, where the most intense γ -ray in the spectrum is the by far the transition from the first excited level to the ground state, this limit is very close to the exact value.

The present results agree well with the measurement of Dickens *et al.* [161] at energies around 6 MeV. As in the case of the gamma production cross-section of the 2614.5 keV transition, the Talys calculation describes well the measured cross-section up to about 7 MeV. Above this energy the calculation gives higher values. The evaluated total inelastic cross-section from the ENDF-BVI library is plotted together with the present results in Fig. 5.86 *Left*. The JEFF-3.1 evaluation was not given explicitly in this figure because it coincides with the default Talys calculation.

Level 2614.5 keV

The cross-section of the level at 2614.5 keV is shown in Fig. 5.87. The following gamma productions were used for the construction of the cross-section of the level at 2614.5 keV: 583.19 keV, 860.56 keV, 1381.1 keV, 1436.0 keV, 1614.9 keV,

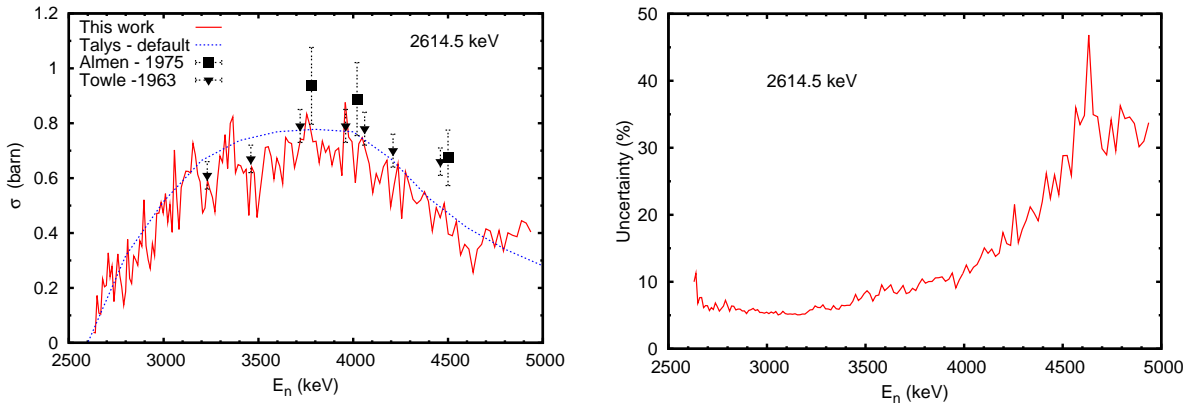


Figure 5.87: *Left:* The cross-section of the 2614.5 keV level in ^{208}Pb . *Right:* The corresponding total uncertainty.

1639 keV and 1647.9 keV. Therefore, the cross-section of the first excited level of ^{208}Pb (Fig. 5.87) is exact up to 4.3 MeV neutron energy. Above this energy the cross-section presented here is an upper limit. Considering that the maximum observed excited level has energy of 5563 keV, the so constructed upper limit for the first excited level is close to the exact value. The levels that were not observed have to have a low cross-sections, in general lower than 15 mb at the maximum.

The level at 3708.44 keV, that is not observed because it decays through a 510.7 keV transition, does not affect the cross-section of the 2614.5 keV level.

Taking into account the uncertainties (Fig. 5.87 *Right*), the measured data of Almen *et al.* [130] and Towle *et al.* [163] agree with the present results. The same is valid for the default Talys calculation.

Levels with higher excitation energy

The cross-section of the higher energy excited levels was also constructed. The results for the levels up to 4323.2 keV excitation energy are shown in Figs. 5.87 and 5.89. These cross-sections are exact up to 4.4 MeV which is the energy of first excited level that was not observed in the present measurement. Above 4.4 MeV the present results are upper limits for the level cross-sections. The cross-section of the level at 3197.74 keV is overestimated because the production cross-section of the 510.77 keV γ -ray that feeds this level was not subtracted here.

Other experimental data were found only for the levels at 3197 keV and 3475 keV. The data of Towle *et al.* [163] agree well with the present results.

Data calculated with the Talys code were available only up to 4229.5 keV excitation energy. Levels as 3197 keV, 3475.1 keV are described well by the calculation. Differences in both directions, higher or lower values, were observed for other levels as 3946 keV, 4085.4 keV and 4180 keV.

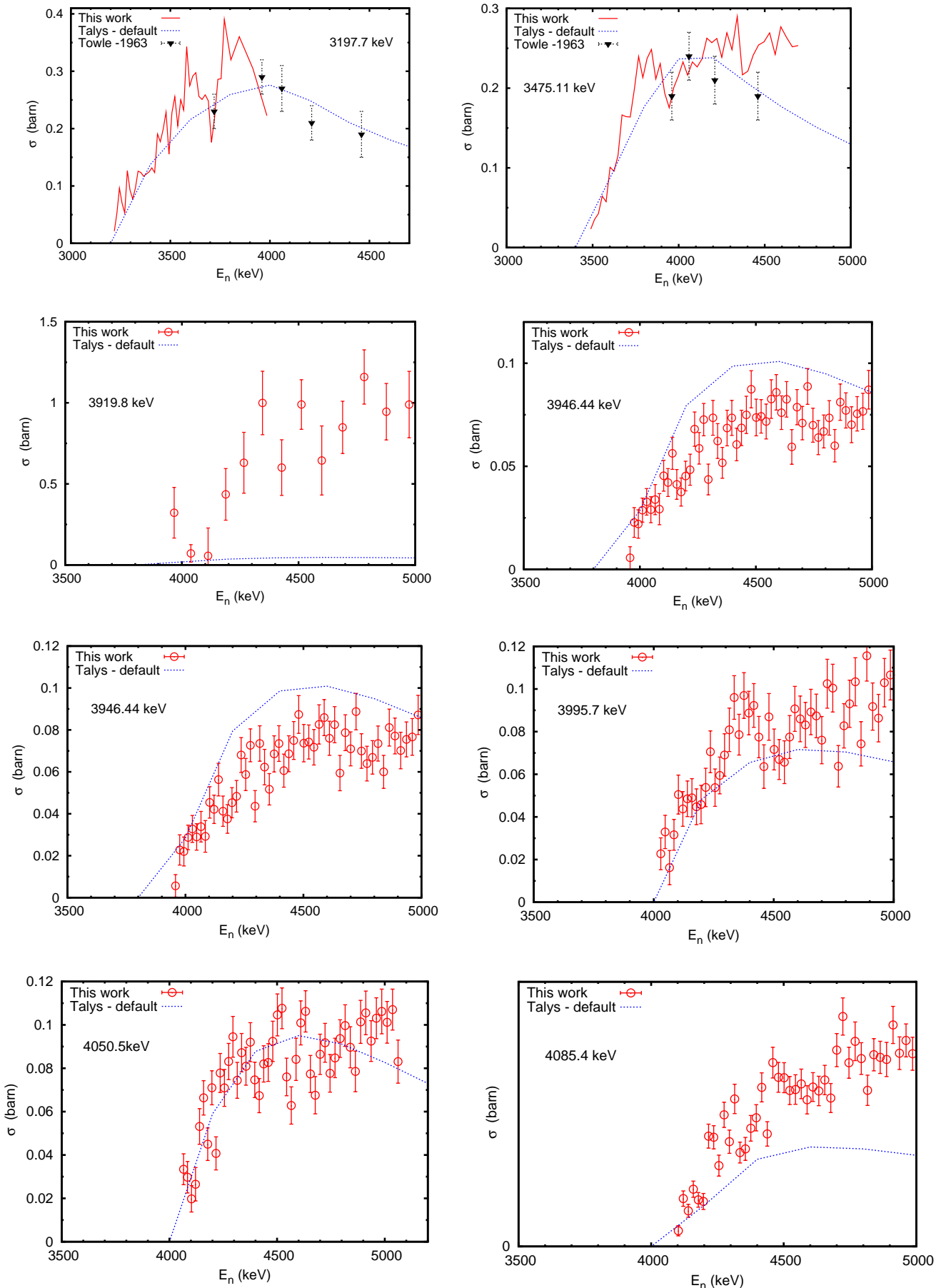
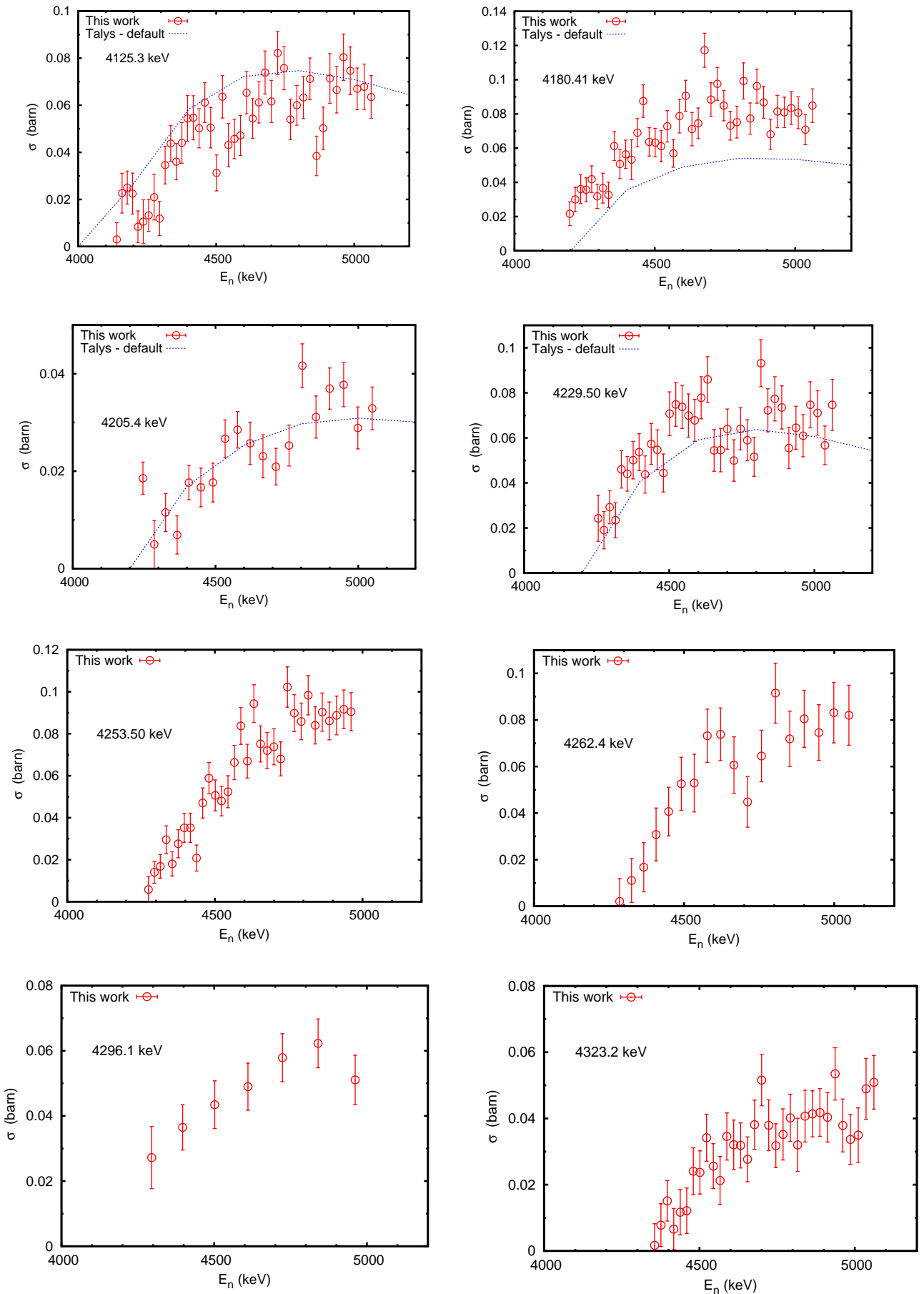


Figure 5.88: The cross-section of the excited levels above 2614 keV in ^{208}Pb .

Figure 5.89: The cross-section of the excited levels above 2614 keV in ^{208}Pb .

5.5.4 Conclusions

Using an 88.11 % enriched ^{208}Pb sample, the production cross-section of the γ -rays from the neutron inelastic, (n,2n) and (n,3n) reaction on ^{208}Pb was measured with an unprecedented neutron energy resolution and total uncertainty. The production cross-section of the intense γ -rays was measured over the full energy range, from the threshold up to about 20 MeV, in only one run.

The production cross-section was measured for 29 γ -rays of the inelastic reaction. The neutron energy resolution was 1.1 keV at 1 MeV up to 35 keV at 10 MeV. This resolution was equivalent to time-of-flight bins of 8 ns. A total uncertainty of about 5 % below 8 MeV neutron energy was achieved for the most intense γ -ray transition in ^{208}Pb , 2614.5 keV. The excited level at 3708.44 keV was not observed because the main transition from the decay of this level has an energy of 510.77 keV and cannot be distinguished from the 511 keV background peak. Except for the level at 3708.44 keV, at least one γ -ray was observed to decay from every excited level up to 4.3 MeV excitation energy. The maximum observed excited level has an energy of 5.563 MeV. The only reason for not observing all the levels between 4.3 MeV and 5.5 MeV is their low cross-section.

Based on the ^{208}Pb level scheme and on the measured gamma production cross-sections the total inelastic cross-section was constructed up to about 20 MeV neutron energy. The level at 3708.44 keV that was not observed does not affect the total inelastic cross-section. The cross-sections of the levels up to 4323.2 keV excitation energy were obtained up to about 5 MeV neutron energy.

Five γ -rays from the (n,2n) reaction and one γ -ray from the (n,3n) reaction on ^{208}Pb were observed. ^{208}Pb nucleus was the only case from the nuclei presented in this work where the production cross-section was measured for a γ -ray from the (n,3n) reaction.

All the cross-sections presented here were corrected for the isotopic composition of ^{208}Pb sample. The best neutron energy resolution used for these transitions was of 50 keV at 8 MeV (350 keV at 18 MeV). The uncertainties at the maximum of the cross-section ranged between 6 % and 15 % depending on the γ -ray.

The present results were compared with existing experimental data and with the Talys code calculation with the default input parameters. The general good agreement can be noted with the experimental data of Vonach *et al.* [152] and the data of Dickens *et al.* [161]. The Vonach *et al.* data agree relatively well with the present measurement also for the (n,2n) and (n,3n) gamma production cross-sections.

The default Talys calculation describes well the gamma production of the 2614.53 keV transition. For the second most intense transition in the ^{208}Pb spectrum, 583.19 keV, the calculation differs from the measurement in the middle energy range and at energies above 12 MeV. The other inelastic gamma production cross-sections are described well at low energies. Important differences were observed at high energies for some transitions.

The total inelastic cross-section is described well by the calculation below 7 MeV. The higher values given by the calculation at higher energies do not contradict the

fact that the curve presented here is a lower limit for the total inelastic cross-section above 4.5 MeV neutron energy. The good agreement observed for the total inelastic cross-section may be reflected by the good description of the integral gamma production cross-section of the 2614.53 keV transition which are the most intense in the ^{208}Pb spectrum.

The neutron inelastic, (n,2n) and (n,3n) cross-sections measured in this experiment for the ^{208}Pb nucleus can be used in further neutron data evaluations and as benchmark for the nuclear codes. Further tuning can still be done for the Talys code for a better description of the ^{208}Pb cross-sections presented here.

Chapter 6

Conclusions

The project described in the present work had two main results:

- The $(n, xn\gamma)$ ($x=1,2,3$) cross-sections were measured for five nuclei (^{52}Cr , ^{209}Bi and $^{206,207,208}\text{Pb}$) with an unprecedented neutron energy resolution and total uncertainty of about 5 % for the most intense γ -rays.
- It was proven that a 12 bits and 420 MSPS fast digitizer can be successfully used at GELINA for the $(n, xn\gamma)$ ($x=1,2,3$) cross-sections measurements with large volume HPGe detectors.

An experimental setup based on large volume HPGe detectors was used for the measurement of the production cross-section of the γ -rays from the neutron inelastic, $(n, 2n)$ and $(n, 3n)$ ¹ reactions on 5 nuclei: ^{52}Cr , ^{209}Bi and $^{206,207,208}\text{Pb}$. The very good energy resolution of the germanium detectors allowed the precise identification of a large number of γ -rays from the reactions of interest in complex γ -ray spectra. Table. 6.1 gives the number of γ -rays in every studied reaction for which the production cross-section was measured. The maximum energy of an observed excited level is also given.

Using the white neutron spectrum from Gelina, the production cross-sections were measured quasi-continuously over the full energy range from the threshold up to about 20 MeV in only one long run for every nucleus. The neutron energy resolution of 1.1 keV at 1 MeV up to 35 keV at 10 MeV was realized for the most intense γ -rays. This neutron energy resolution corresponds to 8 ns resolution in the time-of-flight for a flight-path length of 200 m. To achieve such neutron energy resolution and small total uncertainties runs of about 500 to 1000 hours of effective data acquisition were needed for every nucleus.

The measured cross-section were normalized to the well known standard fission cross-section of ^{235}U . The neutron flux was measured simultaneously with the γ -ray yield avoiding the errors introduced by the sample-in sample-out normalization techniques.

The smallest cross-section that was measured in the present experiment was around 15 mb at the maximum. Just above the thresholds or at higher energies

¹The $(n, 3n\gamma)$ cross-section was measured only for the ^{208}Pb nucleus

Table 6.1: The number of observed γ -ray in every studied reaction and the maximum energy of an observed excited level.

Nucleus	Reaction	Nbr. of observed γ -rays	E^{max} (MeV)
^{52}Cr	(n,n'γ)	12	3.77
	(n,2nγ)	2	1.16
^{209}Bi	(n,n'γ)	39	3.80
	(n,2nγ)	8	1.09
^{206}Pb	(n,n'γ)	23	3.56
	(n,2nγ)	2	0.70
^{207}Pb	(n,n'γ)	15	4.32
	(n,2nγ)	4	1.70
^{208}Pb	(n,n'γ)	29	5.56
	(n,2nγ)	5	3.22
	(n,3nγ)	1	0.80

these cross-sections were even smaller. This observation limit depends by the γ -ray energy and in some cases by the threshold.

Using the measured gamma production cross-sections, the total inelastic and the inelastic level cross-sections were constructed. The construction of these cross-sections relies completely on the accuracy of the evaluated level schemes of the studied nuclei. The determination of several γ -ray branching ratios was the only possible verification of the level scheme in the absence of any γ - γ coincidence measurement. The γ -ray branching ratios were determined only in several cases, when two γ -rays that decay from the same level were observed.

Above the maximum observed excitation energy, the total inelastic cross-sections presented here are only lower limits, because the missed γ -ray transitions that decay directly from the higher levels to the ground state were neglected. For the even-even nuclei these lower limits are very close to the exact values.

For the total inelastic cross-sections and for the production cross-section of the most intense γ -ray it was achieved a total uncertainty of about 5 % below 10 MeV. Higher uncertainties were obtained just above the thresholds and at high energies because of the poor statistics.

For ^{52}Cr , ^{206}Pb and ^{207}Pb nuclei, very well defined resonance structures were observed below about 2.5 MeV neutron energy. Many of these resonances can be easily identified between the resonances observed in the neutron total cross-sections measured in transmission experiments performed in different laboratories.

The present measured cross-sections were compared with existing experimental data and with the Talys code calculation with the default input parameters. The Talys calculation describes well the present measured data taking into account that the default input parameters were used. Fine tuning of the Talys parameters can still be done for a better description of the measured data. The large set of precise cross-section data that were measured in the experiments described in this work can be successfully used in further neutron data evaluations and as benchmark for the

nuclear codes.

The detailed results will be sent to the online databases as EXFOR files. Part of them is already available for online download.

In parallel with the cross-section measurement with the conventional electronics, a commercially available fast digitizer was tested for the use in time-of-flight measurements at Gelina with large volume HPGe detectors. Different pulse processing algorithms were tested and the one with the best performances was implemented for an online data acquisition. In the online data acquisition only the values of the time and amplitude were saved for all recorded signals.

The tests for the use of the fast digitizer were concluded with the measurement of the neutron inelastic cross-sections for the ^{206}Pb and for the ^{208}Pb nucleus. For these two nuclei, the data acquisition system with the fast digitizer run in parallel with the acquisition system based on conventional electronics. After the complete data analysis of the two data sets, from the fast digitizer and from the conventional electronics, the same values were obtained for the differential gamma production cross-sections. This showed that the fast digitizer can be successfully used for the $(n, xn\gamma)$ cross-section measurements at GELINA in favor of the data acquisition system based on conventional electronics.

The advantage of the fast digitizer is the higher acquisition efficiency preserving the time and amplitude resolution of the acquisition system based on conventional electronics. The increase in the efficiency is due to the following:

- The digitizer resolves the pile-up of the neutron induced events with the gamma-flash induced events. The resolving time of the digitizer is $2.5 \mu\text{s}$, smaller than the conventional electronics.
- The tail of the time resolution spectrum is significantly reduced for the digitizer compared with the CF function and no pulse is rejected.

The performances of the tested digitizer can be improved in terms of acquisition rate if an on-board signal processing could be available by means of an FPGA opened to be programmable by the user.

Bibliography

- [1] **L. C. Mihailescu**, C. Borcea, L. Oláh, A. J. M. Plompen, A new HPGe setup at Gelina for measurement of gamma-ray production cross-sections from inelastic neutron scattering, Nucl.Instr. and Meth A531 (2004) 375-391.
- [2] **L. C. Mihailescu**, C. Borcea, A. J. M. Plompen, Measurements of neutron inelastic scattering cross-sections for ^{52}Cr from threshold up to 18 MeV, Radiation Protection Dosimetry, Vol. 115, No. 1-4, pp. 136-138, 2005
- [3] **L. C. Mihailescu**, C. Borcea, A. J. M. Plompen, Measurements of neutron inelastic scattering cross-sections for ^{209}Bi from threshold up to 18 MeV, in Proceedings of the International Conference on Nuclear Data for Science and Technology - ND2004, Sep.26-Oct.1,2004, Santa Fe, USA
- [4] **L. C. Mihailescu**, C. Borcea, A. J. M. Plompen, Tests for the use of a fast digitizer in a time-of-flight measurement with large volume HPGe detectors in Proceedings of the NEMEA 2 Workshop, Bucharest, October 20-23, 2004.
- [5] **L. C. Mihailescu**, C. Borcea, A. J. M. Plompen, Measurements of high-resolution neutron inelastic scattering cross-sections for ^{52}Cr from threshold up to 18 MeV, in Proceedings of the NEMEA 1 Workshop, Budapest, October, 2003.
- [6] A.J.Koning, S.Hilaire and M.C.Duijvestijn, Talys: comprehensive nuclear reaction modeling, Proceedings of the International Conference on Nuclear Data for Science and Technology - ND2004, Sep.26-Oct.1,2004, Santa Fe, USA
- [7] G. Aliberti, G. Palmiotti, M. Salvatores, C. Stenberg, Impact of nuclear data uncertainties on transmutation of actinides in accelerator-driven assemblies, Nucl. Sci. Eng. 146 (2004) 13.
- [8] I. G. Birn, A. Meister, E. Wattecamps, H. Weigmann, Measurement of the $(\text{n},\text{n}'\gamma)$ excitation functions of low-lying levels of molybdenum isotopes, in: A. V. G. Reffo, C. Grandi (Eds.), Proc. Conf. for Nuclear Data for Science and Technology, Editrice Compositori, 40128 Bologna, Italy, Trieste, Italy, 1997, p. 526.
- [9] J.Q.Shao,G.P.Couchell,J.J.Egan,G.H.R.Kegel,S.Q.Li,A.Mittler,D.J.Pullen, anddW.A.Schier,Fast neutron inelastic scattering cross-section of ^{238}U for states between 680 and 1530 keV, Nucl. Sci. Eng. 92 (1986) 350-371

- [10] N.V.Kornilov and A.B.Kagalenko, Inelastic neutron scattering by ^{235}U and ^{238}U nuclei, *Nucl. Sci. Eng.* 120 (1995) 55–64
- [11] E. Sheldon, D. Van Patter, Compound inelastic nucleon and gamma-ray angular distribution for even and odd-mass nuclei, *Rev. of Mod. Physics* 38 (1966) 143.
- [12] G. Palmiotti, P. Finck, I. Gomes, B. Micklich, M. Salvatores, Uncertainty assessment for accelerator driven systems, in: Proc. Int. Conf. Global 1999, ANS, Jackson Hole, Wyoming, USA, 1999.
- [13] M. Salvatores, G. Palmiotti, LMFBR design parameter uncertainties and target accuracies, *Ann. Nucl. Energy* 12 (1985) 291.
- [14] G. Palmiotti, M. Salvatores, Use of integral experiments in the assessment of large liquid-metal fast breeder reactor basic design parameters, *Nucl. Sci. Eng.* 87 (1984) 333.
- [15] A. Fessler, D. L. Smith, Parameter sensitivities in nuclear reaction cross-section calculations, *Ann. Nucl. Energy* 29 (2002) 363.
- [16] C. Y. Fu, D. C. Larson, Effects of shape differences in the level densities of three formalisms on calculated cross sections, Report NEA/WPEC-16, OECD, Paris (1998).
- [17] T. Kawano, Y. Watanabe, M. Kawai, Validity of DWBA calculations for neutron inelastic scattering from molybdenum isotopes, *J. of Nucl. Sci. and Technol.* 35 (1998) 519.
- [18] K. Shibata, Sensitivities of calculated cross sections of ^{56}Fe to model parameters, NEA Report OECD/GD(94)21, OECD, Paris (1994).
- [19] A. Hogenbirk, Extensive neutronic sensitivity-uncertainty analysis of a fusion reactor shielding blanket, *Fusion Eng. and Design* 24 (1994) 275.
- [20] A. J. Koning, H. Gruppelaar, A. Hogenbirk, The EFF-3.0 evaluation for ^{56}Fe , *Fusion Eng. and Design* 37 (1997) 211.
- [21] C. L. Dunford, R. R. Kinsey, The NuDat System for Access to Nuclear Data, Report IAEA-NDC-205 (BNL-NCS-65687), IAEA, Vienna, Austria, also available online from www.nndc.bnl.gov (1998).
- [22] M. Bhat, Evaluated Nuclear Structure Data File, www.nndc.bnl.gov, NNDC, Brookhaven, USA (2003).
- [23] S. Traiforos, A. Mittler, W. A. Schier, B. K. Barnes, L. E. Beghian, P. Harihar, Gamma-ray production and inferred inelastic neutron cross sections for nickel isotopes, *Nucl. Sci. Eng.* 72 (1979) 191–201.

- [24] T. Yamamoto, Y. Hino, S. Itagaki, K. Sugiyama, Gamma-ray production cross section for interaction of 14.8 MeV neutrons with O, Na, Al, Cl, Cr, Fe, Ni, Cu, Pb, J. of Nucl. Sci. and Technol. 15 (1978) 797.
- [25] A. Meister, E. Wattecamps, A. Koning, A. Hogenbirk, H. Gruppelaar, Cross sections of inelastic neutron scattering for palladium isotope nuclei, in: A. V. G. Reffo, C. Grandi (Eds.), Proc. Conf. for Nuclear Data for Science and Technology, Editrice Compositori, 40128 Bologna, Italy, Trieste, Italy, 1997, p. 586.
- [26] F. Voss and C. Cierjacks and D. Erbe and G. Schmalz, Measurement of the γ -ray production cross sections from inelastic neutron scattering in some chromium and nickel isotopes between 0.5 and 10 MeV, in: Conf. on Nuclear Cross Sections and Technology, Washington USA, 1975, p. 916.
- [27] H. Vonach, A. Pavlik, M. B. Chadwick, R. C. Haight, R. O. Nelson, S. A. Wender, P. G. Young, $^{207,208}\text{Pb}(n,xn\gamma)$ reactions for neutron energies from 3 to 200 MeV, Phys. Rev. C 50 (1994) 1952.
- [28] N. Fotiades, G. D. Johns, R. O. Nelson, M. B. Chadwick, M. Devlin, W. S. Wilburn, P. G. Young, D. E. Archer, J. A. Becker, L. A. Becker, L. A. Bernstein, P. E. Garrett, C. A. McGrath, D. P. McNabb, W. Younes, Absolute partial γ -ray cross sections in $^{238}\text{U}(n,xn\gamma)$ reactions, J. of Nucl. Sci. and Technol. Suppl. 2 (2002) 234.
- [29] G. F. Knoll, Radiation Detection and Measurement, 3rd edition, John Wiley and Sons, Inc., New York, USA, 2000.
- [30] K. H. Böckhoff, A. D. Carlson, O. A. Wasson, J. A. Harvey, D. C. Larson, Electron linear accelerators for fast neutron data measurements in support of fusion energy applications, Nucl. Sci. Eng. 106 (1990) 192.
- [31] D. Tronc, J. M. Salomé, K. Böckhoff, A new pulse compression system for intense relativistic electron beams, Nucl. Instrum. Methods Phys. Res. 228 (1985) 346.
- [32] A. Benussan, J. M. Salomé, Gelina: a modern accelerator for high resolution neutron time-of-flight measurements, Nucl. Instrum. Methods Phys. Res. 155 (1978) 11.
- [33] J. Gonzalez, C. Bastian, S. de Jonge, K. Hofmans, Modular MultiParameter Multiplexer, MMPM, hardware description and user manual, Internal Report GE/R/INF/06/97, JRC-IRMM, Geel (1997).
- [34] S. de Jonge, Fast Time Digitizer, Internal Report GE/DE/R/24/87, JRC-CBNM, Geel (1987).
- [35] H. Condé, Nuclear Data Standards for Nuclear Measurements, Report NEANDC-311 "U", OECD-Nuclear Energy Agency, Paris, France (1992).

- [36] H. J. Rose, D. M. Brink, Angular distributions of gamma rays in terms of phase-defined reduced matrix elements, *Rev. Mod. Phys.* 39 (1976) 306.
- [37] R. D. Gill, *Gamma-ray angular correlations and distributions*, Academic Press, London, UK, 1975.
- [38] K. E. Atkinson, An introduction to numerical analysis, 2nd edition, John Wiley and Sons, New York, USA, 1989.
- [39] J. F. Briesmeister, MCNPTM - A General Monte Carlo N-Particle Transport Code, Report LA-13709-M, Los Alamos National Laboratory, Los Alamos NM, USA (2000).
- [40] J.Q.Shao,G.P.Couchell,J.J.Egan,G.H.R.Kegel,S.Q.Li,A.Mittler,D.J.Pullen, and W.A.Schier, Fast neutron inelastic scattering cross-section of ^{238}U for states between 680 and 1530 keV, *Nucl. Sci. Eng.* 92 (1986) 350–371
- [41] N.V.Kornilov and A.B.Kagalenko, Inelastic neutron scattering by ^{235}U and ^{238}U nuclei, *Nucl. Sci. Eng.* 120 (1995) 55–64
- [42] E. Sheldon, D. Van Patter, Compound inelastic nucleon and gamma-ray angular distribution for even and odd-mass nuclei, *Rev. of Mod. Physics* 38 (1966) 143.
- [43] G. Aliberti, G. Palmiotti, M. Salvatores, C. Stenberg, Impact of nuclear data uncertainties on transmutation of actinides in accelerator-driven assemblies, *Nucl. Sci. Eng.* 146 (2004) 13.
- [44] G. Palmiotti, P. Finck, I. Gomes, B. Micklich, M. Salvatores, Uncertainty assessment for accelerator driven systems, in: Proc. Int. Conf. Global 1999, ANS, Jackson Hole, Wyoming, USA, 1999.
- [45] M. Salvatores, G. Palmiotti, LMFBR design parameter uncertainties and target accuracies, *Ann. Nucl. Energy* 12 (1985) 291.
- [46] G. Palmiotti, M. Salvatores, Use of integral experiments in the assessment of large liquid-metal fast breeder reactor basic design parameters, *Nucl. Sci. Eng.* 87 (1984) 333.
- [47] A. Fessler, D. L. Smith, Parameter sensitivities in nuclear reaction cross-section calculations, *Ann. Nucl. Energy* 29 (2002) 363.
- [48] C. Y. Fu, D. C. Larson, Effects of shape differences in the level densities of three formalisms on calculated cross sections, Report NEA/WPEC-16, OECD, Paris (1998).
- [49] T. Kawano, Y. Watanabe, M. Kawai, Validity of DWBA calculations for neutron inelastic scattering from molybdenum isotopes, *J. of Nucl. Sci. and Technol.* 35 (1998) 519.

- [50] K. Shibata, Sensitivities of calculated cross sections of ^{56}Fe to model parameters, NEA Report OECD/GD(94)21, OECD, Paris (1994).
- [51] A. Hogenbirk, Extensive neutronic sensitivity-uncertainty analysis of a fusion reactor shielding blanket, *Fusion Eng. and Design* 24 (1994) 275.
- [52] A. J. Koning, H. Gruppelaar, A. Hogenbirk, The EFF-3.0 evaluation for ^{56}Fe , *Fusion Eng. and Design* 37 (1997) 211.
- [53] C. L. Dunford, R. R. Kinsey, The NuDat System for Access to Nuclear Data, Report IAEA-NDC-205 (BNL-NCS-65687), IAEA, Vienna, Austria, also available online from www.nndc.bnl.gov (1998).
- [54] M. Bhat, Evaluated Nuclear Structure Data File, www.nndc.bnl.gov, NNDC, Brookhaven, USA (2003).
- [55] A.H. Wapstra, G. Audi, and C. Thibault, Atomic mass table , www.nndc.bnl.gov, NNDC, Brookhaven, USA (2003).
- [56] S. Traiforos, A. Mittler, W. A. Schier, B. K. Barnes, L. E. Beghian, P. Harihar, Gamma-ray production and inferred inelastic neutron cross sections for nickel isotopes, *Nucl. Sci. Eng.* 72 (1979) 191–201.
- [57] T. Yamamoto, Y. Hino, S. Itagaki, K. Sugiyama, Gamma-ray production cross section for interaction of 14.8 MeV neutrons with O, Na, Al, Cl, Cr, Fe, Ni, Cu, Pb, *J. of Nucl. Sci. and Technol.* 15 (1978) 797.
- [58] A. Meister, E. Wattecamps, A. Koning, A. Hogenbirk, H. Gruppelaar, Cross sections of inelastic neutron scattering for palladium isotope nuclei, in: A. V. G. Reffo, C. Grandi (Eds.), *Proc. Conf. for Nuclear Data for Science and Technology*, Editrice Compositori, 40128 Bologna, Italy, Trieste, Italy, 1997, p. 586.
- [59] I. G. Birn, A. Meister, E. Wattecamps, H. Weigmann, Measurement of the $(n,n'\gamma)$ excitation functions of low-lying levels of molybdenum isotopes, in: A. V. G. Reffo, C. Grandi (Eds.), *Proc. Conf. for Nuclear Data for Science and Technology*, Editrice Compositori, 40128 Bologna, Italy, Trieste, Italy, 1997, p. 526.
- [60] F. Voss and C. Cierjacks and D. Erbe and G. Schmalz, Measurement of the γ -ray production cross sections from inelastic neutron scattering in some chromium and nickel isotopes between 0.5 and 10 MeV, in: *Conf. on Nuclear Cross Sections and Technology*, Washington USA, 1975, p. 916.
- [61] H. Vonach, A. Pavlik, M. B. Chadwick, R. C. Haight, R. O. Nelson, S. A. Wender, P. G. Young, $^{207,208}\text{Pb}(n,xn\gamma)$ reactions for neutron energies from 3 to 200 MeV, *Phys. Rev. C* 50 (1994) 1952.

- [62] N. Fotiades, G. D. Johns, R. O. Nelson, M. B. Chadwick, M. Devlin, W. S. Wilburn, P. G. Young, D. E. Archer, J. A. Becker, L. A. Becker, L. A. Bernstein, P. E. Garrett, C. A. McGrath, D. P. McNabb, W. Younes, Absolute partial γ -ray cross sections in $^{238}\text{U}(\text{n},\text{xn}\gamma)$ reactions, *J. of Nucl. Sci. and Technol. Suppl.* 2 (2002) 234.
- [63] G. F. Knoll, *Radiation Detection and Measurement*, 3rd edition, John Wiley and Sons, Inc., New York, USA, 2000.
- [64] K. H. Böckhoff, A. D. Carlson, O. A. Wasson, J. A. Harvey, D. C. Larson, Electron linear accelerators for fast neutron data measurements in support of fusion energy applications, *Nucl. Sci. Eng.* 106 (1990) 192.
- [65] D. Tronc, J. M. Salomé, K. Böckhoff, A new pulse compression system for intense relativistic electron beams, *Nucl. Instrum. Methods Phys. Res.* 228 (1985) 346.
- [66] A. Benussan, J. M. Salomé, Gelina: a modern accelerator for high resolution neutron time-of-flight measurements, *Nucl. Instrum. Methods Phys. Res.* 155 (1978) 11.
- [67] J. Gonzalez, C. Bastian, S. de Jonge, K. Hofmans, Modular MultiParameter Multiplexer, MMPM, hardware description and user manual, Internal Report GE/R/INF/06/97, JRC-IRMM, Geel (1997).
- [68] S. de Jonge, Fast Time Digitizer, Internal Report GE/DE/R/24/87, JRC-CBNM, Geel (1987).
- [69] H. Condé, Nuclear Data Standards for Nuclear Measurements, Report NEANDC-311 "U", OECD-Nuclear Energy Agency, Paris, France (1992).
- [70] H. J. Rose, D. M. Brink, Angular distributions of gamma rays in terms of phase-defined reduced matrix elements, *Rev. Mod. Phys.* 39 (1976) 306.
- [71] R. D. Gill, *Gamma-ray angular correlations and distributions*, Academic Press, London, UK, 1975.
- [72] K. E. Atkinson, *An introduction to numerical analysis*, 2nd edition, John Wiley and Sons, New York, USA, 1989.
- [73] J. F. Briesmeister, MCNPTM - A General Monte Carlo N-Particle Transport Code, Report LA-13709-M, Los Alamos National Laboratory, Los Alamos NM, USA (2000).
- [74] Z. H. Cho, R. L. Chase, Comparative Study of the Timing Techniques Currently Employed with Ge Detectors, *Nucl. Instr. and Meth A* 356 (1995) 335-347.
- [75] A. R. Frolov, T. V. Oslopova, Yu. N. Pestov, Double Threshold Discriminator for Timing Measurements, *Nucl. Instr. and Meth A* 98 (1972) 447-451 .

- [76] J. P. Fouan, J. P. Passerieux, A time Compansation Method for Coincidences Using Large Coaxial Ge(Li) Detetors, Nucl.Instr. and Meth A 62 (1968) 327-329 .
- [77] A. Georgiev, W. Gast, Digital Pulse Processing in High Resolution, High Throughput Gamma-Ray Spectroscopy, IEEE Trans.Nucl.Sci, NS-40, No. 4, 1993, 770-779.
- [78] G. F. Knoll, Radiation Detection and Measurement, 3rd edition, John Wiley and Sons, Inc., New York, USA, 2000.
- [79] V. T. Jordanov, G. F. Knoll, Digital Syntesis of the Pulse Shapes in Real Time for High Resolution Radiation Spectroscopy, Nucl.Instr. and Meth. A 345 (1994) 337-345.
- [80] V. Radeka, Trapezoidal Filtering of Signals from Large Germanium Detectors at High Rates, IEEE Trans.Nucl.Sci, NS-19, No. 1, 1972, 412-428.
- [81] P. Ryge, R. R. Borchers, Coincidence Resolving Time of Large Coaxial Ge(Li) Detectors, Nucl.Instr. and Meth A 95 (1971) 137-140 .
- [82] Z. H. Cho, R. L. Chase, Comparative Study of the Timing Techniques Currently Employed with Ge Detectors, Nucl.Instr. and Meth A 356 (1995) 335-347.
- [83] A. R. Frolov,T. V. Oslopova, Yu. N. Pestov, Double Treshold Discriminator for Timing Measurements, Nucl.Instr. and Meth A 98 (1972) 447-451 .
- [84] J. P. Fouan, J. P. Passerieux, A time Compansation Method for Coincidences Using Large Coaxial Ge(Li) Detetors, Nucl.Instr. and Meth A 62 (1968) 327-329 .
- [85] A. Georgiev, W. Gast, Digital Pulse Processing in High Resolution, High Throughput Gamma-Ray Spectroscopy, IEEE Trans.Nucl.Sci, NS-40, No. 4, 1993, 770-779.
- [86] G. F. Knoll, Radiation Detection and Measurement, 3rd edition, John Wiley and Sons, Inc., New York, USA, 2000.
- [87] V. T. Jordanov, G. F. Knoll, Digital Syntesis of the Pulse Shapes in Real Time for High Resolution Radiation Spectroscopy, Nucl.Instr. and Meth. A 345 (1994) 337-345.
- [88] V. Radeka, Trapezoidal Filtering of Signals from Large Germanium Detectors at High Rates, IEEE Trans.Nucl.Sci, NS-19, No. 1, 1972, 412-428.
- [89] P. Ryge, R. R. Borchers, Coincidence Resolving Time of Large Coaxial Ge(Li) Detectors, Nucl.Instr. and Meth A 95 (1971) 137-140 .
- [90] EXFOR - Nuclear reaction experimental data files, www.nndc.bnl.gov

- [91] ENSDF - Evaluated Nuclear Structure Data Files, www.nndc.bnl.gov
- [92] Y. Han, Calculations and analysis of $n + ^{50,52,53,54}\text{Cr}$ reactions in the $E_n \leq 250\text{MeV}$ energy range, Nucl.Phys.A 748 (2005) 75-111.
- [93] P. Oblozinsky, S. Hlavac, G. Maino, A. Mengoni, Gamma-ray production from $^{52}\text{Cr}(n,xn\gamma)$ reactions at 14.6 MeV, Il Nuovo Cimento vol.105 A, N7, 965.
- [94] N. Olsson, E. Ramstrom, B. Trostell, Neutron elastic and inelastic scattering from Mg, Si, S, Ca, Cr, Fe and Ni at $E_n = 21.6\text{ MeV}$, Nucl.Phys. A 513 (1990) 205-238.
- [95] T. Yamamoto, Y. Hino, S. Itagaki, K. Sugiyama, Gamma-ray production cross section for interaction of 14.8 MeV neutrons with O, Na, Al, Cl, Cr, Fe, Ni, Cu, Pb, J. of Nucl. Sci. and Technol. 15 (1978) 797.
- [96] P. T. Karatzas, G. Couchell, B. K. Barnes, L. E. Beghian, P. Harihar, A. Mittler, D. J. Pullen, E. Sheldon, N. B. Sullivan, neutron Inelastic scattering cross-section for natural chromium determined from the $(n,n'\gamma)$ reaction, Nucl. Sci. and Eng. 67 (1978) 34-53.
- [97] I. A. Korzh, V. A. Mishchenko, E. N. Mozhzhukhin, M. V. Pasechnik, N. M. Pravdivyi, I. E. Sanzhur, Study of neutron scattering in the energy region 1.5-3.0 MeV by even-even isotopes of Cr, Sov. J. Nucl. Phys. 26(6), Dec.1977.
- [98] F. I. Habbani, A. H. Jiggins, Gamma emmision cross-sections for 23 elements using 3.29 MeV neutron inelastic scattering Nucl.Instr. and Meth I34 (1976) 545-552.
- [99] F. Voss and C. Cierjacks and D. Erbe and G. Schmalz, Measurement of the γ -ray production cross sections from inelastic neutron scattering in some chromium and nickel isotopes between 0.5 and 10 MeV, in: Conf. on Nuclear Cross Sections and Technology, Washington USA, 1975, p. 916.
- [100] E. M. Burimov, Cross-sections for excitation of ^{16}O , ^{27}Al , ^{52}Cr and $^{64,66,68}\text{Zn}$ levels by 14.6 MeV neutrons, Sov. J. Nucl. Phys. 9(5), Nov.1969.
- [101] Y. G. Degtyarev, N. V. Protopopov, Excitation of low-lying levels of ^{27}Al , Cr, Fe and Bi in the inelastic scattering of 1-4 MeV neutrons, Atomnaya Energiya, Vol.23, No.6, 568-571, Dec. 1967.
- [102] D. M. Van Patter, N. Nath, S. M. Shadroth, S. .S. Malik, M. A. Rothman, Gamma rays from inelastic neutron scattering in chromium, Phys. Rev. 128, 1246 (1962).
- [103] R. M. Kiehn, C. Goodman, neutron inelastic scattering, Phys. Rev. 95, 989 (1954).
- [104] A. Fessler, E. Wattecamps, D. L. Smith, S. M. Qaim, Excitation functions of $(n,2n)$, (n,p) , $(n,np+pn+d)$, and (n,α) reactions, Phys. Rev. C58, 996 (1998).

- [105] J. A. Harvey, D. C. Larson, N. W. Hill, Neutron resonance spectroscopy for n+⁵²Cr: total and differential elastic scattering cross-sections, Phys.Rev. C62, 014608 (2000)
- [106] R.B.Galloway and J.Rahighi, A novel fast neutron time-of-flight system, Nucl.Instr. and Meth in Phys Research A 297 (1990) 452-456.
- [107] X.Wang, Y.Wang, D.Wang, J.Rapaport Neutron scattering and neutron emission cross-sections on 27-Al, 93-Nb and 209-Bi at 7 MeV, Nucl. Phys. A465(1987) 483-496.
- [108] A.Smith, P.Guenther, J.Whalen Fast neutron cross-sections of elemental Bismuth, Nucl. Sci. and Eng. 75 (1980) 69-75.
- [109] J.K.Dickens Neutron-induced gamma-ray production in Lead-208 for incident-neutron energies between 4.9 and 8.0 MeV and in Bismuth-209 for an incident-neutron energy of 5.4 MeV.,Nucl. Sci. and Eng. 63 (1977) 101-109.
- [110] M.Matoba, M.Hyakutake, H.Tawaram, K.Thuji, H.Hasuyama, S.Matsuki, A.Katase, M.Sonoda, Scattering of 14.1 MeV from ²⁰⁹Bi, Nucl. Phys. A204 (1973) 129-137.
- [111] S.Tanaka, Y.Tomita, K.Ideno, S.Kikuchi, Fast neutron scattering from ¹³⁹La, ¹⁴¹Pr, Er, and ²⁰⁹Bi Nucl. Phys. A179 (1972) 513-523.
- [112] P.Kuijper, J.C.Veefkind, C.C.Jonker, Neutron scattering from Bismuth, Strontium and Sodium at 14.8 MeV Nucl. Phys. A181 (1972) 545-565.
- [113] A.B.Smith, J.F.Whalen, Fast-neutron total and scattering cross sections of Bismuth Nucl. Sci. and Eng. 41 (1970) 63-69.
- [114] R.O.Owens, J.H.Towle, The level density of the deformed rare-earth nuclei Nucl. Phys. A112 (1968) 337-359.
- [115] L.Cranberg, T.A.Oliphant, J.Levin, C.D.Zafiratos, Fast-neutron scattering from nuclides in the lead region Phys. Rev. vol.159 4(1967).
- [116] R.M.Wilenzick, K.K.Seth, P.R.Bevington, H.W.Lewis, Elastic and inelastic scattering of 6 MeV neutrons Nucl. Phys. 62 (1965) 511-525.
- [117] P.H.Stelson, R.L.Robinson, H.J.Kim, J.Rapaport, G.R.Satchler, Excitation of collective states by the inelastic scattering of 14 MeV neutrons Nucl. Phys. 68 (1965) 97-140.
- [118] D.B.Thomson, Nuclear level densities and reaction mechanisms from inelastic neutron scattering Phys. rev. vol.129 4(1963).
- [119] L.Rosen, L.Stewart, Neutron emission probabilities from the interaction of 14 MeV neutrons with Be, Ta, and Bi Phys. Rev. vol.107 3(1957).

- [120] L.Cranberg, J.S.Levin, Neutron scattering at 2.45 MeV by a time-of-flight method Phys. Rev. vol.103 2(1956).
- [121] J.Rethmeier, C.C.Jonker, M.Rodenburg, J.W.Hovenier, D.R.v.d.Meulen, Differential cross sections for d-t neutrons by time of flight methods Nucl.Instr. and Meth 17 (1962) 273-285.
- [122] J.B.Weddell, Scattering of 4.4 MeV neutrons by Aluminum, Calcium, Chromium, and Bismuth Phys. Rev. vol.104 4(1956).
- [123] V.E.Scherrer, B.A.Allison, W.R.Faust, Gamma radiation from interaction of 3.2 MeV neutrons with various materials Phys. Rev. vol.96 2(1954).
- [124] H.B.Levy, I.Perlman, Long-lived isomer of RaE (^{210}Bi) Phys. Rev. vol.94 1(1953).
- [125] E.A.Eliot, D.Hicks, L.E.Beghian, H.Halban, Inelastic scattering of neutrons Phys. Rev. vol.94 1(1953).
- [126] R.M.Laszewski, P.Axel, Interaction of photons with ^{208}Pb and neighboring isotopes at energies below the neutron emmission threshold, Phys. Rev. C19, no.2-342 (1979).
- [127] L.R.Vesser, E.D.Arthur, P.G.Young, Cross sections for (n,2n) and (n,3n) reactions above 14 MeV, Phys. Rev. C 16, no.5 - 1792 (1977).
- [128] A.Adam, P.Hrasko, G.Palla, P.Quittner, The mechanism of the (n,2n) reaction, Nucl. Phys. 49 (1963) 489-495
- [129] V.J.Ashby, H.C.Catron, L.L.Newkirk, C.J.Taylor, Absolute measurement of (n,2n) cross-sections at 14.1 MeV Phys. Rev. vol. 111, no.2 - 616 (1958).
- [130] EXFOR files, www.nndc.bnl.gov
- [131] ENSDF files, www.nndc.bnl.gov
- [132] R.M.Laszewski, P.Axel, Interaction of photons with ^{208}Pb and neighboring isotopes at energies below the neutron emmission threshold, Phys. Rev. C19, no.2-342 (1979).
- [133] H.Zhou, X.Wang, C.Wang, M.Hua, G.Huang, G.Fan, T.Lu, S.Bartel, Discrete gamma radiation in interaction of 14.9 MeV neutrons with natural Lead Nucl. Sci. and Eng. 134 (2000) 106-113
- [134] S.F.Hicks, J.M.Hanly, S.E.Hicks, G.R.Shen, M.T.McEllistrem, Neutron scattering cross sections for $^{204,206}\text{Pb}$ and neutron and proton amplitudes of E2 and E3 excitations Phys. Rev. C 49, no.1 (1994).
- [135] J.K.Dickens, Gamma-ray transitions among levels of ^{206}Pb Phys. Rev. C 28, no.2 (1983).

- [136] T.Yamamoto, Y.Hino, S.Itagaki, K.Sugiyama, Gamma-ray production cross sections for interactions of 14.8 MeV neutrons with O, Na, Al, Cl, Cr, Fe, Ni, Cu and Pb J. of Nucl. Sci. and Technol. 15[11] (1978) 797-805.
- [137] G.N.Salaita, P.K.Eapen, Isomeric cross sections for (n, 2n) reactions in Thallium, Lead and Bismuth at 14.8 MeV J. inorg. nucl. Chem. 35, (1973) 2139-2143.
- [138] L.Cranberg, T.A.Oliphant, J.Levin, C.D.Zafiratos, Fast-neutron scattering from nuclides in the Lead region Phys. Rev. 159, no.4 (1967).
- [139] L.Cranberg, C.D.Zafiratos, Excitation of a 3-collective state by low-energy neutron scattering Phys. Rev. 142, no.3 (1966).
- [140] S.G.Buccino, C.E. Hollandsworth, H.W.Lewis, P.R.Bevington, Inelastic scattering of neutrons from medium and heavy nuclei Nucl. Phys. 60, (1964) 17-34.
- [141] D.B.Thomson, Nuclear level densities and reaction mechanisms from inelastic neutron scattering Phys. Rev. 129, no.4 (1963).
- [142] J.W.Boring, M.T.McEllistrem, Differentialcross sections for (n,n'γ) reactions in several nuclei Phys. Rev. 124, no.5 (1961).
- [143] H.H.Landon, A.J.Elwyn, G.N.Glasoe, S.Oleksa, Neutron scattering at 2.2 MeV by time of flight Phys. Rev. 112, no.4 (1958).
- [144] R.B.Day, Gamma rays from neutron inelastic scattering Phys. Rev. 102, no.3 (1956).
- [145] R.M.Kiehn, C.Goodman, Neutron inelastic scattering Phys. Rev. 95, no.4 (1954).
- [146] D.J.Horen, J.A.Harvey and N.W.Hill $^{206}\text{Pb}+\text{n}$ resonances fro E=600-900 keV: Neutron strength functions Phys. Rev. C24, 1961-1968 (1981).
- [147] T.Yamamoto, Y.Hino, S.Itagaki, K.Sugiyama, Gamma-ray production cross sections for interactions of 14.8 MeV neutrons with O, Na, Al, Cl, Cr, Fe, Ni, Cu and Pb J. of Nucl. Sci. and Technol. 15[11] (1978) 797-805.
- [148] L.Cranberg, T.A.Oliphant, J.Levin, C.D.Zafiratos, Fast-neutron scattering from nuclides in the Lead region Phys. Rev. 159, no.4 (1967).
- [149] R.B.Day, Gamma rays from neutron inelastic scattering Phys. Rev. 102, no.3 (1956).
- [150] H.Vonach, A.Pavlik, M.B.Chadwick, R.C.Haight, R.O.Nelson, S.A.Wender, P.G.Young $^{207,208}\text{Pb}(\text{n},\text{xn}\gamma)$ reactions for neutron energies from 3 to 200 MeV, Phys. Rev. C 50, no. 4 1952 (1994).
- [151] D.J.Horen, J.A.Harvey and N.W.Hill Doorway staes in s-, p-, and d-wave entrance channels in $^{207}\text{Pb}+\text{n}$ reaction Phys. Rev. C 18, 722-735 (1978).

- [152] H.Vonach, A.Pavlik, M.B.Chadwick, R.C.Haight, R.O.Nelson, S.A.Wender, P.G.Young $^{207,208}\text{Pb}(n,xn\gamma)$ reactions for neutron energies from 3 to 200 MeV, Phys. Rev. C 50, 1952 (1994).
- [153] H.Zhou, X.Wang, C.Wang, M.Hua, G.Huang, G.Fan, T.Lu, S.Bartel, Discrete gamma radiation in interaction of 14.9 MeV neutrons with natural Lead Nucl. Sci. and Eng. 134 (2000) 106-113
- [154] S.Hlavac, P.Oblozinsky, L.Dostal, I.Turzo, V.Vonach, A.Pavlik, S.Somakov Study of gamma radiation from interaction of 14.7 MEv neutrons with ^{208}Pb Nucl. Sci. and Eng. 119 (1995) 195-202
- [155] M.Yeh, P.E.Garretr, C.A.McGrath, S.W.Yates, T.Belgya Search for a 2485 keV γ ray in ^{208}Pb with the inelastic neutron scattering reaction, Phys. Rev. C 54, 942 (1996)
- [156] M.Yeh, P.E.Garretr, C.A.McGrath, S.W.Yates, T.Belgya Two phonon octupole excitation in ^{208}Pb , Phys. Rev. Lett 76, 1208 (1996)
- [157] R.W.Finlay, J.R.M.Annand, T.S.Cheema, J.Rapaport, F.S.Dietricht Energy dependence of neutron scattering from ^{208}Pb in the energy range 7-50 MeV Phys. Rev. C 30, 796 (1984)
- [158] F.S.Dietrich, R.W.Finlay, S.Mellema, G.Randers-Pehrson, F.Petrovich Isospin dependence of the microscopic optical model for nucleon scattering Phys. Rev. Lett 51, 1629 (1983)
- [159] P.P.Guss, C.E.Floyd, K.Murphy, C.R.Howell et al. Spin-orbit deformations deduced from analysing powers fro inelastic neutron scattering from ^{54}Fe , ^{56}Fe , ^{58}Ni , ^{60}Ni , ^{120}Sn and ^{208}Pb Phys. Rev. C 25, 2854 (1982)
- [160] D.E.bainum, R.W.Finlay, J.Rapaport, J.D.Carlson, W.G.Love Excitation of low-lying collective states in ^{40}Ca and ^{208}Pb by inelastci neutron scattering Phys. Rev. C 16, 1377 (1977)
- [161] J.K.Dickens Neutron-induced gamma-ray production in Lead-208 for incident-neutron energies between 4.9 and 8.0 MeV and in Bismuth-209 for an incident-neutron energy of 5.4 MeV.,Nucl. Sci. and Eng. 63 (1977) 101-109.
- [162] D.O.Nellis, I.L.Morgan, E.L.Hudspeth Neutron induced gamma-ray production in 208 Phys. Rev. C 9, 1972 (1974)
- [163] J.H.Towle, W.B.Gilboy Inelastic neutron scattering in ^{208}Pb , Nucl.Phys. 44 (1963) 256-267
- [164] V.L.Glagolev, P.A.Yampolskii An investigation of (n,2n) reactions leading to isomer formation Sov.Phys. JETP 13, no. 3, 520 (1961)
- [165] R.Prasad, D.C.Sarkar Measurement of (n,2n) reaction cross-sections at 14.8 MeV Nucl.Phys. 88 (1966) 349-352

- [166] O.Hausser, F.C.Khanna, D.Ward Gamma decay of low-lying states near the ^{208}Pb closed shell, Nucl.Phys. A194 (1972) 113-139

Acknowledgements

I would like to thank several people who, in different ways, contributed to the accomplishment of this Ph.D.

Firstly, I have to thank the promotor of this thesis, Prof.Dr. D.Bucurescu, for his support and relevant advice. This work would have not been possible without the daily supervision of Dr. A.J.M.Plompen who helped me significantly in the development of this work. Moreover, I have to thank Prof. P.Rullhusen for accepting me as a fellow at IRMM.

I am grateful to Dr. C.Borcea for many fruitful discussions and advice during our daily collaboration.

A special thank should go to J.Gonzalez for his help and advice in setting up the data acquisition system. I thank to V.Fitsch and the Informatics Unit Helpdesk for their continuous help in solving many PC-related problems. I appreciated also the help of W.Shubert during the short period in which we had the chance to collaborate.

I want to mention especially Dr. W.Mondelaers and all the operators of GELINA and all the colleagues of NP unit for the support during these three years at IRMM.

I really appreciated the friendship of A.Porada, L.D.Smet, S.Vermote, A.Borrela, M.Flaska, I.Ivailov, P.Siegler, K.Volev and R.Wynants, who made more pleasant my stay in Belgium.

I would also like to thank everyone else who I have not mentioned personally and contributed to this work.

Finally but the most important I have to thank my family for their continuous support during these three years and not only. From my family, special thanks go to my wife Mihaela Mihailescu for her continuous support and understanding.

Summary

The present work was motivated by the need of precise nuclear data for applications. The transmutation of long lived nuclear waste in subcritical reactors as the Accelerator Driven System (ADS) is one of the current application to which a large amount of research is dedicated. Precise calculation of the reactor parameters requires complete and precise nuclear data sets. Such nuclear data cannot be produced only with the present nuclear codes and experimental data are still needed for the validation of these codes.

The $(n, xn\gamma)$ reactions ($x=1,2,3$) are important nuclear processes that have to be considered in the reactor calculations for their influence on the neutron propagation calculations in the reactor. These reactions have an impact also for the dosimetry calculation and shielding design because γ -rays are emitted. In the $(n, xn\gamma)$ reactions on the materials present in the reactor an important amount of energy is lost by the incident neutrons.

To answer to the needs of the nuclear applications, the neutron $(n, xn\gamma)$ cross-sections ($x=1,2,3$) were measured for five different nuclei ^{52}Cr , ^{209}Bi and $^{206,207,208}\text{Pb}$. ^{52}Cr is present in the stainless steels used as structure materials of the new generations of reactors. Bi and Pb are considered for the spallation target and for the cooling system of the ADS as Pb-Bi eutectic alloy.

A new experimental setup was developed at GELINA for the measurements of the $(n, xn\gamma)$ reaction cross-sections ($x=1,2,3$) from the threshold up to 20 MeV neutron energy using the $(n, xn\gamma)$ -technique. The experimental setup was placed at 200 m flight length. The $(n, xn\gamma)$ -technique involves the detection of the γ -rays from the (n, xn) reactions. Large volume HPGe detectors were used for the γ -ray detection. The advantage of these detectors consists of their very good energy resolution that allows the γ -ray identification in complex spectra and the increased detection efficiency. The time resolution for the present setup was 8 ns for all HPGe detectors. The neutron energy resolution that resulted from this time resolution was 1.1 keV at 1 MeV (35 keV at 10 MeV).

Up to four large volume HPGe detectors were used in the experimental setup. The detectors are placed at 110° and 150° with respect to the beam directions. These angles are the roots of the fourth order Legendre polynomial and allowed precise angle integration through a Gauss quadrature. The neutron flux was measured with a multilayer ^{235}U fission chamber. In this way, the measured cross-sections were normalized to the standard ^{235}U neutron induced fission cross-section.

The data acquisition system used for the HPGe detectors was based on conventional electronics, with standard NIM modules. No γ - γ coincidence was done

between the HPGe detectors. The HPGe data were recorded simultaneously with the data from the fission chamber to avoid any systematic errors from the neutron flux fluctuations. The dead time of the data acquisition systems for both HPGe detectors and fission chamber was negligible. Special care was taken for the absolute efficiency determination of the HPGe detectors.

Highly enriched isotopic samples were used in the present experiments to reduce the number of peaks in the γ -ray spectrum and to easily separate different $(n, xn\gamma)$ reactions in the sample. To achieve a small total uncertainty of about 5 % for the most intense γ -rays, samples with diameters between 5 cm and 8 cm and thicknesses of several mm were used. Therefore, the measured data had to be corrected for neutron attenuation and multiple scattering in the sample.

The good precision in measuring the $(n, xn\gamma)$ cross-sections (good neutron energy resolution and small total uncertainty) was obtained by extended runs of minimum 500 hours of data acquisition. To reduce the time for the data acquisition, special attention was given for the increase in of the detection efficiency. The data acquisition system based on conventional electronics has two limitations regarding the detection efficiency. Firstly, at neutron sources as GELINA, a γ -flash from the accelerator target arrives at the measurement station before every neutron burst and this γ -flash produces a variable dead time in the conventional acquisition system. To avoid this situation, an inhibit signal was created to reject all the neutron bursts in which a γ -flash induced event was detected in the HPGe detectors. The second limitation of the conventional acquisition system is due to the use of the Slow Rise Time Rejection (SRTR) function of the Constant Fraction Discriminator (CFD) module. This function gives a very good time resolution, but at the expense of a decrease of efficiency, especially at low energies.

One solution for solving these two limitations of the conventional acquisition system and to increase the detection efficiency of the present experimental setup is a new data acquisition system based on fast digitizers. Therefore, a commercially available fast digitizer with 12-bits and 420 MSPS was tested for use in time-of-flight measurement at GELINA with large volume HPGe detectors. The difficulty of implementing such data acquisition is coming from the diversity of signal shapes in the large volume HPGe detectors. With the increase of the detector volume, the changes in the pulse shape and in the pulse rise time from the preamplifier of the HPGe detector are even more important. Different time and amplitude algorithms were tested and compared off-line, on the same data sets recorded with the fast digitizer. The algorithms with the best performances were implemented for an online data acquisition.

To prove the digitizer performances in real conditions, the $(n, xn\gamma)$ cross-sections of ^{206}Pb and ^{208}Pb nuclei were measured in parallel with both acquisition systems, with the conventional electronics and with the fast digitizer. The output signals from the HPGe detectors were split and given simultaneously to both systems. After the analysis of the data from both systems the same values were obtained for the differential gamma production cross-sections of ^{206}Pb and ^{208}Pb . From the comparison between the differential gamma production cross-sections obtained with the two different acquisition systems it resulted that the fast digitizer can be success-

fully used for the $(n, xn\gamma)$ cross-sections measurements ($x=1,2,3$) with large volume HPGe detectors at GELINA. The conventional acquisition system can be replaced completely by the fast digitizer. The advantage of the fast digitizer compared with the conventional data acquisition system is the increased efficiency especially at low γ -ray energies, below 500 keV. The fast digitizer has almost the same time and γ -ray energy resolution as the system based on conventional electronics. Moreover, the electronic scheme of the setup is much simplified when the fast digitizer is used.

The detailed results for the $(n, xn\gamma)$ cross-sections measurements ($x=1,2,3$) for the five nuclei which were studied in this project, ^{52}Cr , ^{209}Bi and $^{206,207,208}\text{Pb}$, are presented in Chapter 5. These results were obtained only with the conventional data acquisition system. The data from the digitizer were not used here. One different section was dedicated to every nucleus.

The differential gamma production cross-sections at 110° and 150° were the primary measured quantities in the present experiments. From these quantities, the angle integrated gamma production cross-sections were obtained through a Gauss quadrature. Based on the evaluated level scheme of the every nucleus and on the integral gamma production cross-sections, the total inelastic and the inelastic level cross-sections were constructed. For each nucleus, at least one gamma ray was observed from the decay of the levels up to about 3.5-4 MeV excitation energy. Therefore, above this energy, the total inelastic and the level cross-sections constructed here are lower and respectively higher limits because of the decay that was neglected from higher excited levels.

In the present experiments, the gamma production cross-section was measured for a minimum of 12 γ -rays (in ^{52}Cr) and a maximum of 39 γ -rays (in ^{209}Bi) from inelastic reaction channel. For the $(n, 2n)$ reaction channel, the gamma production cross-section was measured for at least two γ -rays in each nucleus. The $(n, 3n)$ gamma production cross-section was measured only for one γ -ray from ^{208}Pb nucleus.

The $(n, xn\gamma)$ cross-sections were measured from the threshold up to 20 MeV, in one long run for each sample, with unprecedented neutron energy resolution and total uncertainty. The present results were compared with the existing experimental data and with calculations performed with the Talys code with the default input parameters. Compared with the present results, the previous measured data are scarce and sometimes not in agreement with each other. For a default calculation, the Talys code describes well the present measured values.

Shortly, the $(n, xn\gamma)$ cross-sections ($x=1,2,3$) were measured for five different nuclei ^{52}Cr , ^{209}Bi and $^{206,207,208}\text{Pb}$ on the full neutron energy range, from the threshold up to 20 MeV in only one run for every nucleus. In these measurements, an extensive set of precise cross-sections data was obtained. The precision of the data consist of neutron energy resolution and total relative uncertainty of about 5% for the most intense γ -rays and for the total inelastic cross-section. These data will be sent to the databases as EXFOR file and part of them are already available for online access.

Special attention was given to the increase of the detection efficiency of the experimental setup. As a result, a new data acquisition system based on a fast digitizer was implemented for online acquisition. This fast digitizer can replace completely the system based on conventional electronics in the further experiments. The present

acquisition system based on the fast digitizer is one of the first experiments were a fast digitizer is used with large volume HPGe detectors for time-of-flight measurements and comparable time and amplitude resolutions were obtained as in the case of the conventional electronics.

Rezumat

Această lucrare a fost motivată de nevoie de date nucleare precise pentru diferite aplicații. Transmutarea deseurilor radioactive cu timpi de viață lungi în reactori subcritici precum Accelerator Driven System (ADS) este una din aplicațiile curente căreia îi este dedicată o mare parte din cercetarea curentă în domeniul nuclear. Calculele precise de reactori nucleari necesită seturi complete și precise de date nucleare. Astfel de date nucleare nu pot fi produse numai cu ajutorul codurilor nucleare actuale și încă este nevoie de date experimentale care să valideze rezultatele codurilor.

Reacțiile $(n,xn\gamma)$ cu $x=1,2,3$ sunt procese nucleare importante care trebuie considerate în calculele de reactori pentru modul în care influențează propagarea neutronilor în reactor. În reacțiile $(n,xn\gamma)$ pe materiale prezente într-un reactor nuclear, neutronul incident pierde o importantă cantitate de energie într-o sigură interacție și mai mult, secțiunile acestor reacții reprezintă o fracțiune importantă din secțiunea neutronică totală. Aceste reacții sunt considerate de asemenea în calculele de dozimetrie și de proiectare a sistemelor de ecranare și de radioprotecție pentru faptul că în urma acestor reacții sunt emise radiații γ .

Pentru a răspunde cerințelor aplicațiilor nucleare, în cadrul proiectului prezentat în această lucrare am măsurat secțiunile pentru reacțiile $(n,xn\gamma)$ cu $x=1,2,3$ pentru cinci nuclei diferite: ^{52}Cr , ^{209}Bi și $^{206,207,208}\text{Pb}$. ^{52}Cr este prezent în oțelurile inoxidabile folosite în materialele de structură ale noii generații de reactori nucleari. Bismutul și plumbul sunt materiale ce ar putea fi folosite în aliaj eutectic Pb-Bi pentru ținta de spalărie și pentru sistemul de răcire ale ADS.

Pentru aceste măsurători de secțiuni de reacție $(n,xn\gamma)$ ($x=1,2,3$) de la prag până la aproximativ 20 MeV a fost creat un nou aranjament experimental la sursa de neutroni GELINA. Aranjamentul experimental a fost amplasat la 200 m distanță de zbor. Secțiunile de reacție au fost măsurate prin tehnica $(n,xn\gamma)$, care presupune detecția radiațiilor γ emise în urma reacțiilor (n,xn) . Pentru detecția γ au fost folosiți detectori de volum mare de tip HPGe. Avantajul acestor detectori constă într-o rezoluție energetică foarte bună care permite identificarea precisă a picurilor γ în spectre complexe și în același timp acești detectori au o eficacitate de detecție sporită. Pentru detectorii de tip HPGe folosiți în acest experiment am folosit o rezoluție temporală de 8 ns. Această rezoluție temporală împreună cu baza de zbor de 200 m conduc la o rezoluție în energie a neutronilor incidenti de 1.1 keV la 1 MeV (35 keV la 10 MeV).

În prezentul aranjament experimental au fost folosiți maximum 4 detectori de volum mare (eficacitate relativă de detecție între 80 % și 104 %) de tip HPGe. Acești

detectori au fost așezați la unghiuri de 110° și respectiv 150° de grade față de direcția fasciculului incident de neutroni. Aceste două unghiuri reprezintă rădăcinile polinomului Legendre de ordinul 4 și permit integrarea unghiulară precisă a secțiunilor, printr-o cuadratură Gauss. Fluxul de neutroni a fost măsurat cu o cameră de fisiune cu ^{235}U . În acest fel secțiunile măsurate au fost normate la secțiunea standard de fisiune indusă de neutroni a ^{235}U .

Achiziția datelor a fost făcută cu un sistem de achiziție bazat pe electronică de tip NIM cu module convenționale. În aceste experimente nu au fost făcute măsurători de coincidență γ - γ între detectorii de tip HPGe. Datele de la aceștia din urmă au fost înregistrate simultan cu datele de la camera de fisiune pentru a evita posibilele erori sistematice introduse de fluctuațiile în fluxul de neutroni. Atât pentru achiziția detectorilor de germaniu cât și pentru cea a camerei de fisiune timpul mort de achiziție a fost neglijabil. O atenție sporită a fost acordată determinării eficacității de detecție a detectorilor de tip HPGe.

În experimentele descrise în această lucrare au fost folosite ținte îmbogățite pentru a reduce numărul de picuri în spectrele γ și pentru a facilita separarea diferitelor reacții ($n, xn\gamma$) în fiecare țintă. Pentru a obține o eroare totală de aproximativ 5 % pentru cele mai intense tranziții γ , am folosit ținte cu diametrul cuprins între 5 cm și 8 cm și grosimea de câțiva mm. De aceea secțiunile de reacție măsurate în aceste experimente au fost corectate pentru atenuarea și împărtierea multiplă a neutronilor în țintă.

Pentru a obține o bună precizie a măsurătorilor de secțiuni ($n, xn\gamma$), prin aceasta înțelegând o bună rezoluție în energie a neutronilor incidenti și o eroare totală mică, cel puțin 500 de ore de achiziție efectivă de date au fost necesare. Pentru a reduce timpul necesar achiziției de date, am acordat o atenție specială creșterii eficacității de detecție. Sistemul de achiziție bazat pe electronică convențională are două limitări privind eficacitatea de detecție. Mai întâi, la sursele de neutroni precum GELINA, fiecare puls de neutroni este precedat de un "flash" γ , care poate introduce un timp mort în sistemul de achiziție. Pentru a evita apariția unui astfel de timp mort variabil în sistemul de achiziție am creat un semnal de inhibit pentru a elimina toate pulsurile de neutroni în care a fost detectat un eveniment indus de γ -flash. Cea de-a doua limită a sistemului de achiziție bazat pe electronică convențională se datorează folosirii funcției Slow Rise Time Rejection (SRTR) a modulelor Constant Fraction Discriminator (CFD). Cu această funcție se obține o rezoluție temporală foarte bună, dar cu prețul unei scăderi în eficiență.

O soluție pentru rezolvarea acestor două limitări ale sistemului de achiziție convențional și pentru a mări eficacitatea de detecție a aranjamentului experimental este un nou sistem de achiziție bazat pe un digitizer rapid. Pentru aceasta, am testat un digitizer rapid, cu 12-biți și 420 MSPS pentru a fi folosit în măsurători de timp de zbor la GELINA cu detectori de volum mare de tip HPGe. Dificultatea folosirii unui astfel de digitizer rapid provine din diversitatea de forme a semnalelor de ieșire de la preamplificatorii detectorilor de volum mare de tip HPGe. Schimbările în forma și în timpul de creștere ale pulsurilor de la detectorii de tip HPGe se accentuează cu creșterea volumului detectorilor. Diferiți algoritmi pentru determinarea timpului și amplitudinii pulsurilor de la preamplificator au fost comparați off-line, pe ace-

leași seturi de date înregistrate cu digitizerul rapid. Algoritmii cu cele mai bune performante au fost implementați pentru o achiziție de date online.

Pentru a dovedi performanțele digitizerului rapid în condiții reale, secțiunile $(n, xn\gamma)$ pentru ^{206}Pb și ^{208}Pb au fost măsurate în paralel cu ambele sisteme de achiziție. Semnalele de ieșire de la detectorii de germaniu au fost împărțite și date simultan la cele două sisteme de achiziție. Valorile pentru secțiunile diferențiale de producție gama pentru ^{206}Pb și ^{208}Pb obținute în paralel cu cele două sisteme de achiziție sunt într-o concordanță foarte bună. Din această comparație între rezultatele obținute în paralel cu cele două sisteme de achiziție a rezultat ca digitizerul rapid poate fi folosit cu succes la GELINA pentru măsurători de secțiuni în reacțiile $(n, xn\gamma)$ ($x=1,2,3$) cu detectori de volum mare de tip HPGe. Sistemul de achiziție convențional poate fi înlocuit în experimentele viitoare cu sistemul de achiziție bazat pe digitizerul rapid. Avantajul acestui digitizer comparat cu sistemul de achiziție bazat pe electronică convențională constă în eficacitatea de detecție sporită, în special la energii gama joase, sub 500 keV. Rezoluțiile temporale și energetice ale digitizerului rapid sunt comparabile cu cele obținute cu module electronice convenționale. Mai mult schema electronică a aranjamentului experimental este mult simplificată în cazul în care digitizerul rapid este folosit.

Rezultatele detaliate ale măsurătorilor de secțiuni în reacțiile $(n, xn\gamma)$ pentru $x=1,2,3$ sunt prezentate în Capitolul 5 pentru toate cele 5 nucleu studiate: ^{52}Cr , ^{209}Bi și $^{206,207,208}\text{Pb}$. În fiecare din cele 5 secțiuni ale acestui capitol este prezentat câte un nucleu. Aceste rezultate au fost obținute numai cu sistemul de achiziție bazat pe electronică convențională. Datele înregistrate cu digitizerul rapid nu au fost folosite aici.

Secțiunile diferențiale de producție gama la 110° și 150° au fost mărimile primare determinate în aceste experimente. Din aceste secțiuni au fost obținute secțiunile integrate după unghi printr-o integrare de cuadratură Gauss. Pe baza schemelor de nivele evaluate ale acestor nucleu și folosind secțiunile de producție gama integrale au fost construite secțiunea totală inelastica și secțiunile nivelelor excitate inelastice. Pentru fiecare nucleu a fost observată cel puțin o tranziție gama din dezintegrarea fiecarui nivel până la 3.5-4 MeV energie de excitare. De aceea, deasupra acestei energii, secțiunea totală inelastica și secțiunile de nivel prezentate aici sunt limite inferioare și respectiv superioare pentru că dezintegrările de pe nivelele superioare au fost neglijate.

În aceste experimente secțiunile inelastice de producție gama au fost măsurate pentru cel puțin 12 tranziții γ pentru ^{52}Cr și maximum 39 tranziții pentru ^{209}Bi . Pentru canalul de reacție $(n, 2n)$, secțiunile de producție gama au fost măsurate pentru cel puțin 2 tranziții gama în fiecare nucleu. În cazul reacției $(n, 3n)$ secțiunea de producție gama a fost măsurată doar pentru o tranziție gama din nucleul ^{208}Pb .

Secțiunile de reacție $(n, xn\gamma)$ au fost măsurate de la energia de prag a neutronilor incidenti până la 20 MeV, într-un sigur experiment pentru fiecare nucleu, cu o rezoluție în energie a neutronilor incidenti fără precedent și cu o eroare relative totală mică. Rezultatele acestor experimente au fost comparate cu rezultate experimentale existente și cu calcule făcute cu codul Talys cu parametrii de intrare inițiali. În comparație cu rezultatele prezentate în această lucrare, rezultatele găsite

în literatură sunt foarte puține și uneori nu sunt în concordanță între ele. Calculele de secțiuni de reacție făcute cu Tallys descriu bine rezultatele măsurătorilor actuale ținând cont de faptul de în calcule au fost folosiți parametrii inițiali ai codului.

În concluzie, secțiunile în reacțiile $(n, xn\gamma)$ ($x=1,2,3$) au fost măsurate pentru 5 nuclei diferiti ^{52}Cr , ^{209}Bi și $^{206,207,208}\text{Pb}$ pe întreaga scală de energie a neutronilor incidenti, de la energia de prag până la 20 MeV, într-un singur experiment pentru fiecare nucleu. Din aceste măsurători au rezultat un set mare de secțiuni de reacții măsurate cu precizie. Precizia datelor constă în rezoluția energetică a neutronilor incidenti și în eroarea totală de aproximativ 5 % pentru secțiunea de producție a celor mai intense tranziții γ și pentru secțiunile totale inelastice. Aceste date vor fi trimise la bazele de date nucleare în format EXFOR și deja o parte din ele sunt accesibile online.

În cadrul acestui proiect a fost acordată atenție deosebită creșterii eficienței de detecție a aranjamentului experimental. Ca rezultat al acestor eforturi a fost creat un nou sistem de achiziție bazat pe un digitizer rapid care va înlocui sistemul de achiziție actual bazat pe electronică convențională în urmatoarele experimente. Acest sistem de achiziție bazat pe un digitizer rapid reprezintă unul dintre primele experimente în care un digitizer rapid a fost folosit împreună cu detectori de volum mare de tip HPGe în măsurători de timp de zbor și au fost obținute rezoluții temporale și de amplitudine comparabile cu cele ale electronicii convenționale.

European Commission

EUR 22343 EN – DG Joint Research Centre, Institute for Reference Materials and Measurements

Title: Neutron ($n,xn\gamma$) cross-section measurements for ^{52}Cr , ^{209}Bi and $^{206,207,208}\text{Pb}$ from threshold up to 20 MeV

Authors: Liviu Cristian Mihailescu

Luxembourg: Office for Official Publications of the European Communities

2006 – 236 pp. – 29.7 x 20.9 cm

EUR - Scientific and Technical Research series; ISSN 1018-5593

ISBN 92-79-02885-5

Abstract

The present report contains the thesis prepared by the author to obtain the degree of Doctor of Science from the University of Bucharest, Faculty of Physics. The work presented in this thesis was carried out at the GELINA facility and in the Neutron Physics Unit of the IRMM in Geel, Belgium. The work was performed while the author was employed as a JRC grant holder (contract number 20207) under the supervision of A. Plompen. This work received financial support from the EUROTRANS Integrated Project under contract number 22390.

The mission of the JRC is to provide customer-driven scientific and technical support for the conception, development, implementation and monitoring of EU policies. As a service of the European Commission, the JRC functions as a reference centre of science and technology for the Union. Close to the policy-making process, it serves the common interest of the Member States, while being independent of special interests, whether private or national.

ISBN 92-79-02885-5



9 789279 028854



Publications Office
Publications.eu.int